

UC Berkeley

UC Berkeley Electronic Theses and Dissertations

Title

Composition Optimization of Lithium-Based Ternary Alloy Blankets for Fusion Reactors

Permalink

<https://escholarship.org/uc/item/50j054mh>

Author

Jolodosky, Alejandra

Publication Date

2017

Peer reviewed|Thesis/dissertation

Composition Optimization of Lithium-Based Ternary Alloy Blankets for Fusion
Reactors

by

Alejandra Jolodosky

A dissertation submitted in partial satisfaction of the

requirements for the degree of

Doctor of Philosophy

in

Engineering - Nuclear Engineering

in the

Graduate Division

of the

University of California, Berkeley

Committee in charge:

Professor Massimiliano Fratoni, Chair

Professor Jasmina Vujic

Professor Michael Nacht

Spring 2017

Composition Optimization of Lithium-Based Ternary Alloy Blankets for Fusion
Reactors

Copyright 2017

by

Alejandra Jolodosky

Abstract

Composition Optimization of Lithium-Based Ternary Alloy Blankets for Fusion Reactors

by

Alejandra Jolodosky

Doctor of Philosophy in Engineering - Nuclear Engineering

University of California, Berkeley

Professor Massimiliano Fratoni, Chair

The goal of this dissertation is to examine the neutronic properties of a novel type of fusion reactor blanket material in the form of lithium-based ternary alloys. Pure liquid lithium, first proposed as a blanket for fusion reactors, is utilized as both a tritium breeder and a coolant. It has many attractive features such as high heat transfer and low corrosion properties, but most importantly, it has a very high tritium solubility and results in very low levels of tritium permeation throughout the facility infrastructure. However, lithium metal vigorously reacts with air and water and presents plant safety concerns including degradation of the concrete containment structure. The work of this thesis began as a collaboration with Lawrence Livermore National Laboratory in an effort to develop a lithium-based ternary alloy that can maintain the beneficial properties of lithium while reducing the reactivity concerns. The first studies down-selected alloys based on the analysis and performance of both neutronic and activation characteristics. First, 3-D Monte Carlo calculations were performed to evaluate two main neutronics performance parameters for the blanket: tritium breeding ratio (TBR), and energy multiplication factor (EMF). It was found that the elements that exhibit low absorption cross sections and higher Q-values, such as Pb, Sn, and Sr, perform well with those that have high neutron multiplication such as Pb and Bi. These elements meet TBR constraints ranging from 1.02 to 1.1. However, most alloys do not reach EMFs greater than 1.15. Alloys with adequate results based on TBR and EMF calculations were considered for activation analysis. Activation simulations were executed with 50 years of irradiation and 300 years of cooling. It was discovered that bismuth is a poor choice due to achieving the highest decay heat, contact dose rates, and accident doses. In addition, it does not meet the waste disposal ratings (WDR).

The straightforward approach to obtain Monte Carlo TBR and EMF results required 231 simulations per alloy and became computationally expensive, time consuming, and inefficient. Consequently, alternate methods were pursued. A collision history-based methodology recently developed for the Monte Carlo code Serpent, calculates perturbation effects on practically any quantity of interest. This allows multiple responses to be calculated by perturbing the input parameter without having to directly perform separate calculations. The approach is strictly created for critical systems, but was utilized as the basis of a new methodology implemented for fixed source problems, known as Exact Perturbation Theory (EPT). EPT can calculate the tritium breeding ratio response, caused by a perturbation in

the composition of the ternary alloy. The downfall of EPT methodology is that it cannot account for the collision history at large perturbations and thus, produces results with high uncertainties. Preliminary analysis for EPT with Serpent for a LiPbBa alloy demonstrated that 25 simulations per ternary must be completed so that most uncertainties calculated at large perturbations do not exceed 0.05. To reduce the uncertainties of the results, generalized least squares (GSL) method was implemented, to replace imprecise TBR results with more accurate ones. It was demonstrated that a combination of EPT Serpent calculations with the application of GLS for results with high uncertainties is the most effective and produces values with the highest fidelity. This approach was used to create an optimization scheme. The scheme finds an alloy composition that has a TBR within a range of interest, while imposing constraint on the EMF, and a requirement to minimize lithium concentration. It involved a three-level iteration process with each level zooming in closer on the area of interest to fine tune the correct composition. Both alloys studied, LiPbBa and LiSnZn, had optimized compositions close to the leftmost edge of the ternary, increasing the complexity of optimization due to the highly uncertain results found in these regions.

Additional GPT methodologies were considered for optimization studies, specifically with the use of deterministic codes. Currently, an optimization deterministic code, SMORES, is available in the SCALE code package, but only for critical systems. Subsequently, it was desired to change this code to solve problems for fusion reactors similarly to what was done in SWAN. So far, the fixed and adjoint source declaration and definition was added to the input file. As a result, alterations were made to the source code so that it can read in and utilize the new input information. Due to time constraints, only a detailed outline has been created that includes the steps one has to take to make the transition of SMORES from critical systems to fixed source problems. Additional time constraints limited the goal to perform chemical reactivity experiments on candidate alloys. Nevertheless, a review of past experiments was done and it was determined that large-scale experiments seem more appropriate for the purpose of this work, as they would better depict how the alloys would behave in the actual reactor environment. Both air and water reactions should be considered when examining the potential chemical reactions of the lithium alloy.

To the past, present, and future women in STEM.

Contents

List of Figures	vi
List of Tables	xii
I Introduction, Background, and Theory	1
1 Introduction and Background	2
1.1 Fusion Power	2
1.2 Overview of National Ignition Facility and Inertial Fusion Energy Reactor . .	3
1.3 Issues with Current Blanket Concepts	6
1.4 Thesis Outline	8
2 Theoretical Framework	10
2.1 Derivation of the Transport Equation	10
2.1.1 Neutron Transport	10
2.1.2 Photon Transport	11
2.2 Variational Methods and Perturbation Theory Concepts	11
2.2.1 The Adjoint Function and Neutron Importance	11
2.2.2 Variational Methods	13
2.2.3 Generalized Perturbation Theory and Sensitivity Functions	14
2.3 Optimization Methods for Fusion Reactor Blankets	16
2.3.1 Optimization Theory	16
2.4 Monte Carlo Theory	19
2.4.1 Variance Reduction Techniques	20
2.5 Perturbation Theory in Monte Carlo	21
2.5.1 Monte Carlo Implementation of the Adjoint Operator in MCNP	21
2.5.2 Serpent Estimate of the Iteration Fission Probability	24
2.6 Collision History-based Approach to Perturbation with Monte Carlo	24
2.6.1 Accepted and Rejected Events	25
2.6.2 Exact Perturbation Theory for Use in Fixed Source Problems	25
2.6.3 Extension of Exact Perturbation Theory to Generalized Perturbation Theory	28
2.7 Activation Analysis Governing Equations	29
2.7.1 Decay Heat	30

2.7.2	Internal and External Dose Exposures	31
2.7.3	Contact Dose Rate	33
II	Results and Discussion	35
3	Neutronic and Activation Analysis of Lithium-based Ternary Alloys in Inertial Fusion Energy (IFE) Blankets	36
3.1	Introduction	36
3.2	Models and Methodology	38
3.2.1	Chamber Model	38
3.2.2	Computational Approach	41
3.2.3	Activation Analysis	41
3.2.4	Safety and Environmental Parameters	43
3.3	Results and Discussion	45
3.3.1	Preliminary Evaluations	45
3.3.2	Tritium Breeding and Energy Multiplication	47
3.3.3	Lithium Enrichment	48
3.3.4	Activation Analysis	54
3.4	Conclusions	61
4	Exact Perturbation Theory to Determine and Optimize the Tritium Breeding Ratio of Fusion Reactor Blankets	64
4.1	Introduction	64
4.2	Exact Perturbation Theory Methodology	66
4.2.1	Accepted and Rejected Events	66
4.2.2	Exact Perturbation Theory for Use in Fixed Source Problems	67
4.2.3	Implementation of EPT into Serpent Code	68
4.2.4	EPT setback	70
4.2.5	Inertial Fusion Energy Reactor Model	70
4.3	Selection of Simulations per Ternary Alloy	72
4.4	EPT Results with LiPbBa	76
4.5	Methods to Eliminate High Uncertainties	79
4.5.1	Uncertainty Cut-off Method	81
4.5.2	Generalized Least Squares for Uncertainties Method	82
4.5.3	Validity of GLS	90
4.5.4	Particle History Comparison	91
4.5.5	GLS effectiveness on Smaller Triangle Subdivision	94
4.6	Composition Optimization	96
4.6.1	Optimization Scheme and First Iteration	96
4.6.2	Second Iteration	98
4.6.3	Third Iteration	104
4.7	EPT and Optimization of LiSnZn	107
4.7.1	First Iteration	107
4.7.2	Second and Third Iterations	111

4.8	Conclusions	112
5	SMORES code implementation	115
5.1	SWAN Methodology	115
5.1.1	Effectiveness Functions	116
5.1.2	Convergence Criteria	118
5.1.3	Calculation of Composition Variation	118
5.1.4	Differences between SWAN and SMORES	119
5.2	Implementation of Fixed Sourced Problems into SMORES	120
5.2.1	Current implementation	120
5.2.2	Future Work	129
5.3	Conclusion	131
6	Review of Chemical Reactivity Experiments for Lithium Ternary Alloys	134
6.1	Introduction	134
6.2	Lithium Reactions with Air	134
6.2.1	Handford Engineering Development Laboratory (HEDL) Experiments	135
6.2.2	MIT Liquid Lithium Reactions with Oxygen-Nitrogen Mixtures	137
6.3	Lithium Reactions with Water	141
6.3.1	Small Scale Experiments	141
6.3.2	Large Scale Experiments	142
6.4	Experimental Recommendations	146
7	Policy Issues Related Inertial Fusion Energy Reactors	148
7.1	Safety of Fusion Reactors	148
7.1.1	Lithium Chemical Reactivity	148
7.1.2	Tritium Release	149
7.1.3	Waste and Disposal of Blanket Materials	150
7.2	Nuclear Security of Fusion Reactors	151
7.2.1	Proliferation Risks in Fusion Reactors	151
7.2.2	Use of Lithium and Tritium from Fusion Reactors for Weapons	153
7.2.3	General Recommendations Regarding Proliferation in Nuclear Reactors	154
7.2.4	Obtaining Lithium and Tritium Currently	157
III	Concluding Remarks	159
8	Conclusions and Future Work	160
8.1	Summary and Conclusions	160
8.2	Future Work	164
	Bibliography	166
A	Neutronic Blanket Functions	177
A.0.1	Tritium Breeding Ratio	177
A.0.2	Energy Multiplication Factor	178

B	Source Reciprocity Relationship	179
C	Binary Plot Results	181
D	MCNP Lithium-based Ternary Alloy TBR and EMF Results	185
E	EPT Serpent Subroutines	204
	E.1 AGPTFunctionsInit.c subroutine	204
	E.2 AGPTScoreArbitraryFunctions.c subroutine	206
F	Generalized Least Squares Subroutine for Ternary Alloys	208
G	SMORES Source Subroutine	213

List of Figures

1.1	Illustration of inertial confinement fusion at NIF [2].	4
1.2	Illustration of IFE reactor [39].	4
1.3	Self-sufficient cycle between D-T source and Lithium blanket.	5
2.1	Collision history and weight perturbation (adapted from Ref. [15]).	27
3.1	Illustration of absorption of products from fusion reactions in the Xenon chamber except for neutrons, which travel to the blanket.	39
3.2	MCNP model of the IFE reactor viewed from the xz plane (left) compared to real-life model (right).	40
3.3	Fusion source neutron energy distribution. [106]	40
3.4	Flowchart of computational approach to choose alloys for Monte Carlo analysis.	42
3.5	Comparison of neutronic properties of significant elements.	46
3.6	TBR and EMF for lithium (a) LiSn and (b) LiPb alloys as a function of lithium concentration; the horizontal red line coincides with the minimum value for both TBR (1.02) and EMF (1.10), the shaded yellow area indicates the range of lithium concentration within which both constraints are met.	47
3.7	Range of lithium (atom%) for each ternary alloy that meet specific TBR and EMF criteria. Aggressive: TBR 1.02, EMF 1.2. Conservative: TBR 1.1, EMF 1.1. Semi-conservative: TBR 1.05, EMF 1.1. When an alloy does not meet one of the criteria at any composition, it is left blank.	49
3.8	Ternary Plots for (a) LiBaBi, (b) LiPbBa, (c) LiGaPb, (d) LiSrPb, (e) LiNaSn, and (f) LiSnZn; solid lines represent TBR; dotted lines represent EMF.	50
3.9	${}^6\text{Li}$ and ${}^7\text{Li}$ (n,t) cross sections [1].	51
3.10	LiSnZn diagram showing area where all three criteria (aggressive, conservative, semi-conservative) are met. Chosen point is within shaded region and also minimizes lithium concentration.	52
3.11	TBR, EMF, and (n,T) and (n,xn) reaction rates as a function of ${}^6\text{Li}$ concentration in lithium for Li(65%)Sn(20%)Zn(15%) alloy.	52
3.12	Range of lithium (atom%) for LiSnZn with natural, 40%, and 90% enrichment, that meet specific TBR and EMF criteria. Aggressive: TBR 1.02, EMF 1.2. Conservative: TBR 1.1, EMF 1.1. Semi-conservative: TBR 1.05, EMF 1.1.	53

3.13 Ternary diagrams for LiSnZn with lithium enriched to (a) 40% and (b) 90%; the solid lines represent TBR; dotted lines represent EMF.	54
3.14 Decay heat (W/m^3) as a function of time after irradiation for breeder/coolant ternary alloys. The wet cooling and dry cooling constrains are indicated by the horizontal lines.	56
3.15 Isotopics of decay heat (W/cm^3) after irradiation for (a) LiBaBi, LiPbBa, and LiGaPb and (b) LiPbZn, LiSnZn, and LiNaSn. The wet cooling and dry cooling constrains are indicated by the horizontal lines.	57
3.16 Contact Dose Rates ($\text{Sv}/\text{h}\cdot\text{m}^3$) as a function of time after irradiation for breeder/coolant ternary alloys. The remote handling limit is indicated by the dotted line.	58
3.17 Isotopics of Contact Dose Rates (Sv/h) for (a) LiBaBi, LiPbBa, and LiGaPb and (b) LiPbZn, LiSnZn, and LiNaSn. The remote handling limit is indicated by the dotted line.	59
4.1 Collision history and weight perturbation (adapted from Ref. [15]).	68
4.2 Example of Serpent input materials definition for a pure lithium blanket.	69
4.3 Example of perturbation file, <code>filePert</code> , for pure lithium. The perturbation entries correspond to the two lithium isotopes in the same order as the materials definition in Fig. 4.2 (^6Li first, ^7Li second).	69
4.4 Simplified Serpent model of IFE reactor viewed from the xz plane.	72
4.4 LiPbBa ternary subdivisions of (a) 4 triangles, (b) 9 triangles, (c) 16 triangles, and (d) 25 triangles; each case has the number of representative triangles labeled.	75
4.5 LiPbBa uncertainties for a specific triangle chosen in the case the ternary is divided into (a) 4 triangles, (b) 9 triangles, (c) 16 triangles, and (d) 25 triangles; each case has the number of representative triangles labeled.	77
4.6 Comparison of LiPbBa TBR results with (a) Serpent using EPT and (b) MCNP	80
4.7 Uncertainties for TBR results of LiPbBa simulated with Serpent EPT.	80
4.8 Points remaining for uncertainty cut-off cases with (a) 30 points/triangle, (b) 50 points/triangle, (c) 70 points/triangle, (d) 90 points/triangle, (e) 110 points/triangle.	83
4.9 TBR results for uncertainty cut-off cases with (a) 30 points/triangle, (b) 50 points/triangle, (c) 70 points/triangle, (d) 90 points/triangle, and (e) 110 points/triangle.	84
4.10 TBR relative uncertainty results for uncertainty cut-off cases with (a) 30 points/triangle, (b) 50 points/triangle, (c) 70 points/triangle, (d) 90 points/triangle, and (e) 110 points/triangle.	85
4.11 Example of GLS application to a point in a closeup of the LiPbBa ternary. The point to be replaced is shown by the larger purple circle. The area of points used in the GLS calculation is outlined by the black triangle.	86
4.12 TBR results for GLS case (a) A (2×10^{-2} threshold), (b) B (1.5×10^{-2} threshold), (c) C (1×10^{-2} threshold), (d) D (9.5×10^{-3} threshold), and (e) E (9×10^{-3} threshold).	88

4.13	TBR uncertainty plots calculated with GLS for Case (a) A (2×10^{-2} threshold), (b) B (1.5×10^{-2} threshold), (c) C (1×10^{-2} threshold), (d) D (9.5×10^{-3} threshold), and (e) E (9×10^{-3} threshold).	89
4.14	Plot of original TBR results obtained with EPT in Serpent. Triangles are outlined in areas where deviations occur. Extra simulations were executed in these regions.	92
4.15	Comparison of TBR results in a ternary with (a) additional simulations added to the areas of deviation in original EPT results and (b) GLS applied to uncertainties greater than 9.5×10^{-3} (Case C).	92
4.16	Comparison of TBR uncertainties from EPT Serpent calculations only for triangles 17-21 when simulated with a number of particle histories of (a) 1×10^8 and (b) 1×10^9	94
4.17	TBR (before applying GLS) comparison of triangles 17-21 when simulated with a number of particle histories of (a) 1×10^8 and (b) 1×10^9	95
4.18	TBR (after applying GLS) comparison of triangles 17-21 when simulated with a number of particle histories of (a) 1×10^8 and (b) 1×10^9	95
4.19	Results of the (a) TBR and (b) relative uncertainty for simulations performed with Serpent EPT where the entire ternary was divided into 16 triangles.	96
4.20	Results of the (a) TBR and (b) relative uncertainty after GLS is applied to TBR values with uncertainties greater than 9.5×10^{-3} . The simulations performed with Serpent EPT were done for 16 subdivided triangles of the ternary.	97
4.21	Plot of EMF for LiPbBa. Results for this plot were obtained in Chapter 3.	98
4.22	Combination of TBR results of second iteration and Case C of first iteration (Table 4.5). The interval between in the second iteration is smaller so points are more condensed.	99
4.23	Comparison of uncertainty results of second iteration when simulated with a number of particle histories of (a) 1×10^9 and (b) 1×10^8 . The plots show the second iteration, outlined by the white triangle, combined with Case C of the first iteration.	99
4.24	Comparison of TBR results of second iteration when simulated with a number of particle histories of (a) 1×10^9 and (b) 1×10^8 . Results from the first two iterations are combined before GLS is applied to points with uncertainties $> 9.5 \times 10^{-3}$	101
4.25	Comparison of relative uncertainties of second iteration when simulated with a number of particle histories of (a) 1×10^9 and (b) 1×10^8 . Results from the first two iterations are combined before GLS is applied to points with uncertainties $> 9.5 \times 10^{-3}$	101
4.26	Combination of TBR results of the second iteration triangle outlined (and transparently shaded) in dark orange-red and Case C of first iteration (Table 4.5). A new suggested case to be simulated is outlined (and transparently shaded) in black.	102

4.27	Comparison of second iteration TBR with (a) results straight out of Serpent EPT combined with GLS Case C from first iteration and (b) results of first and second iteration first combined, then GLS applied to values with uncertainties $> 9.5 \times 10^{-3}$	103
4.28	Comparison of second iteration TBR relative uncertainties for (a) results straight out of Serpent EPT combined with GLS Case C from first iteration and (b) results of first and second iteration first combined, then GLS applied to values with uncertainties $> 9.5 \times 10^{-3}$	104
4.29	Plot of first two iteration results with GLS implementation (Fig. 4.27(b)). Suggested cases for third iteration are outlined. Case 3.1 is outlined in blue while case 3.2 is outlined in red.	105
4.30	Third iteration results for (a) TBR and (b) relative uncertainty. To plot results, the values of all three iterations were combined followed by GLS applied to uncertainties $> 9.5 \times 10^{-3}$	107
4.31	Flowchart of Optimization with Serpent EPT for a single ternary alloy.	108
4.32	Comparison of LiSnZn TBR results with (a) Serpent using EPT and (b) MCNP109	
4.33	Uncertainties for TBR results of LiSnZn simulated with Serpent EPT.	110
4.34	First iteration results for (a) TBR and (b) relative uncertainty, after GLS was applied to uncertainties are $> 5.5 \times 10^{-3}$. The areas that will be simulated in the second iteration are shown in the triangles outlined in red and blue in (a).	110
4.35	TBR results of first and second iterations combined and GLS utilized for points containing uncertainties greater than 5.5×10^{-3} . Area of triangles simulated in third iteration are outlined by the triangles in red and blue.	112
4.36	First iteration results for (a) TBR and (b) relative uncertainty. Results of all three iterations are combined and GLS was applied to TBR values whose uncertainties $> 5.5 \times 10^{-3}$	113
5.1	Flowchart of Optimization Module (adpated from SWAN manual [22])	117
5.2	Standard SMORES input modeled with an IFE reactor.	123
5.3	1-dimensional chamber model of IFE reactor.	124
5.4	Geometry section of SMORES input with added source specification. The zone with a volumetric forward source is highlighted in blue. The zones with a volumetric adjoint source are highlighted in yellow.	124
5.5	Example of the forward source section of new SMORES input.	126
5.6	Example of the adjoint source section of new SMORES input. First source is highlighted in yellow. Last source is highlighted in green. The line in between both sources signifies the fourteen additional sources that would be defined (omitted to take up less space).	127
5.7	Flowchart of hybrid optimization method. Deterministic steps are defined in orange. Monte Carlo steps are defined in green.	133
6.1	Geometry of HEDL lithium-atmosphere reaction experiments [74].	136
6.2	Experimental set-up for MIT 1984 lithium-nitrogen experiments [113].	138
6.3	MIT 1986 lithium-nitrogen/oxygen experimental setup [113].	139
6.4	BLAST experimental facility [34].	142

6.5	HEDL LiPb/steam experiments facility [69].	144
6.6	University of Wisconsin lithium-lead/water tests facility [69].	145
C.1	TBR and EMF for various lithium-based binary alloys as a function of lithium concentration; the horizontal red line coincides with the minimum value for both TBR (1.02) and EMF (1.10), the shaded yellow area indicates the range of lithium concentration within which both constraints are met.	182
C.1	TBR and EMF for various lithium-based binary alloys as a function of lithium concentration; the horizontal red line coincides with the minimum value for both TBR (1.02) and EMF (1.10), the shaded yellow area indicates the range of lithium concentration within which both constraints are met.	183
C.1	TBR and EMF for various lithium-based binary alloys as a function of lithium concentration; the horizontal red line coincides with the minimum value for both TBR (1.02) and EMF (1.10), the shaded yellow area indicates the range of lithium concentration within which both constraints are met.	184
D.1	Ternary Plots for various ternary alloys; TBR plots are on left, EMF plots are on right.	186
D.1	Ternary Plots for various ternary alloys; TBR plots are on left, EMF plots are on right.	187
D.1	Ternary Plots for various ternary alloys; TBR plots are on left, EMF plots are on right.	188
D.2	Ternary Plots for various ternary alloys; TBR plots are on left, EMF plots are on right.	189
D.2	Ternary Plots for various ternary alloys; TBR plots are on left, EMF plots are on right.	190
D.2	Ternary Plots for various ternary alloys; TBR plots are on left, EMF plots are on right.	191
D.3	Ternary Plots for various ternary alloys; TBR plots are on left, EMF plots are on right.	192
D.3	Ternary Plots for various ternary alloys (Continued); TBR plots are on left, EMF plots are on right.	193
D.3	Ternary Plots for various ternary alloys; TBR plots are on left, EMF plots are on right.	194
D.3	Ternary Plots for various ternary alloys; TBR plots are on left, EMF plots are on right.	195
D.4	Ternary Plots for various ternary alloys; TBR plots are on left, EMF plots are on right.	196
D.4	Ternary Plots for various ternary alloys; TBR plots are on left, EMF plots are on right.	197
D.4	Ternary Plots for various ternary alloys; TBR plots are on left, EMF plots are on right.	198
D.4	Ternary Plots for various ternary alloys; TBR plots are on left, EMF plots are on right.	199

D.5 Ternary Plots for various ternary alloys; TBR plots are on left, EMF plots are on right.	200
D.5 Ternary Plots for various ternary alloys; TBR plots are on left, EMF plots are on right.	201
D.5 Ternary Plots for various ternary alloys; TBR plots are on left, EMF plots are on right.	202
D.5 Ternary Plots for various ternary alloys; TBR plots are on left, EMF plots are on right.	203

List of Tables

1.1	Overview of issues with existing blanket concepts.	7
3.1	Composition and dimensions of the blanket components.	38
3.2	Effective cross sections and Q-values for selected elements.	46
3.3	Compositions of Alloys Chosen for Activation Analysis.	54
3.4	Accident Dose (AD) and Waste Disposal Ratings (WDR) for alloys.	60
3.5	Summary of Ternary Alloy Neutronic and Activation Analysis Results.	63
4.1	Composition and dimensions of the blanket components.	71
4.2	Chosen triangle to simulate for each split ternary case in Fig. 4.4.	76
4.3	Top 20 uncertainties for each subdivided ternary case.	78
4.4	List of points removed/remaining for each uncertainty cut-off case.	82
4.5	List of points removed/remaining for each uncertainty cut-off case.	87
4.6	Comparison of results from original ETP, additional EPT, and GLS applied to original values.	93
4.7	Comparison of CPU time taken to run simulations with 1×10^8 and 1×10^9 particle histories.	93
4.8	Optimal composition for each iteration.	97
4.9	Optimal composition for each iteration. The uncertainties for the first two iterations are calculated after GLS is implemented.	111
4.10	Comparison of CPU time taken to run simulations in LiPbBa versus LiSnZn .	111
5.1	Composition and dimensions of the blanket components.	122

Acknowledgments

First I would like to thank my dissertation committee: Professors Massimiliano Fratoni, Jasmina Vujic, and Michael Nacht.

To my research advisor, Professor Max Fratoni, thank you for giving me a chance in 2013, when it was critical for me to change directions. This project began as part of a larger effort with Lawrence Livermore National Laboratory but you've always managed to steer me in the right direction, provide help when I needed it, and continue to challenge me until the very end. I didn't always agree with your opinions, but I'm grateful that you pushed me, specially at the end, to continue to think critically and take part of difficult but rewarding work.

To Professor Jasmina Vujic, thank you for giving me a chance to come to Berkeley in the first place. I'm grateful for the support you provided throughout the years, for being 100% transparent and honest with me, and for giving me advise when I needed it the most. You have been one of the most influential people in my time at Berkeley.

To Lisa Zemelman, you are a crucial piece in my graduate school career. You have provided an immense amount of support to me during some of the hardest times of my life. You were always there to answer questions and give advise and I'm forever thankful.

To Wayne Meier, the head of the fusion project at Lawrence Livermore National Laboratory. Thank you for the meaningful discussions and essential feedback. Also thank you for taking time to write recommendations for various applications I requested.

To Manuele Aufiero, thank you for your mentorship through the last part of my PhD. You are one of the most intelligent and humble people I have ever met, always taking time to offer help and support to anyone that needs it. Specifically for me, you planted the seeds that allowed me to create the missing part of my work, which is now the longest chapter of my dissertation. I will metaphorically give you unlimited espressos for the rest of eternity.

To the Netronics Research Group, thank you for always being there to answer random questions I had. Specifically, thank you to Dr. Guanheng Zhang for being a great companion in my first project. Also Kelly Rowland, thank you for answering all cluster and build related questions.

To my friends that have been there through it all. Thanks to Madicken Munk, one of the few people in the universe who understands my emotions, struggles, and this thing we call life. I know there was a time that we drifted apart, but I feel like our friendship has become even stronger because of it. You are a soul sister and one of my greatest friends. Thank you to Lakshana Huddar, for always being there with open arms and ears to listen to my frustrations and struggles. Our little walks/hikes where we laughed and talked about an array of topics will always be close to my heart. Thanks to Sandra Bogetic for being a great friend through all of these years. You are one of the best people to have a chat over a cup of coffee, wine, and a great (Italian) meal. Thanks to Jess Weisz for being a lovely

human being who has been there to provide advise when I needed it the most. To everyone else, thanks for the times we shared at Berkeley.

I am forever grateful to my family, who have always believed in me and my potential, Thank you to my grandparents, Fanny and Marcos. To Fanny, who has one of the strongest spirits of anyone I know. You are a source of admiration and inspiration to me every single day of my life. To Marcos, you are the calmest person in our family and this always reminds me to step back and take a breath. To my parents, Mirta and Mario Jolodosky, this thesis is not enough to thank you for everything you have always done for me. Thank you for taking one of the biggest risks in your life and moving to the United States to provide the family, specially my sister and me, with a brighter future. Thank you for all the hardships you've endured, gray hairs that you've grown, and challenges you faced just so my life can be easier. Both you are my biggest inspiration, and your strength has helped me push through all the obstacles in my life. I would not be at this point in my life if it wasn't for having you as my mom and dad.

Thank you to the rest of my family, both immediate and extended for the love you have given me. Thank you to Y. Solomon who has been a source of therapy throughout all of these years. Even on the worst days, you somehow make me smile.

Last but not least, thank you Jonathan. I always like to say that I could have gone through everything I have on my own, but honestly you and I both know that your presence has kept me going. You have been there for and with me throughout the most critical times of my life. I won't list every single thing here, but you know you were always by my side through every one of those things and have always bolstered me in times where I wasn't sure I could continue. You have encouraged and believed me in a way no one else has. You have always seen my full potential. You understand who I am more than any other human being. I am happy to continue this journey with you and have you along as I start the next chapter.

Chapters 3 and 6 of this dissertation was supported by LLNL LDRD Project 14-ERD-035. Portions of this work were performed under the auspices of the U.S.Department of Energy by Lawrence Livermore National Laboratory under Contract DE-AC52-07NA27344.

Part I

Introduction, Background, and Theory

Chapter 1

Introduction and Background

The energy needs of the future require the reduction of dependence on fossil fuel and emission of greenhouse gases. Nuclear energy offers a solution by creating clean and sustainable energy. Fission reactors are currently operated throughout the world and new designs are constantly being developed. In addition to nuclear fission, nuclear fusion offers attractive features such as potentially limitless fuel supply, inherent safety, and little to no long-lived radioactive waste [108]. Fusion technology and reactor design, however requires a great deal of research and analysis due to its extreme conditions. The following sections introduce the concept of fusion for power generation, describe a specific type of fusion reactor, and emphasize the importance of an essential component of the reactor, the blanket, which motivates this work.

1.1 Fusion Power

Fusion reactions occur when the strong nuclear force, that attracts atomic nucleons, overcomes the electrostatic force, that causes nuclei, which contain positively charged protons, to repel each other [50]. Two lighter elements, most commonly hydrogen isotopes deuterium and tritium, come together and form a heavier element with higher binding energy. The mass of the product will be lower than the combined mass of the reactants and therefore energy will be released. Fusion reactions are much more energy dense than fission reactions in a per unit mass basis. A deuterium-tritium reaction indeed releases four times more energy than a U-235 fission reaction [3].

The only way fusion can occur is to bring the two nuclei within a short enough range of each other that they overcome the Coulomb barrier [18]. This is very difficult to achieve but can be done through the use of particle accelerators or more commonly, by heating the nuclei to extremely high temperatures. At such high temperatures, in the range of 4 to 40 x 10⁷ Kelvin, a plasma is created, where the electrons are separated from the rest of atom leaving instead a free floating cloud of positively charged ions and electrons. To create controlled thermonuclear fusion reactions, an extremely hot and particle dense plasma must be effectively confined with a large amount of energy. To quantify if a fusion reaction will create more energy that what is needed for the reaction to take place, a set of requirements were created [35, 88]. These requirements, known as the triple product are: 1. temperature

(T), 2. particle density (n) and 3. confinement time (τ_E). To allow the nuclear force to take over, the particle temperatures must be high enough so their kinetic energies overcome the electrostatic force. Additionally, the particle density must be high enough to increase the probability of collision between the atomic nuclei. Since energy will be lost within the plasma, heating must constantly occur in the system for the temperature to remain over a million degrees. This is where the confinement time term comes in the triple product: it quantifies the time that the system is kept above the critical ignition temperature.

Two methods are currently being developed to create fusion energy: magnetic confinement fusion (MFC) [121], and inertial confinement fusion (ICF) [98]. The MCF approach tries to create the environment necessary for fusion to occur by utilizing magnets and their magnetic fields to confine the electrical current of the plasma. On the other hand, ICF creates its environment by heating and compressing the fuel, most commonly with lasers, allowing the plasma to be confined by its own inertial mass. The triple product still applies to both MCF and ICF. However, where as magnetic confinement usually operates at low densities with longer confinement times, inertial confinement does the opposite: operates at high densities with very short confinement times. This work focuses on a component, the blanket, of an ICF reactor and will be discussed in the following section.

1.2 Overview of National Ignition Facility and Inertial Fusion Energy Reactor

The National Ignition Facility (NIF) located at the Lawrence Livermore National Laboratory (LLNL) currently contains the world's largest laser utilized to create inertial confinement fusion [111]. This is done by utilizing optics to convert a weak laser pulse with an energy of a billionth of a Joule into 192 laser beams that have a total of 4 million joules of energy [99, 107]. The target is comprised of a tiny capsule of a frozen deuterium and tritium mixture, and is surrounded by a hohlraum, a small cylinder made of a high-Z material. Lasers enter the hohlraum from the top and bottom and heat its inner surface to high temperatures allowing uniform x-rays to be released [97]. These x-rays then heat up the outer layer of the deuterium-tritium (D-T) capsule causing the surface to ablate and the rest of the capsule to implode. The compression of the fuel releases shockwaves that travel to the center of the fuel pellet and condenses even further. This forms a hot spot in the center that allows fusion reactions to occur. The reactions releases energy that travels outward through the capsule, creating additional fusion events. Known as a thermonuclear burn, the reactions continue to spread throughout the compressed fuel until it disassembles. This entire process is illustrated in Fig. 1.1. The goal at LLNL is to design an inertial fusion energy reactor, based on the technology of NIF, to deliver commercial electricity.

The inertial fusion energy reactor takes the concept of NIF and surrounds it with a fusion chamber consisting of a first wall, blanket, and shield [39], shown in Fig. 1.2. Its purpose is to take the energy released from the ICF reactions and convert it into electricity. This can be done by recovering the energy from neutrons produced by D-T reactions. The D-T reaction is expressed as:



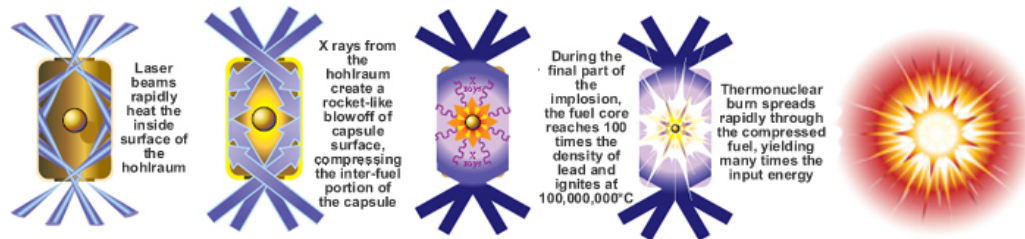


Figure 1.1: Illustration of inertial confinement fusion at NIF [2].

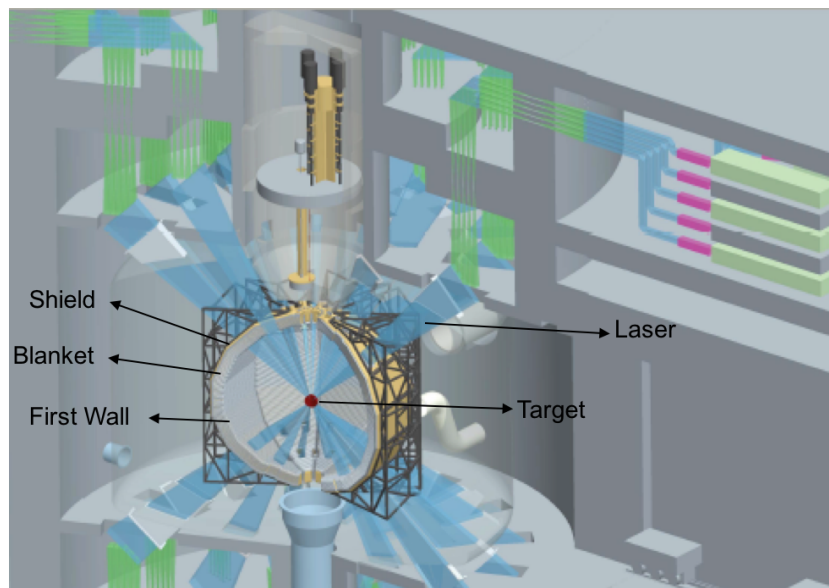


Figure 1.2: Illustration of IFE reactor [39].

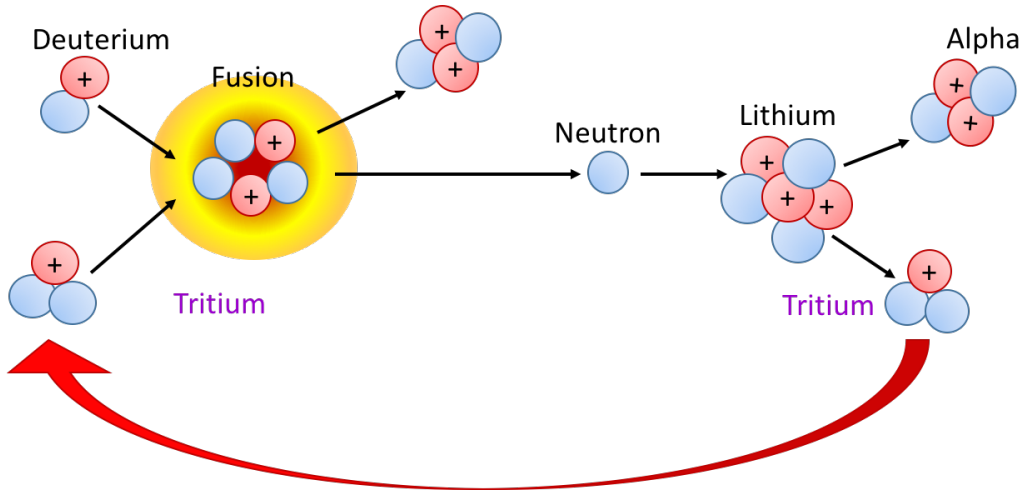


Figure 1.3: Self-sufficient cycle between D-T source and Lithium blanket.

As one can see in the reaction above, D-T fusion produces an alpha particle and a neutron. The reactor is designed with a large volume of xenon surrounding the source to absorb alpha particles and x-rays caused by the fusion event [39]. Additional x-rays are absorbed in the plasma-facing first wall, designed to protect the rest of the reactor components from high radiation damage. Most of the neutrons in the above reaction will be able to travel past the first wall and reach the reactor blanket [86]. It is in this region that neutrons will be absorbed by the blanket material and react to generate heat. Moreover, the choice of the blanket material can allow additional neutron interactions to produce tritium. Deuterium is an abundant fuel, found in salt water. On the other hand, trace amounts of tritium are found in the atmosphere through its interaction with cosmic rays. It cannot be found anywhere else on Earth due to its very short half-life of 12.3 years. Therefore, creating tritium in the reactor allows for a self-sustaining system that produces its own fuel as it is demonstrated in Fig. 1.3.

Pure lithium was the first candidate to be studied as a blanket material of a fusion reactor. It is composed of 7.5% ${}^6\text{Li}$ and 92.5% ${}^7\text{Li}$. Both isotopes can create tritium:



The advantage of ${}^6\text{Li}$ -n reactions is twofold: they can occur in a wide range of energies with the cross section increasing with decreasing incident neutron energy, and they are exothermic. Although ${}^7\text{Li}$ -n reactions are endothermic, they create additional neutrons that will continue to generate more tritium and energy. The amount of tritium created in the blanket is quantified by the tritium breeding ratio (TBR) and the heat generated by the energy multiplication factor (EMF). A detailed discussion of these quantities can be found in Appendix A, and a discussion in Chapter 3.

1.3 Issues with Current Blanket Concepts

The nuclear properties of lithium are not the only ones that make it an attractive blanket candidate. Other characteristics (Fig. 1.1) include a low melting point, low density, high specific heat, and high thermal conductivity, which allow the material to circulate through the blanket and act as a coolant [10]. Nevertheless, lithium has one major downfall. It is an alkali metal and therefore is extremely chemically reactive [34]. As a result, the structural integrity of the surrounding plant components is highly compromised. In the case of an accident, lithium reactions with the concrete containment can result in a breach, releasing highly radioactive tritium into the environment. Reactions of lithium with air or water are highly exothermic and can induce lithium fires. Numerous blanket concepts have been proposed in order to address this issue, as summarized Table 1.1 (for more information on these concepts the reader is referred to [8, 11, 73]). Nevertheless, these alternative blanket concepts, reduce many of the desirable properties exhibited by pure lithium. Consequently, this work focuses on examining a brand new type of alloy in the form of lithium-based ternaries. Adding a third component, as oppose to looking at a binary alloy, adds an extra degree of freedom which can perhaps mitigate some of the adverse effects found in the blankets in Table 1.1.

Table 1.1: Overview of issues with existing blanket concepts.

Properties of Interest	Lithium	Li ₁₇ Pb ₈₃	Molten Salt*	Ceramic**
Melt (°C)	181	235	363	N/A
Density (kg/m ³)	505	9500	1970	1600-3600
Specific heat (J/kg-K)	4260	188	2380	1176
Th. conductivity (W/m-K)	46	13	1	1-4
Tritium permeation/ Separation issues	Low	High	High	High
Beryllium required	No	No	Maybe	Yes
⁶ Li enrichment	No	No	Maybe	Yes
Corrosion issues	Low	High	Med.	Low
Chemical reactivity	High	Med.	Low	Low

*Molten Salt: FLiBe

**Ceramic breeders:

Li₂O, LiAlO₂, Li₄SiO₄,

Li₂TiO₃, Li₂ZrO₃

■ Excellent
■ Acceptable (could be improved)
■ Needs to be improved

1.4 Thesis Outline

The scope of this work focuses in studying lithium-based ternary in various ways. The first two parts of this dissertation describe the bulk of the work. This focuses on studying lithium-based ternary alloys through its neutronic characteristics and finding ways to optimize a response based on specific input parameters. All of the results developed in this work have been calculated with the aid of computational codes that simulate the transport of neutrons and photons in a given system utilizing a variety of numerical techniques to determine the particle distribution in the system. By solving for the distribution of neutrons and photons, other quantities such as reaction rates of interest can be obtained. Chapter 2 discusses the theoretical framework of all the computational methods and tools employed in this work. It also discusses generalized perturbation theory and sensitivity functions to develop an understanding of its uses. Sensitivity functions are specifically important because they are able to find the response in a system by slightly varying a characteristic of interest. This will be directly utilized in Chapter 4 and is the basis for optimization theory utilized in Chapter 5.

Chapter 3 addresses the issues discussed previously and begins the examination of the neutronic performance of lithium-based ternary alloys in the blanket of an IFE chamber. 3-D Monte Carlo calculations were performed to evaluate the two main neutronic performance parameters for the blanket, the TBR and the EMF. Results for various alloys are presented and compared. Additionally, a study on the effectiveness of ^6Li enrichment is presented, and its results are discussed. Alloys that performed well in the TBR and EMF calculations were considered for activation analysis, which was accomplished next. Activation analysis was performed to determine if the alloys posed any safety or environmental concerns to the surroundings and public. Specifically, how effectively the alloys can be cooled, recycled, and disposed of underground were quantified and analyzed. Additionally, the dose that an individual would receive in the case of an accident was evaluated. After completing both neutronic and activation analysis, top candidate alloys that exhibited the best performance in all categories were chosen.

The Monte Carlo approach that calculated the TBR and EMF for various alloys of a fusion reactor was inefficient and computationally expensive. It required 231 individual simulations per alloy. To study all 150 alloys of interest, over 35,000 simulations are necessary. As a result, Chapter 4 introduces and discusses a new method which would allow multiple responses to be calculated by perturbing the input parameter without having to directly perform separate calculations. In addition, this method can be utilized for optimizing the compositions of each alloy of interest. The method is a simplified technique that has already been developed for the Serpent Monte Carlo code to calculate sensitivity functions in fission systems. This new method is specifically designed so that it can be used with fixed sourced problems, and is based on variance reduction techniques that are already part of most Monte Carlo codes. The entire chapter focuses on the effectiveness of this method's goal. The main setback of this methodology is that it can create large uncertainties. Therefore, different techniques are also presented and implemented to abate this issue. Once the method is properly validated, an optimization scheme is proposed that goes through various iterations to find a composition of the alloy that can meet specific criteria based on the TBR and EMF, and most importantly minimize lithium concentration due to the chemical

reactivity concerns previously discussed.

The study of optimization of fusion reactor blankets is continued in Chapter 5 by introducing a deterministic method that could be used to solve specific types of optimization problems by incorporating first order generalized perturbation theory. In the case of fixed source problems, the code SWAN, a 1D deterministic code, was written in the 1970s to solve deterministic optimization problems for fusion reactors. Unfortunately, the code was created a few decades ago and cannot be executed in most modern computer systems. Different versions of this code were developed throughout the years. The latest, called SMORES, is found in the SCALE code package and can only solve optimization problems for fission systems. The goal of this chapter is to describe how SMORES can be altered so that it solves problems for fixed sources, similarly to what was done in SWAN. If this is accomplished, optimization problems solved with this method would only require one calculation per alloy that would solve for an optimal composition that maximizes the EMF while restraining the TBR.

The last part of this dissertation examines two extraneous topics related to lithium-based reactor blankets. Chemical reactivity concerns of pure lithium were already presented and are emphasized throughout most of this work. Experiments have been conducted in the past to study the effects of lithium/air reactions and lithium/water reactions. This type of experiments can serve as a basis for future chemical reactivity experimentation conducted on lithium-based ternary alloys. Chapter 6 outlines the past experiments executed to examine the behavior of lithium interactions with water and air. Specifically, both small scale and large scale experiments are discussed to determine what would be the best fit for the materials of interest. Looking at what was done in the past gives a general idea of how future experiments can be setup to test a variety of lithium-based alloys.

In addition to all the work discussed, it was of interest in Chapter 7 to examine the policy issues and concerns related to fusion reactors. First policy issues related to the safety of fusion reactors were discussed. These included issues on the chemical reactivity, tritium release, and waste disposal of blanket materials. The recommendations for these issues were specifically addressed in Chapter 3 and Chapter 6. The next set of policy issues considered in this chapter involve the nuclear security of fusion reactors and proliferation concerns that can arise from fusion facilities. These issues were divided into two types of concerns. The first is concerns to create weapon's grade plutonium and uranium with fusion facilities, and the second is concerns to create lithium and tritium, two elements utilized in thermonuclear weapons. This chapter also discusses the current state of nuclear security with a specific example related to materials that would be found in fusion facilities. Lastly, Chapter 8 offers a summary and conclusions of the current work, and recommendations for future work.

Chapter 2

Theoretical Framework

The design of a nuclear reactor is performed with the aid of computational codes. Such codes simulate the transport of neutrons and photons in a given system using a variety of numerical techniques to determine their distribution in the system. Solving for the distribution of neutrons and photons in a system is extremely important so that other quantities such as reaction rates of interest can be obtained. Optimizing an aspect of the reactor adds complexity to the calculations by quantifying the effects of perturbations in a system to some type of response. In addition to the design and optimization of fusion reactor blankets, this work included calculating quantities that determine the safety and environmental impacts of the nuclides found in various blanket alloy compositions. In the following sections, the theoretical framework underlying the computational methods employed in this work, including new methods added to already existing ones, are presented.

2.1 Derivation of the Transport Equation

2.1.1 Neutron Transport

The neutron transport equation [38] is derived from the Boltzmann equation for the kinetic theory of gases since both neutrons and gas particles behave similarly. The equation creates a balance relationship between the gains and losses of neutrons within a system. This conservation relation is outlined below:

$$\begin{aligned} \frac{\partial n}{\partial t} + v\hat{\Omega} \cdot \nabla n(\mathbf{r}, E, \hat{\Omega}, t) + v\Sigma_t(\mathbf{r}, E, t)n(\mathbf{r}, E, \hat{\Omega}, t) = \\ \int_{4\pi} d\hat{\Omega}' \int_0^\infty dE' v'\Sigma_s(E' \rightarrow E, \hat{\Omega}' \rightarrow \hat{\Omega})n(\mathbf{r}, E, \hat{\Omega}, t) + S(\mathbf{r}, E, \hat{\Omega}, t) \end{aligned} \quad (2.1)$$

The first term in the equation, $\frac{\partial n}{\partial t}$, is the rate of change in the neutron number density. This rate of change is equal to the gain of neutrons in the system minus the losses. As seen above, the loss terms are moved over to the other side of the equation. The first loss term, $v\hat{\Omega} \cdot \nabla n(\mathbf{r}, E, \hat{\Omega}, t)$ characterizes the net number of neutrons that stream from one phase space to another through the system. Neutrons can also be lost by many types

of collisions, such as absorption and scattering, and the loss term is thus represented by $v\Sigma_t(\mathbf{r}, E, t)n(\mathbf{r}, E, \hat{\Omega}, t)$, where the neutron speed, v , is the distance traveled by a neutron in a unit time, the macroscopic cross section, $\Sigma_t(\mathbf{r}, E)$, is the probability per unit path length that a neutron will have an interaction, and $n(\mathbf{r}, E, \hat{\Omega}, t)$ is the neutron number density. The right hand side of the equation presents the two ways in which neutrons are added to the system: from any type of source, $S(\mathbf{r}, E, \hat{\Omega}, t)$, or through scattering reactions from a different energy, E' , and direction, $\hat{\Omega}'$, to energy and direction, E and $\hat{\Omega}$, that are currently under consideration. The latter is represented by the double scattering cross section, $\Sigma_s(E' \rightarrow E, \hat{\Omega}' \rightarrow \hat{\Omega})$, which determines the probability that a neutron will scatter from $E', \hat{\Omega}'$ to $E, \hat{\Omega}$. It is important to note that equation is written in terms of neutron density, $n(\mathbf{r}, E, \hat{\Omega}, t)$, which when multiplied by the speed, v , produces $\psi(\mathbf{r}, E, \hat{\Omega}, t)$, known as the angular neutron flux.

The transport equation is used for many different types of systems. In the case of fission reactors, the source term is replaced with a fission source rate describing the number of neutrons produced from fission interactions at the energy and angle of interest. For the purposes of this work, $S(\mathbf{r}, E, \hat{\Omega}, t)$ is the fusion source rate, represented by an isotropic steady state source of neutrons. Additionally, when optimizing the ICF reactor directly with Monte Carlo methods in Section 2.4 or with perturbation theory in Subsection 2.2.1, the transport equation will become the time independent version of Eq. 2.1.

2.1.2 Photon Transport

When looking at the energy multiplication in the ICF blanket, it is important not only to account for energy deposited by neutron interactions, but also account for the energy deposition from secondary photon interactions. To do so the same type of energy balance is created for photons in the system [70]. The photon transport equation is very similar to Eq. 2.1. Different notation is used for some of the terms such as the macroscopic cross sections; in photon transport, they are defined as attenuation coefficients, μ . However, we will not make note of this here since the equation is essentially the same type of particle balance or conservation equations, as in the case of the neutron transport equation. The source term for this equation, S_γ , comes from secondary photons produced by neutron interactions:

$$S_\gamma(\mathbf{r}, E, \hat{\Omega}) = \int \sigma_p(E_n, E_\gamma)\psi(\mathbf{r}, E_n, \hat{\Omega})dE_n dE_\gamma \quad (2.2)$$

2.2 Variational Methods and Perturbation Theory Concepts

2.2.1 The Adjoint Function and Neutron Importance

To introduce the meaning of the adjoint flux and operator, consider a fusion system consisting of a steady-state neutron source, $S(\mathbf{r}, \hat{\Omega}, E)$, in the center surrounded by a blanket region composed of lithium. The time-independent transport equation for this reactor can be written as [20]:

$$\mathbf{L}\psi(\mathbf{r}, \hat{\Omega}, E) = S(\mathbf{r}, \hat{\Omega}, E) \quad (2.3)$$

where \mathbf{L} is the transport operator:

$$\begin{aligned} \mathbf{L}\psi(\mathbf{r}, \hat{\Omega}, E) &= \hat{\Omega}\nabla\psi(\mathbf{r}, \hat{\Omega}, E) + \Sigma_t(\mathbf{r}, E, t)\psi(\mathbf{r}, \hat{\Omega}, E) \\ &\quad - \iint \Sigma_s(E' \rightarrow E, \hat{\Omega}' \rightarrow \hat{\Omega})\psi(\mathbf{r}, \hat{\Omega}', E')d\hat{\Omega}'dE' \end{aligned} \quad (2.4)$$

This problem satisfies the free-surface boundary condition which does not allow any neutrons that exit the system to reenter it; therefore, $\psi(\mathbf{r}, \hat{\Omega}, E) = 0$ for $\mathbf{e}_s \cdot \hat{\Omega} < 0$. The reactor also satisfies the adjoint transport equation:

$$\mathbf{L}^\dagger\psi^\dagger(\mathbf{r}, \hat{\Omega}, E) = S^\dagger(\mathbf{r}, \hat{\Omega}, E) \quad (2.5)$$

where $\psi^\dagger(\mathbf{r}, \hat{\Omega}, E)$ is the adjoint flux, and \mathbf{L}^\dagger , as the adjoint operator:

$$\begin{aligned} \mathbf{L}^\dagger\psi^\dagger(\mathbf{r}, \hat{\Omega}, E) &= -\hat{\Omega}\nabla\psi^\dagger(\mathbf{r}, \hat{\Omega}, E) + \Sigma_t(\mathbf{r}, E, t)\psi^\dagger(\mathbf{r}, \hat{\Omega}, E) \\ &\quad - \iint \Sigma_s(E \rightarrow E', \hat{\Omega} \rightarrow \hat{\Omega}')\psi^\dagger(\mathbf{r}, \hat{\Omega}', E')d\hat{\Omega}'dE' \end{aligned} \quad (2.6)$$

There are two major differences between the adjoint operator and transport operator: (1) the sign of the streaming terms are opposite to one another and (2) the energies and angles in the scattering terms are interchanged, i.e., for \mathbf{L}^\dagger , the neutrons scatter from E and $\hat{\Omega}$ to E' and $\hat{\Omega}'$. This can be referred to as the reversal operator, where the sense of energy and angle in the scattering term are reversed [52]. As the name suggests, the \mathbf{L}^\dagger is adjoint to \mathbf{L} and therefore satisfies the relationship (detailed derivation is found in Appendix B):

$$\langle \psi^\dagger, \mathbf{L}\psi \rangle = \langle \psi, \mathbf{L}^\dagger\psi^\dagger \rangle \quad (2.7)$$

The notation $\langle \psi^\dagger, \mathbf{L}\psi \rangle$ represents the inner product of ψ^\dagger and $\mathbf{L}\psi$:

$$\langle \psi^\dagger, \mathbf{L}\psi \rangle = \int \psi^\dagger \mathbf{L}\psi dVd\hat{\Omega}dE \quad (2.8)$$

where the brackets $\langle \rangle$ indicate the integration over the space, angle, and energy in the entire system [52]. Just like ψ meets the free-surface boundary condition, the adjoint equation's boundary condition does not account for any neutrons exiting the reactor and therefore ψ^\dagger will be zero for all outgoing neutrons, $\mathbf{e}_s \cdot \hat{\Omega} > 0$. Additionally, if there was a neutron detector inside the blanket region that determined a property of interest, such as the macroscopic cross section for the ${}^6\text{Li}(n,t)$ reaction, then the adjoint source, S^\dagger , could be replaced with $\Sigma_{(n,t)}(\mathbf{r}, E, t)$, which signifies the probability of a detector count (for an (n,t) reaction) per unit distance that a neutron travels. By utilizing Eq. 2.7 and multiplying Eq. 2.3 by ψ^\dagger and Eq. 2.5 by ψ , subtracting the results, and integrating them over all variables, it can be seen that:

$$\int S(\mathbf{r}, \hat{\Omega}, E)\psi^\dagger(\mathbf{r}, \hat{\Omega}, E) dVd\hat{\Omega}dE = \int \Sigma_{(n,t)}(\mathbf{r}, E, t)\psi(\mathbf{r}, \hat{\Omega}, E) dVd\hat{\Omega}dE \quad (2.9)$$

From this equation, one can start to see the relation between ψ^\dagger to the response of the detector from the source. To explain this even further, the source is made to be a unit source with its values as a product of delta functions, $\mathbf{r}_0, \hat{\mathbf{\Omega}}_0, E_0$. Then, Eq. 2.9 becomes:

$$\psi^\dagger(\mathbf{r}_0, \hat{\mathbf{\Omega}}_0, E_0) = \int \Sigma_{(n,t)}(\mathbf{r}, E, t) \psi(\mathbf{r}, \hat{\mathbf{\Omega}}, E) dV d\hat{\mathbf{\Omega}} dE \quad (2.10)$$

The meaning of $\psi^\dagger(\mathbf{r}_0, \hat{\mathbf{\Omega}}_0, E_0)$ can be seen from this relation as the expected contribution of neutrons to the response of the detector from a unit source. For this reason, the adjoint flux is also known as the *importance function*, which determines how likely a neutron is to adding a count to the detector [96]. In other words, a neutron's importance is directly related to the magnitude of the detector's response. When neutrons exit the reactor their importance diminishes, hence the reason the adjoint flux is zero at the free-surface boundary.

2.2.2 Variational Methods

Many reactor design applications involve estimating an integral property that is defined by a functional, a function that depends on one more other functions. This property is usually a flux-weighted integral such as the tritium reaction rate defined in the numerator of Eq. 2.43. Instead of solving the transport equation explicitly for the correct flux to calculate the reaction rate, variational methods can be implemented that approximate the flux-weighted integral by utilizing approximated values of the flux and adjoint flux. This section briefly presents variational methods for reactor physics, and is based on Refs. [20, 33, 27, 104, 139].

Assume that it is of interest to compute a type of reaction rate from a known source, S , such as the tritium reaction rate for the ICF reactor. We will keep the discussion general and define an arbitrary reaction rate, or detector response, by the inner product of the cross section with the flux:

$$R = \langle \Sigma, \phi_e \rangle \quad (2.11)$$

Where ϕ_e is the exact value of the flux.¹ The macroscopic cross section, Σ , is also the adjoint source term defined in equation 2.5. Variational methods can be implemented to estimate R from an approximate value of the flux, ϕ , where:

$$\delta\phi = \phi_e - \phi \quad \text{and} \quad \delta\phi^\dagger = \phi_e^\dagger - \phi^\dagger \quad (2.12)$$

By using variational techniques, the value of R will be accurate to the second order. This is done by implementing Roussopoulos functional, which adds the inner product of Σ and ϕ with the inner product of the adjoint with Eq. 2.3:

$$F = \langle \Sigma, \phi \rangle + \left\langle \phi^\dagger, (S - \mathbf{L}\phi) \right\rangle \quad (2.13)$$

By substituting Eq. 2.12 into Eq. 2.13 it is shown that:

$$F = \langle \Sigma, \phi_e \rangle - \langle \Sigma, \delta\phi \rangle + \left\langle \phi_e^\dagger - \delta\phi^\dagger, (S - \mathbf{L}\phi_e + \mathbf{L}\delta\phi) \right\rangle \quad (2.14)$$

¹The values of ϕ indicates scalar flux. However ψ and ϕ can also be used interchangeably as will be here.

Because of the relationship in Eq. 2.3, F then becomes:

$$F = \langle \Sigma, \phi_e \rangle - \langle \Sigma, \delta\phi \rangle + \langle \phi_e^\dagger, \mathbf{L}\delta\phi \rangle - \langle \delta\phi^\dagger, \mathbf{L}\delta\phi \rangle \quad (2.15)$$

Due to the relationship defined in Eq. 2.7, one can write the third term in the equation above as:

$$\langle \phi_e^\dagger, \mathbf{L}\delta\phi \rangle = \langle \mathbf{L}^\dagger \phi_e^\dagger, \delta\phi \rangle = \langle \Sigma, \delta\phi \rangle \quad (2.16)$$

This allows the second and third terms of Eq. 2.15 to vanish, and thus:

$$F = \langle \Sigma, \phi_e \rangle - \langle \delta\phi^\dagger, \mathbf{L}\delta\phi \rangle \quad (2.17)$$

This demonstrates that the functional is equal to the exact value of the reaction rate plus a correction factor accurate to the second order.

2.2.3 Generalized Perturbation Theory and Sensitivity Functions

Generalized perturbation theory (GPT) can be derived from variational methods, as referred in [19, 59, 139]. Perturbation theory uses the unperturbed flux and adjoint to calculate the response of the perturbed system. This is similar to variational methods, which estimates the exact response from approximate values of the flux and adjoint. The methodology that will be used to derive GPT is not explicitly from variational principles but rather utilizes the adjoint difference and forward difference methods developed by Hoffman [71], and described in detail by Stacy [139], and Greenspan [60]. This approach is useful for determining the effect of the properties of a system, such as a reaction rate, from some type of perturbation. Instead of solving the transport equation every time the system is altered to acquire the perturbed flux and predict the effect of some type of detector response, GPT will solve for the response in terms of unperturbed quantities. The focus of GPT for this work will be on inhomogeneous systems with a fixed source.

As previously described, the transport equation for an inhomogeneous system is given by:

$$\mathbf{L}\phi = S \quad (2.18)$$

If there is a small change in the system, the transport equation is written as:

$$\bar{\mathbf{L}}\bar{\phi} = \bar{S} \quad (2.19)$$

where the bar on top of each term signifies the perturbed quantity. The perturbed parameters are defined by the sum of the unperturbed quantity and a small change of each quantity as shown:

$$\bar{\mathbf{L}} = \mathbf{L} + \delta\mathbf{L}, \quad \bar{\phi} = \phi + \delta\phi, \quad \text{and} \quad \bar{S} = S + \delta S \quad (2.20)$$

It is important to note that the source term doesn't actually change when the system is perturbed. However, if the adjoint equation was used for the derivation, the adjoint source term would have a perturbed value. Thus, for the purposes of derivation, the source term

is assumed to change values when perturbed, as presented in the above equation. A flux difference equation can now be derived by substituting the quantities of Eq. 2.19 by Eq. 2.20:

$$(\mathbf{L} + \delta\mathbf{L})(\phi + \delta\phi) = S + \delta S \quad (2.21)$$

expanding the equation above gives:

$$\mathbf{L}\phi + \mathbf{L}\delta\phi + \delta\mathbf{L}\phi + \delta\mathbf{L}\delta\phi = S + \delta S \quad (2.22)$$

Using the definition of Eq. 2.18 and simplifying results in the equation shown below:

$$\delta\phi(\mathbf{L} + \delta\mathbf{L}) = \delta S - \delta\mathbf{L}\phi \quad \text{or} \quad \bar{\mathbf{L}}\delta\phi = \delta S - \delta\mathbf{L}\phi \quad (2.23)$$

a precise solution of $\delta\phi$ can be obtained with Eq. 2.23 if the value for the unperturbed flux is known. This equation will be useful in the derivation of GPT for a detector response, which will now be described. Suppose there is a system, such as a fusion reactor with a fixed source, having a known unperturbed response. The response is described by Eq. 2.11, where the unperturbed flux will be denoted by ϕ without the subscript. If an alteration in the system was made, perturbation theory can then be used to find the change between the perturbed and unperturbed response [119]:

$$\begin{aligned} \delta R = \bar{R} - R &= \langle \bar{\Sigma}, \bar{\phi} \rangle - \langle \Sigma, \phi \rangle \\ &= \langle \bar{\Sigma}, (\phi + \delta\phi) \rangle - \langle \Sigma, \phi \rangle \\ &= \langle \bar{\Sigma}, \phi \rangle + \langle \bar{\Sigma}, \delta\phi \rangle - \langle \Sigma, \phi \rangle \\ &= \langle \Sigma, \phi \rangle + \langle \delta\Sigma, \phi \rangle + \langle \bar{\Sigma}, \delta\phi \rangle - \langle \Sigma, \phi \rangle \\ &= \langle \delta\Sigma, \phi \rangle + \langle \bar{\Sigma}, \delta\phi \rangle \end{aligned} \quad (2.24)$$

Eq. 2.7 and 2.23 can be used on the second term as follows:

$$\langle \bar{\Sigma}, \delta\phi \rangle = \langle \bar{\mathbf{L}}^\dagger \bar{\phi}^\dagger, \delta\phi \rangle = \langle \bar{\phi}^\dagger, \bar{\mathbf{L}}\delta\phi \rangle = \langle \bar{\phi}^\dagger, (\delta S - \delta\mathbf{L}\phi) \rangle \quad (2.25)$$

Now, the change in the response can be written as:

$$\begin{aligned} \delta R &= \langle \delta\Sigma, \phi \rangle + \langle \bar{\phi}^\dagger, (\delta S - \delta\mathbf{L}\phi) \rangle \\ &= \langle \delta\Sigma, \phi \rangle + \langle \phi^\dagger, (\delta S - \delta\mathbf{L}\phi) \rangle + \langle \delta\phi^\dagger, (\delta S - \delta\mathbf{L}\phi) \rangle \end{aligned} \quad (2.26)$$

When the equation above is assumed to be linear, second-order effects that appear on the third term from $\delta\phi^\dagger$ are ignored [60]. The perturbation theory derivations just described can be utilized to predict the effect of a type of variation in the system on the response. A perturbation in the system that causes a change in the response must occur from some type of alteration of an input parameter, such as a cross section. The relationship that describes the relative change of some integral parameter due to the change in an input parameter is known as a sensitivity function. Sensitivity functions have been most widely used to evaluate uncertainties in nuclear data, specifically cross sections [16, 17, 42, 146]. The functions can determine which cross section have the greatest effect on the response

and demonstrate how uncertainties affect the results, specially when the cross sections are energy dependent. Additionally, sensitivity functions can be utilized to optimize systems by observing how the changes in the material densities or compositions maximize or minimize some type of design parameter. This was first implemented for inhomogeneous systems such as fusion reaction blanket and shields [63], and later altered for homogeneous criticality problems [61]. To derive sensitivity functions from perturbation theory, consider Eq. 2.26 for the change in some response, R . If this change was caused by an input parameter, P , the sensitivity function is defined to be proportional to the relative change of the response over the fractional change of the input parameter:

$$\mathbf{S} = \frac{\delta R/R}{\delta P/P} = \frac{P}{R} \left(\left\langle \phi, \frac{\delta \Sigma}{\delta P} \right\rangle + \left\langle \phi^\dagger, \frac{\delta S}{\delta P} \right\rangle - \left\langle \phi^\dagger, \frac{\delta \mathbf{L}}{\delta P} \phi \right\rangle \right) \quad (2.27)$$

2.3 Optimization Methods for Fusion Reactor Blankets

Sensitivity functions that describe the change of some type of integral parameter of a nuclear system due to a perturbation in the composition of materials can be utilized for optimization studies. Optimization of neutronic characteristics of a system that models the inhomogeneous transport equation can be applied to shielding and fusion reactor blanket problems [6, 62, 79, 95]. Greenspan developed a method for specifically optimizing characteristics of fusion blankets with the option to include an additional characteristic acting as a restraint [58, 60, 63]. The types of parameters that can be optimized and restrained include the tritium breeding ratio (TBR), energy multiplication factor (EMF), radiation damage, and transmutation. For example, this work would focus on maximizing the energy multiplication of a fusion blanket while maintaining the TBR at or above a certain value. The following sections will describe the methodology and techniques employed to solve this type of problem.

2.3.1 Optimization Theory

The goal of optimization problem is to find a density distribution that will either maximize or minimize a property in the system. This can either be done alone or by imposing a restraint based on another characteristic. The density can be distributed in multiple zones, or it can represent one zone in the entire model. Either way, each material density that is varied must be constrained² by:

$$0 \leq N_i^{min}(\mathbf{r}) \leq N_i(\mathbf{r}) \leq N_i^{max}(\mathbf{r}) \leq N_i^o(\mathbf{r}) \quad (2.28)$$

where $N_i(\mathbf{r})$ is constrained within a minimum amount, usually zero, and a maximum, which can be less than or equal to $N_i^o(\mathbf{r})$, the pure density of the material. Furthermore, the volume in each zone of interest does not change throughout the problem. Thus, an additional constraint can be included for all materials such that:

²Greenspan refers to constraints as limits on independent variables and restraints as limits on dependent variables

$$\sum_{i=1}^I \frac{N_i(\mathbf{r})}{N_i^o(\mathbf{r})} = \text{constant} \leq 1 \quad (2.29)$$

which indicates the limit on the volume fraction occupied by each material, i , in each zone. If the entire volume of the zone was occupied by material i , the density would be $N_i^o(\mathbf{r})$. When material i is part of a mixture, only a fraction of the volume in the zone is occupied by it, defined by $N_i(\mathbf{r})$. The total volume fraction summed over all materials is one if all the materials in the zone are of variable composition. When part of the zone is made up of materials of fixed composition, such as structural materials or a reflector, the total volume fraction will be a constant that is less than one.

The functionals that are optimized can be of two types. The first is called a weight functional:

$$F_w(N_1, N_2, \dots, N_I) = \sum_{i=1}^I \int C_{w,i} N_i(\mathbf{r}) d\mathbf{r} \quad (2.30)$$

This functional only depends on some kind of coefficient that helps to determine a physical characteristic of the system, such as the total weight or total volume. The other type of functional is some type of detector response, which depends on the transport of neutrons in the system such as the EMF. It is based on an integral parameter and is defined as:

$$F_b(N_1, N_2, \dots, N_I) = \int \langle \Sigma_b, \phi \rangle d\mathbf{r} \quad (2.31)$$

Alterations in the functional are directly caused by a perturbation the density. For a change in material i this is defined as:

$$(\delta F_b) = \int E_{b,i}(\mathbf{r}) \delta N_i d\mathbf{r} \quad (2.32)$$

where the function:

$$E_{b,i} = R \mathbf{S}_{N_i}(\mathbf{r}) / N_i(\mathbf{r}) = \left(\left\langle \phi, \frac{\delta \Sigma_b}{\delta N_i} \right\rangle - \left\langle \phi^\dagger, \frac{\delta \mathbf{L}}{\delta N_i} \phi \right\rangle \right) \quad (2.33)$$

is called the "effectiveness function". It multiplies the sensitivity function defined in Eq. 2.27 by R , which is the response of the reference system, and $N_i(\mathbf{r})$, which is the input parameter so that R and P from Eq. 2.27 cancel. What is left, the effectiveness function, describing the absolute change of a neutronic characteristic of type b due to a unit change in the density of material i at a position, \mathbf{r} . The total change of the functional F_b caused by all variable materials in the system is:

$$(\delta F_b) = \sum_{i=1}^I \int E_{b,i}(\mathbf{r}) \delta N_i d\mathbf{r} \quad (2.34)$$

Additionally, an observation on δN_i can be made based on the fact that when the quantity of a material in the system increases, the quantity of another material must decrease. From Eq. 2.29, can be expressed as:

$$\sum_{i=1}^I \frac{\delta N_i(\mathbf{r})}{N_i^o(\mathbf{r})} = 0 \quad (2.35)$$

This implies that the sum of the variations in volume fractions for all materials in a zone must be equal to zero, to maintain constant volume in each zone. The above equation can also be rewritten such that:

$$\begin{aligned} \frac{\delta N_j(\mathbf{r})}{N_j^o(\mathbf{r})} &= - \sum_{i \neq j} \frac{\delta N_i(\mathbf{r})}{N_i^o(\mathbf{r})} \\ \delta N_j(\mathbf{r}) &= - \sum_{i \neq j} \frac{N_j^o(\mathbf{r})}{N_i^o(\mathbf{r})} \delta N_i(\mathbf{r}) \end{aligned} \quad (2.36)$$

This means that when there is a fractional change in material j , there must be an equal but opposite change in all the other materials. In other words, if the density of material j is decreased, the density of the other components must increase or vice versa. The condition allows the number of independent variables to be reduced by one. If material j is equal to material I Eq. 2.34 becomes:

$$\delta F_b = \int \sum_{i=1}^{I-1} E_{b,i}(\mathbf{r}) \delta N_i(\mathbf{r}) + E_{b,I}(\mathbf{r}) \delta N_I \, d\mathbf{r} \quad (2.37)$$

or by substituting δN_j from Eq. 2.36:

$$\delta F_b = \sum_{i=1}^{I-1} \int \left[E_{b,i}(\mathbf{r}) - E_{b,I}(\mathbf{r}) \frac{N_I^o(\mathbf{r})}{N_i^o(\mathbf{r})} \right] \delta N_i(\mathbf{r}) \, d\mathbf{r} \quad (2.38)$$

The inside of the brackets is defined as Q_b , the "substitution effectiveness function" (SEF):

$$Q_{b,i} = E_{b,i}(\mathbf{r}) - E_{b,j}(\mathbf{r}) \frac{N_I^o(\mathbf{r})}{N_i^o(\mathbf{r})} \quad (2.39)$$

It describes the change in parameter F_b that was caused by substituting a unit quantity of material I with the same quantity of material i in a zone of the system, whose volume does not change. Using the above equation, Eq. 2.38 can be rewritten as:

$$\delta F_b = \sum_{i=1}^{I-1} \int Q_{b,i}(\mathbf{r}) \delta N_i \, d\mathbf{r} \quad (2.40)$$

The optimal density is reached when the functional is either maximized or minimized:

$$\delta F_m = \sum_{i=1}^{I-1} \int Q_{m,i}(\mathbf{r}) \delta N_i \, d\mathbf{r} = 0 \quad (2.41)$$

where δF_m denotes the functional that will be maximized/minimized, which can either be a weight functional or a neutronic characteristic. This means that when the functional

reaches its optimal condition, it will not be affected by an additional minuscule change in the density. For this to be true, the value of $Q_{m,i}$ must adhere to the following:

$$Q_{m,i}(\mathbf{r}) = \begin{cases} > 0 & N_i(\mathbf{r}) = N_i^{max}(\mathbf{r}) \\ 0 & N_i^{min}(\mathbf{r}) < N_i(\mathbf{r}) < N_i^{max}(\mathbf{r}) \\ < 0 & N_i(\mathbf{r}) = N_i^{min}(\mathbf{r}) \end{cases} \quad (2.42)$$

However when a restraint is imposed on the problem, the value for all cases of $Q_{m,i}$ above will change from zero to some constant. The equation for the restraint functional is the same as Eq. 2.42 but with the subscript r in place of m . The value of the restraint functional depends on its type and will most likely not be zero.

The optimization theory just described was implemented in a deterministic code SWAN, specifically created to optimize responses of fusion reactors [63]. This implementation will be briefly discussed in Chapter 5.

2.4 Monte Carlo Theory

Computational methods are needed to solve the incredibly complex transport equation. Two types of methods are used: Monte Carlo, and deterministic. Monte Carlo methods stochastically model event-based problems and the solutions to the equations that govern these events. Events are sampled sequentially with each characterized by a probability distribution that is statistically sampled. As a result, all of the sampled events describe the entire behavior of the problem. The statistical sampling for each event originates from the selection of random numbers. This method can easily be applied to particle transport by following a particle throughout its lifetime while sampling its path and collisions. Each step the particle takes throughout its life is determined with probability distributions that are randomly sampled utilizing transport data. Eventually enough data is gathered from the outcomes of multiple particle paths to determine a particular result of interest. Various Monte Carlo codes for nuclear applications exist, with Monte Carlo N-Particle Transport (MCNP) being the most widely used [23]. The premise of all the codes are the same; follow the particle throughout its lifetime and keep track of various physical properties such as the neutron flux, number of absorptions, etc. The quantities of interest, referred to as "tallies" by MCNP, are specified by the user.

In this work, a fusion reactor was modeled with Monte Carlo to tally two main properties in the blanket region of the system. These properties consisted of the tritium breeding ratio (TBR) and energy multiplication factor (EMF). The TBR is defined as:

$$TBR = \frac{\int N(\mathbf{r})\sigma_T(\mathbf{r}, E)\psi(\mathbf{r}, E, \hat{\Omega})d\mathbf{r}dEd\hat{\Omega}}{\int S(\mathbf{r}, E, \hat{\Omega})dEd\hat{\Omega}} \quad (2.43)$$

The numerator is equal to the (n,t) reaction rate, where $N(\mathbf{r})$ is the atom density of the alloy, $\sigma_T(\mathbf{r}, E)$ is the tritium production microscopic cross section, and $\psi(\mathbf{r}, E, \hat{\Omega})$ is the angular flux. The tritium reaction rate is divided by the source rate, $S(\mathbf{r}, E, \hat{\Omega})$ which is equal to the tritium consumption rate.

The EMF includes two components: the energy deposited from neutrons and secondary gamma particles, E_d , and the energy deposited from X-rays and ions in the first wall of the system, E_α . E_α comes from the product of D-T fusion and is always 3.5 MeV. On the other hand, E_d is calculated as:

$$E_{d_{neutron}} = \frac{\int N(\mathbf{r}), \sigma_t(\mathbf{r}, E) H_n(E) \psi(\mathbf{r}, E, \hat{\Omega}) d\mathbf{r} dE d\hat{\Omega}}{\int S(\mathbf{r}, E, \hat{\Omega}) dE d\hat{\Omega}} \quad (2.44)$$

where $\sigma_t(\mathbf{r}, E)$ is the total cross section, including all types of absorption and scattering reactions. $H_n(E)$ can be thought of as the energy transferred from neutrons to the recoil nucleus and charged particles. Once transferred, the energy is locally deposited close to the collision site. The heating number is calculated as an energy balance between the incident neutron energy, Q -value, and secondary neutron and photon energies [9, 46, 120]:

$$H_n(E) = E - \sum_i p_i(E) [(\bar{E}_{i,n}(E) + \bar{E}_{i,\gamma}(E) - Q_i)] \quad (2.45)$$

where E is the incident neutron energy, p_i is the probability of reaction i , calculated by dividing σ_i by σ_t , $\bar{E}_{i,n}$ is the average energy of secondary neutrons emitted from reaction i with neutron incident energy, E , $\bar{E}_{i,\gamma}(E)$ is the average energy of secondary photons emitted from reaction i , and Q_i is the Q -value for reaction i . For photon reactions, the energy deposited is calculated in the same way as Eq. 2.44. The energy that is released from charged particles, $H_\gamma(E)$ comes from photon interactions. Thus, it is calculated as:

$$H_\gamma(E) = E - \sum_{i=3}^3 p_i(E) [\bar{E}_{i,\gamma}(E)] \quad (2.46)$$

Similar to Eq. 2.45, p_i is the probability of reaction i for an incident gamma energy, E , and $\bar{E}_{i,\gamma}(E)$ is the average energy of the exiting gamma particle from reaction i with incident photon energy, E . In this equation there are only three reactions of interest: 1. Compton scattering, 2. pair production with $\bar{E}_{2,\gamma}(E)$ equal to 1.022 MeV (the rest mass energy of the outgoing electron/positron pair), and 3. photoelectric effect where $\bar{E}_{3,\gamma}(E)$ is equal to zero. Once both neutron and gamma energy depositions are calculated, they can be summed to yield the total energy deposited in the blanket.

2.4.1 Variance Reduction Techniques

An analog Monte Carlo calculation depicts the random walk of a particle according to the actual physical laws of transport [23]. Each particle would represent a physical particle with a unit weight. However, often times the natural process is altered to bias specific events and reduce the intrinsic variance of the problem. Consequently, the particle weight is altered to account for the bias in the probabilities that are sampled during the random walk. Biasing is usually done to increase the number of particles in a region of interest without altering sampling that occurs in other regions or impacting the expected result of interest. As particles travel along their path and sampled with biased probabilities, the weight is adjusted accordingly. The final weight, representing the relative physical contribution to the

final result, is used as a multiplicative factor in the calculation of the final result of interest. The equation below describes the relation between the biased and unbiased weights [65]:

$$w^0 p_{unbiased} = w^* p_{biased} \quad (2.47)$$

where $p_{unbiased}$ is the actual physical probability distribution found in nature of the considered event sampled, and w^0 is the natural weight of the particles (usually unity). The biased probability is noted by p_{biased} with the corresponding weight, w^* , that accounts for such bias.

An example of a variance reduction method is implicit capture. This type of technique can be utilized in a system where there is a large shield between the source and detector whose response is of interest. Most of the particles will be absorbed in the shield before reaching the detector, and thus, only a few particles will reach the detector with a large statistical uncertainty. Instead of sampling an absorption event of isotope i with a probability of $(\sigma_{ai}/\sigma_{t,i})$, the particle is allowed to survive so it can continue its path and reach the detector. This means that the unbiased probability of scattering, $(1 - \frac{\sigma_{a,i}}{\sigma_{t,i}})$, is increased to a biased probability of 1. Using Eq. 2.47, one can see that the adjusted weight, w^* , is equal to $w^0 \times (1 - \frac{\sigma_{a,i}}{\sigma_{t,i}})$.

In Section 2.6, perturbation applications in the continuous energy Monte Carlo code Serpent [91] will be described by utilizing the same principles of variance reduction and Eq. 2.47.

2.5 Perturbation Theory in Monte Carlo

The implementation of the adjoint operator and perturbation theory into Monte Carlo began from an interest in calculating reactor kinetic parameters and reactivity changes in critical systems. The first implementations of the adjoint function in Monte Carlo involved following the random walk backwards, from the response to the source. This method proved difficult to implement and thus, the focus turned to approaches that utilize adjoint-weighting factors from forward calculations. Although the scope of this work focuses on fixed source systems, the use of perturbation in Monte Carlo described for this work in Section 4.2.2 would not have been possible without previous developments based on fission reactors. Hence, a short description of the calculation of the adjoint operator in both, MCNP and Serpent, will be detailed.

2.5.1 Monte Carlo Implementation of the Adjoint Operator in MCNP

Systems where fission occurs and there is no external source are described by the k -eigenvalue homogenous transport equation:

$$\mathbf{L}\phi = \frac{1}{k}\mathbf{F}\phi \quad (2.48)$$

Where \mathbf{L} is the transport operator previously described, k is the eigenvalue that describes the criticality of the system, and \mathbf{F} is the fission operator which includes both

prompt and delayed neutrons. When the system is critical, $k = 1$, multiple fission generations are created from previous generations. After numerous fission generations, the neutron population in the reactor will reach the fundamental eigenmode, and eventually will converge. In the adjoint k -eigenvalue equation, the adjoint flux determines the importance of neutrons and their previous generations to contributing to a detector response:

$$\mathbf{L}^\dagger \phi^\dagger = \frac{1}{k} \mathbf{F}^\dagger \phi^\dagger \quad (2.49)$$

The equation begins at the current generation and reverses back through generations. Therefore time, or generations, move backwards. The neutrons that will contribute to the response are a product of continuing fission reactions from neutrons of prior generation, and are independent of their original location. It is the ability of neutrons to sustain the chain reactions throughout generations that creates what is called the importance, or fundamental adjoint mode. In other words, the importance only depends on the ability of neutrons from early generations to continue fission reactions that will contribute to the response at the asymptotic generation. The derivation of the fundamental adjoint mode is given Ref. [82] whose final expression is as follows:

$$\phi_0^\dagger(\mathbf{r}, \hat{\boldsymbol{\Omega}}_0, E_0) = \frac{1}{C} A(\mathbf{r}, \hat{\boldsymbol{\Omega}}_0, E_0) \left\langle R, \frac{1}{v} \phi_0 \right\rangle \quad (2.50)$$

where C is a constant used as an amplitude on the adjoint flux that only depends on the detector response, R , and $A(\mathbf{r}, \hat{\boldsymbol{\Omega}}_0, E_0)$ is a function that describes an amplitude for the forward flux and only depends on the location of the original source. Because the value of the detector response does not affect the shape of the importance, ϕ_0^\dagger , it is of interest to make R equal to one, such that the term in the functional of the equation becomes a constant describing the entire population of the reactor. The result is the iterated fission probability (IFP) function of the importance, where the only factor that the fundamental adjoint mode depends on is the amplitude function A . This probability describes the expected number of fission neutrons in the system after many generations, resulting from a neutron in the original (zeroth) generation. This is proportional to the adjoint function and is what MCNP utilizes as "adjoint weights" for tallies, or scores for particular information of interest [115].

The idea behind this methodology is to weight a tally by the importance of neutrons from the original generation contributing to the neutron population at the asymptotic generation. The series of generations, from original to asymptotic is composed of a block. Each block contains the original generation, also known as the progenitors (the parents of the subsequent generations). The tallies, T , of this generation are recorded so that they can later be weighted by the importance. Additionally, an index is assigned to each progenitor that is tracked and passed down to all of its progeny. The neutron population is calculated in the last generation of the block, the asymptotic generation. It is assumed that population has well converged by this generation. The generations that fall between the progenitor and the asymptotic are referred to as the latent generations. No additional information is stored in these generations other than tracking the progenitor index. Mathematically, the adjoint-weighted tally is presented as:

$$S_p = R_p T_p \quad (2.51)$$

where S_p is the score for a specific progenitor, and T_p is the tally contribution calculated only for neutrons at the progenitor generation with index, p , and R_p is the neutron population at the asymptotic generation. During the progenitor generation, every neutron becomes a candidate with an assigned index, and T_p is recorded for every candidate. After the tally is recorded at the end of the generation, only the index of progenitor neutrons that created additional fission neutrons are saved. Latent generations continue to pass along the progenitor index until they reach the asymptotic generation. At this point R_p , known as the track length estimator of neutron production, is calculated:

$$R_p = \sum_{\tau \in p} \nu \Sigma_f w \ell \quad (2.52)$$

where ν is the average number of neutrons per fission, Σ_f is the macroscopic fission cross section (at current energy and material), w is the particle weight, and ℓ is the length of track τ . Each estimate is summed over all the tracks, τ in the asymptotic generation that originated from from progenitor p . Once R_p is obtained, it is plugged back into Eq. 2.51, summed over all progenitor indexes. When the score for a block is recorded, a new block is created and the same process is repeated until the end of the MCNP run.

A simple example of an adjoint-weighted tally is the flux in a region r of the reactor. This is approximated by:

$$\phi^\dagger \approx \frac{\langle \phi^\dagger, \phi \rangle_r}{\langle 1, \phi \rangle_r} \quad (2.53)$$

This example is considered angular independent. Additionally, the approximation is valid only around the phase space of r . The denominator in the equation is simply calculated using the standard MCNP track length estimator:

$$\langle 1, \phi \rangle_r = \frac{1}{V_r} \sum_{\tau} w \ell \delta_{sr} \quad (2.54)$$

In the above equation, w is the particle weight, ℓ is the length of track τ , and V_r is the volume of region r . The summation is carried over all tracks in region r . The product in the summation is only performed when the current phase space region of the track, s , is equal to r . Otherwise the product is zero. For the numerator of Eq. 2.53, we can use Eq. 2.51. The value of T_p is equivalent to Eq. 2.54 with an additional factor of $\frac{1}{w}$. This results in [81]:

$$\langle \phi^\dagger, \phi \rangle_r = \frac{1}{N} \frac{1}{V_r} \sum_p R_p \sum_{\tau \in p} \ell \delta_{sr} \quad (2.55)$$

N is a normalization factor equal to the total source weights of all progenitor particles from the original generation. The incorporation of adjoint-weighted tallies in MCNP kinetic parameters and perturbation theory in the form of reactivity approximations can be found in Refs. [81, 82].

2.5.2 Serpent Estimate of the Iteration Fission Probability

Similarly to MCNP, Serpent takes advantage of the proportionality between the IFP and importance or adjoint flux, to approximate ϕ^\dagger . Nevertheless, its approach relies on a ratio between the calculated weights of the descendants to the weight of their ancestor, from the original generation [94]. This is due to the fact that in non-analog Monte Carlo simulations the particle weight is adjusted in each generation and thus, the total number of neutrons in the system changes. In an analog simulation, the importance of an ancestor neutron in sustaining fission chains and contributing to the response would simply equal the total number of neutrons in the asymptotic generation that came from that specific ancestor. In non-analog, each neutron in the every generation that contributes to the response has a unique weight. Therefore the importance is approximated as:

$$I_n^{(\gamma)} = \frac{1}{w_n} \sum_{k \in d_n^{(\gamma)}} w_k \cdot \prod_{i=\alpha}^{\alpha+\gamma-1} k_{\text{eff},i} \quad (2.56)$$

where w_n is the weight of neutron n in the original generation α , γ is the number of latent generations, and w_k is the weight of a descendant neutron k , summed over all of the descendants of n in generation $\alpha + \gamma$. The sum is multiplied by the product of the multiplication factors, utilized as a normalization factor that accounts for the fission source neutrons between successive generations α and $(\alpha + \gamma - 1)$. This normalization factor preserves the total weight (product of weight and probability in Eq. 2.47) in every generation.

Implementation of Eq. 2.56 for reactor kinetic parameters can be found in Ref. [94]. Unlike MCNP, these parameters are calculated for every generation, in which neutrons end up fulfilling the roles of progenitors, latent generation neutrons, and neutrons in the asymptotic generation at one point in the calculation. This is accomplished by utilizing arrays comprised of values in the calculation of the specific parameter of interest. The first value of the array is the ancestor, α , and the last value is the current generation, $(\alpha + \gamma)$. The values of the array are updated with each generation such that the first value is discarded, and all values are moved a position to the left. New values can only be added to the array when a fission occurs since any other reaction does not contribute to new generations of neutrons. The only drawback to this method is the additional memory space needed to store all values in the array. However this is not a huge issue since it takes around 10 generations to reach the asymptotic population. Therefore, ten array values are stored at a time.

2.6 Collision History-based Approach to Perturbation with Monte Carlo

The previous section introduced the use of adjoint theory to calculate kinetics parameter in Monte Carlo codes which has recently been expanded to generalized perturbation calculations and sensitivity functions [115, 124]. However, all of these implementations only apply to fission systems. There is only a small amount of work on Monte Carlo approaches solving for the responses caused by a perturbation in a model with a fixed source

[36, 67, 136]. Nevertheless, the theory currently adapted to Serpent [15] can be used to find the exact response, i.e. tritium breeding ratio, caused by a perturbation in the system such as the change of blanket composition.

The approach taken by Serpent is based on similar techniques utilized for variance reduction. Probability density functions of parameters of interest are biased and are then sampled as accepted or rejected events to account for the bias on the probability. A collision history is created from these events which will in turn be used to calculate perturbed fluxes for the use in the new response functions. In the following sections, this theory, known as Exact Perturbation Theory (EPT), is detailed and its implementation for fusion systems is described. Afterwards, the expansion of EPT to GPT to calculate sensitivity coefficients in fission reactors, which was the original goal of Serpent, is briefly described.

2.6.1 Accepted and Rejected Events

The perturbation approach adopted in Serpent begins with biasing the probabilities of events of interest, i.e. cross sections that are perturbed. In the case of changing compositions of a fusion blanket, there is a desire to increase sampling of all reactions from every isotope in this region. Therefore, $\Sigma_{t,i}$ of every isotope i will be increased by a factor f_r . To account for the increase in the total cross section, accepted and rejected probabilities are created. Once the total cross section of isotope i is sampled with an increased factor of f_r , the event is subsequently sampled to see if it is accepted with a probability of $(\frac{1}{f_r})$, or rejected with a probability of $(1 - \frac{1}{f_r})$. Events must be rejected to restore fair neutron transport such as it is done with variance reduction methods. Both accepted and rejected events are recorded in the collision history of the particle through its random walk. A factor of 2 was chosen for f_r which means that events are accepted and rejected with an equal probability of 0.5. The choice of 2 for f_r made the most sense. However, this factor is arbitrary and other numbers can be utilized. Future work will involve optimizing this number.

2.6.2 Exact Perturbation Theory for Use in Fixed Source Problems

The next step in this approach is to adjust the weights of the particle sampled according to the perturbations. As discussed in Section 2.4.1, particles sampled naturally with analog Monte Carlo will follow the physical laws of transport and maintain their original weights. In the event that a probability distribution is biased, the particle weight must be adjusted to compensate for the increase/decrease in the probability as described by Eq. 2.47.

Consider the Monte Carlo application of a fusion reactor (fixed source) with a reference blanket composition. The random walks will be sampled with probability distributions based on the macroscopic cross sections, $\Sigma_{r,i}$, of reaction r and nuclide i . When the compositions of each blanket component are altered, the densities change, and therefore the probability distributions of the perturbed blanket will be different. The perturbed composition is usually studied by running an additional Monte Carlo case and sampling the new particle paths. However, instead of running a new case per perturbed blanket composition, the particle path of the reference case could be utilized. From the unperturbed case, perturbed responses are calculated by adjusting particle weights according to the perturbed

probability distributions. The probability distributions of the reference case, which determine the path of the particle, can be referred to as p_{biased} and the perturbed as $p_{unbiased}$ in Eq. 2.47. With these substituted, the new for equation for a neutron history n becomes:

$$w_n^0 \bar{\Sigma}_{r,i} = w_n^* \Sigma_{r,i} \quad (2.57)$$

where $\bar{\Sigma}_{r,i}$ is the perturbed cross section of any reaction r for any nuclide in the blanket and $\Sigma_{r,i}$ is the cross section for the reference case. If Monte Carlo is ran as analog, the original particle weight, w_n^0 , of the perturbed case will be unity. However, this might not be the case if variance reduction methods are utilized. With w_n^0 and the probabilities known, we can then solve for w_n^* :

$$w_n^* = w_n^0 \frac{\bar{\Sigma}_{r,i}}{\Sigma_{r,i}} \quad (2.58)$$

The biased particle weight, w_n^* , is viewed as the adjustment accounting for the change from the *unbiased* (perturbed) probability to the *biased* (reference) probability. Positive perturbations ($\bar{\Sigma}_{r,i} > \Sigma_{r,i}$) will increase w^* in the case that the cross section sampled is counted as accepted. On the other hand, rejected or virtual events in the collision history will lower w_n^* . This means that $\bar{\Sigma}_{r,i}$ in Eq. 2.58 will be equivalent to $(\Sigma_{r,i} + d\Sigma_{r,i})$ for accepted events and $(\Sigma_{r,i} - d\Sigma_{r,i})$ for rejected events. The opposite will be true if the perturbation is negative. An example is illustrated in Fig. 2.1 which follows the collision history of a neutron's random walk in the blanket region of the reactor. Eq. 2.59 shows the implementation of Eq. 2.58 for this case. It is assumed that the probability of an accepted and rejected collision is the same (0.5). Additionally, the isotope of the blanket sampled in each of the collisions was not included in the notation. One can see from Eq. 2.59 that the biased weight, w_n^* , is equal to the product of w^0 , and a factor that includes the relative change in each sampled cross section.

Once all the histories are completed, the perturbed flux is obtained from the biased weights and the reference flux. Serpent employs the collision estimator to calculate flux [92]:

$$\bar{\phi} = \sum_{n=1}^N \sum_{i=1}^I \frac{w_n^*}{\Sigma_{tot,i}} = \sum_{n=1}^N \sum_{i=1}^I w_n^* \phi_i \quad (2.60)$$

where $\bar{\phi}$ is the total perturbed flux, and $\Sigma_{tot,n}$ is the reference total cross section of the material and at the location of collision i . The sums are performed over every collision i that occurred within the region of interest, i.e. the fusion blanket, and over every neutron history n . The reciprocal of the cross section in this equation is equivalent to the reference flux.

The Exact Perturbation Theory (EPT) methodology demonstrates that the biased weight is an estimator of the *exact* neutron flux distribution in the perturbed system. The biased weight can then be considered as the perturbation response which is directly calculated from the relative change in parameter P without the need of first order approximations such as those from Eq. 2.27. Unlike deterministic methods, which solve the integrodifferential transport equation, Monte Carlo solves for the integral transport equation [60, 147], and thus can account for fixed sourced perturbation in a direct manner.

2.6.3 Extension of Exact Perturbation Theory to Generalized Perturbation Theory

Exact perturbation theory can only be used for fixed source cases and must be extended to Generalized Perturbation Theory in the case that fission is involved. Unlike fixed sources, fission sources create a new generation of neutrons every time a fission event occurs. EPT does not consider the effects of multiple generations and is not valid in systems where multiplication occurs. Instead, a first order GPT must be utilized. First order perturbation effects account for the relative change of the weight due to relative changes in parameter x . For a neutron history n this is written as [15]:

$$\frac{\partial w_n/w_n}{\partial x/x} = \sum_{(g=\alpha-\lambda)}^{\alpha} \left({}^{(n,g)}ACC_x - {}^{(n,g)}REJ_x \right) \quad (2.61)$$

where ${}^{(n,g)}ACC_x$ and ${}^{(n,g)}REJ_x$ are the number of accepted and rejected events, respectively, of parameter x , in history n and generation i . The equation is summed over all generations starting at generation $(\alpha - \lambda)$ and ending at the current generation, α . The number of latent generations utilized is represented by λ . The parameter x represents any cross section that is perturbed in the system.

An application of this methodology is finding the response in the form a linear functional, such as the reaction rate from Eq. 2.11. The first order expansion of this type of functional was demonstrated in Eq. 2.24. Ignoring second order effects and dividing this equation by R gives the relative change of the response:

$$\frac{\delta R}{R} = \frac{\langle \delta \Sigma, \phi \rangle}{\langle \Sigma, \phi \rangle} + \frac{\langle \Sigma, \delta \phi \rangle}{\langle \Sigma, \phi \rangle} \quad (2.62)$$

Dividing the above equation by the relative change of the perturbed parameter x results in the following sensitivity function:

$$S_x^R = \frac{\left\langle \frac{\partial \Sigma}{\partial x/x}, \phi \right\rangle}{\langle \Sigma, \phi \rangle} + \frac{\left\langle \Sigma, \frac{\partial \phi}{\partial x/x} \right\rangle}{\langle \Sigma, \phi \rangle} \quad (2.63)$$

Knowing that the response in the denominator of the equation above can be easily calculated, we will focus on the terms of the numerator. The first term can be solved explicitly with Monte Carlo in the same way as described by the previous section on EPT. This term is known as the "direct effect" of the perturbation in x , since changes in parameter x directly affects the response without accounting for any effects on the flux. The second term referred to as the "indirect effect" describes how the response is affected through changes in the flux caused by perturbations in x . In other words, the response function implicitly depends on the perturbation of x through the change in the flux. This term can be derived, first, by looking at the denominator. For the purposes of this discussion and for consistency with Ref. [15], the track length estimator, rather than the collision estimator, will be utilized. Hence, the response can be defined as:

$$\langle \Sigma, \phi \rangle = \sum_{n \in \alpha} \sum_{t \in n} w_n \ell_t \Sigma \quad (2.64)$$

The reaction rate is estimated as the product of the track length of track t , ℓ_t , the cross section, Σ , and the weight of particle n , w_n . The product is summed over all tracks of each particle that is present in the most current generation, α . The equation also includes a population normalization factor that ends up canceling out and thus is not included in the discussion. The derivative of this equation creates an expression for second term of Eq. 2.63:

$$\begin{aligned} \left\langle \Sigma, \frac{\partial \phi}{\partial x/x} \right\rangle &= \sum_{n \in \alpha} \sum_{t \in n} w_n \cdot \frac{\partial w_n / w_n}{\partial x/x} \cdot \ell_t \Sigma \\ &= \sum_{n \in \alpha} \sum_{t \in n} w_n \left[\sum_{(g=\alpha-\lambda)}^{\alpha} \left({}^{(n,g)}ACC_x - {}^{(n,g)}REJ_x \right) \right] \ell_t \Sigma \end{aligned} \quad (2.65)$$

The meaning of the above is described as the net number of events x that occurred in $\alpha - (\alpha - \lambda) = \lambda$ generations from each particle n present in generation α . When plugged back into Eq. 2.63, this term is weighted on the response calculated from the track length generator in Eq. 2.64. As a result, it is possible to calculate the first order sensitivity, S_x^R . Additional implementation of this methodology can be found in Ref. [15].

2.7 Activation Analysis Governing Equations

So far, the concepts described in this chapter relate to the transport of neutrons throughout a system, such as the fusion reactor. The scope of this work also includes examining the time dependent rate of change of concentrations of many of the nuclides found within the fusion reactor's blanket, both during irradiation and after shutdown. This allows other properties of interest to be calculated that are related to the safety and environmental impact the blanket. This section will present the mathematic formulations for some of these properties calculated with computational methods in Chapter 3 to gather a basic understanding of their physical properties.

Determining the change of a nuclide over time involves calculating the parameters of the following expression [68]:

$$\frac{dN_i}{dt} = \text{Production Rate} - \text{Destruction Rate} - \text{Decay Rate} \quad (2.66)$$

Mathematically, Eq. 2.66 for a non-fissile system, such as a fusion reactor blanket, without additional sources can be written as:

$$\frac{dN_i}{dt} = \sum_{j=1}^X l_{ij} \lambda_j N_j + \phi \sum_{k=1}^X f_{ik} \sigma_{a,k} N_k - \lambda_i N_i - \sigma_{a,i} N_i \phi \quad (2.67)$$

where

N_i = density of nuclide i

X = number of nuclides

l_{ij} = fraction of radioactive disintegration by nuclide j leading to the formation of nuclide i

λ_j = radioactive decay constant of j

ϕ = average neutron flux

f_{ik} = fraction of neutron absorption reaction by nuclide k to create nuclide i . Absorption reactions are all types of neutron capture (γ , α , p , $2n$, $3n$) except for fission.

$\sigma_{a,k}$ = neutron absorption cross section of nuclide k

λ_i = radioactive decay constant of i

$\sigma_{a,i}$ = neutron absorption cross section of nuclide i

This means that $\frac{dN_i}{dt}$ is the rate of change of concentration of N_i , $\sum_{j=1}^X l_{ij}\lambda_j N_j$ is the rate of production of N_i due to the radioactive decay of N_j summed over all nuclides j from 1 to X , $\phi \sum_{k=1}^X f_{ik}\sigma_{a,k} N_k$ is the rate of transmutation into N_i from radioactive neutron capture by nuclide N_j summed over all nuclides k from 1 to X , $\lambda_i N_i$ is the radioactive decay of N_i , and $\sigma_{a,i} N_i \phi$ is the rate of destruction of N_i due to all forms of neutron absorption reactions rather than fission (n,γ , n,α , n,p , $n,2n$, $n,3n$). Eq. 2.67 can be solved for all nuclides of interest present in the system. After shutdown, when the fusion blanket alloy is extracted from the system, Eq. 2.67 can be simplified to:

$$\frac{dN_i}{dt} = \sum_{j=1}^X l_{ij}\lambda_j N_j - \lambda_i N_i \quad (2.68)$$

which is only based on the decay into the nuclide and from the nuclide. Equations 2.66 and 2.67 are the governing equations for activation analysis that give foresight into what kinds of byproducts are accumulated from the fusion blanket throughout time and how quickly they dissipate. By obtaining the radionuclide activity and isotopic concentrations from these equations, additional safety and environmental factors can be determined such as the heat generated from decays in the blanket, the contact dose received, and the dose one would receive in an accident scenario. The next few sections present the formulations utilized by the activation analysis code described in Chapter 3 to obtain these factors, so that a general understanding can be gathered.

2.7.1 Decay Heat

Activation analysis in Chapter 3 examines the heat released as a result radioactive decay from the nuclides present in the blanket's alloy, after the alloy is extracted from the reactor. This quantity, decay heat, is defined as [116]:

$$H_\alpha(t) = \sum_{i=1}^I \lambda_i N_i(t) E_{\alpha,i} \quad (2.69)$$

$$H_{\beta}(t) = \sum_{i=1}^I \lambda_i N_i(t) E_{\beta,i} \quad (2.70)$$

$$H_{\gamma}(t) = \sum_{i=1}^I \lambda_i N_i(t) E_{\gamma,i} \quad (2.71)$$

which can be described as the summation of the products of the activities with respect to the mean energy released for all the isotopes in the blanket. The decay heat is calculated for each type of decay. Therefore, $H_{\alpha}(t)$, $H_{\beta}(t)$, $H_{\gamma}(t)$ are the total alpha, beta, and gamma decay heat respectively at time t after the alloy exits the reactor blanket. The terms $E_{\alpha,i}$, $E_{\beta,i}$, $E_{\gamma,i}$, are the mean alpha, beta, and gamma energy releases per disintegration of nuclide i , and λ_i is the decay constant of that nuclide. The concentration of the nuclide i at time t , $N_i(t)$ is calculated from Eq. 2.67 and 2.68. The total decay heat released from the entire alloy can be obtained by summing the individual contributions from Eq. 2.69, 2.70, and 2.71.

2.7.2 Internal and External Dose Exposures

When an accident occurs in any type of reactor, there is a possibility that radionuclides will be released and travel to the environment. As a result, individuals close to the site are at risk of exposure from the various types of radiation emitted by these nuclides. This includes alpha particles which are stopped by the outer layer of the skin and thus are only dangerous if their emitters are inhaled or ingested (internal contamination). Beta particles can penetrate and contaminate the skin, while beta emitters can be deposited in the body through through inhalation and/or ingestion and through damaged skin. Gamma and neutron particles have much higher energies and will be absorbed into the body through external exposure. External radiation comes from cloudshine, groundshine, and skin contamination, and will deposit a short-term dose to the individual [120]. On the contrary, internal contamination is most likely from inhalation and remains in the body as the radioactive atoms within the body continue to decay and release additional radiation. Internal contamination therefore gives a long-term, or committed dose. The term dose, refers to the energy deposited per gram of matter:

$$D = \frac{dE}{dm} \quad \left(\text{Grays} = \frac{\text{J}}{\text{kg}} \right) \quad (2.72)$$

In the case of an accident, it is more interesting to examine the *equivalent dose*, which accounts for energy absorbed to that tissue, and the type of radiation absorbed. This is calculated as:

$$H_T = w_R D_{T,R} \quad (2.73)$$

where w_R is the radiation weighting factor, and $D_{T,R}$ is the mass-averaged absorbed dose in tissue T due to radiation type R defined as:

$$D_{T,R} = \frac{\int_T D_R(x, y, z) \rho(x, y, z) dV}{\int_T \rho(x, y, z)} \quad (2.74)$$

where D_R is the absorbed dose from radiation type R and ρ is the density at a location. Both terms are integrated over the entire organ or tissue measured. The radiation weighting factor in Eq. 2.73 is a tabulated value related to the stopping power for each type of radiation, referred to as Linear Energy Transfer (LET):

$$LET = \frac{dE}{dx} \quad (2.75)$$

This is defined as the average energy, dE , imparted by a particle through a medium traveling a distance, dx . Alpha and beta particles have high LET, while neutrons have medium LET depending on the kinetic energy. Gamma particles which have high kinetic energies, have the lowest LET. To get the total equivalent dose from all types of radiation, a sum is taken over all radiation weighting factors in Eq. 2.73. To obtain the dose to the entire body as a whole, a summation is performed over the product of the equivalent dose and a tissue weighting factor as such:

$$E = \sum_T w_T \cdot H_T \quad (2.76)$$

where w_T is the tissue weighting factor. The tissue weighting factors in Eq. 2.73 are related to the biological effect or total health risk from radiation exposure to that particular tissue or organ. These are defined by regulation [120] and vary from 0.01 for the skin to 0.20 for the gonads. The sum of the tissues falls between zero and one, where one is the sum over all organs and tissues. Effective dose accounts for both internal and external exposure. A subset of effective dose is the internal dose calculated over the remaining life of an individual after exposure, normally taken to be 50 years for adults and 70 years for children. This term is called the committed effective dose and was formally referred to as the committed effective dose equivalent (CEDE). If short-term exposure effects are also of interest, the total effective dose equivalent (TEDE) is calculated. This is defined as the sum of the CEDE from internal exposures, and the effective dose from external exposures.

In an accident scenario, both inhalation and ingestion are of concern. Whether one is dominant over the other is dependent on the type of nuclide, its chemical form, and its solubility. Either way, once inside the body, the radionuclide can travel to the blood via the lungs or eventually to the bloodstream through the gastrointestinal tract. The fraction of the isotope that stays in the bloodstream is dependent on the isotope itself. Once the nuclide is in the blood, it can travel anywhere in the body and be absorbed by a specific tissue or organ, which depends on the chemistry of the nuclide and nature of the tissue or organ. The calculation for committed effective dose is therefore quite complicated and depends on multiple factors. A simplified calculation of the equivalent dose following acute inhalation of a radionuclide at time, $t = 0$, can be defined as [83]:

$$H_T(t) = H_T(0) \cdot (1 - e^{-\lambda t}) \quad (2.77)$$

where λ here is the sum of the decay constant for the radionuclide and the biological removal rate constant. The biological decay constant is solved from systems of differential equations that model the biokinetics of the nuclide. This type of equation is calculated with computational methods, and utilizes Dose Conversion Factors (DCF) in its calculations. A

DCF is defined as the amount of biological damage given to either an organ or tissue from an isotope. The DCF describes the CEDE per unit of activity intake and accounts for the path the radioisotopes travel inside of the body, the decay of the isotopes, and the formation of daughter isotopes that will release additional radioactivity. Multiplying the DCF by the activity and other factors related to atmospheric conditions and other biological factors can yield the inhalation dose in units of Sieverts. External exposure doses such as the gamma dose received from cloudshine are also calculated with dose conversion factors that depend on the geometry of the plume carrying the radiation and position of the individual with regards to the traveling plume. DCFs for different scenarios have been modeled and are included in the Federal Guidance Report #11 and ICRP 72 [120]. With regards to this work as will be seen in Chapter 3, accident dose to individuals will be calculated by multiplying the activity obtained from Eq. 2.67 during reactor operation, by specific DCFs.

2.7.3 Contact Dose Rate

Another quantity of interest examined is the gamma dose resulting from isotopic radioactive decay of the irradiated alloy, after it exits the blanket. This quantity is referred to as the contact dose rate. It is obtained by calculating the dose in air at the surface of a semi-infinite slab whose material contains concentrations of radionuclides of interest. This quantity is approximated by [48]:

$$H = 5.76 \times 10^{-10} \cdot \frac{B}{2} \sum_{g=1}^G \frac{(\mu_{en}(E_g)/\rho)}{(\mu(E_g)/\rho)} S_{\gamma}(E_g) \quad (2.78)$$

where:

H = surface γ dose rate $\left(\frac{Sv}{h}\right)$

5.76×10^{-10} i= conversion factor from $\left(\frac{MeV}{kg \cdot s}\right)$ to $\left(\frac{Sv}{h}\right)$

B = build up factor to account for the increase in the dose due to the contribution of secondary or scattered gammas (=2) [48, 141]

$\sum_{g=1}^G$ is the sum over all γ energy groups from g to G (number of groups depends on library used in code)

E_g is the mean energy of group g

μ_{en}/ρ = mass energy absorption coefficient of the material $\left(\frac{m^2}{kg}\right)$

μ/ρ = mass attenuation coefficient of the material $\left(\frac{m^2}{kg}\right)$

S_{γ} = rate of gamma emission $\left(\frac{MeV}{kg \cdot s}\right)$

The rate of gamma emission at mean energy i is calculated as:

$$S_{\gamma}(E_i) = I_i A(t) \quad (2.79)$$

where I_i is the intensity of energy group i , and $A(t)$ is the specific activity of the entire material at time t . Within an energy group, the intensity at each branch of the gamma decay scheme is calculated separately. After all individual intensity calculations for that energy group are performed, they are summed together to obtain the total intensity in that group. For a selected group of nuclides who do not have γ spectrum information, the intensity is estimated by the description in Ref.sublet2012fispect. The specific activity (Bq/kg) is calculated as:

$$A(t) = \frac{\sum_{i=1}^I \lambda_i N_i(t)}{m} \quad (2.80)$$

where λ_i is the decay coefficient of nuclide i , and $N_i(t)$ is the concentration of the nuclide obtained from Eq. 2.67 and 2.68. This product, equal to the activity of the radionuclide, is summed over all isotopes found in the material and is then divided by the mass of the material, m .

The contact dose rate is an approximated quantity and does not account for the 3D geometry of the system, and variable build-up factors that depend on geometry, gamma ray energy, and on the material of the shield [122]. Thus, results will probably be overestimated. Nevertheless, this estimate is good enough for the purposes of this work which is to analyze the safety and environmental performance of the alloy without worrying about obtaining the most exact results.

Part II

Results and Discussion

Chapter 3

Neutronic and Activation Analysis of Lithium-based Ternary Alloys in Inertial Fusion Energy (IFE) Blankets

3.1 Introduction

Lithium is often the preferred choice as breeder and coolant in fusion blankets as it offers excellent heat transfer and corrosion properties, and most importantly, it has a very high tritium solubility and results in very low levels of tritium permeation throughout the facility infrastructure [86]. However, lithium metal vigorously reacts with air and water and exacerbates plant safety concerns [34]. For this reason, over the years numerous blanket concepts have been proposed with the scope of reducing concerns associated with lithium [10, 73]. The European helium cooled pebble bed breeding blanket (HCPB) physically confines lithium within ceramic pebbles [73]. The pebbles reside within a low activation martensitic ferritic steel structure and are cooled by helium. The blanket is composed of the tritium breeding lithium ceramic pebbles and neutron multiplying beryllium pebbles. Similar concepts are being investigated in China, Korea, and India [29, 30, 45, 84], while Japan is exploring a ceramic breeder cooled by pressurized water [44]. Other blanket designs utilize lead to lower chemical reactivity [113]; LiPb alone can serve as a breeder, coolant, neutron multiplier, and tritium carrier. India is taking advantage of this with its Lead-Lithium cooled ceramic breeder (LLCB) design. Europe is developing a He cooled lithium lead (HCLL) blanket which utilizes helium as the coolant and LiPb as the breeder, with reduced activation ferritic-martensitic steel (RAFM) as the structural material [21]. The US is also utilizing LiPb in their blanket design with the dual-coolant lead-lithium concept (DCLL); helium is used to cool the first wall and structural components made up of low-activation ferritic steel, whereas lithium-lead (LiPb) acts as a self-cooled breeder in the inner channels of the blanket [73]. The helium-cooled steel and lead-lithium alloy are separated by silicon carbide flow channel inserts which thermally insulate the self-cooled breeder region from the helium cooled steel walls. This creates a LiPb breeder with a much higher exit temperature than the steel which increases the power cycle efficiency and also decreases the magnetohydrodynamic (MHD) pressure drop [109]. MHD physics describe the phenomenon

of an electrically conducting fluid that is impacted by both magnetic and electric fields. In addition, LiPb blankets produce low afterheat and low operation pressures [73]. China is designing a dual functional LiPb (DFLL) test blanket module (TBR) which allows both a helium-cooled quasi-static LiPb (SLL) concept and a He/PbLi dual-cooled LiPb (DLL) concept to be tested [149, 150]. Molten salt blankets with a mixture of lithium, beryllium, and fluorides (FLiBe) offer good tritium breeding, low electrical conductivity and therefore low MHD pressure drop, low chemical reactivity, and extremely low tritium inventory [73]; the addition of sodium (FLiNaBe) has been considered because it retains the properties of Flibe but also lowers the melting point [10]. One of the most recent designs is the Korean He-cooled molten lithium (HCLM) blanket with ferritic steel as a structural material [15]. Although many of these blanket concepts are promising, challenges still remain. The limited amount of beryllium available poses a problem for ceramic breeders such as the HCPB. Additionally, ceramic breeders require high porosity in the pebbles to allow tritium to be extracted, significantly reducing the thermal conductivity [11]. FLiBe and FLiNaBe are highly viscous and have a low thermal conductivity. In liquid metal breeders, corrosion issues occur between LiPb blankets and the steel constituents from structural materials. This negatively impacts the structural integrity of the blanket structures due to wall thinning and transport of corrosion products throughout the liquid metal loop. LiPb blankets in magnetic inertial confinement systems are affected by MHD from the plasma's magnetic field, due to LiPb's nature as a conductor. When it flows through the blanket, it creates an electromagnetic field that generates a current in the liquid. As a result, the induced current decreases the velocity of the liquid's flow, providing additional drag to LiPb and increasing its pressure drop [51]. An important common issue found in all three blanket technologies is tritium permeation. Tritium has a high partial pressure in each of the blankets and thus, low solubility. Tritium then permeates into structural material, heat exchanger, first wall, and containment structure potentially releasing into the environment and posing a high safety concern [11]. Lawrence Livermore National Laboratory (LLNL) decided to combat many of the issues found with the blanket concepts by attempting to develop a new lithium-based alloy—most likely a ternary alloy—which maintains the beneficial properties of lithium (e.g. high tritium breeding and solubility) while reducing overall flammability concerns for use in the blanket of an Inertial Fusion Energy (IFE) power plant [39, 111]. The IFE engine employs inertial confinement fusion (ICF) through the use of lasers aimed at an indirect-driven target composed of deuterium-tritium fuel. The fusion driver/target design implements the same physics currently experimented at the National Ignition Facility (NIF). The IFE reactor uses lithium in both the primary coolant and blanket; therefore, lithium-related hazards are of primary concern. Although reducing chemical reactivity is the primary motivation for the development of new lithium alloys, the successful candidates will have to guarantee acceptable performance in all their functions. The scope of this study is to evaluate the neutronics performance of a large number of lithium-based alloys in the blanket of a fusion reactor. In particular, parameters are set on the tritium breeding ratio (TBR) [40] and energy multiplication factor (EMF) [103] which allow candidate alloys to be selected. Activation analysis is then applied on the selected alloys to assess specific safety and environmental properties. This chapter is organized as follows: Section 3.2 presents the models and methodologies used for the analysis; Section 3.3 discusses the results; Section

Table 3.1: Composition and dimensions of the blanket components.

Layer #	Material	Thickness (cm)
1	HT9	0.5
2	Breeder/Coolant	1
3	HT9	0.5
4	Breeder/Coolant	100
5	HT9	0.5
6	Breeder/Coolant	50
7	HT9	0.5
8	Graphite	100

3.4 summarizes findings and future work.

3.2 Models and Methodology

3.2.1 Chamber Model

The neutronics performance of each alloy was evaluated in the blanket of the LIFE power plant. The blanket is build around the fusion chamber that consists of a central spherical cavity with a 13.004 m radius. Fusion occurs at the center of the void chamber where the laser beams impact the fuel target. The ICF target releases 132 MJ from $D(T,n)\alpha$ reactions; 97.45 MJ is in neutrons kinetic energy and 34.55 MJ is in X-rays and ions [134]. The target also releases 4.69 neutrons from fusion and additional 0.131 neutrons (2.8% of the total) from $(n,2n)$ reactions with the compressed DT fuel and the lead hohlraum. Alpha particles instantly deposit their energy in the surrounding DT fuel, in the ablator materials, and in the lead capsule resulting in the release of X-rays and ions [105]. Xenon fills the void chamber at a density of $6 \mu\text{g}/\text{cm}^3$ and shields the chamber wall (first wall) from ions and X-rays [134]. This phenomenon is illustrated in Fig. 3.1. The blanket surrounds the central chamber and consists of a series of coolant/breeder layers separated by structural components (Table 3.1). The structural material is HT9 (composed of iron (85.9%), chromium (12.1%), and the rest is carbon, silicon niobium, molybdenum, and tungsten with density of $8 \text{ g}/\text{cm}^3$); it features high resistance against radiation damage and low chemical reactivity. In the original design the coolant/breeder material is lithium; this study replaces lithium with a ternary lithium alloy. The blanket is completed by a 100 cm graphite reflector ($1.7 \text{ g}/\text{cm}^3$). The IFE power plant is assumed to generate 2,200 MW of fusion power.

Neutron and photon transport was performed with the three-dimensional Monte Carlo transport code MCNP6 [56]. A simplified model consisting of concentric spherical regions was assumed. Nevertheless, the model was created to resemble its real-life counterpart as show in Fig. 3.2. The model also includes 48 penetrations through the blanket representing the beam ports, as well as the target injection port at the top of the chamber, and the debris exit port at the bottom. Modeling the indirect-driver and target is extremely com-

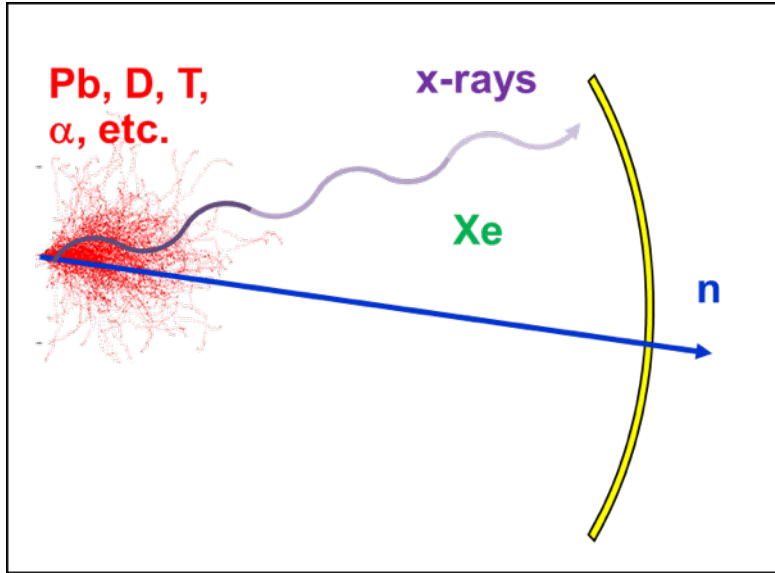


Figure 3.1: Illustration of absorption of products from fusion reactions in the Xenon chamber except for neutrons, which travel to the blanket.

plex, and for the scope of this study, the DT target was represented as a point source at the center of the chamber with a neutron energy distribution obtained through accurate target models (Fig. 3.3). The energy spectrum accounts for the scattering of the fusion neutrons with the DT target and lead hohlraum. All materials in the model utilized ENDF/B-VII.I cross sections at 900 K [26].

The neutronics performance of the alloys was evaluated by two parameters: (1) tritium breeding ratio (TBR), and (2) energy multiplication factor (EMF). TBR is defined as the ratio of tritium produced in the blanket to the tritium consumed in the target [40]. Tritium production was calculated by utilizing the F4 tally in MCNP [56]. The TBR must be greater than unity for the system to be self-sufficient. In this specific study, the TBR accounts for losses due to radioactive decay, and only for a limited storage inventory that is needed under emergencies to continue operation [11]. Earlier studies on the IFE design assumed a minimum TBR constrain of 1.02. This is lower than what other fusion plants require due to the high fractional burn-up ($\sim 30\%$) in the IFE source and lower tritium permeation in the lithium alloy coolant [132]. Additionally, this study excludes the need to produce a startup inventory for other reactors [11].

The EMF is defined as the ratio of power deposited in the blanket and other regions outside the IFE chamber by neutrons, gammas, and alpha particles to the power generated from fusion reactions [103]. It is given by:

$$EMF = \frac{E_d + E_\alpha}{E_f} \quad (3.1)$$

where E_d is the total energy deposited in the chamber (first wall, breeding regions, structures, and reflector) and surrounding regions (shield, beam dumps, etc.) as the result of neutron

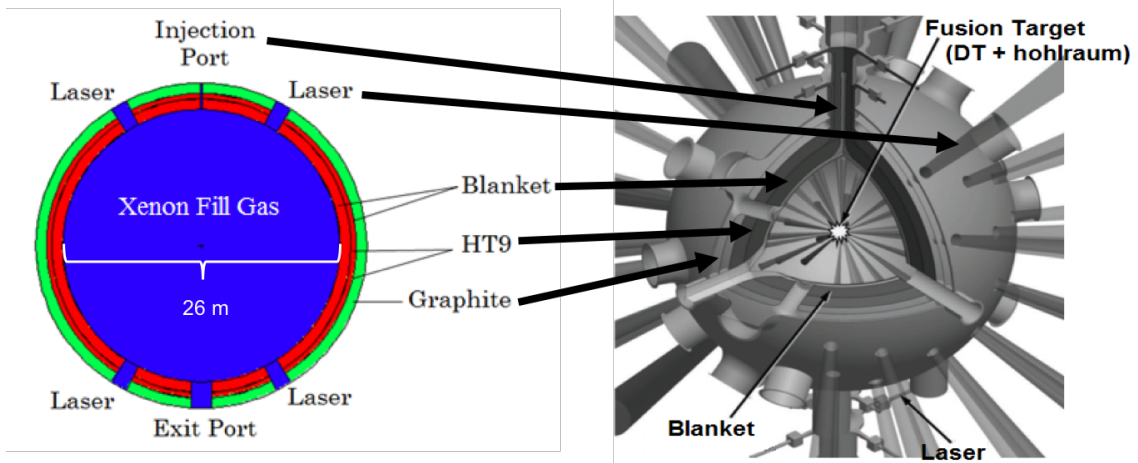


Figure 3.2: MCNP model of the IFE reactor viewed from the xz plane (left) compared to real-life model (right).

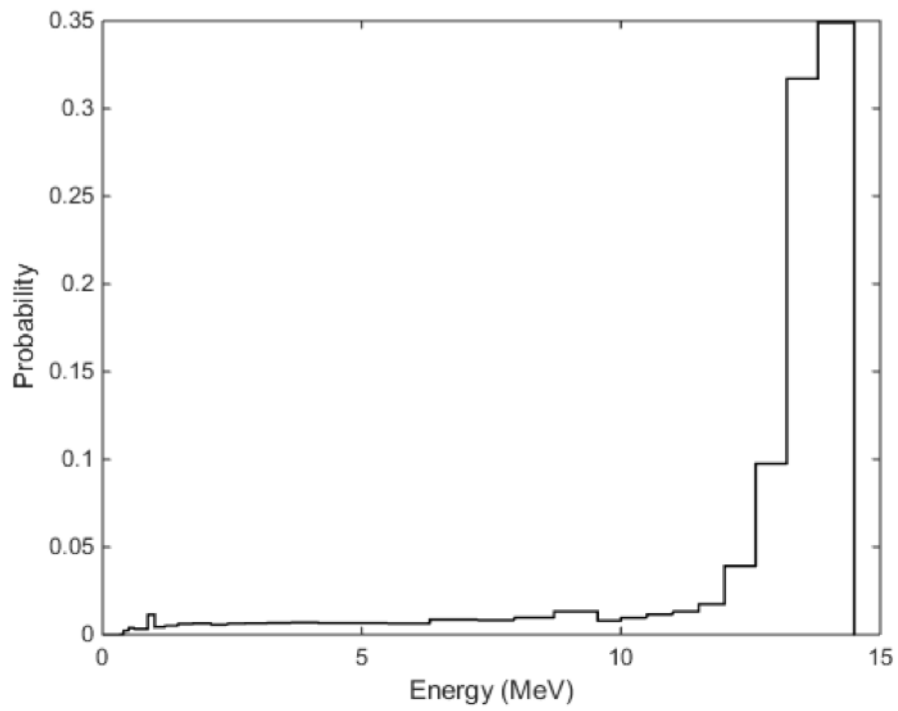


Figure 3.3: Fusion source neutron energy distribution. [106]

reactions; E_α is the energy of the X-rays and ions (from alpha interactions) absorbed in the chamber gas and subsequently the first wall – this is calculated to be 4.607 MeV; E_f is the total fusion energy released per D-T reaction (17.6 MeV). The neutron and neutron induced gamma energy deposited in regions outside the chamber is included with the expectation that this power will be recovered and will contribute to the overall power cycle. There is no hard physical constraint on the EMF, but the higher the EMF, the lower the cost of electricity from a fusion power plant due to more power available for a given target and laser of certain size. For this reason, a goal of at least 1.1 was set for the EMF.

3.2.2 Computational Approach

To determine what elements to combine with lithium and create ternary alloys, a colleague at LLNL performed thermodynamic analysis and concluded that 19 elements can form liquid solutions with lithium [144]. When combined, these 19 elements form 171 ternary alloys. Each ternary then requires 231 simulations, each at a different alloy composition, to cover the entire phase space. The total number of simulations that results is 39,501. Doing this many simulations with a Monte Carlo code containing complex geometry takes up an exhausting amount of CPU time and man power. Consequently, it is necessary to create a computationally efficient approach to sample the ternary alloys. This type of approach is outlined with a flowchart in Fig. 3.4. The first step, in the rounded red rectangle, was to perform qualitative and quantitative preliminary analysis of neutronic properties. This type of preliminary analysis, explained in Section 3.3.1, was crucial for determining the alloys that would exhibit the best performance; it reduced the number of ternaries to simulate by more than 70%. Next, an alloy of interest was chosen to be sampled, based on the previous step, and its density was calculated (yellow diamond Fig. 3.4). The following two steps (illustrated with orange rectangles) were all done automatically with the aid of written Python scripts. The scripts created input files used in the Monte Carlo simulations, extracted needed information from large data sets in the output files, and carried out calculations with the data. These two steps were repeated until all 231 compositions for the alloy were simulated. Once all of the simulations were completed for a ternary, additional scripts automatically plotted the results in ternary diagrams and bar graphs discussed in Section 3.3.2. If more alloys needed to be analyzed, then flowchart can be followed back to the second step (white trapezoid), where a new ternary to sample is decided, and the next steps are repeated all over again. Otherwise, once all the alloys are sampled, they are analyzed, and top candidates are selected. The two essential components of this approach that increased efficiency were the first step, and the automatization of running, analyzing, and plotting.

3.2.3 Activation Analysis

When the coolant exits the blanket it requires operational and maintenance procedures appropriate to its radiological properties. Furthermore, accumulation in the coolant of relatively long-lived isotopes will determine its nuclear waste category and the corresponding procedures for disposal. Neutron activation analysis was performed using ACAB [135], an activation and transmutation code developed for fusion systems. Multigroup activation cross section libraries are selected from one of the group-wise libraries available in EAF-2007 [47]

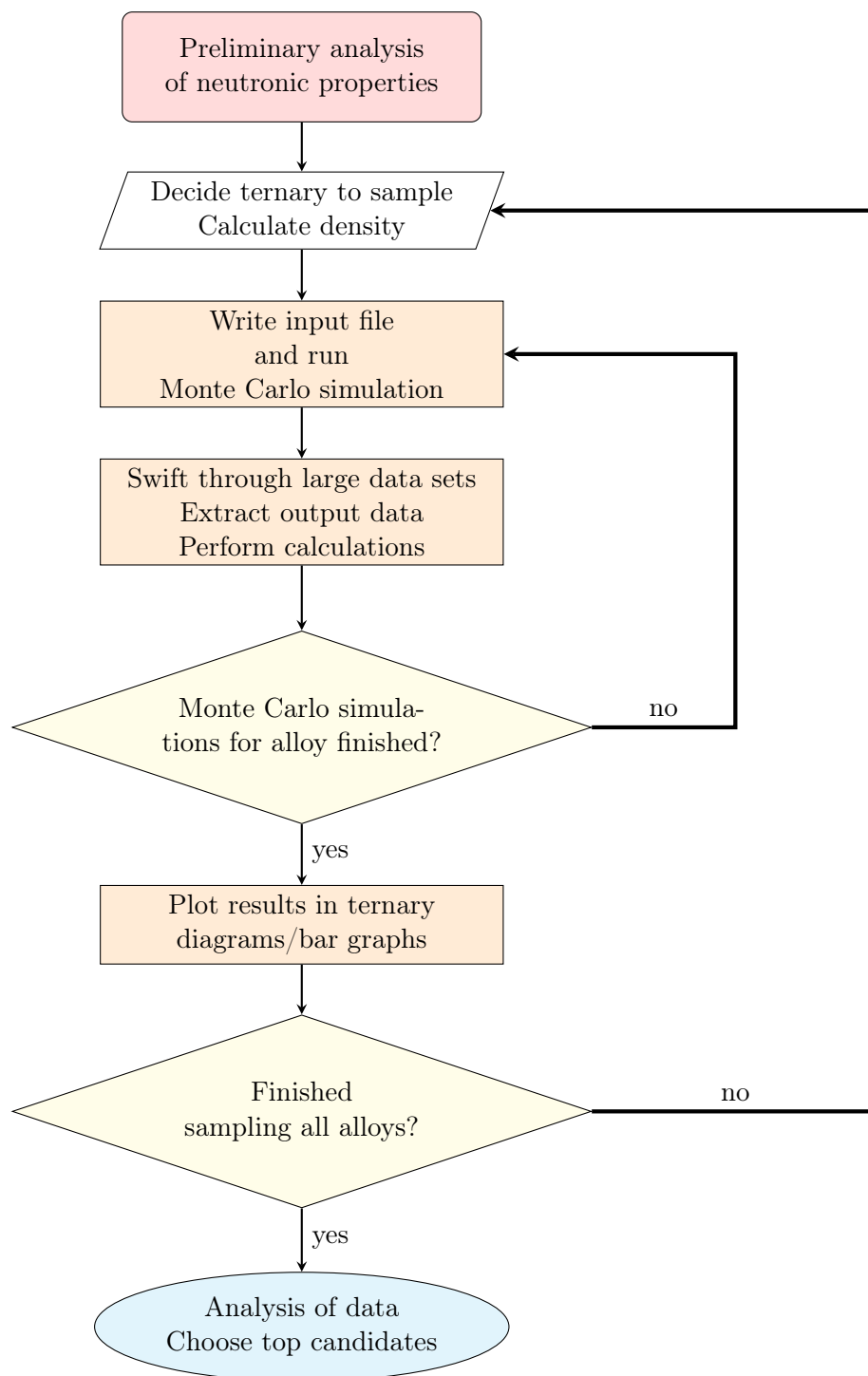


Figure 3.4: Flowchart of computational approach to choose alloys for Monte Carlo analysis.

group-wise libraries. These multi-group files are gathered from a point-wise cross section library in one out of seven group structures; this study used the VITAMIN-J group structure. This group structure was defined in the framework of the JEFF-1 benchmarking for use in reactor shielding and fusion neutronics application (fusion blanket shielding). It is based on the group structures of VITAMIN-C (DLC-41) and VITAMIN-E (DLC-113). VITAMIN-J has 175 neutron energy groups and 42 gamma energy groups [131]. The point-wise library contains data on 65,565 cross sections for 816 targets in modified ENDF/B format ranging from 10⁻⁵ eV to 60 MeV. The EAF-2007 decay data library is primarily based on the JEFF-3.1 radioactive decay data library [47]. MCNP6 provided the multi-group flux required by ACAB for collapsing cross sections. Activation analysis was performed for a 2,200 MW plant with an irradiation history of 50 years and cooling time of up to 300 years. One important thing to note is that the total blanket volume includes 3,478 m³ inside the chamber, and 940 m³ outside during irradiation. This means that the alloy is inside the chamber for 79% of the total residence time. To account for this, the flux is adjusted by a factor of 0.79. The results are divided by this factor to account for the entire blanket volume irradiated. Additionally, it is assumed that feeding additional lithium into the chamber is not necessary due to the small ⁶Li burn-up (ranging from 2%-8%) and only 1% decrease of TBR at end of irradiation. Tritium is assumed to be extracted from the coolant/breeder after irradiation to be reprocessed and reused in the source. All of the activation parameters, except for accident dose, are examined after shutdown and thus do not include tritium in the results. An accident is assumed to occur during operation when tritium is still mixed with the rest of the coolant/breeder.

3.2.4 Safety and Environmental Parameters

Data from the activation analysis allowed to determine the following environmental and safety parameters.

Decay Heat

Decay heat is calculated to ensure that adequate cooling is available for stored coolant at all times. According to limits employed in previous studies, no-active cooling is required if the decay heat is below 10 W/m³, dry cooling is sufficient if it is between 10 W/m³ and 2 kW/m³, and wet cooling is required above 2 kW/m³ [25].

Contact Dose Rate

The contact dose rate determines the feasibility of recycling the ternary alloy. The proposed limits for fusion systems are 10 μ Sv/h for hands-on operation, and 10 mSv/h for remote handling [126]. More detailed work has also suggested the same 10 μ Sv/h hands-on limit, but also includes a shielded hands-on limit of 2 mSv/h [25]. For this study, the hands-on limit was disregarded since the coolant after shutdown could be drained down into cooling tanks. Only remote handling of the breeder/coolant is considered.

Waste Disposal Rating

The waste disposal rating (WDR) determines whether the alloy meets the concentration limits for Class C low-level waste (LLW) under NRC 10CFR61.55 [128]. It is defined as the sum of the ratio of the concentration of a particular isotope to the maximum allowed concentration of that isotope for Class C, taken over all isotopes of the alloy. If the WDR < 1 , the mixture is considered LLW.

Accident Dose

DOE Fusion Safety Standards limit dose in accident scenario to 10 mSv [87]. This value refers to a 50 year committed effective dose calculated to the most exposed individual at the site boundary (1 km) with contributions from direct cloudshine, and inhalation during plume passage [89]. The contribution from groundshine is not included in the limit because it doesn't contribute directly to the accident and is more of public health measure. Nevertheless, this study will include groundshine for more conservative results. The accident dose (AD) is calculated by multiplying the following three factors:

$$AD (Sv) = Radioactivity (Bq) \times DCF \left(\frac{Sv}{Bq} \right) \times RF \quad (3.2)$$

The radioactivity is obtained from ACAB calculations. Dose conversion factors (DCF) are required to convert the radioactivity levels from the released blanket radionuclides to equivalent dose to humans. DCFs for typical radionuclides released from IFE activation of structural materials were specifically calculated using the dispersion and accident consequences software MACCS2 [89]. For this study, the DCFs were chosen with standard conditions such as a 1 km boundary, conservative weather, ground release, and no building wake effects. The release fractions (RF) are usually derived from the combination of detailed modeling of the accident and measurements of the material mobilization under such accident conditions. This determines how much of the component escapes from the accident, and what percentage of that is released into the atmosphere and pose a hazard to the public. Modeling detailed accident scenarios for each alloy would take too long. Approximated release fractions, instead, were utilized. Such release fractions characterize an isotope's mobilization and volatility according to five categories [129]:

1. Elements with species gaseous at room temperature: high mobility – 100%
2. Elements with species gaseous at typical reactor operating temperatures ($< 500^\circ\text{C}$) – 30%
3. Elements with species gaseous at modest accident temperatures ($< 1000^\circ\text{C}$) – 10%
4. Elements with species gaseous at severe accident temperature ($< 1500^\circ\text{C}$) – 3%
5. Elements with species (pure element or oxide) at severe gaseous temperatures such as tokamak dust erosion or oxide spallation – 1%

3.3 Results and Discussion

3.3.1 Preliminary Evaluations

In order to understand the behavior of different elements in the blanket that would infer the behavior of ternaries when combined, preliminary evaluations were performed. This was the first step shown in Fig. 3.4. Using a representative blanket neutron flux (obtained from MCNP calculations with a LiSnZn alloy), effective Q-value, effective absorption cross section, and effective (n,xn) cross section were calculated for an initial set of elements (Na, Mg, Al, Si, Ca, Ti, Cu, Zn, Ga, Sr, Pd, Ag, In, Sn, Sb, Ba, Au, Pb, and Bi) selected by the LLNL based on thermodynamics properties [144]. Their values are reported in Table 3.2.

The effective Q-value was calculated as:

$$Q_e = \frac{\sum_{i=1}^{N_e} a_i \sum_r Q_r^i \sigma_r^i}{\sum_{i=1}^{N_e} a_i \sum_r \sigma_r^i} \quad (3.3)$$

$$Q_{(n,xn)}^i = Q_{(n,xn)} + xQ_e^{Li} \quad (3.4)$$

where i is the specific isotope of an element, r is the type of neutron reaction, σ is the cross section, Q is the Q-value, a is the abundance fraction, and N_e is the number of isotopes in the element. From a neutronics perspective, it is desirable to have low absorption cross section¹ to reduce neutron loss in unwanted reactions that would inhibit the TBR and EMF. A large (n,xn) cross section is necessary to increase the number of neutrons in the blanket which will enhance the TBR. It is assumed that the x (2 or 3) neutrons generated in (n,xn) reactions will go on to be absorbed by lithium and this is accounted for in the Q-value defined in Eq. 3.4. Lastly, a high effective Q-value is crucial to ensure an adequate EMF. The last two features, (n,xn) cross section and Q-value, contradict each other as (n,xn) reactions are endothermic, but overall the availability of extra neutrons upon (n,xn) reactions may compensate for the loss of energy due to subsequent exothermic reaction with ⁶Li and/or other alloy constituents. Additionally, the low absorption cross section also contradicts the high Q-value since heat is produced by absorption cross sections such as (n, γ). This is why a ternary alloy is ideal; the properties of one element can complement the properties of another and result in a successful ternary system, as seen in Fig. 3.5. The figure qualitatively illustrates the properties of the elements found in Table 3.2, by highlighting the elements that exhibit one or more of the desirable properties. Through observation of the highlighted elements, one can easily infer which ones can be combined to create proficient alloys. Ideally, it is best to join elements that exhibit all three properties. For example, an alloy that possesses a low absorption cross section (highlighted in red in Fig. 3.5) and high multiplication cross section (elements highlighted blue), such as Pb, can be combined with an element that has a higher Q-value (elements highlighted in green), such as Zn. Many ternary combinations can be deduced from the properties of all the elements in Table 3.2 and Fig. 3.5. Results reported show that: Pb and Bi are desirable elements for their low absorption and high (n,xn) cross sections; of the elements with high Q-value, Sn, Zn, Cu, and Ti are to be preferred for their relative low absorption.

¹Absorption cross section is equal to the sum of all cross sections, excluding (n,xn)

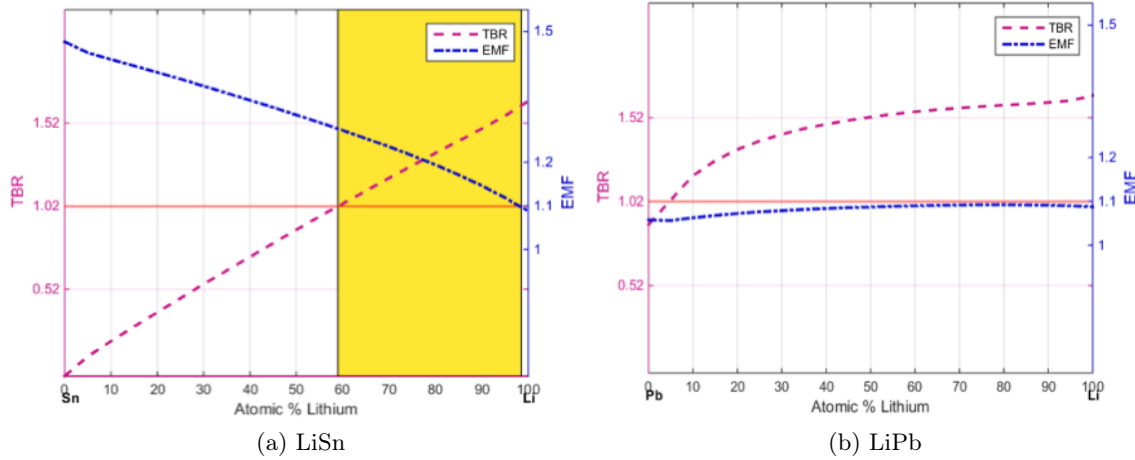


Figure 3.6: TBR and EMF for lithium (a) LiSn and (b) LiPb alloys as a function of lithium concentration; the horizontal red line coincides with the minimum value for both TBR (1.02) and EMF (1.10), the shaded yellow area indicates the range of lithium concentration within which both constraints are met.

The elements in Table 3.2 were also observed in combination with lithium. Binary alloys were analyzed using the MCNP blanket model and varying the lithium concentration from 0 to 100% at 5% intervals. This analysis assumed 1.02 and 1.1 as lower limits for TBR and EMF, respectively. Fig. C.1 shows example results for LiSn and LiPb binary alloys (a complete set is provided in Appendix C). It is observed that: (1) Ba, Sn, Sr, and Ti offer the widest range of acceptable lithium concentrations; (2) Bi and Pb are barely not meeting the EMF requirement, but provide very large TBR even at low concentration of lithium, due to enhanced (n,xn) reactions. Studies in the past demonstrated the potential of LiPb as a coolant and breeder. However, the focus was usually on TBR and possible ways to maximize it such as by increasing the ^6Li enrichment [101]; (3) Pd, In, Au, and Ag feature a narrow acceptable range, but a relatively large EMF; (4) Ga, Cu, Sb and Zn are in the mid-range of acceptable lithium compositions with EMFs slightly higher than 1.1 but no greater than 1.2; (5) Sb, Pd and Au have very narrow acceptable ranges and limited EMF; (6) Na, Mg, Al, Ca, and Si never meet both constraints, mainly due to their detrimental effect on EMF. This results are in line with the observations made from the analysis on individual elements.

3.3.2 Tritium Breeding and Energy Multiplication

TBR and EMF were evaluated for 55 lithium ternary alloys as a function of their composition. Each alloy was evaluated according to three different TBR and EMF criteria:

- Aggressive: lowest achievable TBR – 1.02 and highest EMF – 1.2. This category pushes limits to ideal conditions; a TBR that accounts for the least amount of losses and a high EMF to decrease the cost of electricity.
- Conservative: high TBR – 1.1 and low EMF – 1.1. More on the other side of the spectrum, the TBR is high to account for losses, and EMF puts the lowest demand to

produce power.

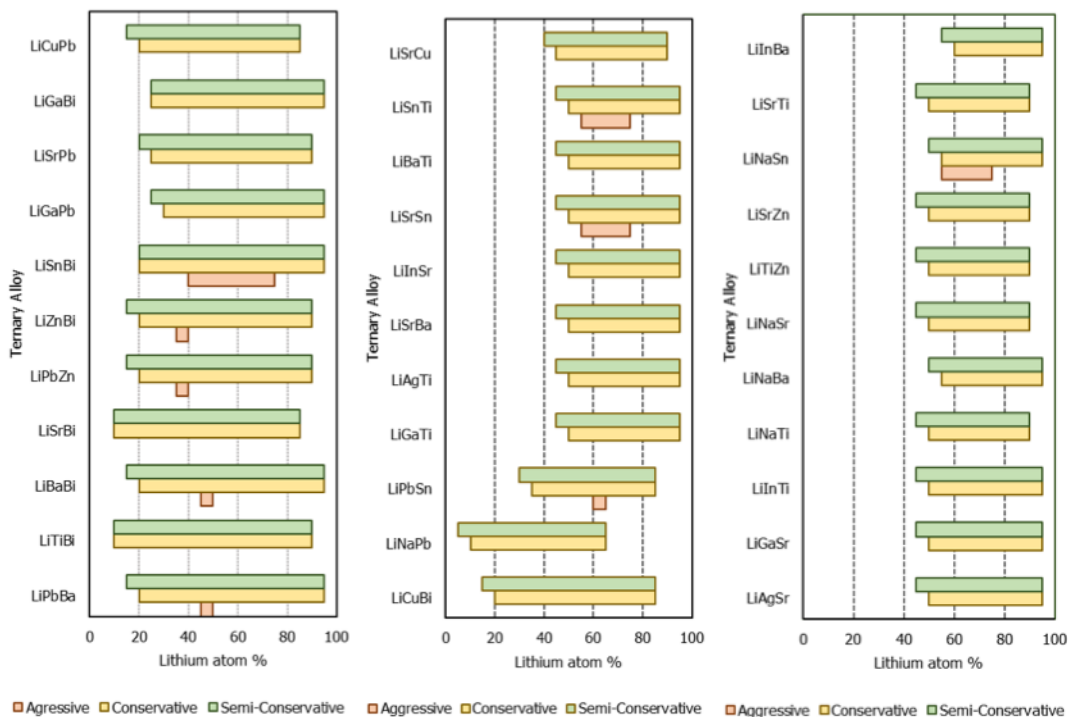
- Semi-conservative (SC): TBR – 1.05 and EMF – 1.1. The TBR here is lowered from the conservative constrain above.

Results containing the range of lithium concentrations for various ternary alloys that meet each of the three sets of criteria are illustrated in Fig. 3.7. All the alloys in Fig. 3.7 meet both the conservative and semi-conservative criteria. The aggressive constrains are mostly met by alloys containing tin (and barium in one case) due to the fact that it has all three desirable properties: a high Q-value, low absorption cross section, and high (n,xn) cross section. This enhances the TBR but more specifically the EMF; most other alloys cannot reach EMFs that are any higher than 1.15. A few Ba-containing alloys and LiPbZn also meet the aggressive criteria for the same reasons. As predicted, the conservative and semi-conservative constrains with the widest range of lithium concentrations were met by elements that performed well in the binary analysis such as barium, tin, and strontium, with lead or bismuth. Elements that have a combination of higher Q-value and lower absorption cross section such as zinc will perform adequately when combined with high neutron multipliers such as bismuth, or elements with similar or better attributes, i.e. barium. Even gallium, whose absorption cross section is on the higher end but has above average Q-value, yields satisfactory results with the elements formerly mentioned, specifically neutron multipliers. The ternaries in Fig. 3.8 give a closer look at some of these alloys. From the figures, one can easily visualize the competition between TBR and EMF; neutrons absorbed by lithium increase the TBR but at the expense of reactions in the other elements that enhance the EMF. Although the ranges for which LiNaSn and LiSnZn alloys meet the limits are not as large as some of the other alloys, they do meet all three categories. Ternary diagram results for all the alloys in Fig. 3.7 are found in Appendix D.

The difference in lithium concentrations between each increase of TBR is not as significant as the change in EMF. Between TBRs of 1.02 and 1.1, respectively, the lithium concentration increases by less than 10%. This allows us to change the TBR constrains if necessary while still maintaining a similar minimum lithium concentration to reduce chemical reactivity. The increase of EMF from 1.1 to 1.2 is dependent on each individual alloy; smaller differences occur for alloys with higher Q-values such as tin, zinc and gallium. Nevertheless, to increase the EMF for all alloys, the lithium concentration must be lowered by several percent to reduce absorption in lithium and enhance it in the other components. As a result, all the alloys in Fig. 3.8 other than tin, barely, if at all, meet any of the TBR limits with an EMF of 1.2.

3.3.3 Lithium Enrichment

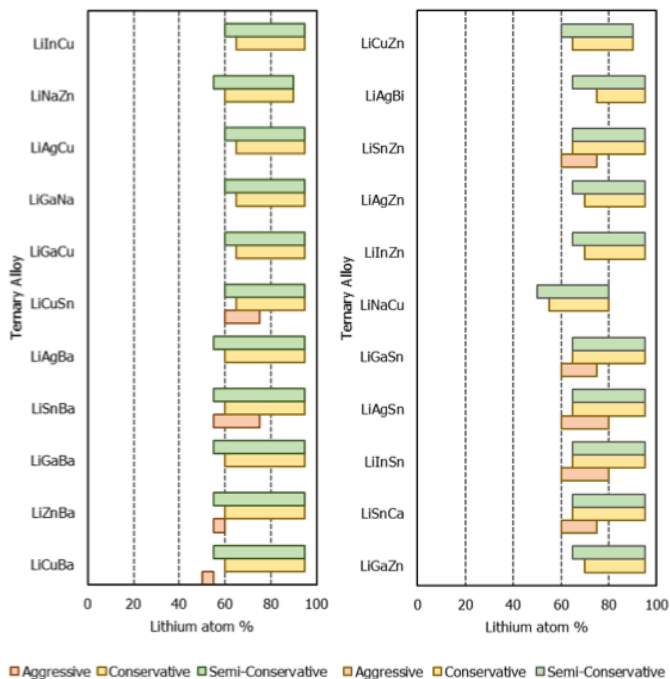
In order to further minimize the amount of lithium in the alloys and to increase TBR, the sensitivity to the concentration of ${}^6\text{Li}$ was tested. The (n,t) cross section of ${}^6\text{Li}$, shown in Fig. 3.9 covers a wide range of energies as opposed to ${}^7\text{Li}$, whose cross section only occurs in the high energy range; therefore, enriching the alloy in ${}^6\text{Li}$ increases neutron absorption in it and boosts TBR. LiSnZn was utilized for this enrichment sensitivity study. The chosen composition (65% Li, 25% Sn, 10% Zn) minimizes lithium concentration while meeting all three sets of criteria described in the previous section, and is demonstrated in



(a)

(b)

(c)



(d)

(e)

Figure 3.7: Range of lithium (atom%) for each ternary alloy that meet specific TBR and EMF criteria. Aggressive: TBR 1.02, EMF 1.2. Conservative: TBR 1.1, EMF 1.1. Semi-conservative: TBR 1.05, EMF 1.1. When an alloy does not meet one of the criteria at any composition, it is left blank.

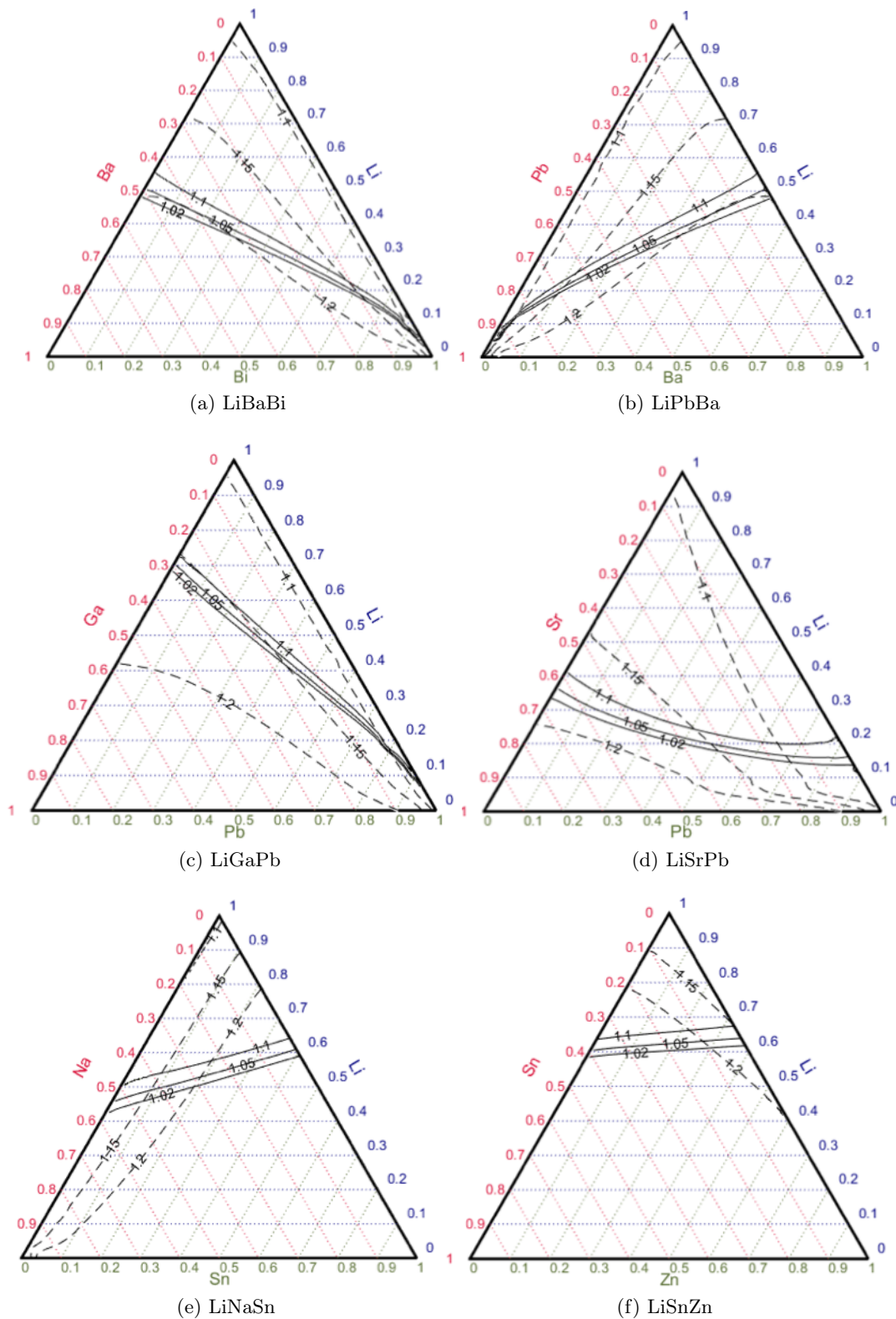


Figure 3.8: Ternary Plots for (a) LiBaBi, (b) LiPbBa, (c) LiGaPb, (d) LiSrPb, (e) LiNaSn, and (f) LiSnZn; solid lines represent TBR; dotted lines represent EMF.

Fig. 3.10. ${}^6\text{Li}$'s concentration was increased from natural (7.5%) to 90% with increments of 5%. Fig. 3.11 shows that the EMF rapidly drops with increasing enrichment whereas TBR increases. The EMF exponentially decreases until around 40% ${}^6\text{Li}$, which is where the TBR reaches its maximum. At such maximum (40%), the TBR is 20% higher than with natural lithium. After this point the TBR becomes saturated and slowly begins to linearly decrease due to the lack of ${}^7\text{Li}(n,n'T)$ reactions. The ${}^7\text{Li}(n,n'T)$ reaction rate linearly decreases as a function of ${}^6\text{Li}$ enrichment, shown in Fig. 3.11. Before 40% the ${}^6\text{Li}(n,T)$ reactions are growing at a faster rate than ${}^7\text{Li}(n,n'T)$ reactions, overcoming them to allow the total TBR to increase. However, after 40%, the lack of additional neutrons from ${}^7\text{Li}(n,n'T)$ reactions prevent ${}^6\text{Li}$ from producing tritium at the same rate as it did with lower enrichments. This, plus the lack of tritium production from ${}^7\text{Li}$ causes the total TBR to decrease at enrichments greater than 40%. The (n,xn) reaction rate, influenced by tin, does not have a strong influence on the behavior of the TBR.

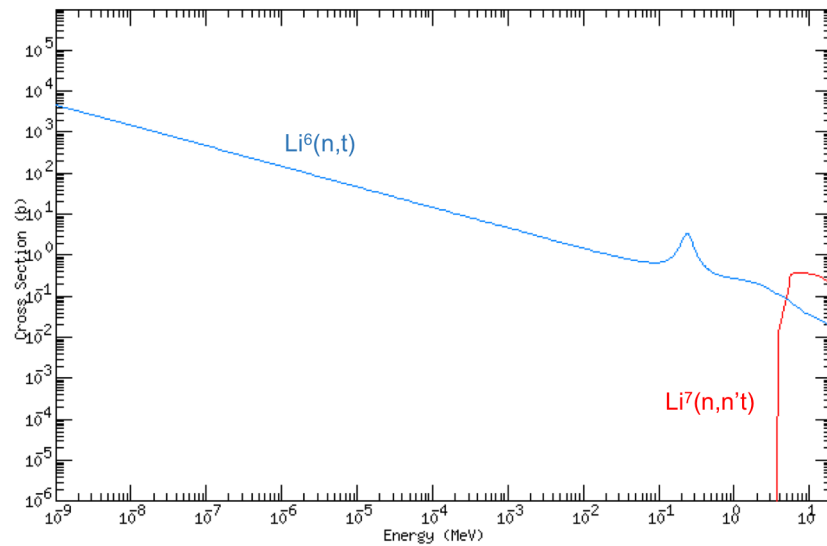


Figure 3.9: ${}^6\text{Li}$ and ${}^7\text{Li}$ (n,t) cross sections [1].

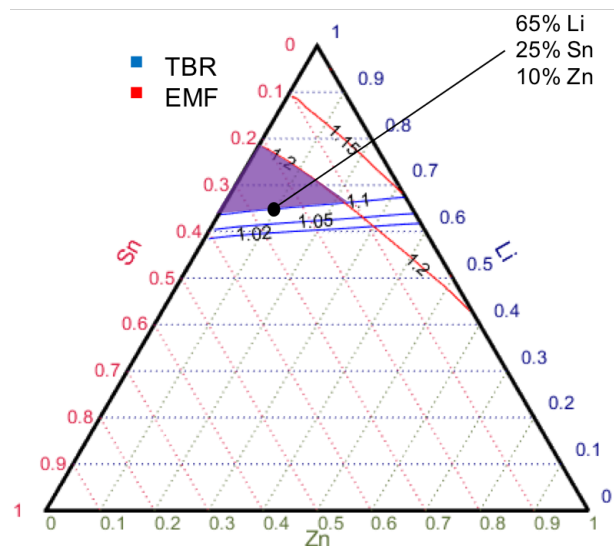


Figure 3.10: LiSnZn diagram showing area where all three criteria (aggressive, conservative, semi-conservative) are met. Chosen point is within shaded region and also minimizes lithium concentration.

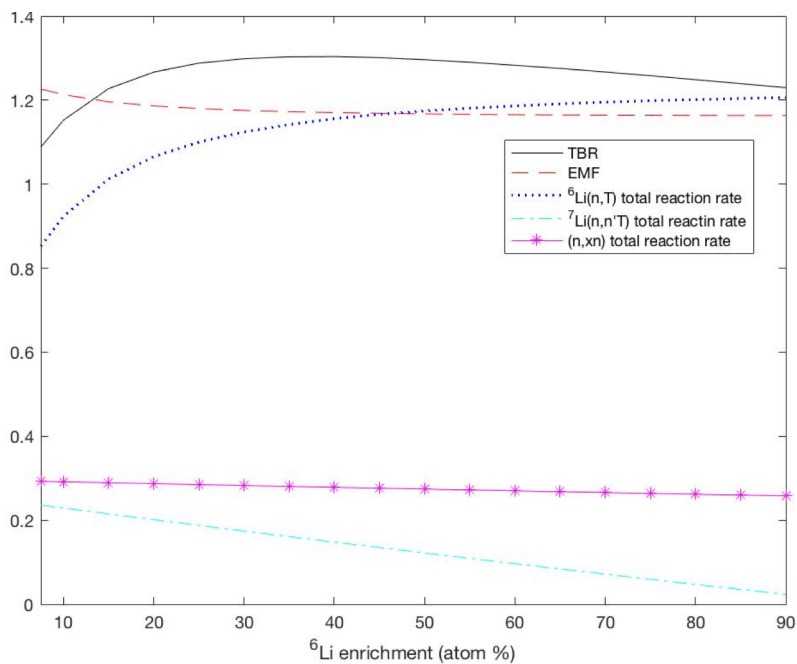


Figure 3.11: TBR, EMF, and (n,T) and (n,xn) reaction rates as a function of ${}^6\text{Li}$ concentration in lithium for Li(65%)Sn(20%)Zn(15%) alloy.

Fig. 3.12 displays the range of total lithium concentrations in the LiSnZn alloy that meet each of the previously discussed criteria for three enrichment cases: natural, 40%,

and 90%. The minimum lithium concentrations for each of the cases decrease as lithium enrichment increases. For example, the aggressive case decreases from 60 atom% for natural enriched lithium to 25 atom% for 40% enriched lithium. It decreases even further to 15 total atom% when lithium is enriched to 90%. Nevertheless, the case with 40% enriched lithium meets this criterion for a 35% range of lithium concentrations (25 atom% to 60 atom% Li) as opposed to the 10% range in the case of 90% enrichment (15 atom% to 25 atom% Li). The EMF is largely compromised as enrichment increases and thus, it is much harder for alloys of different concentrations in the 90% enriched case to meet the 1.2 EMF for the aggressive category. This is visualized in Fig. 3.13 where ternary diagrams with ${}^6\text{Li}$ enriched at 40% and 90% are shown. It can also be seen in the ternaries how, for a constant lithium concentration, the TBR decreases when the amount of zinc in the alloy increases. This is due to the decrease of tin (n, xn) reactions, which lowers the neutron economy and reduces the number of $\text{Li}(n, T)$ reactions. In addition, the phenomenon becomes more pronounced in the 90% enriched Li ternary due to the lack of ${}^7\text{Li}(n, n'T)$ reactions, which lowers the TBR as previously described. As a result, the TBR at 65% Li, 20% Sn, and 15% Zn will be lower (1.2) at 90% enriched lithium, than at 40% (1.31). Minimizing the lithium concentration without exceedingly reducing the EMF needs to be considered when selecting the proper lithium enrichment.

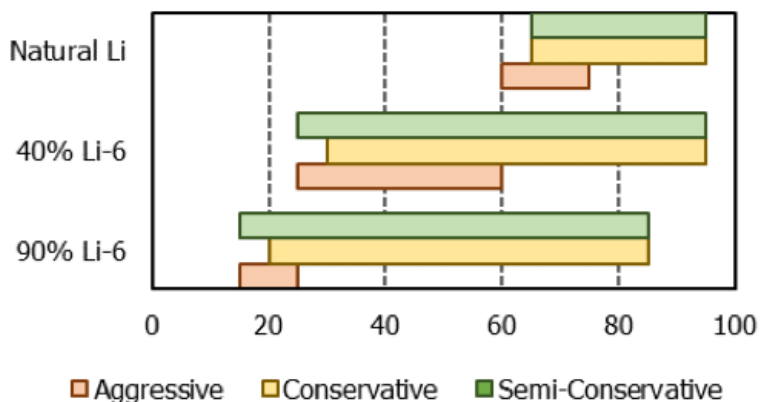


Figure 3.12: Range of lithium (atom%) for LiSnZn with natural, 40%, and 90% enrichment, that meet specific TBR and EMF criteria. Aggressive: TBR 1.02, EMF 1.2. Conservative: TBR 1.1, EMF 1.1. Semi-conservative: TBR 1.05, EMF 1.1.

Table 3.3: Compositions of Alloys Chosen for Activation Analysis.

Alloy	Composition (%)
LiBaBi	20–10–70
LiPbBa	25–60–15
LiSnZn	65–25–10
LiCuPb	40–20–40
LiGaPb	35–10–55
LiSrPb	30–50–20
LiPbZn	30–60–10
LiNaSn	55–30–15

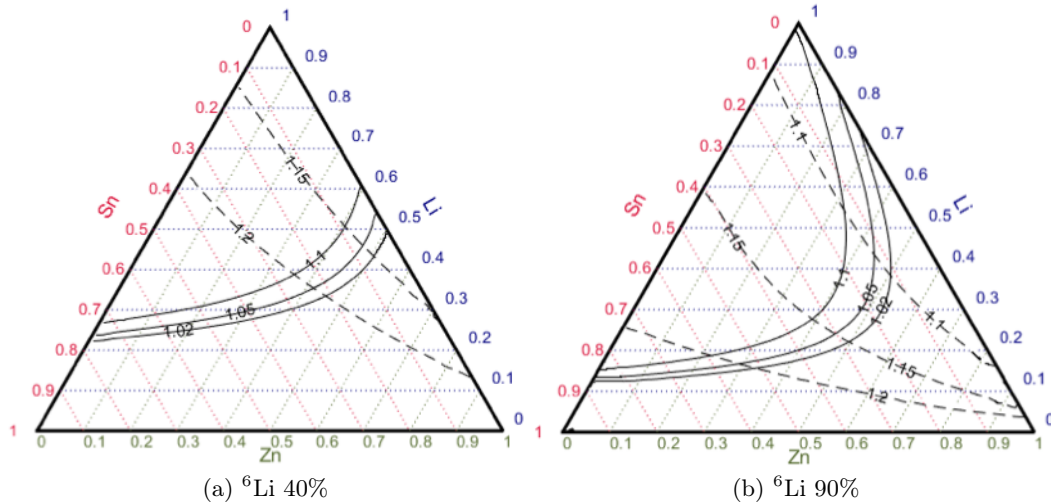


Figure 3.13: Ternary diagrams for LiSnZn with lithium enriched to (a) 40% and (b) 90%; the solid lines represent TBR; dotted lines represent EMF.

3.3.4 Activation Analysis

Eight alloys were chosen for an extensive activation analysis: LiBaBi, LiPbBa, LiSnZn, LiCuPb, LiGaPb, LiSrPb, LiPbZn, and LiNaSn. These alloys were chosen based on their neutronic performance: alloys with Pb and Bi exhibit high neutron multiplication and minimize the amount of lithium in the alloy; alloys with Sn meet all of the three sets of criteria in the previous analysis. The composition for each alloy (Table 3.3) was selected to meet the conservative or semi-conservative set of criteria, while minimizing lithium concentration. These are all with natural lithium.

As stated in Section 3.2.3, the irradiation history for activation is 50 years of operation followed by 300 years of cooling. Results for the parameters described in Section 3.2.3 are analyzed in the following paragraphs.

Decay Heat

The decay heat is plotted in Fig. 3.14. LiPbBa is the alloy with the lowest decay heat and the only one that can utilize dry cooling right after shutdown. Most of the decay heat in this alloy stems from ^{137m}Ba , ^{137}Cs , and ^{133}Ba . On the contrary, LiBaBi exhibits the highest decay heat due to ^{210}Po , a decay product of ^{210}Bi shown in Fig. 3.15(a). The decay heat remains high in this alloy after one and a half years when polonium decays due to contributions from ^{207}Bi and ^{208}Bi . During the first year and a half LiBaBi must be wet cooled; afterwards, dry cooling can be utilized. Alloys containing Sn and Zn behave fairly similar; LiPbZn and LiSnZn have the greatest contribution from ^{65}Zn (Fig. 3.15(b)). After one year the activation products of Sn do not allow the two tin-containing alloys to decay at the same rate as LiPbZn. Nevertheless, all three of the alloys can be switched from wet cooling to dry after one year. Other lead containing alloys such as LiSrPb and LiCuPb decay at faster rates such that dry cooling can be implemented for LiSrPb in less than a month's time, and for LiCuPb in less than a week. LiGaPb is an interesting case — ^{72}Ga causes the decay heat of LiGaPb to be large in the beginning as seen in Fig. 3.15(a). However, it significantly decreases after one week and becomes the alloy with the lowest decay heat. At this time LiGaPb will not need any additional active cooling. Most of the other alloys will not require active cooling after 50 years with the exception of LiBaBi, who does not meet this limit for 200 years.

Contact Dose Rate

Contact dose rates for all the alloys are illustrated in Fig. 3.16. Note that the rates are given per cubic meter, not for the entire volume of the breeder, $4,418\text{ m}^3$. Similar to the decay heat, LiGaPb has the highest contact dose rate for the first week until ^{72}Ga decays, shown in Fig. 3.17(a). After this time, hypothetically speaking, it would be possible to recycle with the appropriate equipment at least 1 m^3 of LiGaPb. Once the gallium alloy decreases, alloys with zinc portray the largest contact dose rates from contributions of ^{65}Zn (Fig. 3.17(a)). LiNaSn is also in the same range of contact dose rates at the beginning before ^{24}Na and ^{22}Na decay, shown in Fig.3.17(b). Lead containing alloys such as LiPbZn, LiSrPb, and LiPbBa, portray the lowest contact dose rates for the first six months. By this time, the contact dose rate of LiSrPb has significantly decreased due to the decay of ^{85}Sr . On the contrary, the decay of LiPbBa occurs much more slowly and LiPbZn decays much later, after five years. At this point the contact dose rates of the other alloys are much lower. The one exception is LiBaBi, whose isotopes decay at the slowest rate of any other alloy, only decreasing the contact dose rate by an order of a magnitude and a half in the first 300 years. Most alloys meet the remote handling limit with 1 m^3 of their volume after 10 years. This allows fractions of the blanket to be recycled at a time. Every alloy except LiPbBa, and LiBaBi will be able to be remotely handled with the entire blanket volume at 100 years. By 300 years, the only alloy that will not meet the 10 mSv/h constrain with 100% of its volume is LiBaBi.

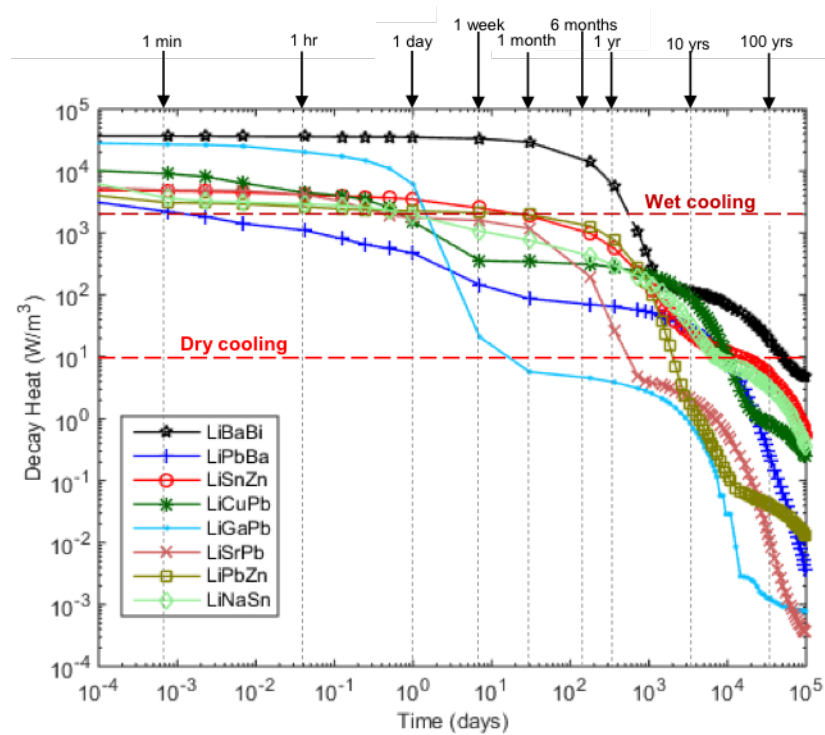


Figure 3.14: Decay heat (W/m^3) as a function of time after irradiation for breeder/coolant ternary alloys. The wet cooling and dry cooling constraints are indicated by the horizontal lines.

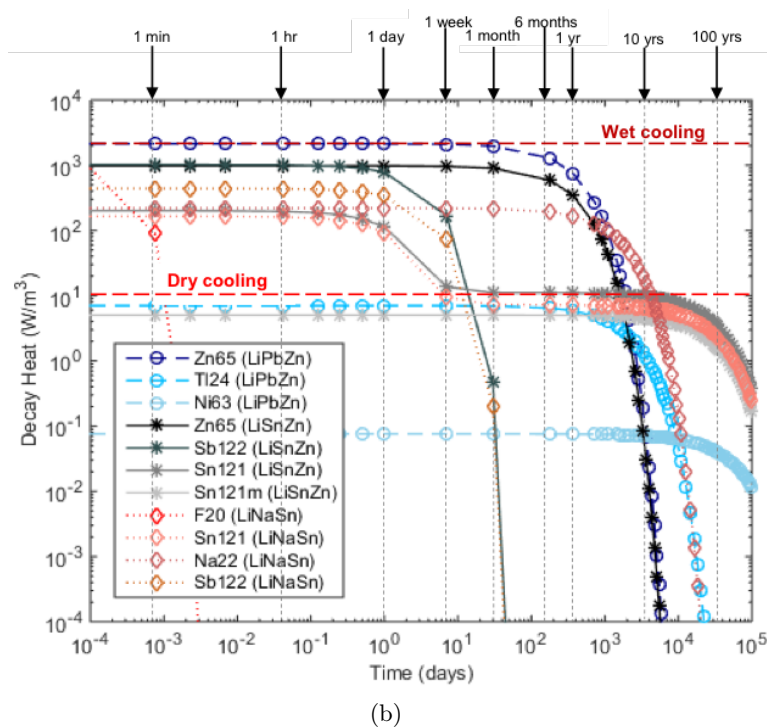
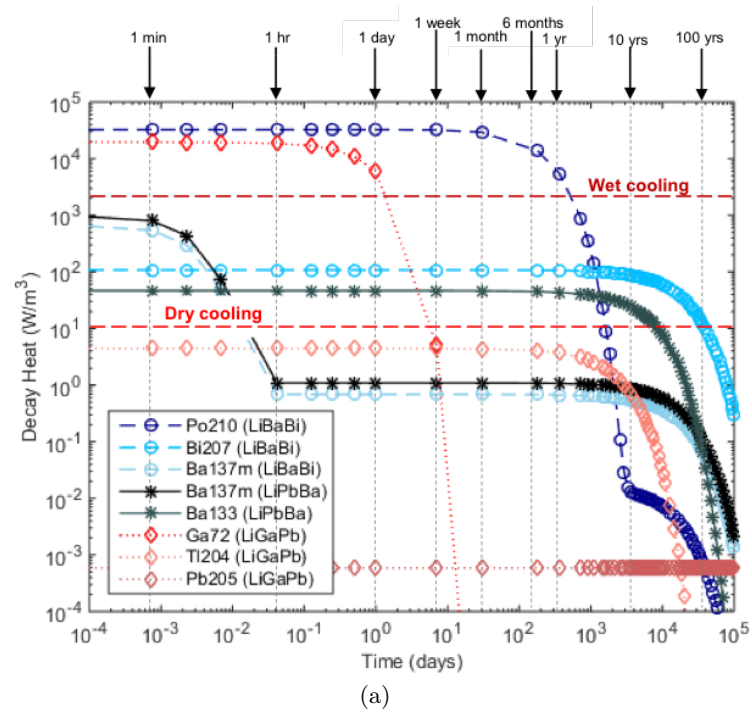


Figure 3.15: Isotopics of decay heat (W/cm^3) after irradiation for (a) LiBaBi, LiPbBa, and LiGaPb and (b) LiPbZn, LiSnZn, and LiNaSn. The wet cooling and dry cooling constrains are indicated by the horizontal lines.

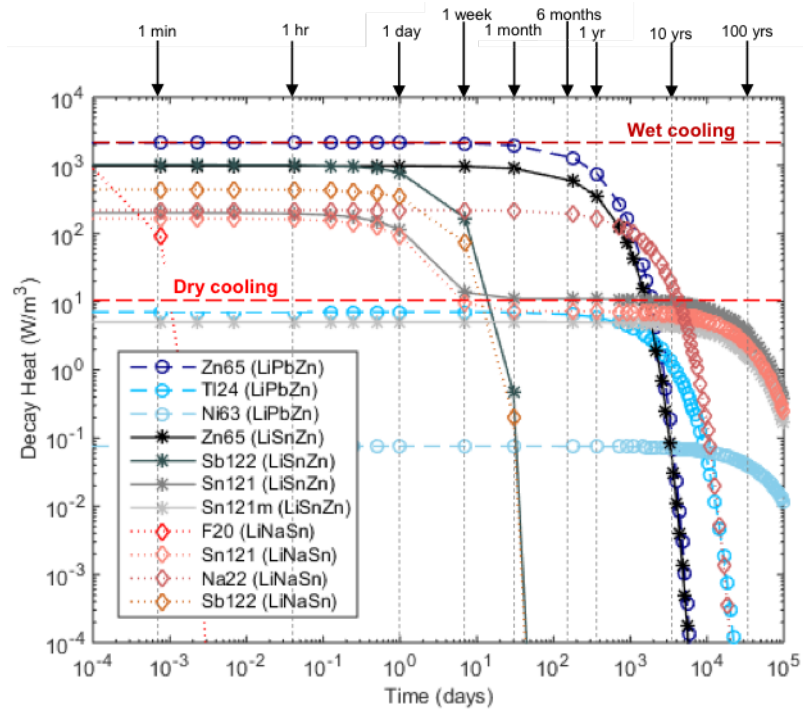
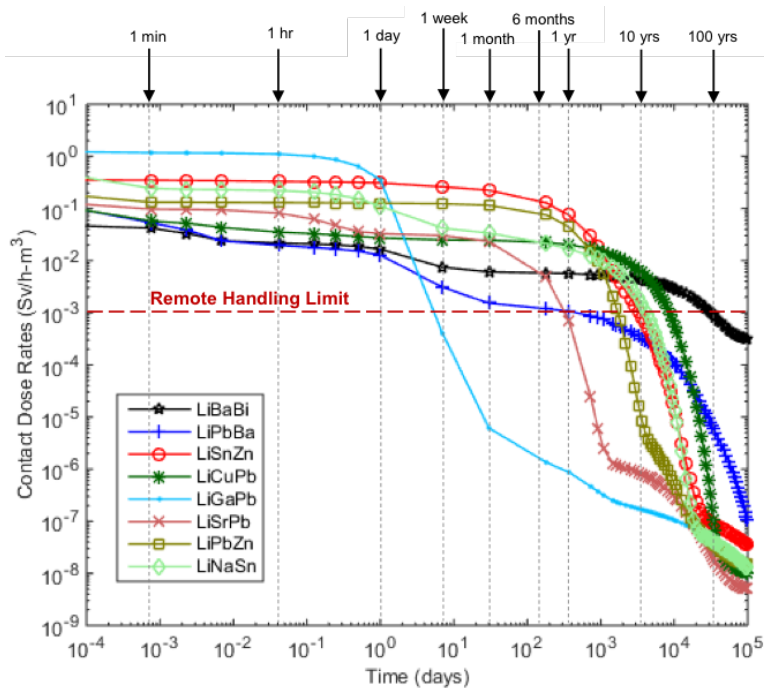
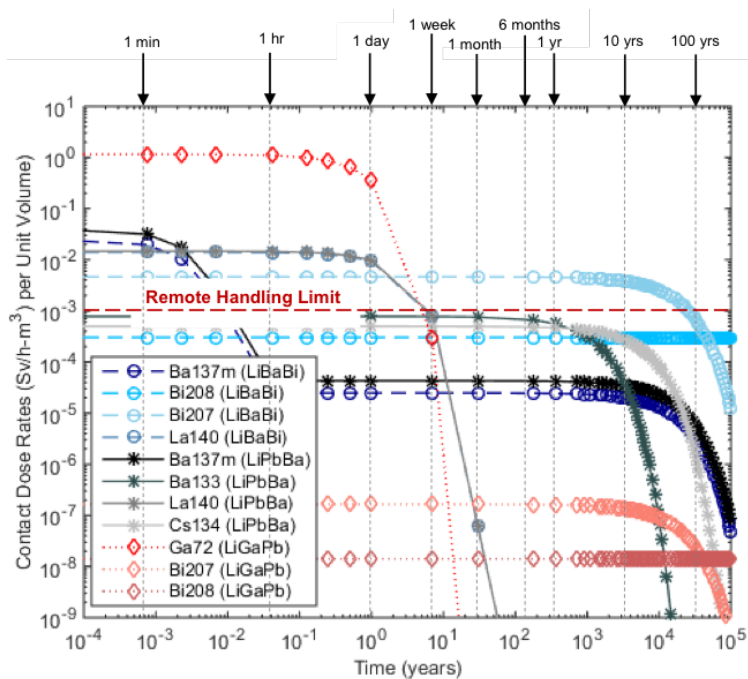


Figure 3.16: Contact Dose Rates (Sv/h-m³) as a function of time after irradiation for breeder/coolant ternary alloys. The remote handling limit is indicated by the dotted line.



(a)



(b)

Figure 3.17: Isotopics of Contact Dose Rates (Sv/h) for (a) LiBaBi, LiPbBa, and LiGaPb and (b) LiPbZn, LiSnZn, and LiNaSn. The remote handling limit is indicated by the dotted line.

Table 3.4: Accident Dose (AD) and Waste Disposal Ratings (WDR) for alloys.

Alloy	AD (mSv/cm ³)	WDR
LiBaBi	1.54	3410
LiPbBa	5.64×10 ⁻⁴	0.19
LiSnZn	1.08×10 ⁻³	0.09
LiSrPb	5.77×10 ⁻⁴	0.05
LiGaPb	1.00×10 ⁻³	0.18
LiCuPb	1.17×10 ⁻³	0.15
LiPbZn	1.25×10 ⁻³	0.2
LiNaSn	6.62×10 ⁻⁴	0.07

Accident Dose

Unlike decay heat and contact dose rates, results for accident dose include the contribution of tritium. Tritium will be separated from the rest of the coolant after shutdown and recycled. Whereas decay heat and contact dose rates are measured after shutdown, a loss of coolant or flow is most likely to occur during normal operation. The accident scenario in this study assumes immediate release of the coolant to the environment without the use of any shielding or containment structure to stop the release. Additionally, it is important to note that results for accident doses, shown in Table 3.4, are conservative due to the use of the Piet release fractions as opposed to release fractions modeled from real accident scenarios. From the results, ²¹⁰Po (decay product of ²¹⁰Bi) contains a high DCF and causes the accident dose to be the highest in LiBaBi. Alloys containing lead such as LiPbBa and LiPbZn will also be compromised by ²¹⁰Po. Nevertheless, direct production of Po from Bi causes the accident dose to be at least three orders of magnitude higher. The accident dose in zinc containing alloys will be dominated by ⁶⁵Zn due to its high radioactivity and release fraction. The lowest accident doses are from LiPbBa and LiSrPb, being only half of what it is for LiCuPb. With the exclusion of LiBaBi, the accident dose constraint will only be met for all the alloys if about 8,000–18,000 cm³ of coolant escapes.

Waste Disposal Rating

The last activation parameter accounted for was the WDR to verify that alloys meet requirements for shallow land burial. These are listed in Table 3.4 for the entirety blanket volume. All the alloys meet the WDR criteria (<1) except for LiBaBi; this is due to ²⁰⁸Bi.

Activation Analysis Summary

From the evaluation above, LiBaBi exhibited the poorest performance from all the alloys, mainly due to Bi. Additionally, the high amounts of Po generated from Bi alloys can be of concern due to its toxic and poisonous qualities [66, 80]. With its high release fraction, it can easily travel and be ingested by the public. Consequently, bismuth-containing alloys

will not be considered as potential candidates for the coolant/breeder. Another chemically toxic nuclide that must be considered is, ^{60}Co , an activation product of Zn [123]. Regarding LiPbGa, although ^{72}Ga had a short life, it still emitted a high decay heat and contact dose rate right after shutdown. Additionally, its accident dose and WDR were in the mid-high range, and thus, should be utilized with caution. Although LiSrPb and LiCuPb were not closely examined in this study, they seemed to perform fairly well compared to other alloys specially those containing Sn and Zn. Future work will take a closer look at the activation of Sr and Cu.

3.4 Conclusions

The Lawrence Livermore National Laboratory is investigating the possibility to design lithium ternary alloys to replace lithium as blanket breeder/coolant of an IFE power plant that have similar breeding, corrosion, and thermal properties, but reduced chemical reactivity as compared to lithium. This study performed neutronic and activation analysis of numerous lithium ternary alloys in order to assess their performance in the IFE blanket and guide the down selection process. The neutronic analysis determined energy multiplication factor and tritium breeding ratio. It was found that the best performing alloys (higher TBR and higher EMF) combine elements that exhibit low absorption cross section and high Q-value such as Sn, Ba, Sr, and Zn, with elements with high neutron multiplying cross sections, and low-absorption cross sections, like Pb and Bi. A large number of alloys, especially with combinations formerly described, met TBR constraints of 1.05 and 1.1 and an EMF constraint of 1.1 for a wide range of lithium concentrations. When the EMF constraint was increased to 1.2, the demand to produce additional power was too high for most alloys except for those containing Sn, and some with Ba. Additionally, it was discovered that alloys with higher quantities of lithium (greater than 50%), doubling the ^6Li content, from 7.5% to 15%, increases TBR by 13%. After a certain percent of enrichment (between 40 and 50 percent), the lack of tritium and additional neutrons produced from $^7\text{Li}(n,n'T)$ reactions ends up reducing the TBR. When the total lithium concentration is less than 50%, the TBR will continue to increase to higher ^6Li enrichments, since the $^7\text{Li}(n,n'T)$ reactions will not be as significant.

Activation calculations were performed for a series of elements that exhibited good TBR and EMF properties. This analysis revealed bismuth as a poor choice; it had the highest numbers for all of the criteria evaluated. Alloys containing Zn and Sn also showed some of the highest decay heats, contact dose rates, and accident doses. Most of the alloys examined can be stored in dry containers at an estimated one year after shutdown. Additionally, after about 10 years, fractions of the volume of most blankets analyzed can be recycled at a time (after adequate cooling) without exceeding the remote handling limit. Accident doses were high in alloys containing Zn, Cu, or Ga, but were not high enough to be alarming. With the exception of LiBaBi, activation analysis demonstrated that all the alloys could be utilized as blankets of the IFE reactor without posing major environmental or safety concerns.

A summary of the eight alloys that were closely looked at in this study is outlined in Table 4.6. From the neutronics point of view, it shows the minimum lithium atom concentrations that meet each of the three criteria. Furthermore, it outlines some requirements

for each alloy to meet certain activation safety and environmental parameters. Overall, one can conclude that the best alloys from these two perspectives are LiPbBa, LiGaPb, LiSrPb, and LiPbZn. They have some of the lowest minimum lithium concentrations to meet the neutronics criteria, while best demonstrating their ability to meet the activation parameters.

Table 3.5: Summary of Ternary Alloy Neutronic and Activation Analysis Results.

Neutronics		Activation Analysis					
Minimum Li atom%		Time Required					
Alloy	Aggressive	Conservative	Semi-Conservative	Decay Heat	Contact Dose	Amount Released to Meet	WDR < 1
				(no active cooling)	Rate (remote handling of 1 m ³)		
LiBaBi	45	20	15	200 years	100 years	6.49	no
LiPbBa	45	20	15	25 years	1 year	1.77×10^4	yes
LiSnZn	60	65	65	50 years	8 years	9.24×10^3	yes
LiSrPb	NA	20	15	26 years	20 years	1.73×10^4	yes
LiGaPb	NA	25	20	18 days	4 days	9.97×10^3	yes
LiCuPb	NA	25	20	1.6 years	10 months	8.54×10^3	yes
LiPbZn	35	20	15	5 years	5 years	8.03×10^3	yes
LiNaSn	55	55	50	18 years	10 years	1.51×10^4	yes

Chapter 4

Exact Perturbation Theory to Determine and Optimize the Tritium Breeding Ratio of Fusion Reactor Blankets

4.1 Introduction

All fusion reactor blanket research and development has included some form of lithium to act as a breeder and coolant due to its capacity to efficaciously produce adequate amounts of tritium and thus create a self-sustaining system. Early blanket designs included pure liquid lithium due to its outstanding properties in addition to breeding such as high heat conductivity, and low tritium permeation [86]. Nevertheless, pure lithium is extremely chemically reactive with air and water, creating safety and environmental concerns [34]. As a result, numerous alternatives have been proposed and are currently under development utilizing liquid LiPb, solid ceramic breeders, and molten-salts [10, 73]. Although these new blanket designs lower the chemical reactivity, they hinder the performance in other important areas, such as heat transfer, solubility, and non-corrosive properties, compared to pure lithium [11]. To combat some of these downfalls, Lawrence Livermore National Lab (LLNL) began to investigate a new type of blanket material in the form of lithium-based ternary alloys [102]. Including a third component in the alloy adds an extra degree of freedom which can perhaps mitigate some of the adverse effects found in the other blanket concepts previously mentioned. From a neutronics perspective, a plethora of lithium-based ternary alloys were analyzed to determine if they met specific tritium breeding ratio (TBR) [40] and energy multiplication factor (EMF) [103] criteria [75]. This was done by running simulations with the Monte Carlo code MCNP [23] at different compositions for each chosen alloy, studying the results, and finding an optimal composition that met specific criteria. For every alloy, the concentration of each element ranged from 0-100%, with simulations conducted at increments of 5%, creating a total of 231 individual compositions that covered the entire phase space of the ternary [75]. By simulating 231 compositions, the effect of each

element on the TBR and EMF, respectively, could be examined. Additionally, obtaining numerous data points allowed a more accurate optimum composition to be chosen. However, the interest to study over 150 alloys required around 35,000 Monte Carlo simulations, proving this direct approach to be exceedingly time consuming, computationally expensive, and inefficient. Consequently, it was necessary to investigate the possibility of utilizing an alternate methodology that was more adept and efficient.

A large area of Generalized Perturbation Theory (GPT) is the study of sensitivity functions which calculates the relative change of some integral response due to the change in an input parameter. Sensitivity functions allows multiple responses to be calculated by perturbing the input parameter without having to directly perform separate calculations. This technique can be applied to the study of lithium-based ternary blankets by calculating the TBR or EMF response due to perturbations in the alloy composition. Sensitivity functions are most widely used to evaluate uncertainties in nuclear data. Specifically, uncertainty analysis of energy-dependent cross sections determines how small changes in cross sections affect the results of different calculations [16, 17, 42, 146]. Deterministic computational approaches implement GPT and sensitivity problems by solving for adjoint functions, becoming more complex as the number of discretization in zones and energy groups increases. Additionally, it becomes exceedingly more difficult to implement deterministic methods as the dimension of the geometry increases from 1D to 2D or 3D. The intricacy of deterministic methods has set forth interests to develop new techniques that solve sensitivity and perturbation problems with the use of Monte Carlo. The first Monte Carlo perturbation technique that solved for a factor proportional to the adjoint operator is known as the iterated fission probability [IFP]. The implementation of the IFP can only be utilized in fission problems to calculate kinetic parameters and eigenvalue sensitivities [94]. Recently, newer developments in Monte Carlo methods enabled the calculation of perturbation effects on a wider range of responses. Nevertheless, these methods are only carried out in criticality source problems [15, 124]. A very limited amount of work has been found regarding the implementation of sensitivity problems for fixed source systems with Monte Carlo [36, 67]. For example, Seifried [136] developed an adjoint-based uncertainty quantification technique with MCNP to calculate sensitivity functions in a fusion-fission hybrid reactor. So far, it has only been tested in a critical system with homogenous transport and adjoint equations. Additionally, the method was performed externally, only extracting information from MCNP for constructing adjoint functionals. The external calculations regarding angular distributions and adjoint source distributions required great man-power and computational times and would be very difficult to recreate. Carole's [36] perturbation method for fixed source problems was specifically created for spatial perturbations in photon-only transport problems. Therefore, it was desired to look for an alternative that could implement the efficiency of Monte Carlo GPT techniques for critical problems, but could calculate perturbation responses for general fixed source problems. This alternative was found through a recent method developed in the Monte Carlo code Serpent, that calculates perturbation effects on practically any quantity of interest [15]. Although created to for critical systems, the generality of the premise in this methodology can easily be transferable to problems with a known external source.

The perturbation approach in Serpent is similar to the techniques utilized for variance reduction. Probability density functions of parameters of interest are biased and sam-

pled as accepted or rejected events to account for the bias on the probability. A collision history is created from these events to compute perturbed fluxes which are then utilized to calculate the response. In the case of this work, the methodology implemented for fixed source problems, known as Exact Perturbation Theory, can calculate the tritium breeding ratio response, caused by a perturbation in the composition of the lithium-based ternary alloy. In the following section, the theory behind Exact Perturbation Theory (EPT), will be briefly explained. The setback of this method, related to high uncertainties for large perturbations, will also be discussed in Section 4.3. Results of the EPT method in Serpent are discussed in Section 4.4. To deal with the uncertainties found in the results, two methods are proposed and discussed in detail in Section 4.5. For a composition to be considered optimal, it had to meet the TBR limit with an imposed EMF constraint while minimizing lithium concentration. Section 4.6 describes this optimization scheme that could efficaciously cover the entire phase space of the ternary for the first iteration, and zone in on a region to calculate the optimal composition in the second and third iterations. This optimization scheme was first tested on LiPbBa. Section 4.7 tests the EPT optimization scheme with LiSnZn. The last section concludes this chapter.

4.2 Exact Perturbation Theory Methodology

The method behind EPT is based on the collision-history of a particle's path in the Monte Carlo simulation in conjunction with the use of biased weights, very similar to variance reduction methods. The EPT methodology was already explained in Chapter 2 (Section 2.6), but it will be reiterated here for completeness. Additionally, the implementation of this methodology will be discussed, along with the main setbacks. Lastly, the model utilized to test the EPT method will be presented.

4.2.1 Accepted and Rejected Events

The perturbation approach adopted in Serpent begins with biasing the probabilities of events of interest, i.e. cross sections that are perturbed. In the case of changing compositions of a fusion blanket, there is a desire to increase sampling of all reactions from every isotope in this region. Therefore, the total cross section, $\Sigma_{t,i}$, of every isotope i will be increased by a factor f_r . To account for the increase in the total cross section, accepted and rejected probabilities are created. Once the total cross section of isotope i is sampled with an increased factor of f_r , the event is subsequently sampled to see if it is accepted with a probability of $(\frac{1}{f_r})$, or rejected with a probability of $(1 - \frac{1}{f_r})$. Events must be rejected to restore fair neutron transport such as it is done with variance reduction methods. Both accepted and rejected events are recorded in the collision history of the particle through its random walk. A factor of 2 was chosen for f_r which means that events are accepted and rejected with an equal probability of 0.5. The choice of 2 for f_r made the most sense. However, this factor is arbitrary and other numbers can be utilized. Future work will involve optimizing this number.

4.2.2 Exact Perturbation Theory for Use in Fixed Source Problems

The next step in this approach is to adjust the weights of the particle sampled according to the perturbations [15]. Particles sampled naturally with analog Monte Carlo will follow the physical laws of transport and maintain their original weights. In the event that a probability distribution is biased, the particle weight must be adjusted to compensate for the increase/decrease in the probability:

$$w^0 p_{unbiased} = w^* p_{biased} \quad (4.1)$$

where $p_{unbiased}$ is the actual physical probability distribution found in nature of the considered event sampled, and w^0 is the natural weight of the particles (usually unity). The biased probability is noted by p_{biased} with the corresponding weight, w^* , to account for such bias. Now, consider the Monte Carlo application of a fusion reactor (fixed source) with a reference blanket composition. The random walks will be sampled with probability distributions based on the macroscopic cross sections, $\Sigma_{r,i}$, of reaction r and nuclide i . When the compositions of each blanket component are altered, the densities change, and therefore the probability distributions of the perturbed blanket will be different. The perturbed composition is usually studied by running an additional Monte Carlo case and sampling the new particle paths. However, instead of running a new case per perturbed blanket composition, the particle path of the reference case could be utilized. From the unperturbed case, perturbed responses are calculated by adjusting particle weights according to the perturbed probability distributions. The probability distributions of the reference case, which determine the path of the particle, can be referred to as p_{biased} and the perturbed as $p_{unbiased}$ in Eq. 2.47. With these substituted, Eq. 4.1 becomes:

$$w_n^0 \bar{\Sigma}_{r,i} = w_n^* \Sigma_{r,i} \quad (4.2)$$

where $\bar{\Sigma}_{r,i}$ is the perturbed cross section of any reaction r for any nuclide i in the blanket and $\Sigma_{r,i}$ is the cross section for the reference case. If Monte Carlo is ran as analog, the original particle weight, w_n^0 , of the perturbed case will be unity. However, this might not be the case if variance reduction methods are utilized. With w_n^0 and the probabilities known, we can then solve for w_n^* :

$$w_n^* = w_n^0 \frac{\bar{\Sigma}_{r,i}}{\Sigma_{r,i}} \quad (4.3)$$

The biased particle weight, w_n^* , is viewed as the adjustment accounting for the change from the *unbiased* (perturbed) probability to the *biased* (reference) probability. Positive perturbations ($\bar{\Sigma}_{r,i} > \Sigma_{r,i}$) will increase w^* in the case that the cross section sampled is counted as accepted. On the other hand, rejected or virtual events in the collision history will lower w_n^* . This means that $\bar{\Sigma}_{r,i}$ in Eq. 4.3 will be equivalent to $(\Sigma_{r,i} + d\Sigma_{r,i})$ for accepted events and $(\Sigma_{r,i} - d\Sigma_{r,i})$ for rejected events. The opposite will be true if the perturbation is negative. An example is illustrated in Fig. 4.1 which follows the collision history of a neutron's random walk in the blanket region of the reactor. Eq. 4.4 shows the implementation of Eq. 4.3 for this case. It is assumed that the probability of an accepted and rejected collision is the same (0.5). Additionally, the isotope of the blanket sampled


```

mat mat2      sum
Li-6.09c     3.07059E-03
Li-7.09c     3.78706E-02

```

Figure 4.2: Example of Serpent input materials definition for a pure lithium blanket.

```

1.015  1.015
0.100  1.000
0.955  0.900
1.110  1.110
1.000  0.120

```

Figure 4.3: Example of perturbation file, `filePert`, for pure lithium. The perturbation entries correspond to the two lithium isotopes in the same order as the materials definition in Fig. 4.2 (^6Li first, ^7Li second).

A simple example is demonstrated in Figures 4.2 and 4.3 for pure lithium. Fig.4.2 shows the Serpent input material definition of a pure lithium blanket with atomic densities of its two isotopes, ^6Li and ^7Li . The perturbation file for the two lithium isotopes is given Fig.4.3 The file consists of a 2×5 matrix with the first column listing all the ^6Li perturbations and the second listing all the ^7Li perturbations. Each row in the matrix is a different perturbed case. For example, only ^6Li is perturbed in the second row with the ratio of the perturbed case over the reference equating to 0.10. The ratio of ^7Li in this row is 1.0 which means its concentration remains the same as the reference. The opposite is seen in row 5 which only perturbs ^7Li by 0.12. The maximum number of perturbed cases (rows) that can be defined in the file is declared as a variable, `AGPT_FUNCTIONS`, in the source code. If the number of rows entered is less than the maximum, the code fills the rest of the rows and columns of matrix with a value of "1.0". Any row entered in the matrix that is greater than maximum allowable number of perturbations, will not be accounted for in the simulation.

There are two main EPT subroutines implemented into the Serpent code. The first, `AGPTFunctionsInit.c`, declares arrays for every isotope of the perturbed material and assigns a value of 1.0 to every entry of the array. The number of entries in the array is equal to `AGPT_FUNCTIONS` (maximum allowable number of perturbations). Next, it loops through the perturbation file defined by the user, `filePert`, and assigns every isotope array the corresponding perturbation value. Overall, this subroutine stores all the perturbation values in arrays for every isotope of the material of interest. The second EPT subroutine, `AGPTScoreArbitraryFunctions.c`, calculates the biased weights according to Eq. 4.3, for every perturbation found in each isotope's array. Both of these subroutines are found in Appendix E. At the present moment, the isotope arrays must be manually defined by the user. This means that when simulating different alloys, the user has to go into both subroutines and change the number of isotope matrix declarations so that they are equal to the number of columns in the matrix of `filePert`. Future work will generalize these subroutines so that they automatically create isotope arrays based on the number of columns found in `filePert`.

4.2.4 EPT setback

The EPT methodology demonstrates that the biased weight is an estimator of the exact neutron flux distribution in the perturbed system. This allows a single simulation with a reference alloy composition to estimate the flux and subsequently the TBR for hundreds of perturbed alloy compositions. Nevertheless, one must be careful in choosing the degree of perturbation; the greater the relative perturbation¹ from the chosen reference, the higher the uncertainty is of the perturbed result. The collision history of the reference point is based on sampling of cross section probability distributions of that point, and relies on the atom densities of the elements making up the alloy. Small perturbations of an element's concentration (making up the alloy) will physically follow similar particle paths as the reference case and calculate relatively accurate results with low uncertainties. As the perturbation increases, the difference in probability distributions between the reference and perturbed case is greater. This means that for large perturbations, the collision history is not accurately modeled by the reference's case collision history and thus, the uncertainty of the results is much higher. It is not feasible to run one simulation for the entire ternary alloy due to the high degree of variation in compositions. Results would only be accurate around the region of the reference point and become ambiguous everywhere else. Therefore, it is important to consider the differences between regions of the entire ternary of the alloy and how to best account for them through simulations with EPT. This will be discussed in Section 4.3.

One other point related to the size of the relative perturbations must be considered. The relative perturbation cannot exceed 100%. For example, if the reference composition has a lithium concentration of 25%, the perturbed lithium concentration cannot exceed 50%. The method renders inaccurate for relative perturbations greater than 100% and will lead to negative results.

4.2.5 Inertial Fusion Energy Reactor Model

The purpose of the Serpent Monte Carlo EPT methodology for this work is to optimize the composition of an inertial fusion energy (IFE) reactor blanket. The model created to test this method is based on the MCNP model presented in Chapter 3. The fusion chamber consists of a xenon spherical cavity with a radius of 13.004 meters. A fusion point source is located in the center of the spherical cavity, and accounts for the release of 4.69 neutrons from fusion plus an additional 2.8% of neutrons originated from (n,2n) reactions with the compressed DT fuel and the lead hohlraum. The point source represents a simplified version of the real indirect-drive target, and is modeled with an energy distribution obtained through accurate target simulations [106]. The energy spectrum of the source distribution takes into account the scattering reactions occurring in both the DT target and the hohlraum. Low density xenon (6 μg) in the spherical chamber acts as a shield for the first wall by absorbing excess X-rays and ions released from alpha particle interactions with the DT fuel, ablator, and surrounding materials [105]. The blanket surrounds the central chamber and consists of a series of coolant/breeder layers separated by a structural

¹We define relative perturbation as the ratio between the difference of the perturbed and reference composition over the reference composition.

Table 4.1: Composition and dimensions of the blanket components.

Layer #	Material	Thickness (cm)
1	HT9	0.5
2	Breeder/Coolant	1
3	HT9	0.5
4	Breeder/Coolant	100
5	HT9	0.5
6	Breeder/Coolant	50
7	HT9	0.5
8	Graphite	100

component made of HT9 (composed of iron at 85.9%, chromium at 12.1%, and small traces of carbon, silicon, niobium, molybdenum, and tungsten) with a density of 8 g/cm^3 . The dimension of each blanket layer is listed in Table 4.1. Two different blanket materials were studied: LiPbBa, and LiSnZn. These materials were studied in Chapter 3, and have proven to be good candidate alloys based on the neutronic properties of the individual elements making up the ternary alloy. For example, Pb has a high neutron multiplication cross section and low absorption cross section; Sn in LiSnZn has a low absorption cross section and a high effective Q-value. The outermost layer of the of the entire spherical chamber is made up of graphite for shielding purposes. The temperature for all material cross sections was 900 K, and the library used for the cross sections was ENDF/B-VII.I at 900 K [26].

Included in the real life IFE chamber are 48 beam ports that direct high energy lasers onto the target. The geometry necessary to incorporate the beam ports into the Monte Carlo Serpent model is quite complex and thus, the beam ports were not included. Additionally, the injection port for the target and exit port that releases target debris after fusion takes place were also excluded from this model. The simplified model is illustrated in Fig. 4.4. The lack of neutron leakage from these components in the model results in a higher TBR. To account for this, various sample input files were simulated utilizing different compositions of LiPbBa and LiSnZn. The same compositions of both of these alloys had been simulated in the past with an MCNP model that included the beam ports, injection port, and exit port. The ratio between the TBR results with the ports and the results without them was taken. On average, this ratio amounted to $\approx 0.93\text{-}0.94$; its average, 0.935, was taken and multiplied by all TBR results generated from Serpent. This was a decent approximation that accounted for the higher TBR. Moreover, results calculated from regular Serpent simulations (without EPT) were successfully verified by performing MCNP simulations with the exact same model. In this work, the relative uncertainty, defined as the ratio between the absolute uncertainty and the value of the result, was chosen to represent the uncertainties of TBRs.

Tritium production in Serpent was calculated by including detectors for each isotope in the blanket, with a response function of 205 [93]. The TBR must be greater than unity for the system to be self-sufficient. For this type of reactor, the TBR accounts for losses due to radioactive decay, low tritium permeation during operation, and for a limited storage

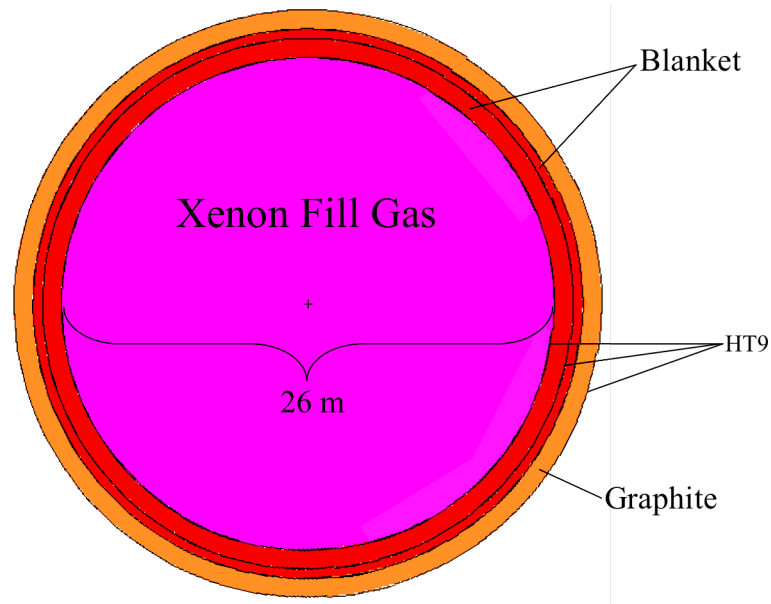


Figure 4.4: Simplified Serpent model of IFE reactor viewed from the xz plane.

inventory that is only used to continue operation during an emergency [11]. Furthermore, the TBR in the IFE reactor reaches a high fractional burn-up of 30% [132]. Consequently, studies on this type of design have approximated a minimum TBR constraint of 1.02, and maximum of 1.1 [75]. A TBR in between these two limits of 1.05 was chosen for the analysis of the for optimization studies in this chapter. Nevertheless, ternary results plotted in later sections will show TBRs at 1.02, 1.05, and 1.1 for completeness and comparison with MCNP results in Chapter 3. Future work will look into analysis of the lower and upper TBR constraints.

Serpent does not have the ability to simulate combined neutron and photon transport. This means that the EMF cannot be calculated in conjunction with the TBR. The EMF constraint instituted in the optimization studies, discussed in Section 4.6, utilized the results obtained from MCNP calculations found in Chapter 3. The EMF constraint imposed was selected to be 1.1, which is a conservative assumption. This value is actually not a real physical constraint but a design choice; the higher the EMF, the lower the cost of electricity [103]. It is easier to set a lower limit for the EMF to ensure that it can be met by the physics of the reactor.

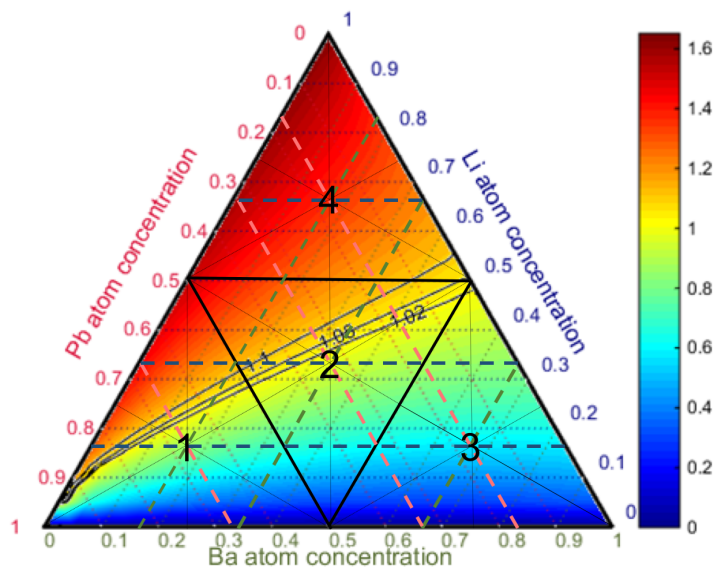
4.3 Selection of Simulations per Ternary Alloy

One of the setbacks previously mentioned of the EPT methodology is the increase in uncertainty as the perturbation becomes larger. It is not feasible to perform one simulation for the entire ternary because of how differently the alloy behaves in various regions, specifically when the concentration of one of the elements is very low. The reference's case collision history cannot account for different behaviors and thus will lead to very high un-

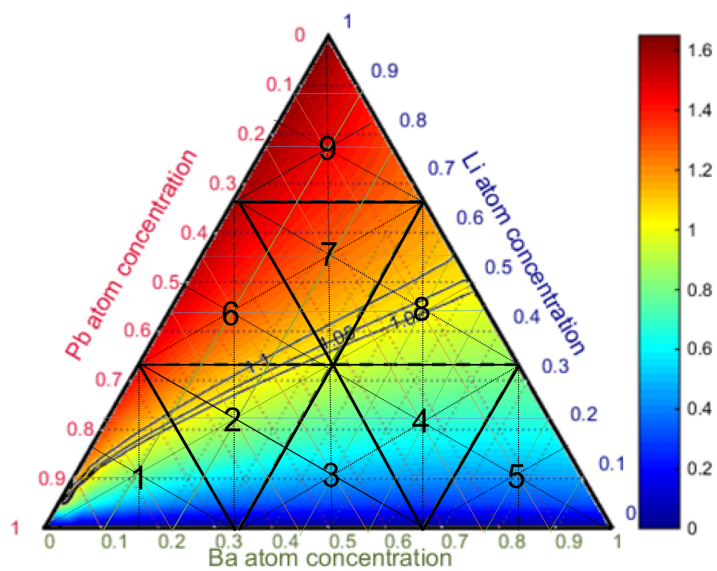
certainties in those regions. It is better to split the ternary into a smaller subset of triangles, where the composition of each of the elements do not vary so much that the paths the particle would hypothetically take are extremely different from the reference case. As a result, four cases splitting a LiPbBa ternary into smaller triangles were created and tested to determine if the relative uncertainties of the TBR obtained in the results were reasonable. Fig. 4.4 shows how each ternary is split, with each case adding a row to the ternary. The ternaries in the figure for LiPbBa were obtained from Chapter 3 and Ref. [75]. In the first case (Fig. 4.5(a)), the ternary is split into four smaller triangles, with two total rows. The composition of the elements within each triangle in this case varies by 50%. The second case (Fig. 4.5(b)) splits the ternary into 9 triangles (3 rows total), each with compositions ranging by 33.3%. The third case (Fig. 4.4(c)) divides the ternary into 16 triangles and the fourth (Fig. 4.4(d)) into 25 triangles, each with four and five rows, respectively. The compositions for each triangle² in the case with 16 vary by 25%, while for the case with 25 triangles they vary by 20%. Simulations are conducted for each triangle within the ternary. For example, the ternary divided into 16 smaller parts will require 16 simulations to cover the entire phase space of compositions. The position of the reference point in each triangle is also important, as it determines the magnitude of the perturbations within the area simulated. The best placement of the reference point is in the center of the triangle, where the largest relative perturbation for a particular element is the same in both directions. It is also important to place the reference point in the center so that relative perturbations do not exceed 100%, where the EPT method is no longer valid. For a given subdivided triangle, calculating the reference composition of each element halfway between the minimum and the maximum is ideal. However, this creates an unrealistic total alloy composition. For example, for triangle #10 in the case with 16 triangles (Fig. 4.4(c)), the reference composition for each element would be chosen at the halfway point, which is 37.5% for all three elements. The sum of the three compositions is greater than 100%, indicating that the makeup of the alloy is unrealistic. Nevertheless, it is possible to simulate artificial compositions for elements of a material in Monte Carlo since the compositions are normalized during the calculation. Therefore, all reference points simulated were fictitious, calculated halfway between the minimum and maximum concentration of each element, so that the uncertainties in the perturbed results could be minimized.

It has been determined that a decent relative uncertainty for a Monte Carlo calculation is less than 0.05. This is based on qualitative and quantitative in depth analysis from past Monte Carlo experience [56]. A test Serpent case was simulated without EPT to evaluate the uncertainty of the TBR, which would be similar to the uncertainty of the reference point in an EPT calculation. The case consisted of a 25% Li, 60% Pb, and 15% Ba. The TBR calculated in this case was 1.06, and its relative uncertainty was 4.83×10^{-4} , which is reasonably low and signifies reliability in the result. The uncertainties for all of the perturbations calculated with EPT will be higher than this number, and depend on the magnitude of the perturbation. For comparison, only one triangle was simulated from each ternary case in Fig. 4.4; the triangle chosen, outlined in Table 4.2, was intended to be in a similar position for each of the ternary cases. The number of compositions simulated for the entire LiPbBa ternary in Chapter 3 was 231; this number was kept consistent for

²To reduce confusion, we will refer to subdivisions within a ternary as triangles instead of ternaries.



(a) 4 triangles



(b) 9 triangles

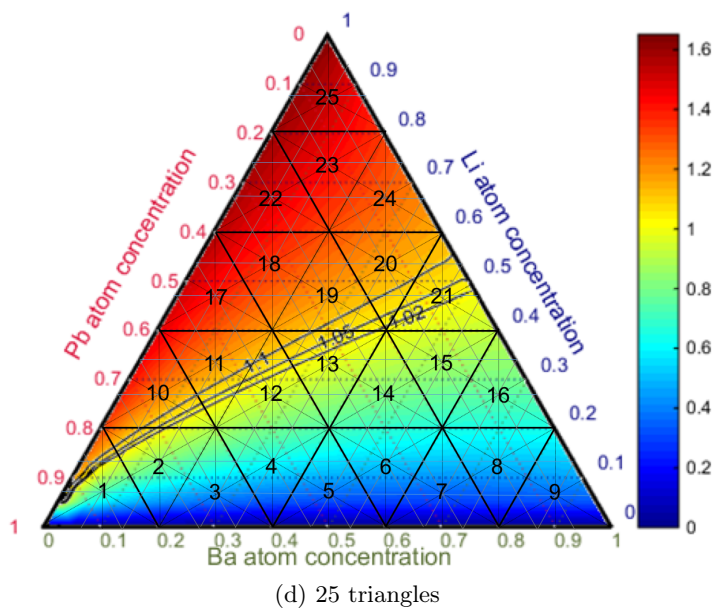
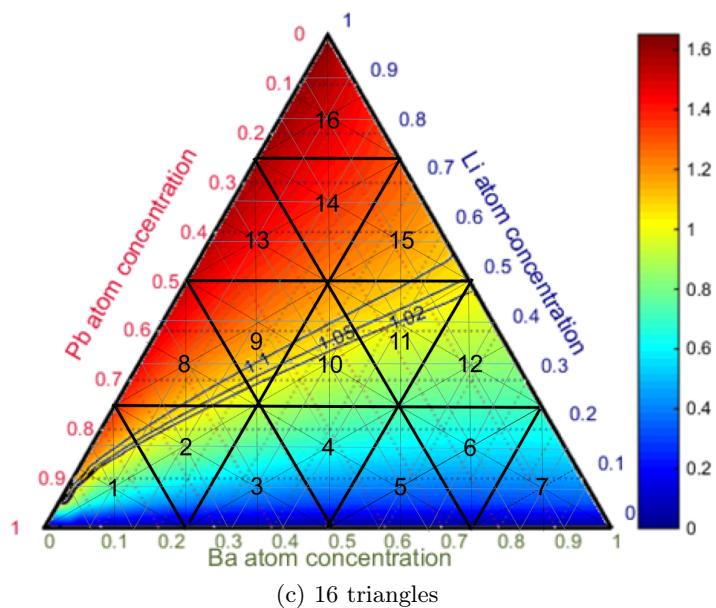


Figure 4.4: LiPbBa ternary subdivisions of (a) 4 triangles, (b) 9 triangles, (c) 16 triangles, and (d) 25 triangles; each case has the number of representative triangles labeled.

Table 4.2: Chosen triangle to simulate for each split ternary case in Fig. 4.4.

Case #	Chosen Triangle
4 triangles	3
9 triangles	7
16 triangles	14
25 triangles	23

perturbed compositions included in each subdivided triangle simulated, which meant that the intervals between each point were different in each of the four cases. The interval between each perturbed point in the triangle was: 2.5% for the ternary with 4 triangles, 1.67% for the ternary with 9 triangles, 1.25% for the ternary with 16 triangles, and 1% for the ternary with 25 triangles. The number of particles histories in all simulations was 5×10^8 . Results for each case are presented in Fig. 4.5. The axes on each of the figures represent the relative perturbation for each element in the ternary. Because of the position of the chosen triangle for each case relative to the entire ternary alloy is similar, the minimum Pb and Ba compositions are 0% for the triangle in each case. Consequently, the relative perturbations for Pb and Ba are the same for each case in Fig. 4.5. For Li, however, the maximum relative perturbation is smaller as the number of triangles for the case increases due to an increase in the minimum lithium concentration in each triangle shown in the figure. As predicted, the highest uncertainties, greater than 0.8, are found in the case with 4 triangles, while the largest uncertainties in the case with 25 triangles are an order of magnitude smaller. Overall, the most precise results will be obtained by simulating 25 triangles within the ternary. This can be better seen in Table 4.3 where the 20 highest uncertainties per case are compared. The uncertainties of twentieth highest points remain greater than 0.05 for the cases with 4, 9, and 16 triangles, respectively, Contrarily, the uncertainty of the nineteenth point in the case with 25 triangles is lower than 0.05. This means that out of the 231 points simulated for the triangle, 213 have uncertainties below the reasonable threshold. From this analysis, it was decided to simulate 25 triangles within the LiPbBa ternary to test the EPT methodology. To decrease the uncertainties even further, more triangles would have to be simulated, which was not desired due to the computational demand on memory and time. Methods to remove unwanted results with high uncertainties will be discussed in later sections.

4.4 EPT Results with LiPbBa

A LiPbBa ternary alloy was split into 25 smaller triangles as described in Fig. 4.4, where the range of concentrations for each element in the triangle is 20%. A fictitious reference point was chosen for each triangle located where the composition of each element is halfway between the minimum and maximum. The only instance where this was not the case was when the minimum composition of one of the elements was 0%. For these cases, the reference composition of that element was set to 11% as opposed to 10%, so that the relative perturbation at the maximum concentration of that element could be lowered from 100% to 81%. A general idea of what the TBR results for the ternary looks like was already

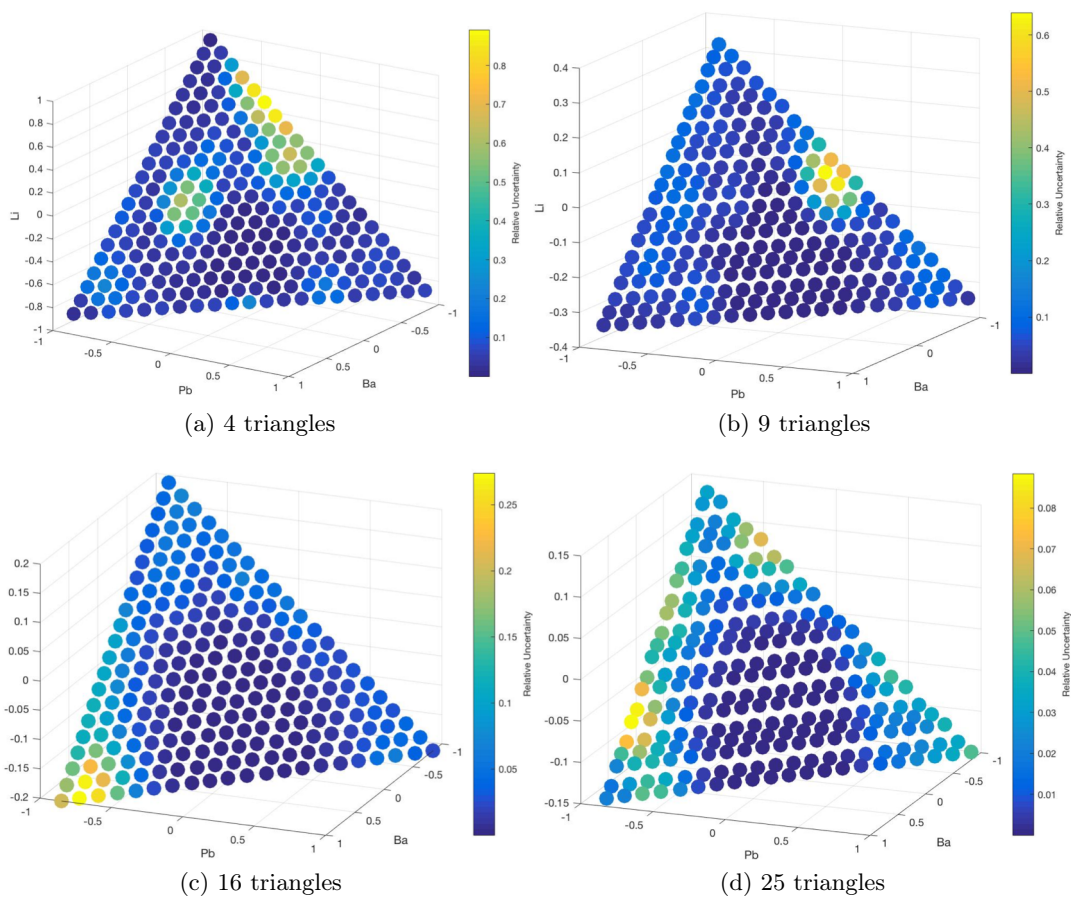


Figure 4.5: LiPbBa uncertainties for a specific triangle chosen in the case the ternary is divided into (a) 4 triangles, (b) 9 triangles, (c) 16 triangles, and (d) 25 triangles; each case has the number of representative triangles labeled.

Table 4.3: Top 20 uncertainties for each subdivided ternary case.

Uncertainties			
4 triangles	9 triangles	16 triangles	25 triangles
8.92×10^{-1}	6.40×10^{-1}	2.74×10^{-1}	8.84×10^{-2}
8.63×10^{-1}	6.17×10^{-1}	2.69×10^{-1}	8.64×10^{-2}
8.50×10^{-1}	5.19×10^{-1}	2.55×10^{-1}	7.34×10^{-2}
7.05×10^{-1}	5.19×10^{-1}	2.25×10^{-1}	7.15×10^{-2}
6.93×10^{-1}	4.91×10^{-1}	2.17×10^{-1}	6.77×10^{-2}
6.51×10^{-1}	4.53×10^{-1}	2.03×10^{-1}	6.75×10^{-2}
6.40×10^{-1}	4.29×10^{-1}	1.79×10^{-1}	6.65×10^{-2}
6.01×10^{-1}	3.80×10^{-1}	1.65×10^{-1}	6.11×10^{-2}
5.72×10^{-1}	3.06×10^{-1}	1.62×10^{-1}	5.82×10^{-2}
5.65×10^{-1}	3.01×10^{-1}	1.61×10^{-1}	5.78×10^{-2}
5.58×10^{-1}	2.98×10^{-1}	1.56×10^{-1}	5.77×10^{-2}
5.56×10^{-1}	2.29×10^{-1}	1.32×10^{-1}	5.72×10^{-2}
5.56×10^{-1}	2.03×10^{-1}	1.19×10^{-1}	5.67×10^{-2}
5.53×10^{-1}	1.74×10^{-1}	1.17×10^{-1}	5.55×10^{-2}
5.41×10^{-1}	1.27×10^{-1}	1.17×10^{-1}	5.45×10^{-2}
5.39×10^{-1}	1.19×10^{-1}	1.17×10^{-1}	5.32×10^{-2}
5.32×10^{-1}	1.18×10^{-1}	1.16×10^{-1}	5.26×10^{-2}
5.26×10^{-1}	1.17×10^{-1}	1.15×10^{-1}	5.22×10^{-2}
5.04×10^{-1}	1.15×10^{-1}	1.11×10^{-1}	4.91×10^{-2}
4.96×10^{-1}	1.13×10^{-1}	1.06×10^{-1}	4.79×10^{-2}

established in Chapter 3. The TBRs of interest, 1.02, 1.05, and 1.1, which were plotted in Fig. 3.8 of Chapter 3, are found in regions located inside triangles labeled 10-21 of Fig. 4.4(d). These triangles were simulated with a 1×10^9 particle histories to reduce uncertainties and increase precision in the results. The rest of the triangles labeled in Fig. 4.4(d) were simulated with 5×10^8 histories. The results for the entire ternary are displayed in Fig. 4.6, and are compared with the MCNP results from the previous chapter. The EPT results show a similar trend to those of MCNP, with increasing TBR as Li concentrations increase, and Ba concentrations decrease. The general trend of the TBR lines at 1.02, 1.05, and 1.1 in the results with Serpent EPT is also similar to the lines plotted with MCNP, where they begin at high Pb concentrations and low Li and Ba concentrations, respectively, and move diagonally upwards towards higher Li concentrations as Pb concentrations decrease, and Ba concentrations increase. Of noticeable difference is the higher range of TBRs calculated with EPT, primarily due to a skewed area found in the upper left region of the ternary, where Li compositions are high, while Pb and Ba compositions are low. The precision of the results within this hot spotted region is poor, exhibiting relative uncertainties, shown in Fig. 4.7, that are greater than 0.3. Moreover, EPT performs poorly in areas where the concentration of one of the three elements is very low, close to 0%. This is most prominent in regions of very low lithium concentrations where the greatest perturbations, whose (n,t) cross section is most sensitive, were simulated. Other deviations in Fig. 4.6(a) are found along Pb concentrations of 20%, 40%, 60%, and 80%. The same is found for Ba concentrations, but to a lesser degree. Looking back at the 25 triangular subdivisions of the ternary in Fig. 4.4(d), one can see that with a reference point located around the center of each triangle, the highest perturbations simulated with EPT are found around the periphery of the triangle where it is furthest from the center. Consequently, the values around the perimeter (of each triangle) are erroneous, and exhibit the highest uncertainties shown in Fig. 4.7. The collision history simulated at the reference point is mostly likely not depicting the same behavior that would be seen in regions of large Pb and Ba perturbations, and because the EPT method cannot account for this, it performs poorly. This is mostly affected by probabilities for (n,xn) reactions in Pb, and absorption reaction cross sections in Ba (a more detailed explanation of the reactions found in each element can be found in Chapter 3). The uncertainties calculated around each triangle's perimeter in the LiPbBa ternary are much higher than 0.05, and range between 0.1-0.8. This means that the TBR in these regions are unreliable and most likely meaningless. Therefore, it was imperative to find a way to either lower their uncertainties, or remove them.

4.5 Methods to Eliminate High Uncertainties

As discussed in the previous section, high uncertainties are found in regions of large perturbations where EPT performs poorly. The following sections introduce two methods that deal with high uncertainties, and discuss how results are affected.

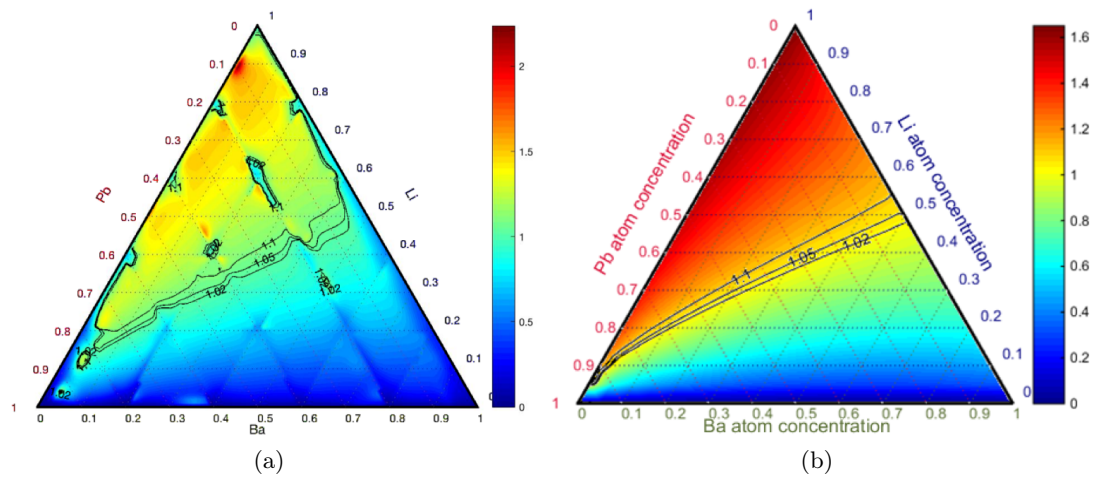


Figure 4.6: Comparison of LiPbBa TBR results with (a) Serpent using EPT and (b) MCNP

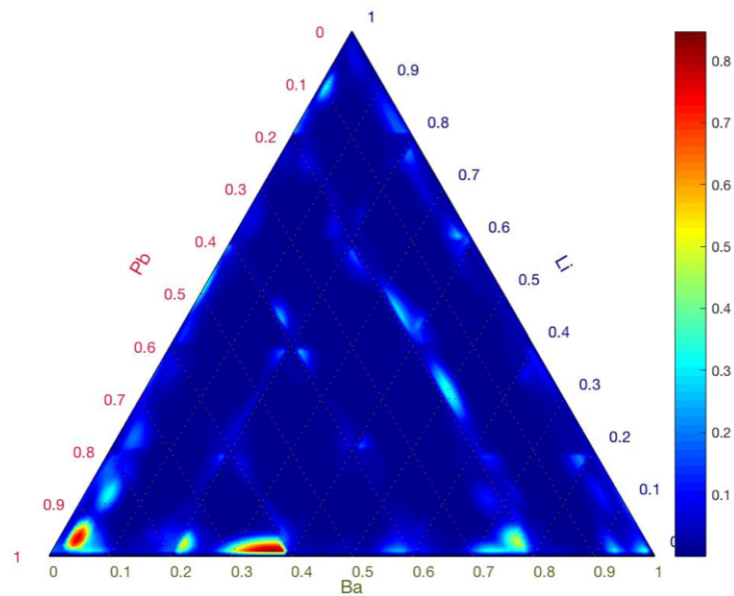


Figure 4.7: Uncertainties for TBR results of LiPbBa simulated with Serpent EPT.

4.5.1 Uncertainty Cut-off Method

The first method, called "uncertainty cut-off" that was employed, simply removes the highest uncertainties in each of the 25 triangles that make up the entire LiPbBa ternary. This method easily removes a few hundred points from the 5,151 points plotted, and relies on the application of Delaunay triangulation and linear interpolation used by Matlab to create ternary plots [64]. A Delaunay triangulation involves connecting nearby points (used as vertices) to form triangles, and ensures that no other points are inside the circumcircle associated with each triangle [90, 110]. This type of triangulation is applied to alloy compositions by creating triangular surfaces that are filled with a TBR value proportional to the surface's height. Afterwards, Matlab linearly interpolates the values of the surfaces, resulting in smoothly shaded ternary plots seen in Fig. 4.6 and others throughout this Chapter. Removing highly uncertain points allows triangulation and interpolation to be performed only on points with more meaningful results and thus creates ternary plots that better predict the behavior of the alloy.

Five cases were tested with the uncertainty cut-off method, and differed by the number of highly uncertain points removed in each of the 25 triangles simulated. This number ranged from 30 to 110, with each case removing an additional 20 points per triangle. One thing to note is that not every triangle out of the 25 had x number of uncertainties removed since the points making up the perimeter of each triangle overlapped with neighboring triangles. The plots in Fig. 4.8 show all the TBR points that remained in the LiPbBa ternary after the highest uncertainties were eliminated, while Table 4.4 lists the number of points removed per case versus the number that remained. As discussed in the previous section, Serpent EPT does not perform well in alloy compositions whose elements have large perturbations. These compositions contain TBR values with the highest uncertainties and happen to be located in the outer peripheries of the triangles. Consequently, compositions within these regions were removed by the uncertainty cut-off method. The results, after applying Delaunay triangulation and interpolation, are plotted in Fig. 4.9, and their corresponding uncertainties in Fig. 4.10. It is clearly seen in Fig. 4.9 that as the number of uncertain points removed increases, the deviations found each triangle's perimeter, specially where both Pb and Ba compositions are 20% and 40%, are abated. Deviations are nearly nonexistent in the 110 uncertainty cut-off case shown by the smoothed out TBR curves in Fig. 4.8(e). The highest uncertainty in this case is an order of magnitude lower than the original case that includes all 5,151 TBR values. Even by only removing 503 values with the 30 point uncertainty cut-off case, the highest uncertainty can be lowered by 56%. The plots of the relative uncertainties in Fig. 4.10, show that as the maximum uncertainty decreases in each plot, the colors filling in the gaps become more visible. Additionally, the hottest area located in the lower left corner of each plot grows as more points are removed and the gap between remaining points increase.

Overall, this method worked fairly well in removing unwanted points that skewed the results. It significantly lowered the maximum uncertainty which increased the validity of the results plotted. Nevertheless, even at the 110 uncertainty cut-off case, the highest uncertainties were still greater than 0.05. By this case, 44% of the 5,151 points were removed. Removing even more points to further lower uncertainties will create larger gaps between remaining points that when interpolated, might not fully portray the true behavior of the

Table 4.4: List of points removed/remaining for each uncertainty cut-off case.

Uncertainty cut-off case	Total points removed (#)	Total points remaining (#)
30 points	503	4648
60 points	911	4240
70 points	1353	3798
90 points	1810	3341
110 points	2274	2877

missing points. As a result, a second method to deal with high uncertainties is proposed in the next section.

4.5.2 Generalized Least Squares for Uncertainties Method

The second method utilizes a form of linear regression modeling to replace highly uncertain TBR points in the LiPbBa ternary with better estimated TBRs that possess much lower uncertainties. Ordinary least squares (OLS) estimates an unknown parameter with the use of a linear regression by minimizing the sum of the squares between the observed response (the TBR) and the values estimated by a linear function based on a set of explanatory variables (the concentration of the elements in the ternary) [133]. The setback of OLS is that it assumes that the variance of all of the observed responses is the same no matter what the values of the explanatory variables associated with the responses are. Results estimated with any Monte Carlo calculation, and particularly the Serpent EPT method, have variable degrees of uncertainties. Therefore, OLS renders invalid at estimating unknown TBRs since the regression it creates weighs all observed TBR points equally when in fact, more accurate points must be weighted more heavily. By weighing points based on their variances, a regression can be created around points with higher weights as it is done with generalized least squares (GLS). Just like OLS, GLS estimates unknown parameters from observations with a linear regression model, but also accounts for the inequality of the variance found in the observations. The mathematical derivation of GLS will not be explained here but can be found in Ref. kariya2004generalized.

TBR results that exhibit high uncertainties can be treated with GLS by removing only that point and creating a linear regression around its vicinity. The number of values utilized in creating the regression around the missing TBR cover an area that is same size as the triangles simulated with EPT. This means that the missing point is located approximately in the center of a triangle that varies by 20% concentration for each element. A visualization of this is given by Fig. 4.11. By applying GLS, the following linear regression can be created:

$$T = T_0 + (Li - Li_0)x_{Li} + (Pb - Pb_0)x_{Pb} + (Ba - Ba_0)x_{Ba} \quad (4.5)$$

where T is an array representing the TBRs of all the points surrounding the missing point. The other side of the equal sign represents a linear function where Li , Pb , and Ba are the concentrations of each element that constitutes all the points that surround the missing

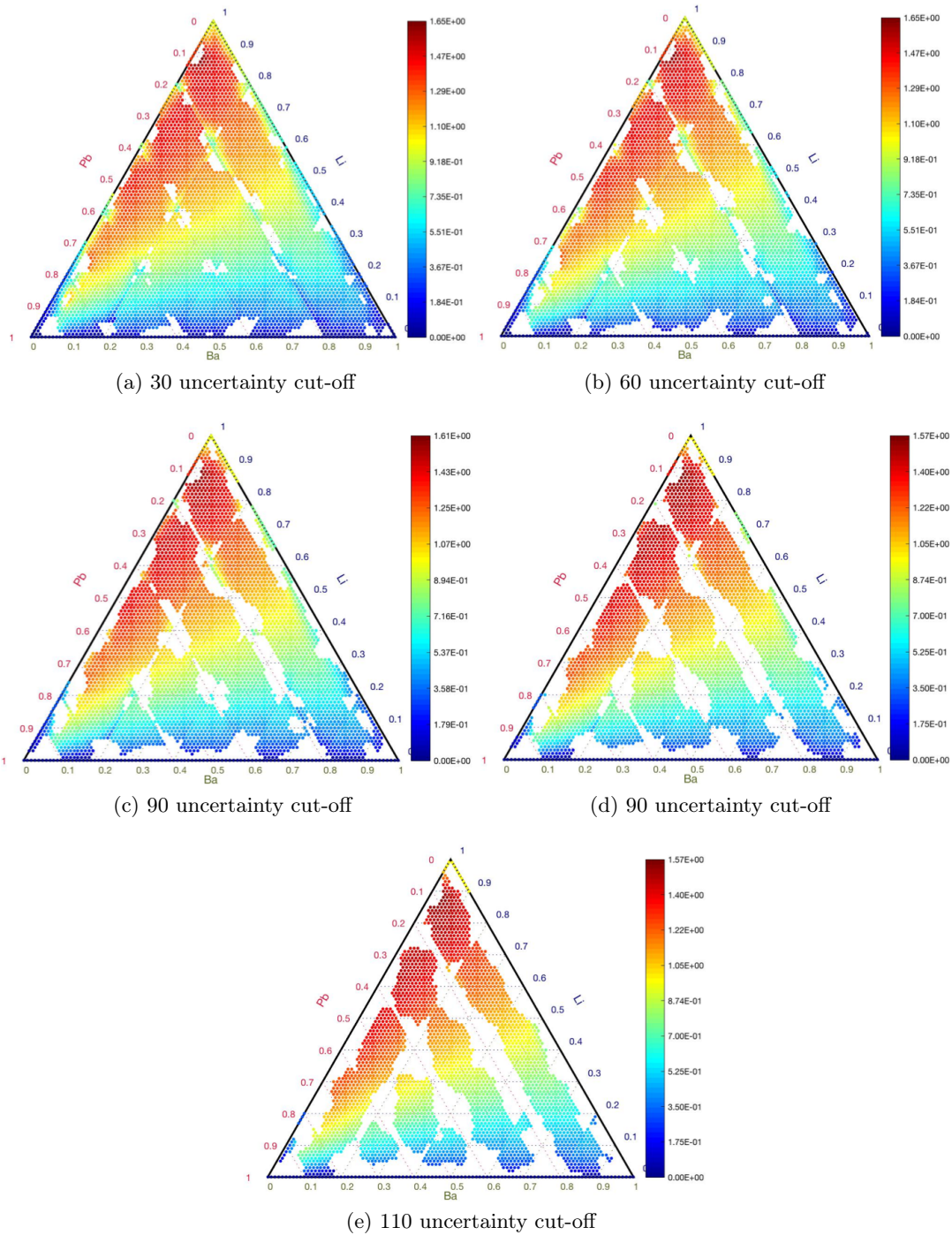


Figure 4.8: Points remaining for uncertainty cut-off cases with (a) 30 points/triangle, (b) 50 points/triangle, (c) 70 points/triangle, (d) 90 points/triangle, (e) 110 points/triangle.

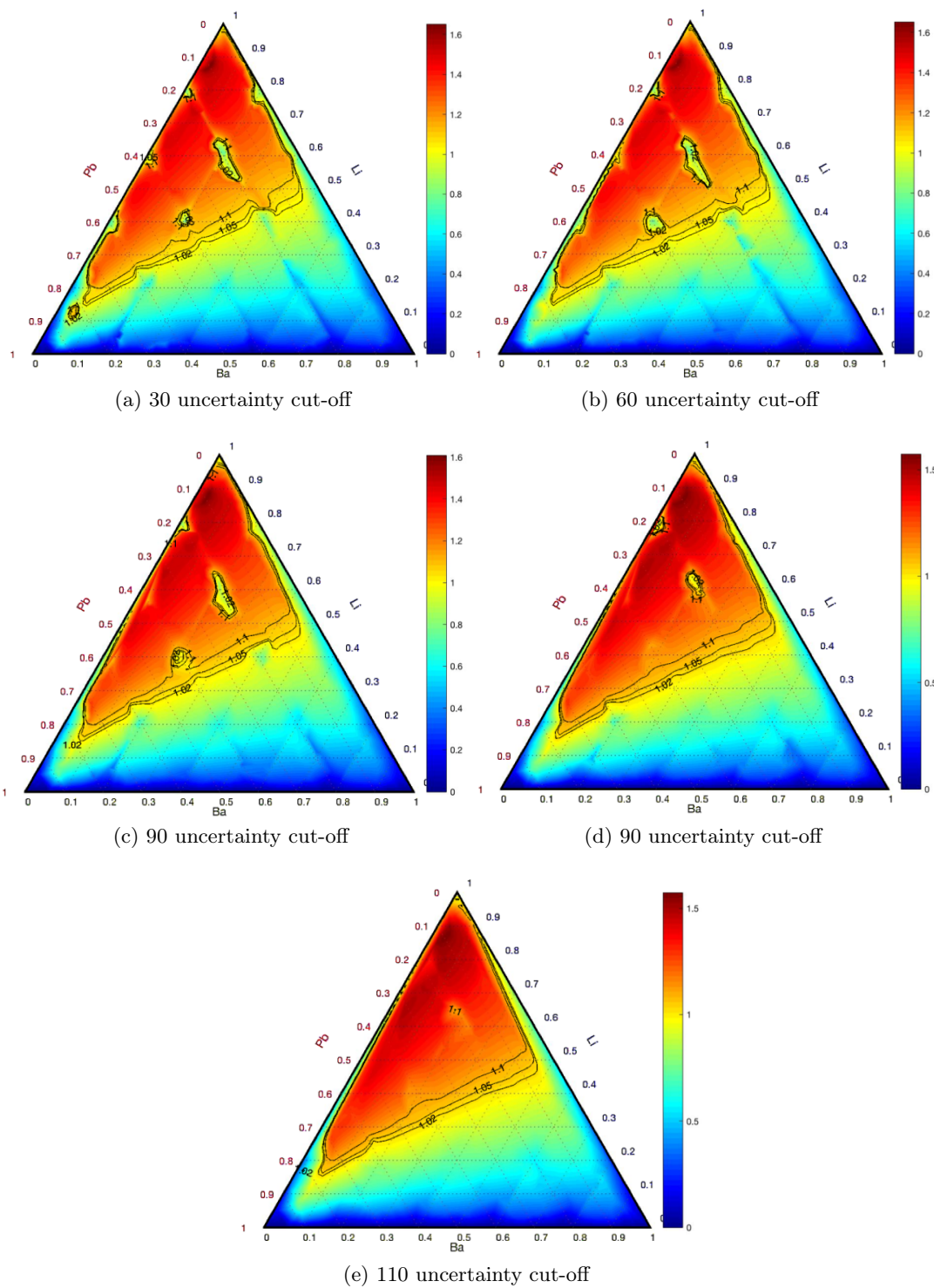


Figure 4.9: TBR results for uncertainty cut-off cases with (a) 30 points/triangle, (b) 50 points/triangle, (c) 70 points/triangle, (d) 90 points/triangle, and (e) 110 points/triangle.

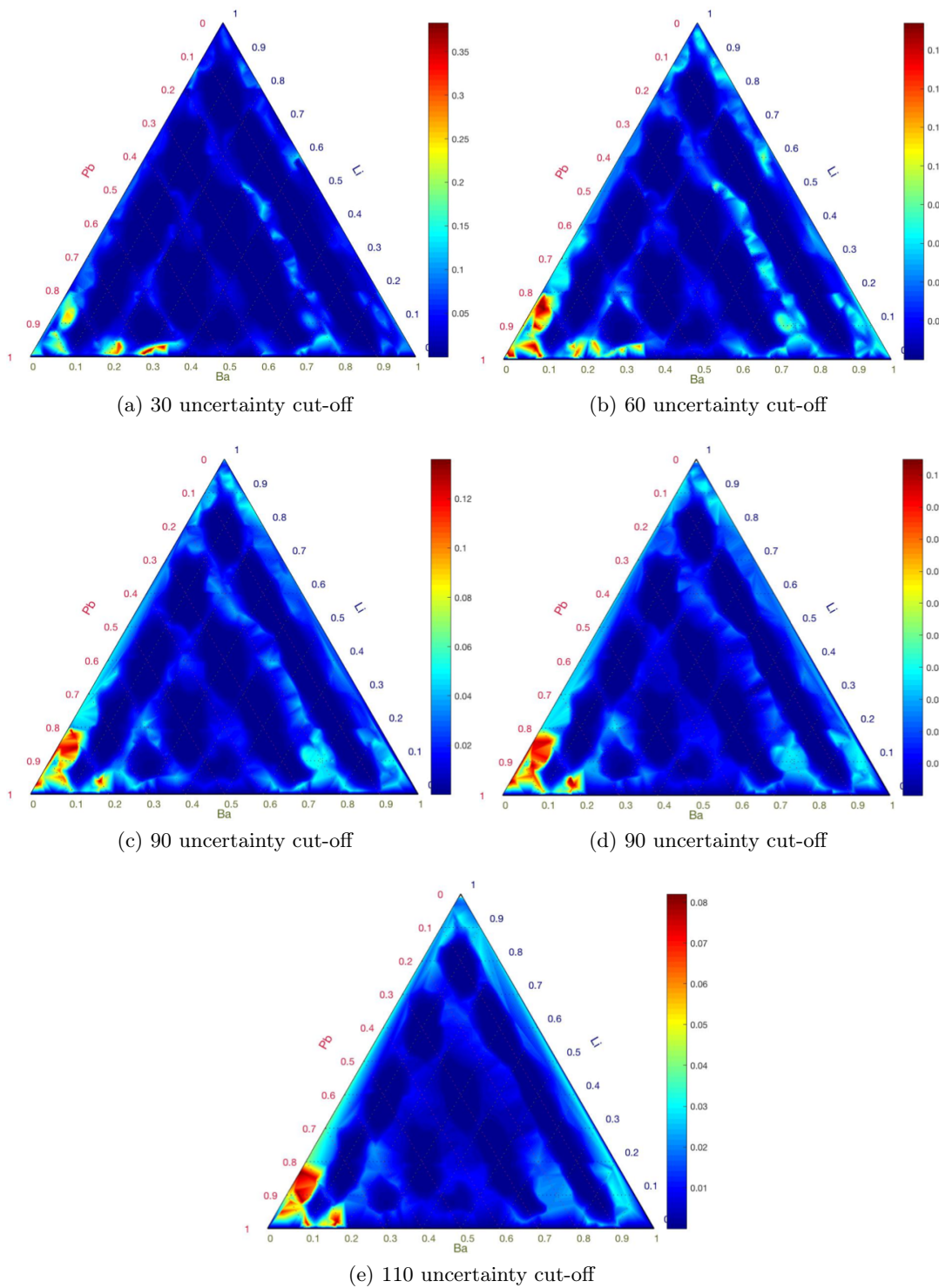


Figure 4.10: TBR relative uncertainty results for uncertainty cut-off cases with (a) 30 points/triangle, (b) 50 points/triangle, (c) 70 points/triangle, (d) 90 points/triangle, and (e) 110 points/triangle.

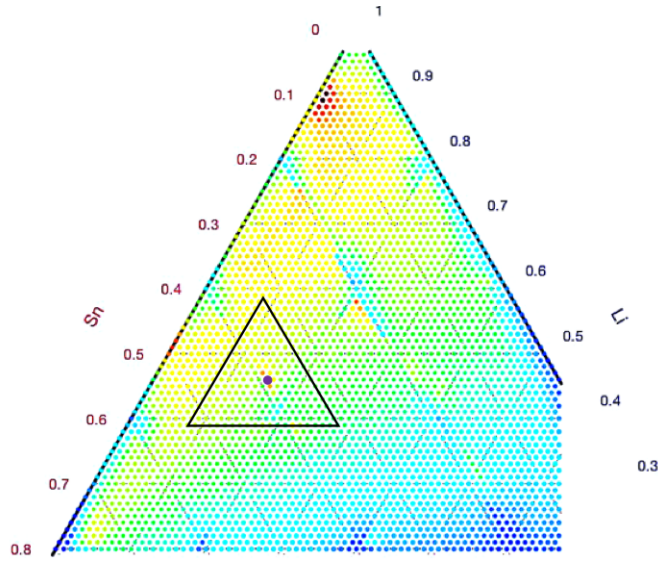


Figure 4.11: Example of GLS application to a point in a closeup of the LiPbBa ternary. The point to be replaced is shown by the larger purple circle. The area of points used in the GLS calculation is outlined by the black triangle.

point, and Li_0 , Pb_0 , and Ba_0 are the concentrations of the elements that make up the chosen missing point. This means that for each element, an array is created with values obtained from the difference between the concentration of a surrounding point and the concentration of the chosen point. The array for each element has a corresponding slope in the function represented by x_{Li} , x_{Pb} , and x_{Ba} , and an intercept given by T_0 . GLS will solve for the slopes and intercept of the linear regression. The value of the intercept is of most importance as it represents the missing TBR. That is, when the Li , Pb , and Ba concentrations are equal to the concentrations of the missing point (Li_0 , Pb_0 , and Ba_0), everything vanishes except for the equality $T = T_0$, demonstrating that the TBR located at the missing point is equal to the intercept. Moreover, GLS will compute an estimated uncertainty (square root of variance) of the intercept. Uncertainties calculated with GLS are weighted by the mean squared error, resulting in conservative values that account for the method's validity to accurately generate results. The script that performs GLS was written with Matlab and can be found in Appendix F.

GLS was implemented to every point whose result had a relative uncertainty that was above a chosen threshold. Six cases were created by choosing different thresholds, which are outlined in Table 4.5. The cases in the first column of the table are labeled with letters from A to F. The uncertainty thresholds in the second column range from 2.5×10^{-2} to 9×10^{-3} . Uncertainties above a certain threshold, found in the third column of the table, will have their point replaced by those calculated with GLS. Uncertainties below the threshold (column four of table) remain intact. For example, the threshold of Case C is 1.5×10^{-2} , with GLS applied to 2,187 values out of the 5,151. Unlike the uncertainty cut-off method, all the points, whose uncertainties are above a specific threshold, are replaced by a new point calculated with GLS. Therefore the number of points that make up the LiPbBa alloy

TBRs will remain 5,151. Additionally it must be emphasized that when GLS is applied to a chosen missing point (above the threshold), only that point is temporarily removed from the data. It does not matter if surrounding points used in the matrixes of Eq. 4.5 also fall above the threshold; GLS accounts for the variance of each value and will create lower weights for these points compared to points with lower variances. Furthermore, a matrix consisting only of points obtained through the Serpent EPT calculation is employed in every GLS calculation. This means that new values calculated with GLS are not used in additional GLS calculations for other points of the ternary. Once all the new values are obtained, ternary plots are created by utilizing Delaunay triangulation and linear interpolation as described in the previous section. The results of the six cases examined (Case A-F) are plotted in Fig. 4.12, and their uncertainties are plotted in Fig. 4.13. It can be seen by the plots in Fig. 4.12 that as the uncertainty threshold becomes lower and GLS replaces more points, the new values remove deviations that were previously located in the periphery of each subdivided triangle simulated, where perturbations are greatest. Additionally, the lines for the specific TBRs in the plots are much smoother compared to the original results plotted in Fig. 4.6(a). This is particularly seen with cases E and F, where the number of points replaced with GLS is more than half. Nevertheless, the TBR curves for these cases are not completely smooth, exhibiting a few peaks due to differences between values calculated with Serpent EPT and those created from the application of GLS. If the threshold was increased even further to allow more points to be recalculated with GLS, the lines will smooth out even more. However, increasing the threshold will replace over 60% of points with GLS and lead to the loss of integrity in the original results.

Table 4.5: List of points removed/remaining for each uncertainty cut-off case.

Case	Uncertainty Threshold	Points Above Threshold (GLS)	Points Below Threshold
A	2.5×10^{-2}	1633	3518
B	2.0×10^{-2}	1879	3272
C	1.5×10^{-2}	2187	2964
D	1.0×10^{-2}	2561	2590
E	9.5×10^{-3}	2599	2552
F	9.0×10^{-3}	2633	2518

One can easily see that uncertainties in the plots from Fig. 4.13 are significantly lower compared to original Serpent EPT results once GLS is applied. About 61%, 70%, and 78% of the results in cases A, C, and E, respectively, have uncertainties that are less than 0.005. Interestingly, the maximum uncertainty for Case C-F, found in the upper left corner of the ternary plots, is larger than for cases A and B. The points that contain these uncertainties had lower uncertainties to begin with, less than the threshold of cases A and B. Thus, these points remain intact for the first two cases but for the rest are recalculated with GLS. GLS has trouble estimating the points in this region, specifically where Ba concentration is 0%, because the formula utilized in the Matlab script to calculate the triangular area that contains all of the points used in Eq. 4.5, creates smaller areas around these regions of the plot. Hence, a smaller number of points are utilized in the

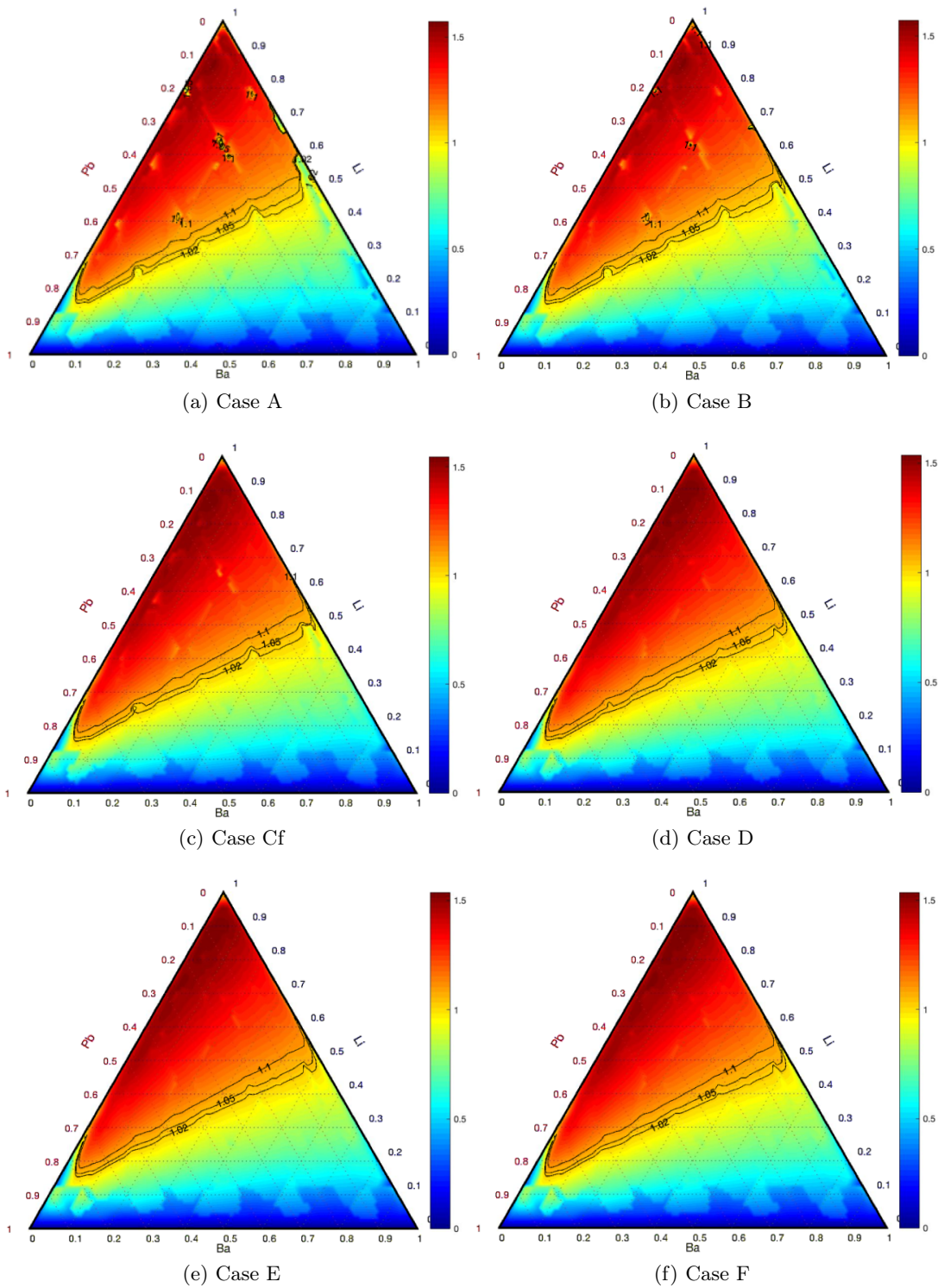


Figure 4.12: TBR results for GLS case (a) A (2×10^{-2} threshold), (b) B (1.5×10^{-2} threshold), (c) C (1×10^{-2} threshold), (d) D (9.5×10^{-3} threshold), and (e) E (9×10^{-3} threshold).

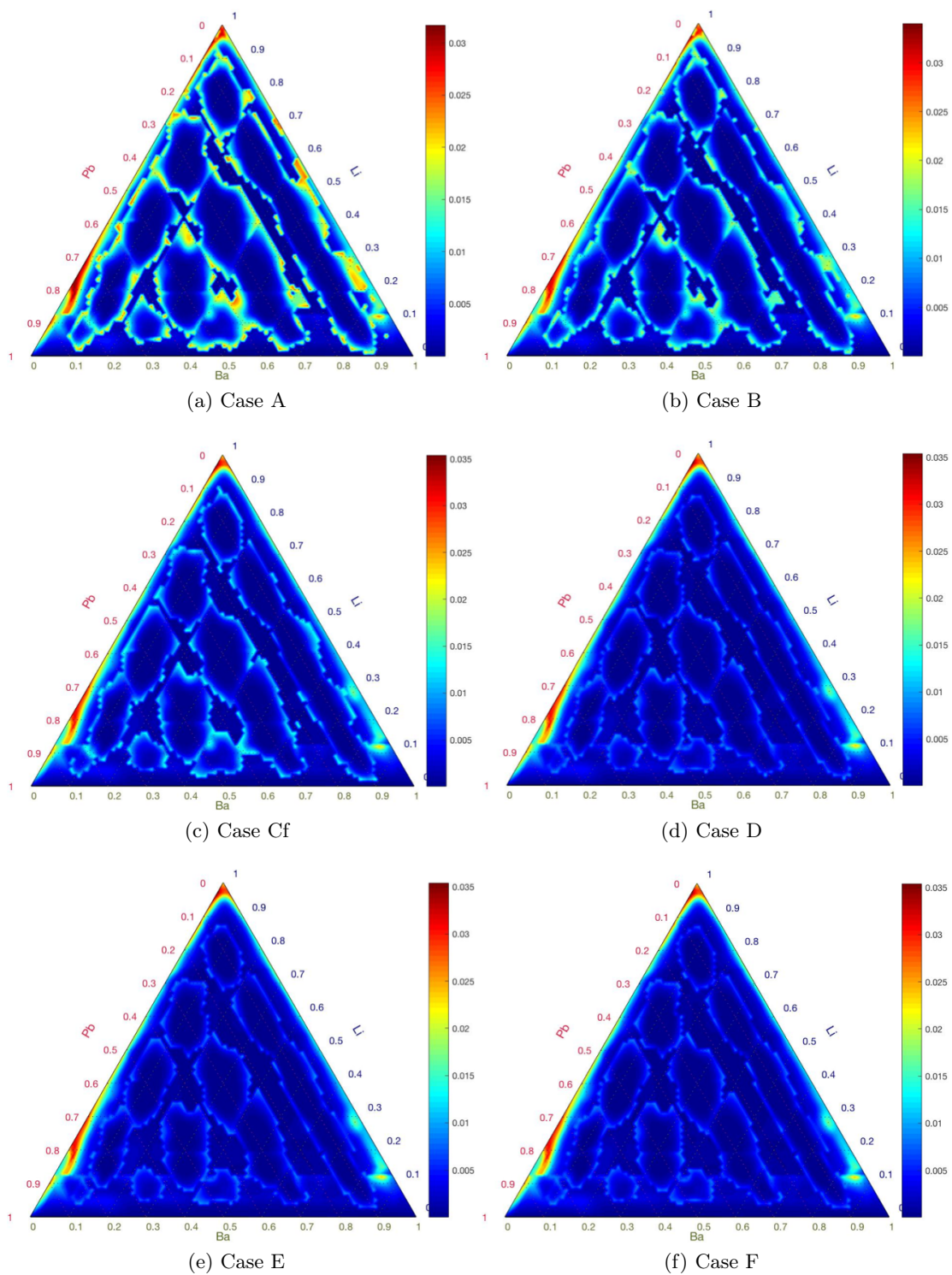


Figure 4.13: TBR uncertainty plots calculated with GLS for Case (a) A (2×10^{-2} threshold), (b) B (1.5×10^{-2} threshold), (c) C (1×10^{-2} threshold), (d) D (9.5×10^{-3} threshold), and (e) E (9×10^{-3} threshold).

GLS formulation such that the uncertainty of the result produced, which includes the mean squared error, is higher. When a greater number of surrounding points were implemented, the uncertainties calculated by GLS decreased; The largest uncertainty of 0.0354 (97% Li, 3% Pb, 0% Ba) was lowered to 0.012. The rest of the points with higher uncertainties in the range of 0.031-0.01, are found around the perimeter of the entire ternary where GLS was not effective in reducing uncertainties to the same magnitude as other points. This is also due to the fact that areas created in these regions which contain points needed in GLS calculations are smaller. Additionally, the entire region surrounding these points was highly uncertain to begin with, and thus, created a poor estimate of points for GLS to use. Again, if larger areas that include better estimated points were included in the GLS calculation, the results would have been more precise. Most of the points around the outer periphery of the entire ternary are of little interest for optimization studies discussed later in the chapter and thus, were not recalculated. Only one specific region in the periphery is nontrivial and is found at the starting point of the 1.05 TBR curve where Ba is 0%. In this case, the formula that determines the area of points used for GLS was slightly altered to include enough points for calculating the linear regression. Furthermore, the optimization methodology described later in the chapter is a multi-level approach that focuses on specific areas of the ternary. As a result, additional simulations were performed in this region for more accuracy. In contrast to the outer edges of the ternary, the GLS method performs very well in regions inside the ternary such as the those located at the outer periphery of the subdivided triangles from Fig. 4.4(d). The uncertainties calculated in these areas are smaller than the surrounding regions which contain the original results calculated by EPT with Serpent. Another trend worth noticing in Fig. 4.12, is the blotchiness found below Li concentrations of 14%. This behavior is most likely due to a combination of smaller areas of points estimated for use in GLS, and higher uncertainties found in the original results, which create skewed results after GLS is applied. Nevertheless, the focus of the rest of the work in the chapter is not in this region, so it was left as is. Further in-depth analysis can be performed around regions of interest, if needed.

It was determined that Case E and F achieved the best results by removing deviations in the TBR and reducing uncertainties below 0.05. As a result, applying GLS to around half of the points obtained from Serpent EPT yields results closer to what the real values would look like. It also allows the integrity of the original Monte Carlo results to be maintained better than with the uncertainty cut-off method. Out of the two methods, GLS was chosen for use in future simulations.

4.5.3 Validity of GLS

The GLS methodology was validated by running several additional simulations as seen in Fig. 4.14, which outlines all locations of these extra simulations. The triangles simulated have compositions that span 10% for each element. Smaller regions were chosen to produce more accurate results, specially in triangles located around the center of the ternary where the highest relative perturbations simulated are smaller than any other perturbation simulated so far. The supplementary simulations were particularly chosen in regions where the TBR curves from the original Serpent EPT results had large deviations. These are the regions that GLS was able to either remove completely or significantly improve. A side by

side comparison of the ternary incorporating GLS Case C and of the ternary with extra simulations added to the original results, is outlined in Fig. 4.15 (uncertainty results are not shown for the ternary of the new case since it looks very similar to Fig. 4.6(a)). The scale of the Serpent EPT results without GLS is still skewed due to the hot spot found in the upper left corner of the ternary. Nevertheless, the regions where new simulations were conducted removed a lot of the deviations. The TBR curves display a positive approximated linear relationship moving from the lower left of the ternary to the upper right. The same type of behavior is found in the plot with GLS. Overall, the GLS plot displays the same trends as the plot without GLS. In addition, it gets rid of high deviations found anywhere in the ternary, not just in regions where the supplementary calculations were made. To validate GLS even further, comparisons were made with certain points between the GLS case and the case with the extra simulations, specially for points where the results in the original Serpent EPT simulation were extremely imprecise. These values are found in Table 4.6. The table compares the results from the Serpent EPT original calculations, with values from the additional simulations and ones obtained after employing GLS. The values obtained with GLS are pretty similar to those calculated in the supplementary simulations, and differ by less than 1%. This validates the effectiveness of GLS, specially for points whose results originally had large deviations. For example, in the first row on Table 4.6, the TBR that was first calculated was 0.796. With GLS, the value was 14% higher at 0.923, and for the extra simulation, the result was very similar to the one calculated with GLS at 0.929. Not every single result calculated with the GLS method will be as accurate as the ones shown in the table. Nevertheless, by looking at the comparison between Fig. 4.15(a) and Fig. 4.15(b), it is concluded that for the most part, GLS can predict the behavior of the ternary successfully in a quick and effective way, without wasting computational time and memory. Doing this comparison further validated the implementation of GLS for simulations with future alloys.

4.5.4 Particle History Comparison

The idea behind simulating triangles 10-21 in Fig. 4.5(d) with 1×10^9 particle histories, compared to 5×10^8 particle histories for the rest of the ternary, was to try to reduce the uncertainty in the results as much as possible. However, this came at a cost of the CPU time, which in many of these triangles was greater than 100 hours. To see if the CPU time could be lowered while maintaining the same level of uncertainties in the results, triangles 17-21 were executed with the EPT method in Serpent with a number of particle histories that was an order of magnitude lower. A comparison of CPU times is outlined in Table 4.7. For every simulation, decreasing the number of particle histories by an order of magnitude subsequently lowered the CPU time by about an order of magnitude. To see if the lower time affected the uncertainty in the results, the triangles for this region of the ternary were plotted and compared for the two cases (Fig. 4.16). The highest uncertainty, greater than 0.45, is found in the case with 1×10^8 particle histories, exhibiting a hot spot concentrated near low Pb concentrations. The other region of high uncertainty, at around 0.3, is seen close to 60% Li and low Ba concentrations. In comparison, the maximum uncertainty of results from simulations with 1×10^9 particle histories is close to 0.35 and found along the 20% Pb concentration line. Similarly to the case with a lower number of particle histories, this case has uncertainties of 0.3 found at a region of low Ba concentration.

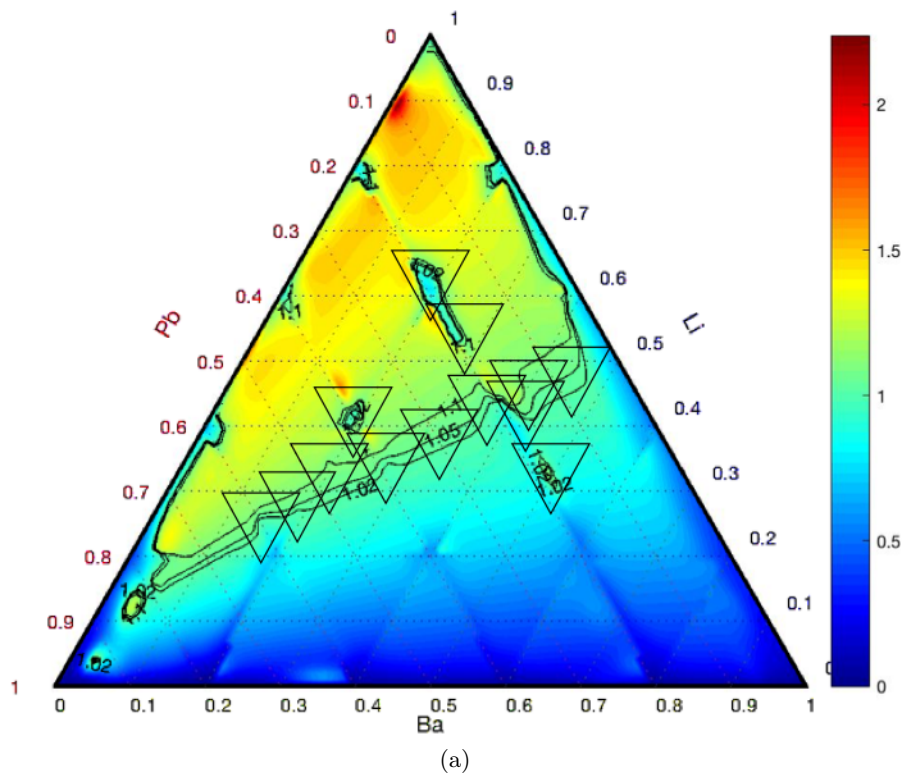


Figure 4.14: Plot of original TBR results obtained with EPT in Serpent. Triangles are outlined in areas where deviations occur. Extra simulations were executed in these regions.

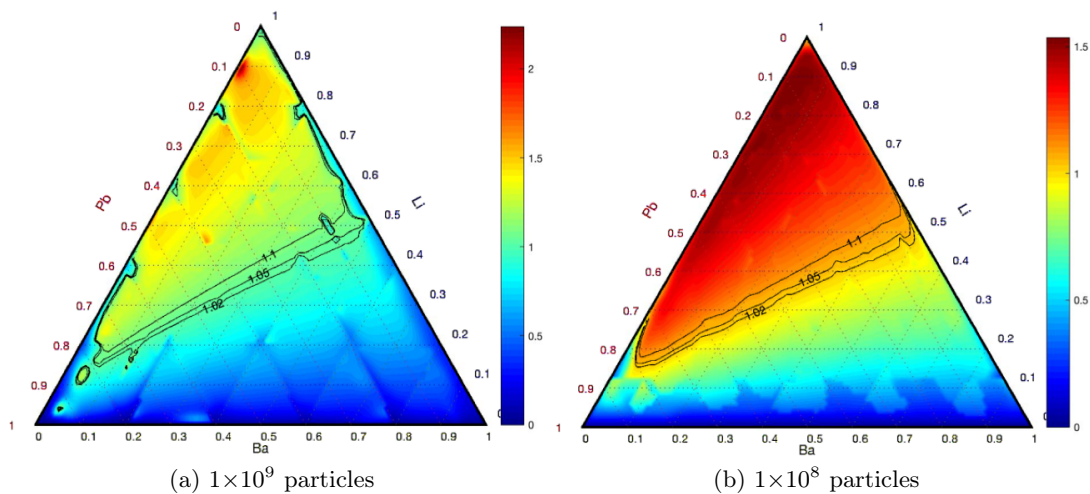


Figure 4.15: Comparison of TBR results in a ternary with (a) additional simulations added to the areas of deviation in original EPT results and (b) GLS applied to uncertainties greater than 9.5×10^{-3} (Case C).

Table 4.6: Comparison of results from original ETP, additional EPT, and GLS applied to original values.

Alloy			Original EPT		Supplemental EPT		GLS	
Li	Pb	Ba	TBR	Uncertainty	TBR	Uncertainty	TBR	Uncertainty
20	62	18	0.796	3.32×10^{-2}	0.929	2.47×10^{-3}	0.923	1.76×10^{-3}
24	58	18	0.927	4.94×10^{-2}	1.007	4.92×10^{-4}	1.010	1.01×10^{-3}
26	55	19	0.981	6.05×10^{-2}	1.026	1.25×10^{-4}	1.034	8.40×10^{-4}
28	55	17	1.077	1.71×10^{-2}	1.08	5.19×10^{-5}	1.084	8.03×10^{-4}
35	19	46	0.872	1.78×10^{-1}	0.921	7.83×10^{-5}	0.920	2.83×10^{-4}
38	39	23	1.319	2.14×10^{-1}	1.127	5.65×10^{-5}	1.125	4.69×10^{-4}
41	18	41	0.969	1.29×10^{-1}	1.014	1.64×10^{-3}	1.014	4.24×10^{-4}
43	39	18	1.093	6.10×10^{-2}	1.226	4.02×10^{-5}	1.227	3.99×10^{-4}
44	18	38	1.082	1.51×10^{-1}	1.06	8.34×10^{-4}	1.062	2.87×10^{-4}
48	18	34	1.235	1.85×10^{-1}	1.121	7.20×10^{-5}	1.119	1.89×10^{-4}
51	19	30	1.127	1.31×10^{-1}	1.174	2.45×10^{-4}	1.169	2.34×10^{-4}
57	22	21	1.447	1.05×10^{-1}	1.286	3.86×10^{-3}	1.285	4.02×10^{-4}
63	21	16	1.458	8.97×10^{-2}	1.365	5.83×10^{-4}	1.359	9.23×10^{-4}
63	20	17	0.875	3.26×10^{-2}	1.359	2.38×10^{-4}	1.351	6.70×10^{-4}
66	19	15	1.13	2.93×10^{-2}	1.385	7.69×10^{-5}	1.382	7.57×10^{-4}

Additionally, in mid Pb and Ba concentrations, hot spots are found containing uncertainties higher than in the case with 1×10^8 particle histories.

To further the analysis, GLS was implemented to results that contained uncertainties greater than 9.5×10^{-3} for both cases and its effectiveness was compared. Fig. 4.17 shows a side by side comparison of the entire ternary, before GLS is implemented, with the results of 1×10^8 particle histories for triangles 17-21 plotted in Fig. 4.17(a) and 1×10^9 particle histories for the same triangles plotted in Fig. 4.17(b). Concentrating in these regions, one can see higher deviations at low Pb concentrations in the case with the smaller number of particle histories. Both cases exhibit high deviations around 20% Pb. When GLS is applied to results, they end up being quite similar as shown in Fig. 4.18. GLS was very effective

Table 4.7: Comparison of CPU time taken to run simulations with 1×10^8 and 1×10^9 particle histories.

Triangle #	CPU Time (hours)	
	10^8 histories	10^9 histories
17	13.8	131.5
18	10.6	100.3
19	11.3	107.3
20	8.5	79.1
21	9.6	89.7

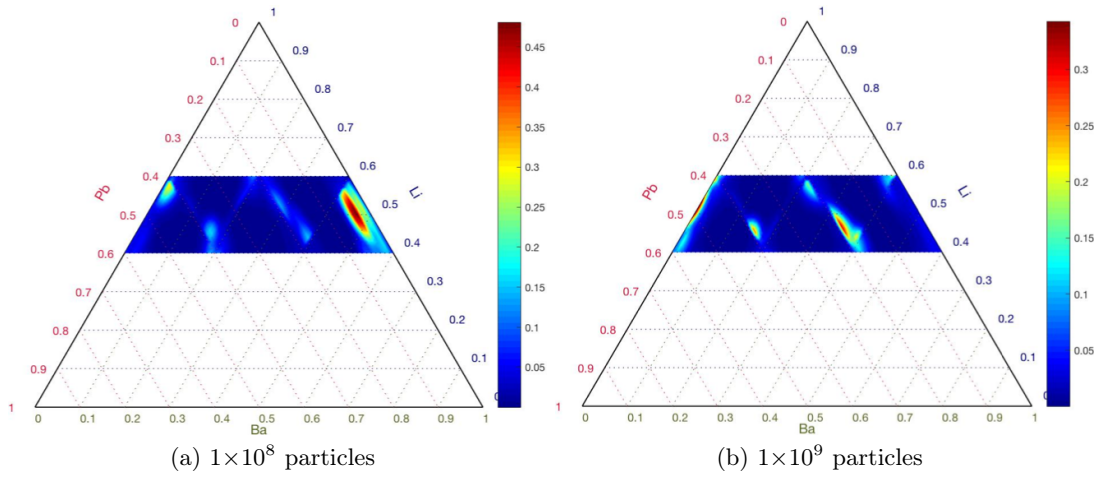


Figure 4.16: Comparison of TBR uncertainties from EPT Serpent calculations only for triangles 17-21 when simulated with a number of particle histories of (a) 1×10^8 and (b) 1×10^9 .

at reducing the high deviations at low Pb concentrations of the case with 1×10^8 particle histories. The uncertainties for the case with 1×10^9 particle histories was shown in Fig. 4.13(e) and is looks very similar to the case with 1×10^8 particle histories. Overall, running simulations with a particle history of 1×10^8 as opposed to 1×10^9 will significantly reduce the CPU time by an order of magnitude while producing relatively similar results, specially when adjusted with GLS. Consequently, it is recommended to run these simulations with 1×10^8 particle histories to save computational time.

4.5.5 GLS effectiveness on Smaller Triangle Subdivision

Generalized least squares has proven to accurately and effectively estimate results that were originally uncertain. It also allowed the number of particle histories in the Serpent simulations to be reduced, as described in the previous section. To further reduce the CPU time of simulations, it was of interest to try changing the number of subdivided triangles in the ternary from 25 to 16 as shown in Fig. 4.4(c). The number of perturbed points per triangle was increased from 231 to 352 so that the interval between each perturbation is 1% for each element. This interval is the same as the ternary simulated with 25 triangles, which allows for better comparison. Additionally, GLS has the ability to create a more accurate linear regression with more points, and thus, calculate TBRs with better precision. The simulations were tested with 1×10^8 particle histories to minimize CPU time. Although the highest uncertainty of the TBR calculated with EPT was smaller for the case with only 16 triangles, the entire ternary as a whole contained higher uncertainties than the case with 25 triangles as seen in Fig. 4.19(b). Because of the higher range of absolute perturbations included per triangle, the results are less accurate (Fig 4.19(a)). The number of points whose uncertainties were greater than 9.5×10^{-3} was 3,774 out of 5,151 total points simulated. Results from the application of GLS to these points are shown in Fig. 4.20.

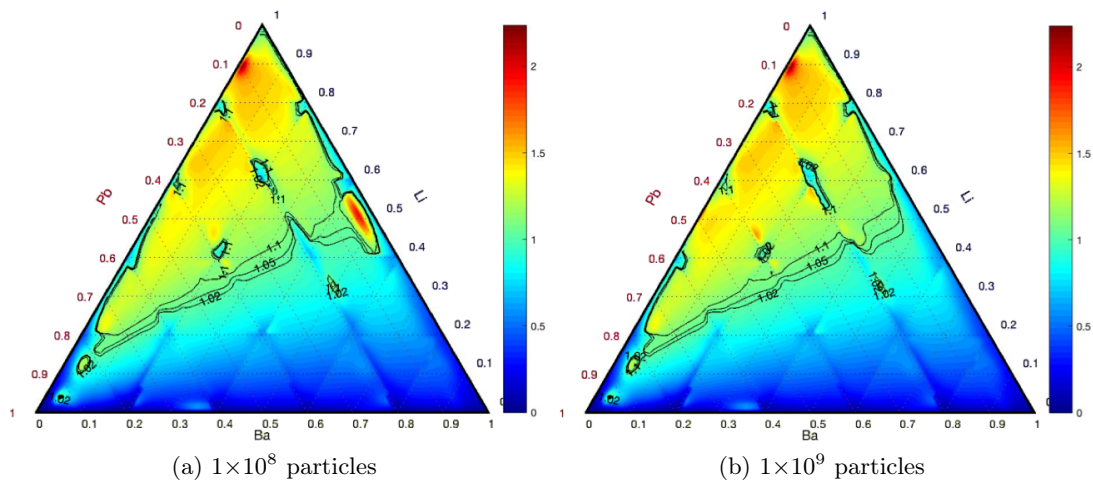


Figure 4.17: TBR (before applying GLS) comparison of triangles 17-21 when simulated with a number of particle histories of (a) 1×10^8 and (b) 1×10^9 .

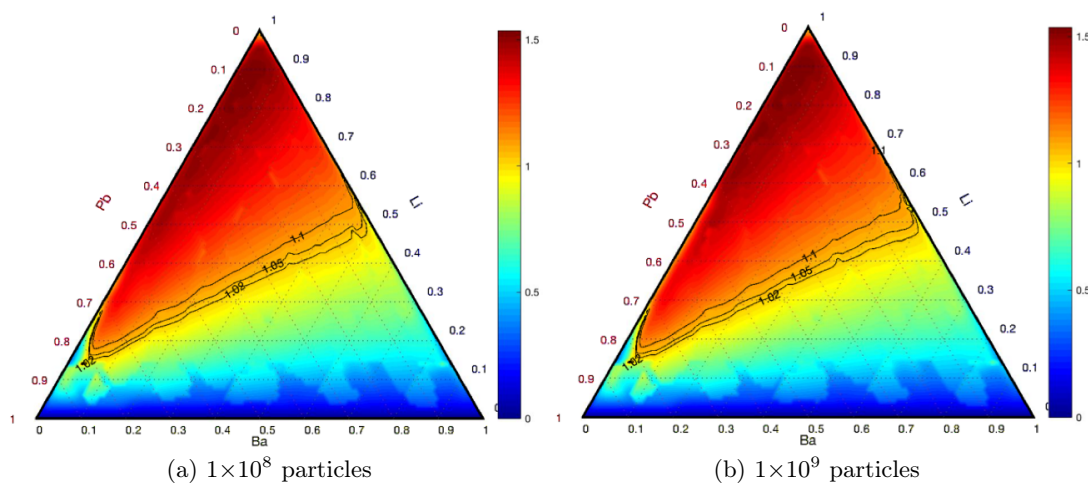


Figure 4.18: TBR (after applying GLS) comparison of triangles 17-21 when simulated with a number of particle histories of (a) 1×10^8 and (b) 1×10^9 .

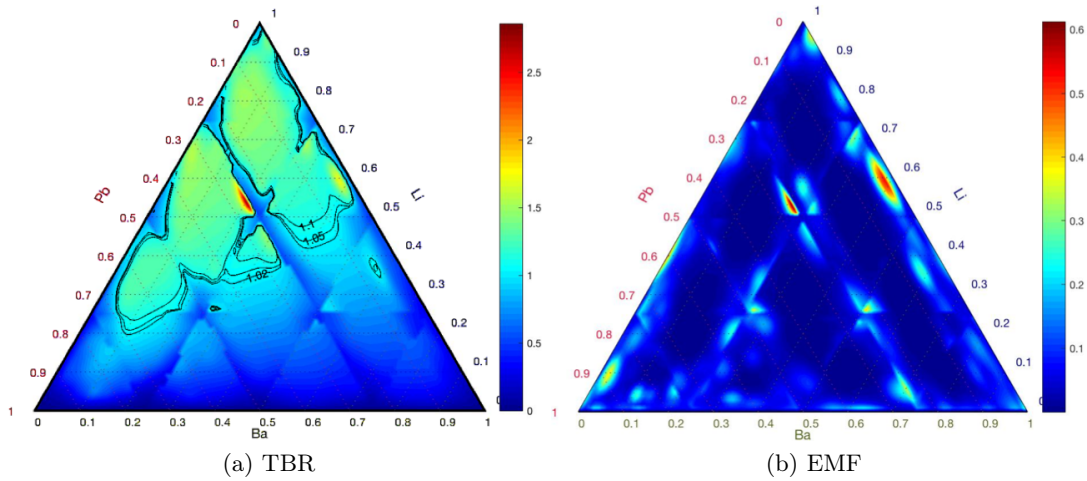


Figure 4.19: Results of the (a) TBR and (b) relative uncertainty for simulations performed with Serpent EPT where the entire ternary was divided into 16 triangles.

Applying GLS to so many points was able to produce much better results. However, the curvature of the TBR lines that is seen at low Ba concentrations displays a rounder shape than the 25 sub-triangle ternary, and begins at higher Li concentrations and further away from the triangle’s periphery. The uncertainties found in this region are some of the highest found in the ternary, and hence, erroneously predict the actual behavior of the alloy. This becomes an issue in the optimization studies reported in the next section and can create inaccuracies in the results. Additionally, the CPU time of running 25 triangles with 1×10^8 particle histories is 400 hours compared to 340 hours for simulations of 16 triangles utilizing the same number of particle histories. The difference of 60 hours is not enough to justify a case that has much more imprecise results, and requires 73% of them to be replaced by implementing GLS. Increasing the number of particle histories for the 16 sub-triangles case to obtain better results would substantially increase the CPU time, which negates the reason behind running a smaller number of triangles in the first place. As a result, and because of time constraints, no further studies and analyses were conducted to compare triangle size. It was decided to continue to utilize 25 triangles per ternary for this alloy, LiPbBa, and any other alloy of interest simulated in the future. Future work can look into combinations of number of particle histories and number of triangle subdivisions to minimize CPU time but also obtain decent results.

4.6 Composition Optimization

4.6.1 Optimization Scheme and First Iteration

Now that results were obtained for the entire LiPbBa ternary through Serpent simulations with EPT and the application of GLS to replace imprecise results, an optimization scheme can be created. As described in Section 4.2.5, the TBR chosen for this study is

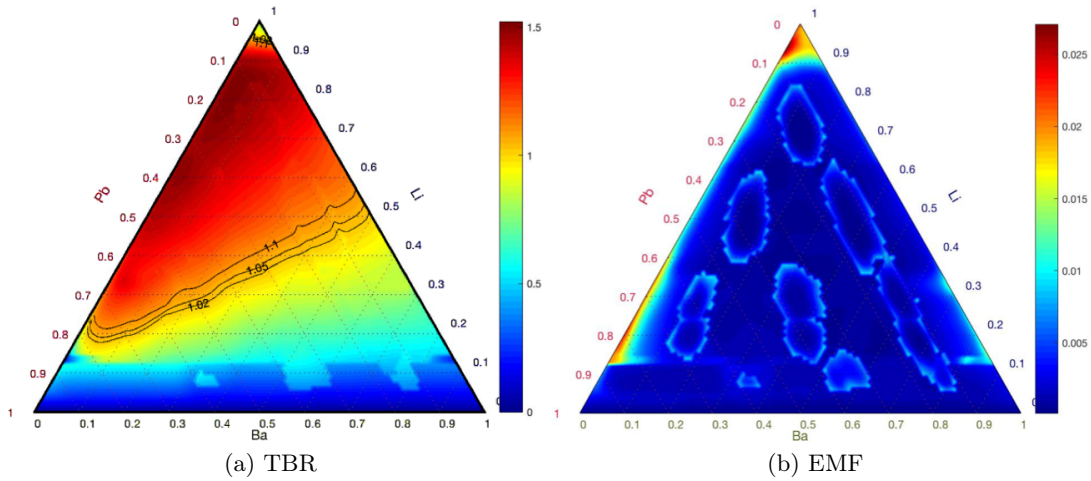


Figure 4.20: Results of the (a) TBR and (b) relative uncertainty after GLS is applied to TBR values with uncertainties greater than 9.5×10^{-3} . The simulations performed with Serpent EPT were done for 16 subdivided triangles of the ternary.

Table 4.8: Optimal composition for each iteration.

Iteration	Li %	Pb %	Ba %	TBR	Uncertainty
1	17.0	76.0	7.0	1.045	3.341×10^{-3}
2	10.5	87.5	2.0	1.050	2.251×10^{-3}
3	9.375	88.625	2.0	1.050	2.473×10^{-4}

1.05, which is in between the upper and lower constrains determined in Chapter 3. The optimal composition should achieve this TBR while minimizing the lithium concentration due to the high chemical reactivity of lithium. Additionally, an EMF constraint ≥ 1.1 was imposed by utilizing the results obtained from the previous Chapter (see Section 4.2.5 for an explanation). A plot of the EMF for LiPbBa obtained with MCNP simulations from Chapter 3 is shown in Fig. 4.21. The plot includes the contour of the imposed 1.1 constraint that is utilized in these optimization studies. Three iterations were performed to find a highly precise alloy composition that met the TBR criteria with the imposed Li and EMF constrains. The first iteration involves the initial simulations of all 25 subdivided triangles with each element's concentration ranging 20%, as previously described. Additionally, it includes the application of GLS to replace uncertain results. Once GLS is applied to the data set, the first optimization search is performed to find the concentration that meets the criteria just described. Instead of finding the composition that has exactly a TBR of 1.05, a range of TBRs was selected between 1.045 and 1.054, since it will equate to 1.05 when rounded. Searching for TBR within a range as opposed to a specific value allowed minimizing the lithium concentration to a greater degree. After scanning through all 5,151 points, the optimal composition found for this iteration is outlined in Table 4.8.

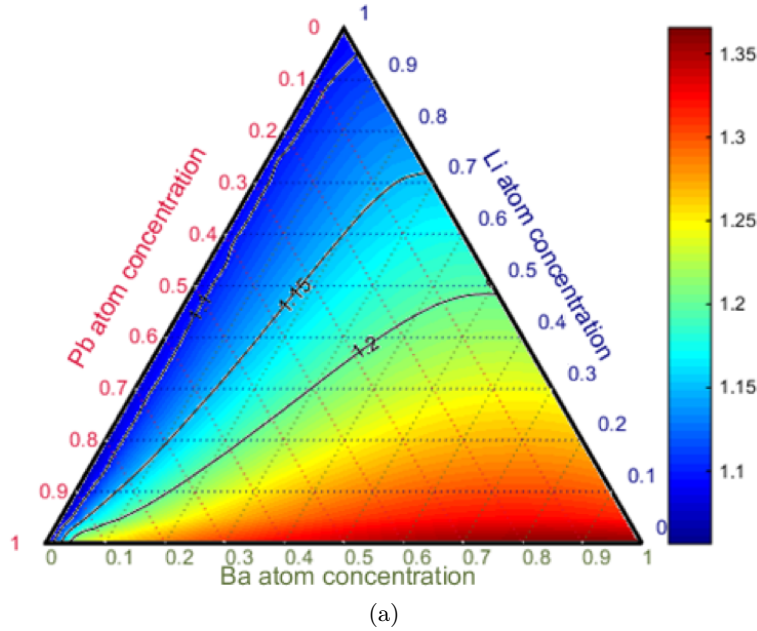


Figure 4.21: Plot of EMF for LiPbBa. Results for this plot were obtained in Chapter 3.

4.6.2 Second Iteration

For the second iteration, a smaller triangle was created with a range of 10% concentration for each element, and that was centered around the optimal concentration obtained from the first iteration. Even though this is a smaller area than the triangles simulated earlier, the number of points in the triangle is kept constant at 231, with an interval of 0.5% concentration between each point. The hope of closing in on a smaller area is to refine the results and reduce their uncertainties. The results from the second iteration, added to the values of the first iteration from Case C in 4.12(f) (GLS applied to points with uncertainties higher than 9.5×10^{-3} in iteration 1), are plotted in Fig. 4.22. The plot is of the actual points before implementing triangulation and interpolation which demonstrates how much more condensed the area of the second iteration is in relation to the first. Although the size of the triangle is smaller in this second-level iteration, the maximum relative perturbation depends on the location of the triangle with respect to the ternary. In the case of Ba, the largest relative perturbation for this simulation is the same as those in the first iteration where the minimum Ba concentration perturbed is 0%. Nevertheless, the absolute perturbation in this iteration is half of the first iteration and thus, it was able to generate more accurate results. Only 25 out of the 231 perturbed points had results with uncertainties greater than 0.05, and were found in the outer periphery of the simulated triangle's area. This can easily be demonstrated in Fig. 4.23(a) where the second iteration's relative uncertainties calculated straight from Serpent EPT are added to the results in Fig. 4.13(e) from the first iteration. The second iteration triangle simulated is outlined in white on the figure.

To determine if CPU time could be reduced, the second iteration was also simulated with 1×10^8 particle histories. The highest uncertainty in this simulation was almost doubled

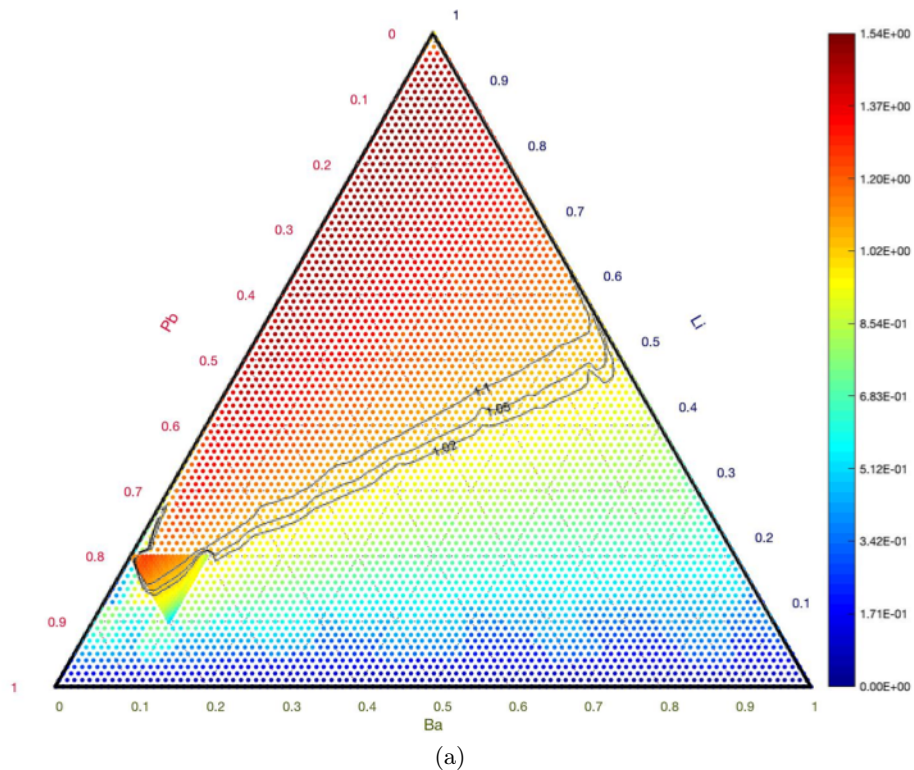


Figure 4.22: Combination of TBR results of second iteration and Case C of first iteration (Table 4.5). The interval between in the second iteration is smaller so points are more condensed.

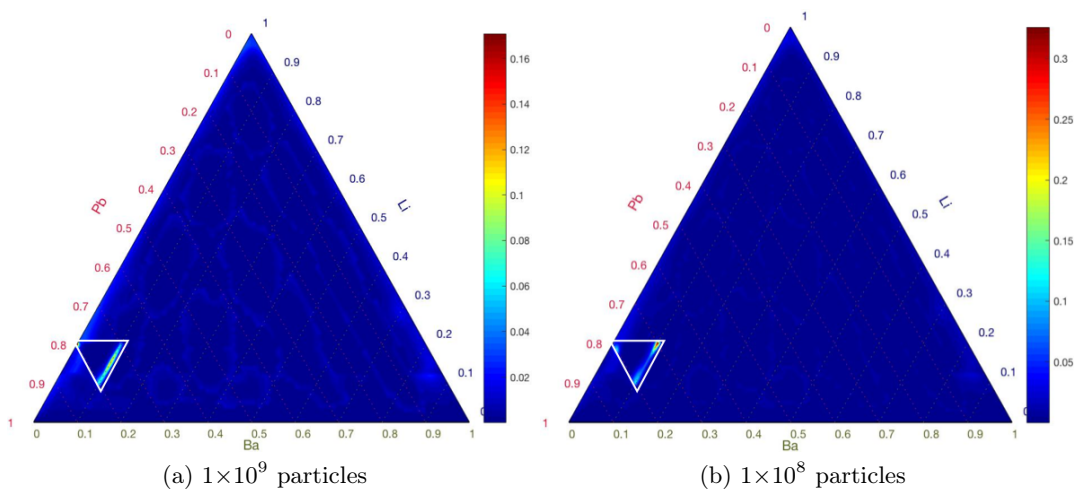


Figure 4.23: Comparison of uncertainty results of second iteration when simulated with a number of particle histories of (a) 1×10^9 and (b) 1×10^8 . The plots show the second iteration, outlined by the white triangle, combined with Case C of the first iteration.

in comparison to the simulation with 1×10^9 particle histories. However, only 4 points contained higher uncertainty values than the results from the simulation with a higher number of particle histories. The total number of points with uncertainties greater than 0.05 increased from 25 to 44, but are only found in the right outer edge of the triangle, seen in Fig. 4.23(b), whose regions are of less interest when performing optimization. The CPU times differ by an order of magnitude from 312 hours to 32 hours. This is a huge difference considering that the lowest uncertainty is less than an order of magnitude different with 5.969×10^{-5} for the case with 1×10^9 particle histories and 2.053×10^{-4} for the case with 1×10^8 particle histories. If GLS is applied to the combined values from the first two iterations, the results end up being very similar, as shown in Fig. 4.24 for the TBRs, and Fig. 4.25 for the uncertainties. Focusing in on the region of interest at around 10-15% Li, and 0-5% Ba, one can see that the curves in both plots follow a linear relationship but become flat on the lower left region, at about 5-6% Ba. If one looks closely, that flat region is found at a lower Li concentration (around 12%) in the plot of 1×10^9 particle histories (Fig. 4.24(a)), compared to the plot of 1×10^8 particle histories. This could make a difference in terms of optimization. However, one is better off performing a third-level iteration to obtain a more accurate composition. Regarding the relative uncertainties of this region in Fig. 4.25, both cases have values below 0.01. One interesting aspect found in both plots of the TBR results compared to Fig. 4.12(e), is that the curves extend beyond 80% Pb, even though this iteration did not simulate points beyond that Pb concentration. The results found beyond 80% Pb where the curves are flat are ambiguous, even if better predicted with GLS. Subsequently, it cannot be easily deciphered if the curves should be continuing the linear relationship that is viewed in the rest of ternary. As a result, an additional simulation was created in this iteration with a triangle of the same size placed right next to the previous one simulated. This is illustrated in Fig. 4.26, where the first triangle discussed is outlined and transparently shaded in red-orange while the new triangle to be simulated is outlined and transparently shaded in black. Based on the comparison of number of particle histories just analyzed, it was decided to utilize 1×10^8 particle histories in this new simulation, to lower the CPU time. This second simulation is referred to as Case 2.2 while the previous is referred to as Case 2.1.

Fig. 4.27(a) shows the results of both cases in this iteration combined with Case C from the first iteration. Fig. 4.27(b) shows all of the results from both iterations combined first, before GLS is applied to points with uncertainties greater than 9.5×10^{-3} . Focusing in on the areas of the second iteration, the main difference between the two plots is the reduction of curvature found at Ba concentration of $\approx 10\%$, located on the upper right vertex of the triangle simulated in Case 2.1. The other major difference is found at very low Ba concentrations, where the TBR curves round upward in Fig. 4.27(a) in points with uncertainties higher than the GLS threshold. Utilizing GLS in those points removes a lot of the higher uncertainties found in Fig. 4.28(a). However, if one looks very closely, tiny points of higher uncertainties, at ≈ 0.15 , are found around this region in Fig. 4.28(b). Even with a smaller area simulated, this location is still quite sensitive because it is near 0% Ba and thus, the collision history between a ternary alloy with a few percent of Ba and a binary alloy with only LiPb, is probably a lot different. Serpent EPT cannot account for this change and as already discussed, calculated values in the periphery of the ternary are very uncertain.

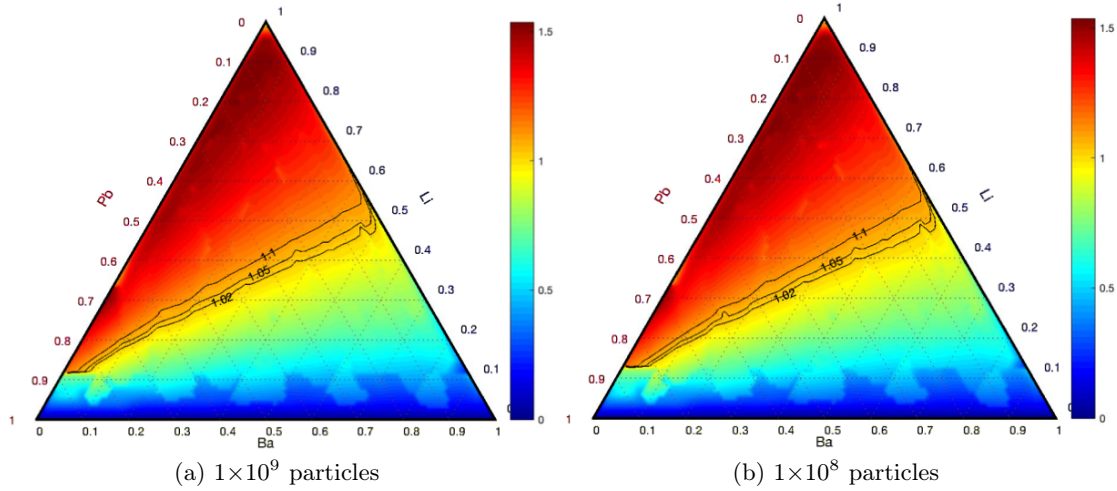


Figure 4.24: Comparison of TBR results of second iteration when simulated with a number of particle histories of (a) 1×10^9 and (b) 1×10^8 . Results from the first two iterations are combined before GLS is applied to points with uncertainties $> 9.5 \times 10^{-3}$.

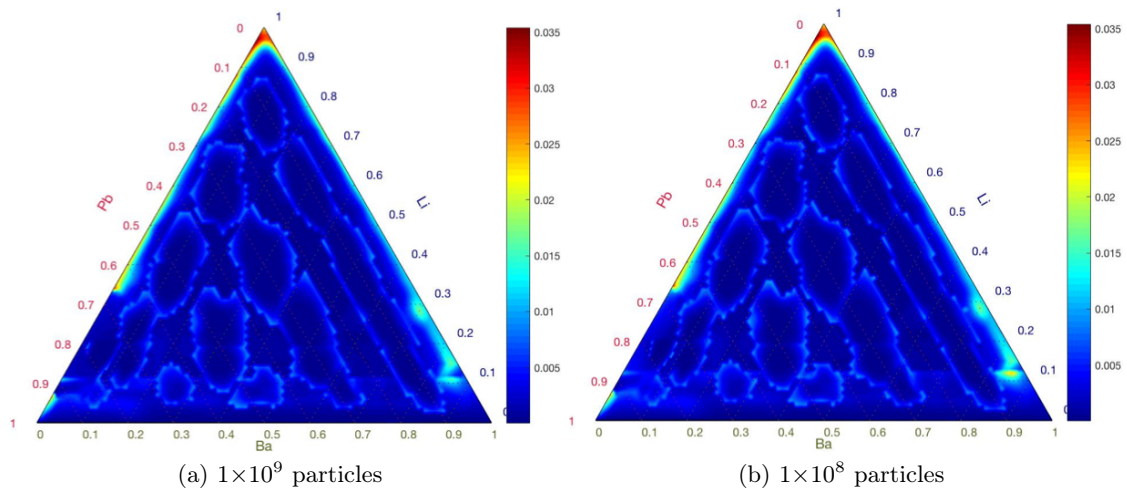


Figure 4.25: Comparison of relative uncertainties of second iteration when simulated with a number of particle histories of (a) 1×10^9 and (b) 1×10^8 . Results from the first two iterations are combined before GLS is applied to points with uncertainties $> 9.5 \times 10^{-3}$.

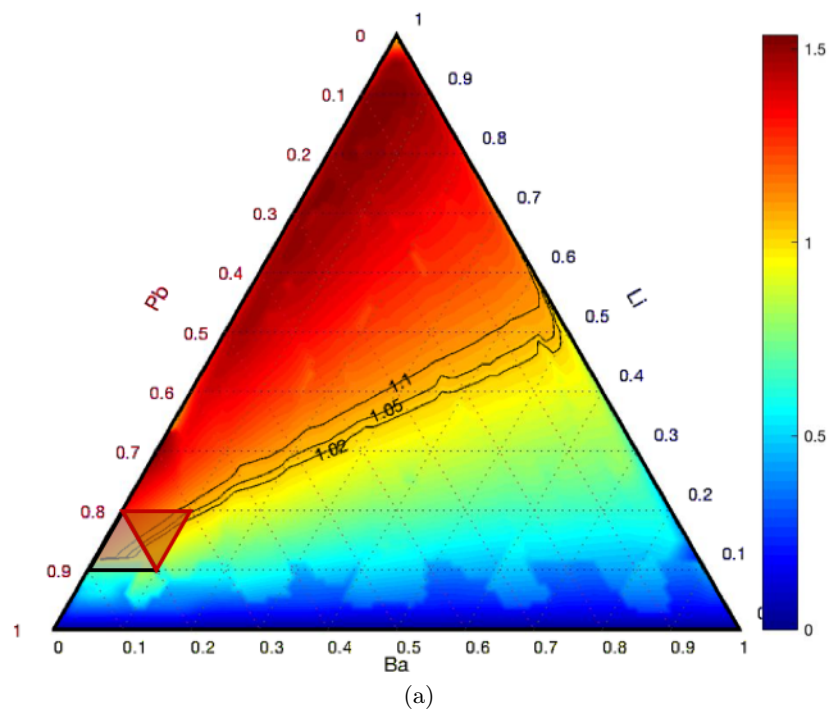


Figure 4.26: Combination of TBR results of the second iteration triangle outlined (and transparently shaded) in dark orange-red and Case C of first iteration (Table 4.5). A new suggested case to be simulated is outlined (and transparently shaded) in black.

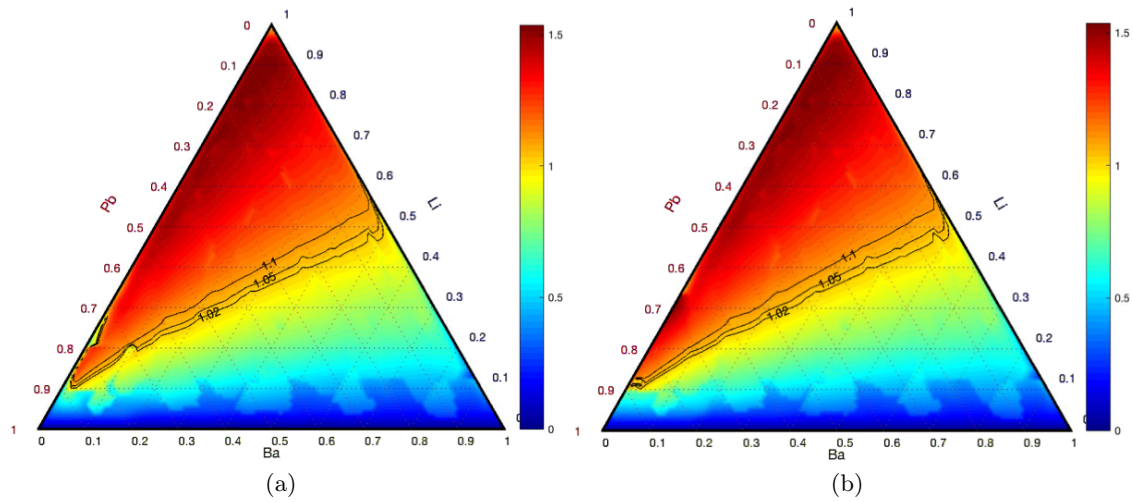


Figure 4.27: Comparison of second iteration TBR with (a) results straight out of Serpent EPT combined with GLS Case C from first iteration and (b) results of first and second iteration first combined, then GLS applied to values with uncertainties $> 9.5 \times 10^{-3}$.

Nevertheless, the difference in this region between the results of the first iteration (Fig. 4.12(e)) and Fig. 4.27(b) are quite drastic, with values of the second simulation depicting much more precise behavior.

After results are obtained, a second optimization search is performed again. The range of TBRs selected for this iteration was narrower, spanning between 1.048 to 1.052. It is most likely only necessary to iterate through the new results from Cases 2.1 and 2.2, as opposed to the entire ternary. Nevertheless, optimization was tested in three different ways: 1. by scanning the points in the triangles of the two cases of the second iteration, 2. by scanning results of the entire ternary after combining the results from both iterations and applying GLS, and 3. by scanning the results of the entire ternary after applying GLS to the results from the first iteration, combining those values with results from the second iteration, and applying GLS a second time. As predicted, the optimized composition found, as given in Table 4.8, was the same in all three cases. This point is located towards the bottom right edge of the triangle in Case 2.2. Compared to the first iteration, the Li concentration was lowered by 6.5%, while the Pb concentration increased by 8.5% so that its (n,xn) reactions can provide additional neutrons to Li for tritium production. The uncertainty for this point obtained from the Serpent EPT calculation was 3.5×10^{-2} , which is higher than other uncertainties calculated, but still low enough (less than 0.05) for the result to be considered in the optimization study. Because of the high uncertainty, it was important to double check the optimization after applying GLS to the results. It is recommended to validate the optimum composition in the second-level iteration with GLS method when the uncertainty is greater than 1×10^{-3} . Finally, the EMF values utilized for the constraint are calculated in intervals of 5% concentration for each element. When it came to applying the constraint at such low Li and Ba concentrations, the interval between EMF values was too large to precisely determine if the constraint was met. Due to the linear relationship found

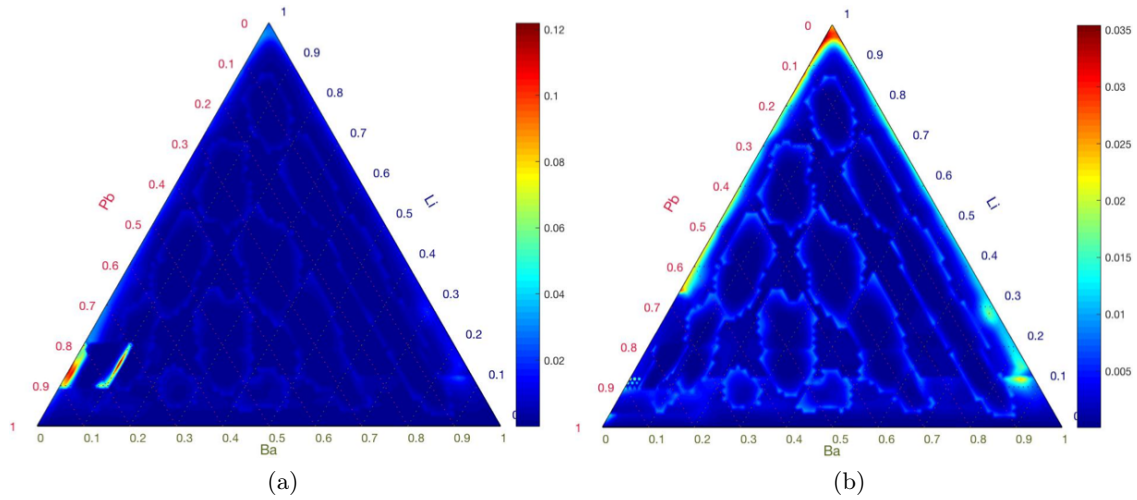


Figure 4.28: Comparison of second iteration TBR relative uncertainties for (a) results straight out of Serpent EPT combined with GLS Case C from first iteration and (b) results of first and second iteration first combined, then GLS applied to values with uncertainties $>9.5 \times 10^{-3}$.

in this region, as seen in Fig. 4.21, values were interpolated in the 1.1 EMF curve around compositions of interest to be able to apply the constraint more accurately.

4.6.3 Third Iteration

The optimized composition went through a last refinement iteration by simulating an even smaller triangular area with compositions ranging 2.5%, as shown by the blue triangular outline in Fig. 4.29. Zooming in this closely creates a very small range of absolute perturbations from the reference point which is placed at the center of the triangle, close to the optimized composition found in the second iteration. Additionally, the small area enables the optimization to be focused around the point of interest and fine tune the optimal composition, while lowering the uncertainties of the results. The number of perturbed points for this simulation was kept at 231, meaning that the interval between each point was 0.125%. Because it was assumed that uncertainties would be low in such a small area, it was decided to use 1×10^8 particle histories instead of 1×10^9 particle histories. One should be able to obtain results with the lower number of particle histories that have similar precision but calculated in much less time. Similarly to the second iteration, this iteration simulated two cases. The first, named Case 3.1, is a triangle that is centered around the optimized point of the previous iteration. The second, Case 3.2, is a triangle placed right next to Case 3.1 that covers a wider range of combined lower Li and Ba concentrations to ensure that all points in the 1.05 TBR curve are accounted for. Case 3.2 was calculated with 231 perturbed points and 1×10^8 particle histories.

The results in both cases simulated had uncertainties lower than 0.05, and thus confirmed that the lower number of particle histories simulated was enough to yield precise

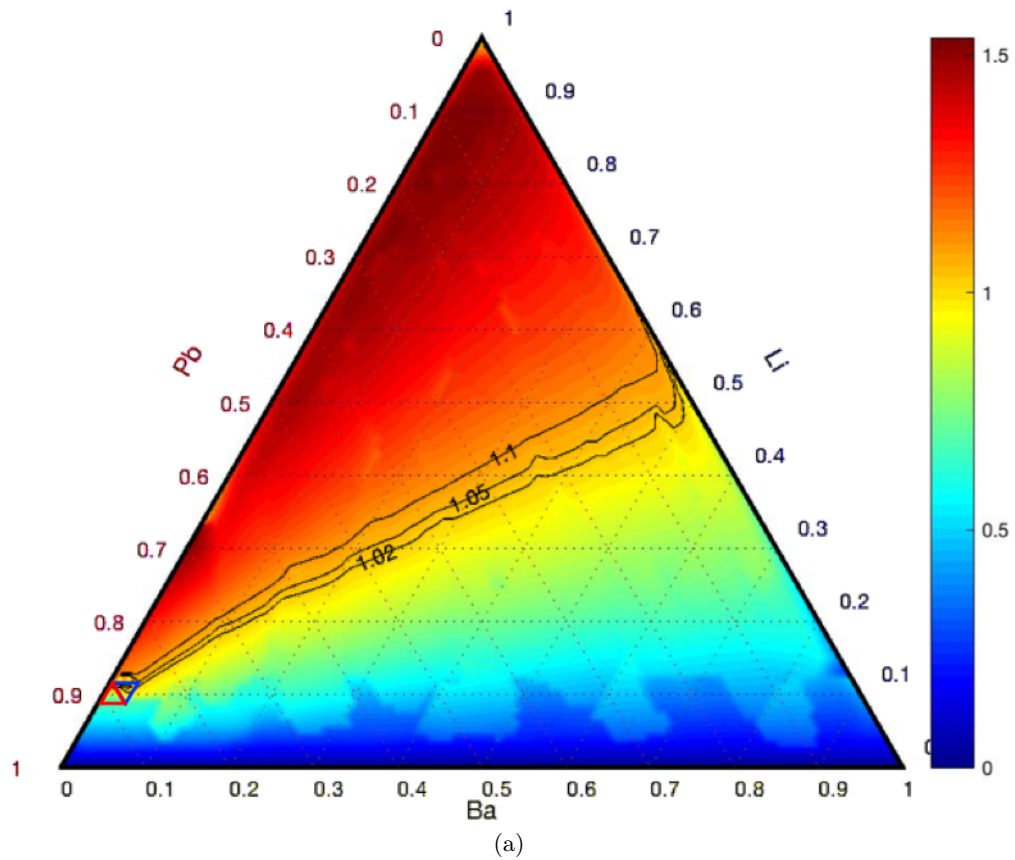


Figure 4.29: Plot of first two iteration results with GLS implementation (Fig. 4.27(b)). Suggested cases for third iteration are outlined. Case 3.1 is outlined in blue while case 3.2 is outlined in red.

results. Out of the 431 results of both simulations combined, only 6 points had uncertainties greater than 9.5×10^{-3} , found in the outer edges of the triangles. Due to the low uncertainties in the results, the optimization search, for a TBR between 1.048 and 1.052, only required the points in the two cases to be scanned, rather than the whole ternary after GLS is implemented. Nevertheless, the optimization was performed for the set of values found in the third iteration only, and also for the values in all iterations combined with GLS applied to results with uncertainties greater than 9.5×10^{-3} . The point optimized in both instances was found inside the area of Case 3.2. The composition and value for the optimized point is given in Table 4.8. The result demonstrates, like the previous iteration, that if the region of interest is close to the periphery of the ternary, a triangle must be simulated in close vicinity to the edge, in order to ensure that an optimized composition is found. If it wasn't for the addition of Case 2.2 in the second iteration and Case 3.2 in this third iteration, the optimized compositions given in Table 4.8 would not have been found. Compared to the second iteration, the optimized composition in this iteration lowers the lithium concentration by 1.125% and increases the Pb concentration by the same amount.

Plots of the combined TBR results from all the three iterations, with GLS implemented to values with uncertainties greater than 9.5×10^{-3} , are displayed in Fig. 4.30(a). The plot of the relative uncertainties corresponding to the TBR results, is shown in Fig. 4.30(b). The smaller uncertainties calculated by the third simulation are clearly visible from surrounding uncertainty values, specifically below the areas simulated. Subsequently, TBR curves at 1.02 and 1.05 mold themselves around the perimeters of the triangles in Case 3.1 and 3.2. In reality, the curves probably continue to decrease in an exponential manner until they reach 100% Pb. This means that there is a possibility that compositions with lower Li and Ba concentrations can achieve TBRs of 1.05. However, the EMF, which also decreases rapidly in this location, does not permit the Li concentrations to decrease without falling below its constraint. Therefore, the composition obtained in this iteration is considered to be optimized such that it achieves a TBR of 1.05, while meeting the EMF constraint, and minimizing Li concentration.

The alloy in this particular case was challenging to optimize due to the higher uncertainties found in perturbations close to the periphery of the ternary. There is a strong relationship between Li and Pb, due to the high (n,xn) reactions in Pb providing neutrons for tritium production in Li. Small perturbations in the Ba concentration will alter the synergistic relationship between Pb and Li, which creates noticeable differences between particle tracks simulated with Monte Carlo. As result, EPT calculated with Serpent cannot properly account for the changes in behavior between collision histories at very low Ba concentrations, resulting in inaccurate TBR values. This is why it was necessary to include three iteration levels with each level zooming in on the region of interest. Because this alloy is most likely one of the more complex cases, it is determined that three iterations are enough for all other alloys. A flowchart of the optimization scheme for a general alloy was created and is presented in Fig. 4.31. The first iteration is presented in the red, the second in orange, and the third in yellow.

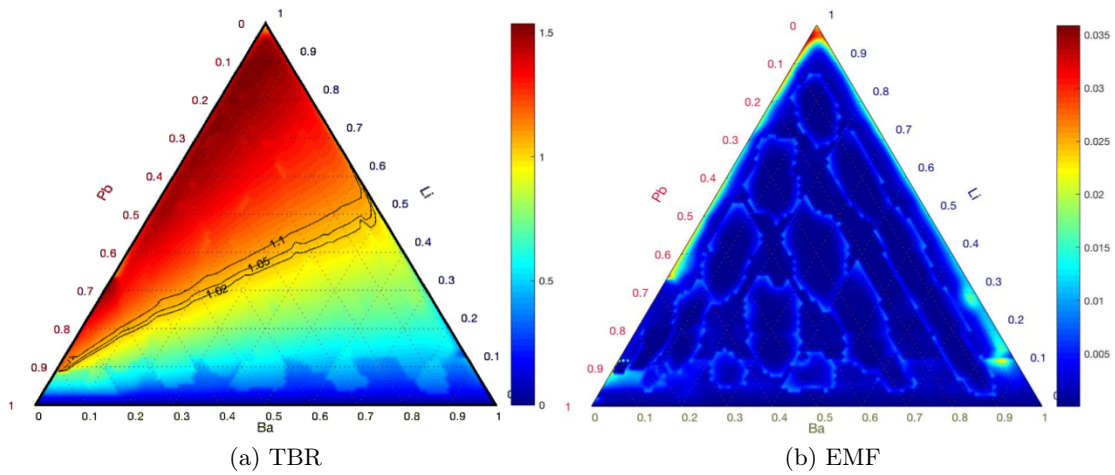


Figure 4.30: Third iteration results for (a) TBR and (b) relative uncertainty. To plot results, the values of all three iterations were combined followed by GLS applied to uncertainties $> 9.5 \times 10^{-3}$.

4.7 EPT and Optimization of LiSnZn

The optimization scheme in Fig. 4.31 was tested on another alloy of interest, LiSnZn. Results are outlined in the following sections.

4.7.1 First Iteration

For the first iteration, the LiSnZn ternary was split into 25 triangles, identically to LiPbBa. Each triangle was simulated with 1×10^8 particle histories. The number of perturbed compositions per triangle was 231. Results of the TBR from the EPT calculations with Serpent are given in Fig. 4.32, and are compared with the MCNP results from Chapter 3. None of the results for this alloy overestimated the TBR which would have created hot spots in the ternary and skewed the range of the TBR scale. The largest deviations are found along 20% concentrations for Zn and Sn, respectively. The perimeters of various subdivided triangles run along these compositions, which is where the largest perturbations simulated are located. As already discussed, the larger the perturbation in EPT, the greater the uncertainty in the results. This can also be seen in the plot of the TBR relative uncertainties found in Fig. 4.33, where the perimeters of every triangle, specially at 20% Sn and Zn concentrations, contain higher uncertainties than their surrounding areas. The highest uncertainties are located at low Li concentrations and high Zn concentrations. This is most likely due to the EPT method not being able to correctly account for the change in particle collision behavior where the Zn concentration is close to 100%. For the same reason, the efficacy of EPT is abated in left and right edges of the ternary where either Sn or Zn concentrations are close to 0%. The effect is observed by the curvature of the TBR lines plotted around these areas, where in reality, as demonstrated in the MCNP results, these lines should extend from edge to edge of the ternary without any curvature. In any case,

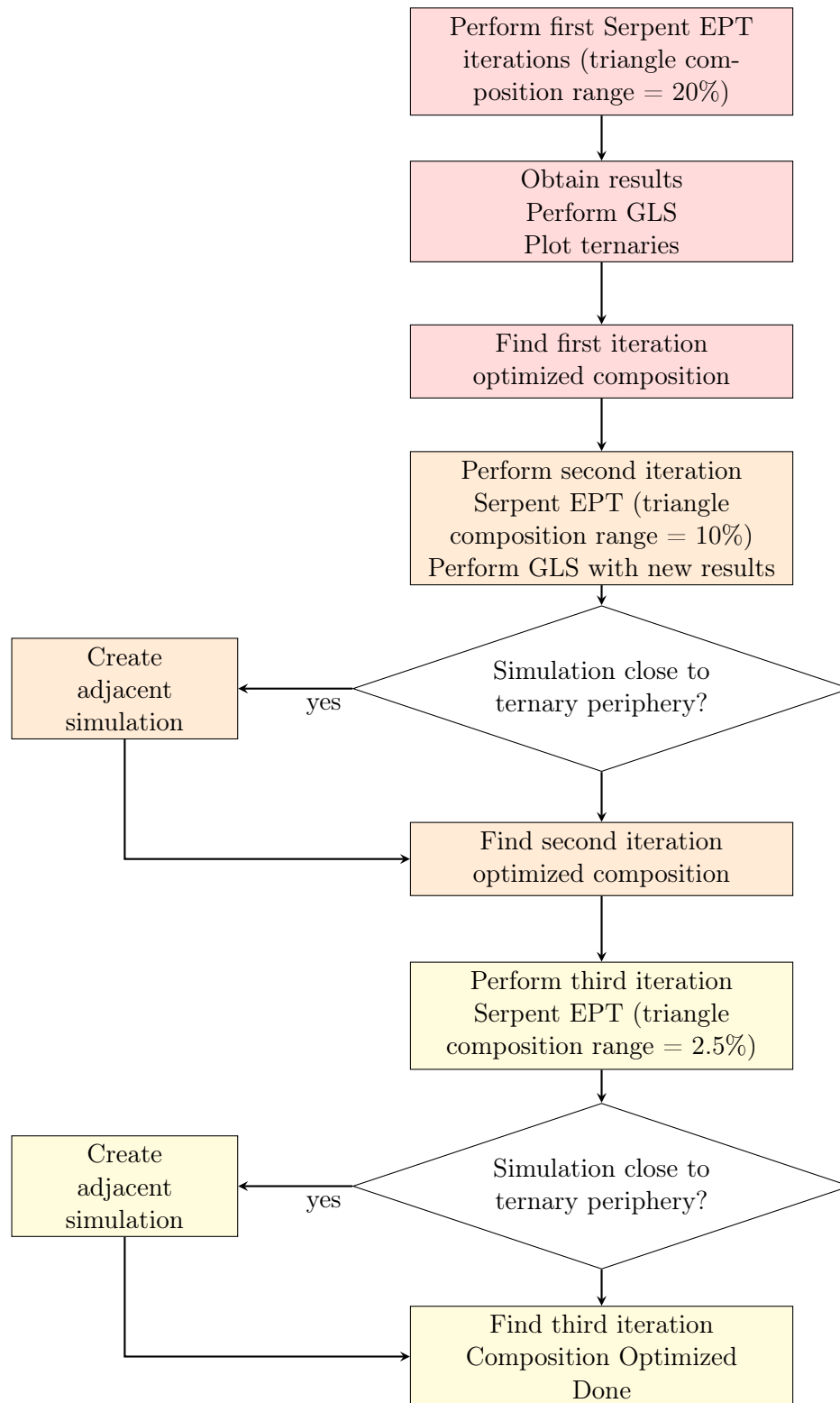


Figure 4.31: Flowchart of Optimization with Serpent EPT for a single ternary alloy.

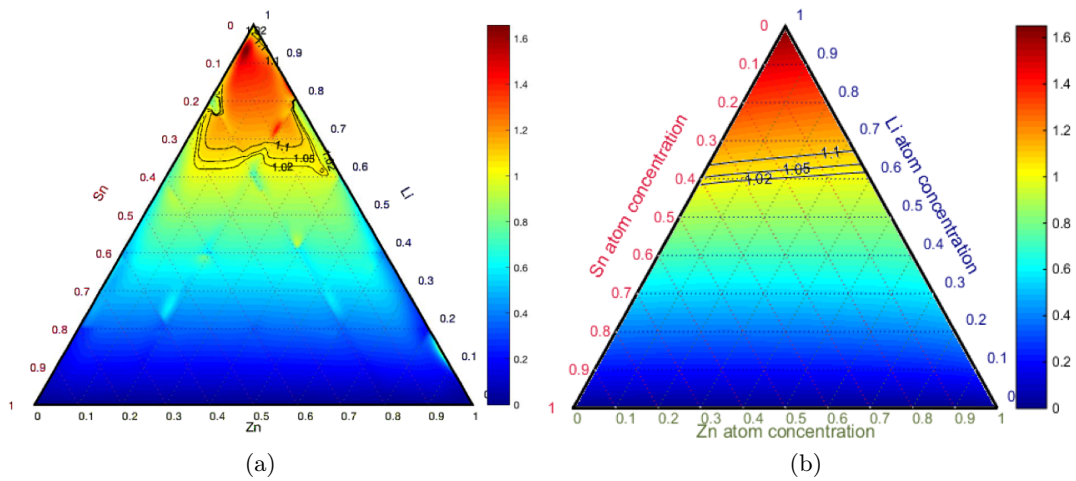


Figure 4.32: Comparison of LiSnZn TBR results with (a) Serpent using EPT and (b) MCNP

most of the uncertainties calculated for this alloy are less than 0.1, lower than those found in LiPbBa. The uncertainty limit with the application of GLS to about half of the points in the results was 5.5×10^{-3} , also lower than the limit for LiPbBa. The TBR and relative uncertainty ternaries after utilizing GLS for results greater than that specific uncertainty limit are plotted in Fig 4.34. The implementation of GLS was able to remove a lot of the deviations found in the original results, and straighten the curvature of the TBR at low Sn concentrations. Uncertainties were significantly reduced, with most falling below 0.0075. Even the largest uncertainties, found in the upper left region of the plot, are less than 0.05. This region of high uncertainty is similar to what was seen with LiPbBa GLS results, and is very sensitive due to the high Li concentrations that control the TBR. Moreover, the formula in the coded script that selects the area of points to be utilized in the GLS calculation is not able to generate a large enough area at regions close to the periphery of the ternary. As a result, the number of points used to create a linear regression are not enough to accurately predict the correct TBRs, specially in this sensitive region. This will be the case for all alloys calculated. Nevertheless, most alloys of interest will not be optimized in this location and thus, the deviation is not of major concern.

The optimization scheme previously described was utilized for LiSnZn. The same criteria was implemented requiring a TBR between 1.045 and 1.055, an EMF constraint (from results in Chapter 3) of 1.1, and a minimized Li concentration. TBR results after implementing GLS were scanned and the composition that met all the criteria is given in Table 4.9. This composition is located where the 1.05 TBR line in Fig. 4.34 begins to curve upwards.

It is interesting to point out that the CPU times of simulations performed for this alloy were less than the CPU times of LiPbBa simulations. A comparison of times between triangles 17-21 simulated in each alloy is given in Table 4.10. For triangle 17, the CPU time in the LiSnZn case is almost half of the CPU time in the LiPbBa case. The difference between times decreases as triangle number increases. It is predicted that the reason for

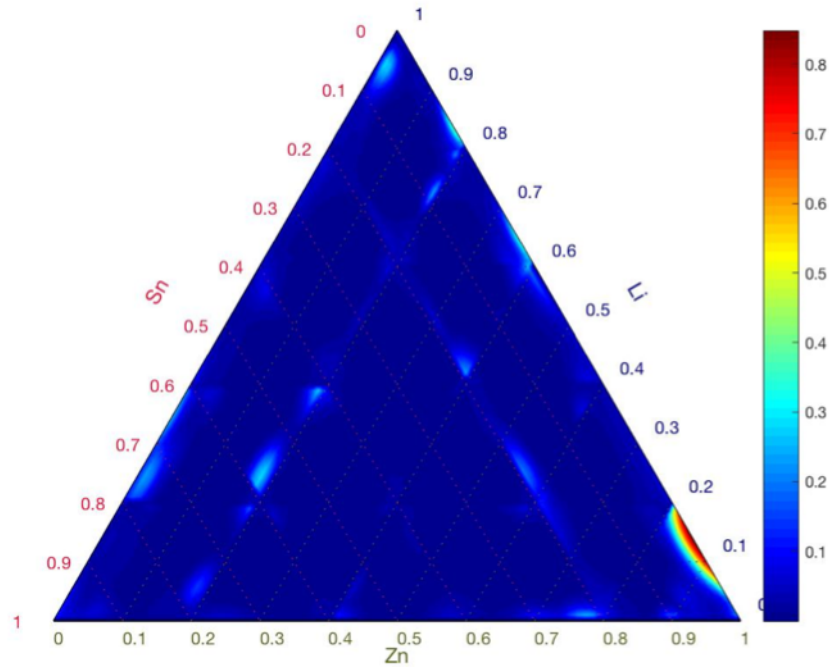


Figure 4.33: Uncertainties for TBR results of LiSnZn simulated with Serpent EPT.

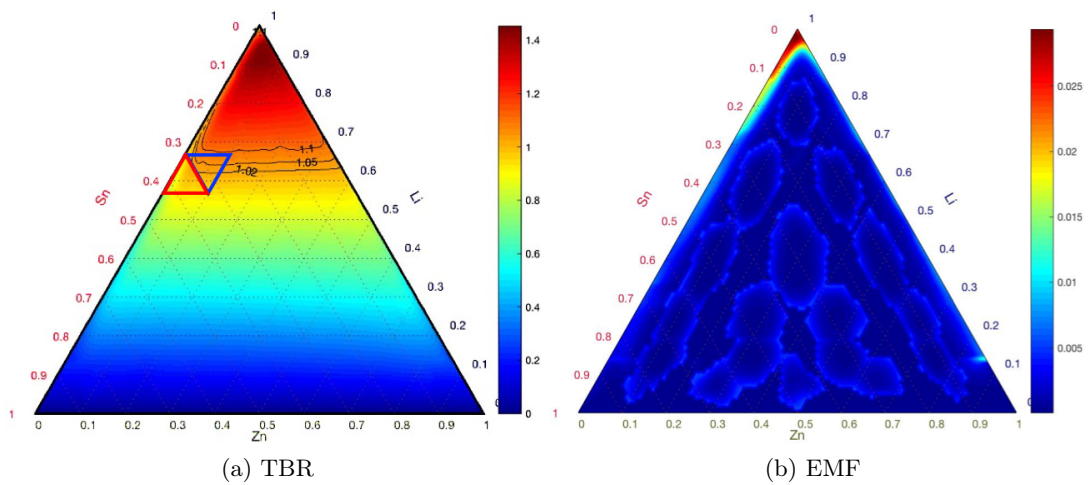


Figure 4.34: First iteration results for (a) TBR and (b) relative uncertainty, after GLS was applied to uncertainties are $> 5.5 \times 10^{-3}$. The areas that will be simulated in the second iteration are shown in the triangles outlined in red and blue in (a).

Table 4.9: Optimal composition for each iteration. The uncertainties for the first two iterations are calculated after GLS is implemented.

Iteration	Li %	Sn %	Zn %	TBR	Uncertainty
1	64.0	30.0	6.0	1.045	2.4×10^{-3}
2	63.5	35.5	1.0	1.048	2.3×10^{-4}
3	63.5	35.5	1.0	1.048	1.077×10^{-4}

Table 4.10: Comparison of CPU time taken to run simulations in LiPbBa versus LiSnZn

Triangle #	CPU Time (hours)	
	LiPbBa	LiSnZn
17	13.8	7.9
18	10.6	6.9
19	11.3	7.5
20	8.5	6.5
21	9.6	7.2

longer times in the LiPbBa case is due to the significant effect Pb has on tritium reactions in Li, which might create more complex collision histories throughout the simulation as opposed to the LiSnZn case, whose results mostly depend on Li (n,t) interactions. This can be studied more closely in future work as more alloys are simulated.

4.7.2 Second and Third Iterations

The triangles that were simulated in this iteration are shown in Fig. 4.36(a). The triangle centered around the optimized point is outlined in red. Because the optimized point for the first iteration is close to the periphery where Zn concentrations are low, a second simulation was executed for the triangle outlined in blue. All of the new results were scanned to find the optimized composition. This was verified by performing a search of the TBRs in the entire ternary after results from the first two simulations were combined, and GLS was applied to values with uncertainties greater than 5.5×10^{-3} . The optimized composition, whose TBR was between 1.048 and 1.052, after scanning the entire ternary, is outlined in Table 4.9. Interestingly, this composition is slightly different from the one obtained by only examining the new results. The Sn concentration is the same, but the Li concentration decreased to 63%, and the Zn concentration increased to 1.5%. The uncertainty of the optimized value gathered from the second iteration cases was on the higher end at approximately 3×10^{-2} . Consequently, it was determined that the composition optimized after applying GLS was more accurate. The results of the first two iterations with GLS implementation are given Fig. 4.35. Compared to first simulation, the Li concentration only decreased by 0.5%. However, Sn went up by 5.5% and Zn went down by 5%, meaning that higher amounts of Sn can aid in minimizing Li concentrations.

As outlined in the optimized scheme of Fig. 4.31, two simulations were created

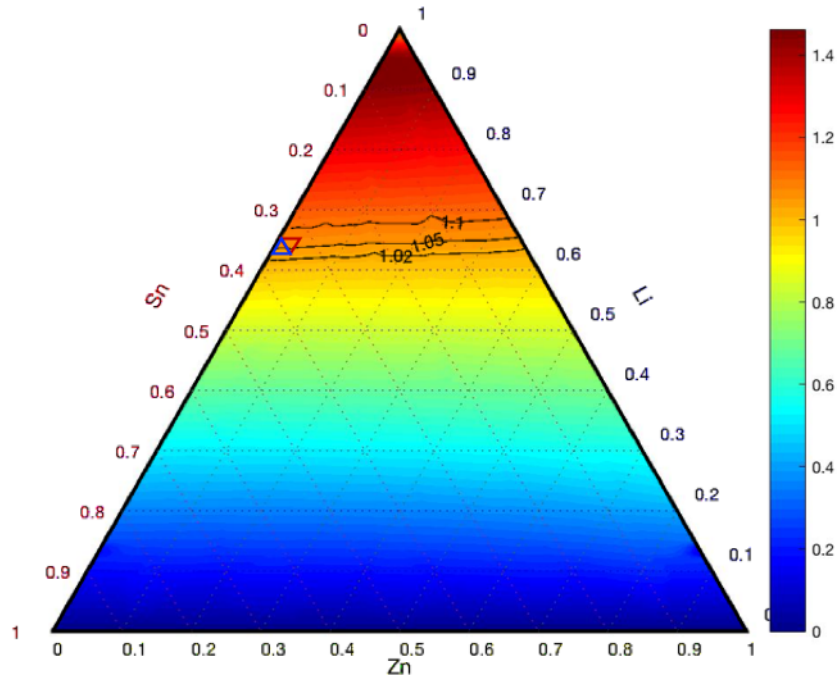


Figure 4.35: TBR results of first and second iterations combined and GLS utilized for points containing uncertainties greater than 5.5×10^{-3} . Area of triangles simulated in third iteration are outlined by the triangles in red and blue.

for the third iteration. The simulation outlined in red in Fig. 4.35 is centered around the optimized point from the previous iteration. The second simulation, outlined in blue, is located next to edge of the ternary. The search for the optimized composition was only performed on TBRs of these two simulations since the majority of the uncertainties were in the order of 10^{-4} . The optimized composition is given in Table 4.9. This composition is exactly the same as the composition optimized in the previous iteration. The results after applying GLS in the second iteration were enough to correctly estimate the optimized composition. Nevertheless, the low uncertainty obtained for the EPT Serpent calculation of the third iteration result reinforced the GLS estimate of the second. This alloy was much easier to optimize than the previous due to reduced complexity in the behavior of the TBR, which mostly depends in Li, more so than the other two alloy components. To summarize the LiSnZn alloy case, the TBR and uncertainty are plotted in Fig. 4.36 for all three iterations combined, and with GLS applied the results (uncertainties greater than 5.5×10^{-3}).

4.8 Conclusions

This chapter introduced a novel Monte Carlo methodology that calculates the response of composition perturbations in a fixed source problem. The perturbation approach in Serpent is similar to the techniques utilized for variance reduction. Probability density functions of parameters of interest are biased and sampled as accepted or rejected events to

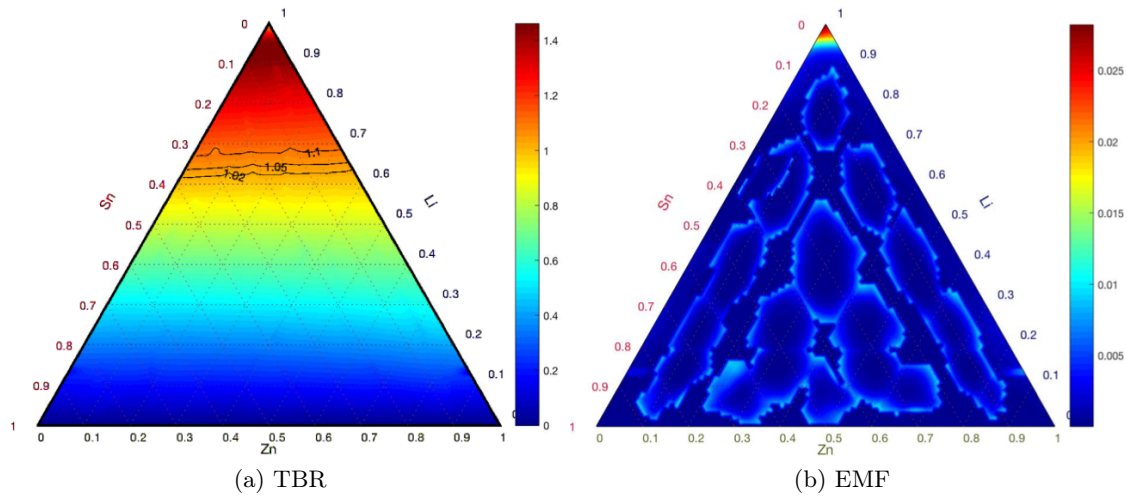


Figure 4.36: First iteration results for (a) TBR and (b) relative uncertainty. Results of all three iterations are combined and GLS was applied to TBR values whose uncertainties $> 5.5 \times 10^{-3}$.

account for the bias on the probability. A collision history is created from these events to compute perturbed fluxes which are then utilized to calculate the response. In the case of this work, the methodology implemented for fixed source problems, known as exact perturbation theory, can calculate the tritium breeding ratio response, caused by a perturbation in the composition of the lithium-based ternary alloy. The one setback of this method is its inability to correctly depict the behavior of the particle history found in large relative perturbations. This leads to high uncertainty in the results. Consequently, the number of simulations performed for a ternary, so that uncertainties are reasonable, was determined to be 25. The 25 triangles simulated within the ternary ranged by 20% concentration of each element in the alloy. The number of points simulated per triangle was 231. Results of Serpent calculations with EPT predicted the correct basic behavior of the alloy. Nevertheless, regions of high uncertainties created deviations throughout the ternary, and this issue was accounted for in two ways. The first method eliminated the highest uncertainties found in every triangle simulated within the ternary. This reduced the maximum uncertainty, but not by enough (less than 0.05), and created large gaps between points such that the true behavior of the ternary could not be correctly characterized. The other method involved implementing a generalized least squares method to TBR values with high uncertainties by removing the point from the results, and creating a linear regression that was the same size of triangles simulated around that point. By doing this, the uncertain point can be replaced with a new more accurate TBR value and corresponding uncertainty. This method proved to be fairly successful by reducing uncertainties to 0.03 or less and removing areas of high deviation. The only regions where this method was unsuccessful were in those located close to the periphery of the ternary resulting from smaller areas calculated which contained a lower number of points that were applied to the GLS method. In addition, these areas had higher relative perturbations, and hence, resulted in high uncertainties when calculated in Serpent

with EPT. For optimization purposes additional simulations must be performed, specially if simulated around regions close to the periphery of the ternary. The use of GLS can remove imprecise regions so efficaciously, that the number of particle histories simulated in Serpent could be reduced by an order of magnitude. Simulations with 1×10^8 particle histories, compared to 1×10^9 particle histories, reduced CPU time by an order of magnitude, while demonstrating similar results.

The optimization scheme included three levels of iterations. The first iteration is previously described, simulating the 25 triangles within the ternary and applying GLS. Afterwards, a search is carried out to find a composition with a TBR between 1.045-1.055 that meets the imposed EMF constraint of 1.1, while minimizing the Li concentration. The second iteration simulates two smaller triangles with compositions ranging 10% as opposed to 20%. One of the triangles simulated surrounds the optimized composition of the first iteration, and the second triangle is located right next to it. The second simulation for this iteration is only performed if the area of interest is found near the periphery where the TBR results are imprecise. Optimization for the second simulation is similar to the first, except for reducing the range of possible TBRs to be 1.048-1.052. Once the composition is optimized a second time, a last iteration is executed. This iteration is the same as the second but reduces the triangle size simulated even further, with each element's concentration ranging by 2.5%. Results for the LiPbBa alloy found the optimized composition after the third iteration to be 9.375% for Li, 88.625% for Pb, and 2.0% for Ba. The alloy in this particular case was challenging to optimize due to the higher uncertainties of perturbations found close to the periphery of the ternary. There is a strong relationship between tritium reactions in Li and multiplication reactions Pb. Small perturbations in the Ba concentration will alter the synergistic relationship between Pb and Li, which creates noticeable differences between particle tracks simulated with Monte Carlo. As result, EPT calculated with Serpent cannot properly account for the changes in behavior between collision histories at very low Ba concentrations, resulting in inaccurate TBR values. This is why it was necessary to include three iteration levels, with each level zooming in on the region of interest.

The same optimization scheme was validated with a new alloy, LiSnZn. This alloy was much easier to optimize, and found the optimized composition only after the second iteration, at 63.5% Li, 35.5% Sn, and 1.0% Zn. Nevertheless, including a third iteration is ideal due to higher uncertainties calculated in the second iteration. In this particular case, the uncertainty of the second iteration was on the order of magnitude of 10^{-2} . The TBR for this alloy primarily depends on Li densities and not on the densities of the other two elements. As a result, the complexity of the collision history within Monte Carlo simulations was lower compared to the LiPbBa case. In conclusion, the EPT methodology simulated with Serpent has proven to be successful, specially when combined with statistical methods like GLS to reduce uncertainties. Utilizing this methodology, any alloy can be simulated with much more detail than previous MCNP simulations whose interval between points was 5%, and each simulation required to be performed individually. Additionally, with EPT, any alloy can be optimized to find the desired composition under selected criteria.

Chapter 5

SMORES code implementation

The study of fusion reactor blankets discussed previously involved a transport simulation utilizing Monte Carlo techniques for a given composition of a ternary alloy to calculate the tritium breeding ratio (TBR) [40] and Energy Multiplication Factor (EMF) [103]. Once this was done, a new composition was created and the process was repeated. Although this method was successful, it proved to be inefficient in terms of computational time and manpower. As a result, a new approach that utilized perturbation theory was created with the Serpent Monte Carlo code [91] in Chapter 4, but still required multiple runs per alloy. Alternatively, deterministic methods could be used to solve specific types of optimization problems by incorporating first order generalized perturbation theory. In the case of fixed source problems, the code SWAN [63], a 1D deterministic code, was written in the 1970s to solve optimization problems for fusion reactors. One of the types of optimization problems the code could solve exactly fits the scenario of the lithium-based ternary alloy fusion blanket: find an alloy composition that maximizes the energy multiplication factor (a design goal) while limiting the tritium breeding ratio to an exact value, or an inequality of a value. Unfortunately, the code SWAN was written around three decades ago and does not compile on most modern systems. The code went through a number iterations and the latest, called SMORES [55], is found in version 6.1 of the SCALE package [22] with its implementation altered to optimize problems for fission systems. The goal is to change SMORES to solve problems for fusion reactors similarly to what was done in the SWAN code. This would allow only one calculation per alloy that would solve for an optimal composition that maximizes EMF while restraining the TBR. Additionally, each blanket layer can be optimized individually in the same calculation. The following sections will describe the methodology of SWAN, its similarities and differences to SMORES, and the implementation of fusion systems into the current version of SMORES.

5.1 SWAN Methodology

This section will focus on the methodology originally found in SWAN since it pertains to fusion systems with a fixed source. The complete methodology of SMORES can be found in [55]. Some of the differences between SMORES and SWAN will be pointed out to address what needs to be altered in the current version of the code.

The theory behind SWAN was described in Section 2.3 which involves either maximizing or minimizing a linear functional with the option to include an additional functional that acts as a restrain. In this particular case we are trying to maximize the energy multiplication factor of the fusion blanket while restraining the TBR, both defined in Sections 2.4 and 3.2.1. Any system that will be optimized must be clearly defined by the user. This includes the radius of each zone in the system, the materials that define the zone, candidate materials that may be added to the zone during optimization, and the zones that need to be optimized. Candidate materials are materials which are not originally part of a zone that is of interest for optimization, but are added through the optimization process. Zones can be as small as an interval, or as large as the entire system. This type of information is necessary to be able to correctly model the physics of the problem and know exactly what needs to be optimized.

The optimization procedure of SWAN is iterative and follows a series of steps. Before optimization begins, the code calculates the forward and adjoint flux with a 1D deterministic transport code, and a given reference density distribution. It then passes the information to the optimization module called SWIF, which utilizes those fluxes to solve the effectiveness functions, derived in Eq. 2.33, for all the materials in the system whose compositions are being perturbed. Third, it checks the optimality conditions such as the one defined in Eq. 2.42. If the condition is not met, the density of each variable composition is changed with given parameters defined by the user. The new densities are also calculated in such a way that all the constrains (based on density limits) and restrains (based on some type of linear or weight functional) defined are not violated. Once a new density distribution is calculated, the code loops back and begins the process all over again and iterates until the optimal condition is finally met. A flowchart that outlines these steps is displayed in Fig. 5.1. The colored sections of the flowchart will be described in more detail, particularly the effectiveness functions, calculation of new compositions, and convergence criteria.

5.1.1 Effectiveness Functions

The effectiveness functions govern the optimization module. The functions predict the change of some type of response of interest due to a unit change in the density of material i in zone z . This is defined in Eq. 2.33, but will be reiterated here:

$$E_i = \delta F_i / \delta N_i = \left(\left\langle \phi, \frac{\delta \Sigma_{b,i}}{\delta N_i} \right\rangle - \left\langle \phi^\dagger, \frac{\delta \mathbf{L}}{\delta N_i} \phi \right\rangle \right) \quad (5.1)$$

To implement the effectiveness function into SWAN, the second term of the right hand side of the equation is divided into two separate components, AC_i and BC_i , and the first term on the right hand side is noted as CC_i

$$E_i(z) = -A_i(z) + B_i(z) + C_i(z) \quad (5.2)$$

where,

$$AC_i(z) = \int_r d\mathbf{r} \int dE \int d\hat{\Omega} \left[\phi^\dagger(\mathbf{r}, E, \hat{\Omega}) \Sigma_{t,i}(\mathbf{r}, E) \phi(\mathbf{r}, E, \hat{\Omega}) \right] \quad (5.3)$$

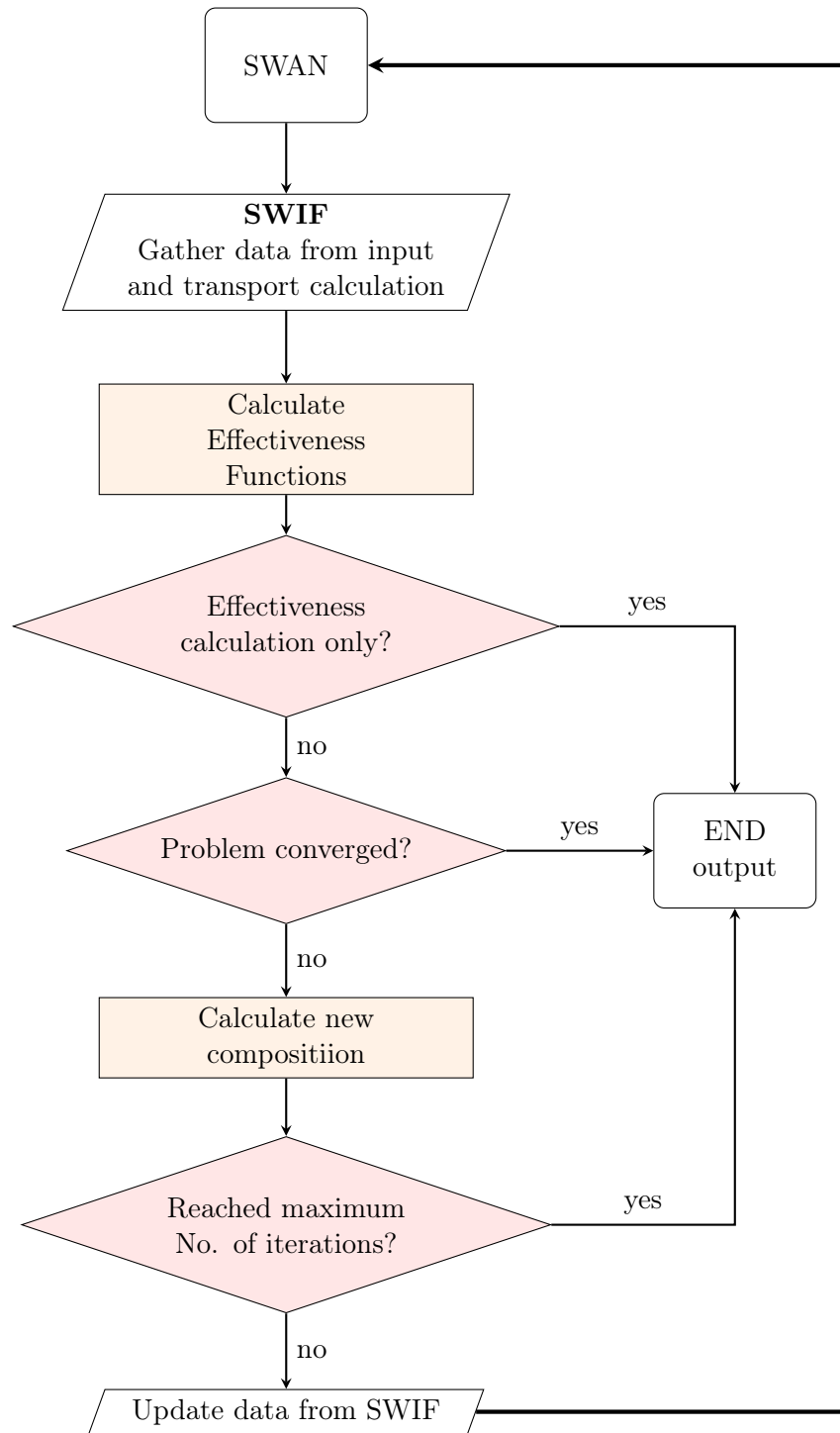


Figure 5.1: Flowchart of Optimization Module (adpated from SWAN manual [22])

$$\text{BC}_i(z) = \int_z d\mathbf{r} \int dE \int d\hat{\Omega} \int dE' \int d\Omega' \left[\phi^\dagger(\mathbf{r}, E, \hat{\Omega}) \Sigma_{s,i}(E \rightarrow E', \hat{\Omega} \rightarrow \hat{\Omega}') \phi(\mathbf{r}, E, \hat{\Omega}) \right] \quad (5.4)$$

$$\text{CC}_i(z) = \int_z d\mathbf{r} \int dE [\Sigma_{b,i}(\mathbf{r}, E) \phi(r, E, \Omega)] \quad (5.5)$$

The AC, BC, CC equations are solved for 1D systems. Additionally, the changes in $\delta\Sigma_{b,i}$ and $\delta\mathbf{L}$ in Eq. 5.1 are only caused by the perturbation of δN_i [16]. Therefore, $\delta\Sigma_{b,i} = \delta N_i \Sigma_{b,i}$ and $\delta\mathbf{L} = \delta N_i \mathbf{L}$, which means that the unperturbed cross sections can be used in Eq. 5.3-5.5. SWAN employs discrete ordinates to computationally solve the above equations. It expands the angular flux and adjoint distributions into spherical harmonics, to account for the angular variable. Moreover, the scattering cross section is treated by expanding it into Legendre Polynomials. Derivations for the discretized equations can be found in Ref.greenspan1973swan.

5.1.2 Convergence Criteria

After the calculation of the effectiveness functions, if the user indicates to perform optimization, the next step in Fig. 5.1 is to check the convergence criteria. The convergence criteria are based on the optimum conditions described in Eq. 2.42 which keeps the functional of the response at the extremum with a small change in density. This usually implies that the substitution effectiveness function (SEF), $Q_{m,i}$, for a variable material should be close to zero (or a constant). The way SWAN implements this condition is by comparing the maximum SEF of a material in all the zones to the minimum SEF of the same material in all zones as such:

$$\frac{|Q_{m,i}^{\max} - Q_{m,i}^{\min}|}{|Q_{m,i}^{\max}|} = \text{CONV}_{m,i} \leq \epsilon_i \quad i = 1, 2, \dots, I-1 \quad (5.6)$$

where $Q_{m,i}^{\max}$ and $Q_{m,i}^{\min}$ are the maximum and minimum SEF functions of all the zones for material i , respectively. The ratio on the left hand side of the equation is referred to $\text{CONV}_{m,i}$. The number for ϵ for convergence is chosen by the user. If the optimization problem includes a functional for the restrain, it might be more accurate to calculate the convergence based on the ratio of $Q_{m,i}$ and $Q_{r,i}$. This is calculated as:

$$\frac{\text{CONV}_{m,i}}{\text{CONV}_{r,i}} \leq \epsilon_i \quad (5.7)$$

where $\text{CONV}_{r,i}$ is the result of Eq. 5.6 for the SEF of the functional that is restrained. The user has a the option to choose which convergence criteria, if any, to use in the problem.

5.1.3 Calculation of Composition Variation

If the convergence criteria test from the previous section fails, a new density distribution must be calculated to sample in the next iteration. The calculation of the density

variation was originated by Abagyan [6] and adopted for the SWAN. There are three steps to calculating a density variation: 1. Determine A_i^n and B_i^n coefficients 2. Calculate variation and new density distribution, and 3. Readjust density if it is above or below its limits. The coefficients A_i^n and B_i^n help determine the new density distribution. The density change of material i in iteration n is calculated as:

$$\delta N_i^n = N_i^n(z) - N_i^{n-1}(z) = A_i^n Q_{m,i}^{n-1}(z) + B_i^n Q_{r,i}^{n-1}(z) \quad (5.8)$$

where $Q_{m,i}$ and $Q_{r,i}$ are the substitution effectiveness functions from Eq. 2.39. Plugging the above equation into Eq. 2.41, the change of the functional for the restrain, gives:

$$\delta F_r^n = \sum_{i=1}^{I-1} \int dr [A_i^n Q_{r,i}^{n-1}(z) Q_{m,i}^{n-1}(z) + B_i^n Q_{r,i}^{n-1}(z) Q_{r,i}^{n-1}(z)] \quad (5.9)$$

To solve for B_i^n the restrain functional is set to 0. Thus:

$$B_i^n = -A_i^n \left[\frac{\int dr Q_{r,i}^{n-1}(z) Q_{m,i}^{n-1}(z)}{\int dr (Q_{r,i}^{n-1}(z))^2} \right] \quad (5.10)$$

Eq. 5.8 can now be re-written by replacing B_i^n with the above equation:

$$\delta N_i^n = A_i^n \left[Q_{m,i}^{n-1}(z) - \frac{\int dr Q_{r,i}^{n-1}(z) Q_{m,i}^{n-1}(z)}{\int dr (Q_{r,i}^{n-1}(z))^2} Q_{r,i}^{n-1}(z) \right] \quad (5.11)$$

This equation can be used to solve for A_i^n as follows:

$$A_i^n = a_i^n / \left[Q_{m,i}^{n-1}(z) - \frac{\int dr Q_{r,i}^{n-1}(z) Q_{m,i}^{n-1}(z)}{\int dr (Q_{r,i}^{n-1}(z))^2} Q_{r,i}^{n-1}(z) \right] \quad (5.12)$$

where z_m is the zone in which max density change occurs. The value of a_i^n is indicative of δN_i^n , and represents the maximum density change for the specified material and iteration. This value is specified by the user in the input. The A_i^n coefficient can also be calculated by specifying either the maximum absolute or relative change in the function to be optimized, δF_m . The derivation for this coefficient can be found in the SWAN manual [63]. Once the coefficients are calculated, the new densities can be obtained. If any density is above or below the limits imposed by the user, the best option is to adjust the value of the A_i^n coefficients to restore the density of the zone which exceeded the limit back to its limit. This option is the most useful if a restrain is imposed on the system since it allows the restraint to be preserved. Otherwise, the user can also choose to bring back an exceeded density to its limit without changing the A_i^n coefficients. This option is better if there is no restraint.

5.1.4 Differences between SWAN and SMORES

The SMORES code is basically an implementation of SWAN, but constructed for critical systems. It follows the same type of flow: obtain adjoint and forward solutions to the transport equation and pass that information to the optimization module, SWIF, which then follows the flowchart in Fig. 5.1. Nevertheless, there are a few differences in both versions.

One of the major recent advances of the code was the processing of cross sections to use in both the transport code and optimization. SWAN employed pre-processed multigroup cross sections and thus did not properly account for resonance self-shielding. As a result, the answer obtained through the optimization was not the true optimum. When the code was adapted into SCALE, this discrepancy was resolved and now cross sections are processed at the beginning of every iteration, which account for resonance self-shielding. This might make more of a difference in fission systems but can still be applicable to fixed source systems as well. Aside from the cross sections, the main difference in the two codes is the type of system the equations are being solved for. SMORES runs the 1D transport code, XSDRNPM [57] in critical mode solving the homogenous transport equation as opposed to solving the inhomogenous transport equation for fixed source problems. The same thing occurs for the effectiveness functions in the optimization module which includes the transport operator. Luckily, XSDRNPM already has the option to solve problems for fixed sources. However, SWIF was completely changed to only solve problems for critical systems and does not have any traces of the original equations utilized in SWAN. The goal would be to incorporate the missing pieces of SWAN for fixed source problems back into SMORES. This way, the code could optimize the composition of each of the blanket layers by just running one simulation per alloy. The process for this type of implementation has been started, and would be continued in future work. This process is outlined in the following section.

5.2 Implementation of Fixed Sourced Problems into SMORES

No robust code is available at the moment that performs optimization for fixed source problems such as shields or fusion systems. Two options are available to solve this issue: 1. Write a brand new code, and 2. Use an existing code and alter it. The framework of SMORES is the same as SWAN's, and thus it makes sense to use this already existing version and alter certain subroutines of the code to adapt it to solve problems of different nature. There are two main components that need alterations. The first is for XSDRNPM to solve the inhomogenous transport equation with a fixed source rather than solving the equation for a fission system. Similarly, the second change is related to effectiveness functions; because these functions include the transport operator, they must be altered for a problem with a fixed source. Work for the first component has already begun and will be outlined in the following section. Time constraints did not allow this work to be completed. Hence, a second section is added to detail the steps one can take to proceed altering the code, specifically components of the optimization module.

5.2.1 Current implementation

This section will describe what has already been done specifically to allow SMORES to optimize fixed source problems. Before the optimization module is called, SMORES must solve the forward and adjoint transport equations for their respective fluxes with XSDRNPM. Currently, SMORES internally generates an XSDRNPM input that is used to run a k calculation. Additionally, the user input does not include any fixed source specification. Therefore, the first goal in modifying SMORES was to change the input to

include a fixed source specification and definition. It was also necessary to change specific subroutines of the code so that they read in the new information, and correctly add it to the internal XSDRNPM input.

Fig. 5.2 shows a standard SMORES sample input. Although SMORES does not support problems without fissionable materials, the figure models an inertial confinement fusion reactor for consistency with this work. The input file in the figure models a 1D model of the Inertial Fusion Energy (IFE) reactor, shown in Fig. 5.3. The model is based on the 3D Monte Carlo model described in Chapter 3. It contains a tiny volumetric fusion source in the center of a void chamber surrounded by xenon to absorb outgoing X-rays and ions from the source. Following the central chamber are three blanket layers divided structurally by HT9 (composed of iron (85.9%), chromium (12.1%), and the rest is carbon, silicon niobium, molybdenum, and tungsten with density of 8 g/cm³), and ending with a graphite shield (Table 5.1).

The first section in the input on Fig. 5.2 identifies all the mixtures in the fusion reactor. Each of the blanket layers has its own defined mixture, made up of pure lithium. The other two candidate materials, lead and barium, are specified in the input with very low concentrations so that they are identified, but added after the first iteration of optimization to maximize the energy multiplication factor. This section of the input does not need to be altered in any way. Next in the input is the geometry optimization section that describes the system's geometry. This section, outlined by the red rectangle in Fig. 5.2, defines every zone in the system. For each zone, the corresponding material, its outer radius, the number of mesh intervals within the zone, if its material is varied during the optimization, and the maximum volume fractions of the material (which can include the fractions of all individual compositions of the material), are listed. Here, new information was added that allows the user to indicate which type of source, if any, is found for each zone listed. This indication is based on the XSDRNPM input, which requires the user to designate the mesh interval where either a volumetric or surface source is found. Therefore, if only one mesh interval contains a source, the zone defined in the SMORES input should only include that mesh. In the case of an adjoint source, multiple consecutive meshes might contain sources that can be combined and specified by one zone. The source specification was implemented as two entries following the input of the radius for each zone. The updated geometry section with the new information is shown in Fig. 5.4. A forward source must be indicated after the radius for each zone as either: 0 = no source, 1 = volumetric, or 2 = surface. The same is done in the next entry for the adjoint source. The two entries for all the zones are outlined by a purple rectangle in Fig. 5.4. In the case of the ternary alloy blanket, the forward source is found in the first mesh of the geometry¹ as a very tiny volumetric source that is seen as point by the blanket volume. Therefore, it is defined as a zone with one mesh and a forward source of 1 (the forward source specification on the input in Fig. 5.4 is highlighted in blue). On the other hand, the adjoint sources are defined based on the functionals that are optimized and restrained. Only one entry is needed if a restraint is included in the problem because the restraint adjoint source must be in the same zones as the optimum adjoint source. The units for these sources depend on the parameter of interest. The lines of the input that define the blanket regions with their adjoint sources are highlighted in yellow

¹Only half the sphere is defined in XSDRNPM due to symmetry.

Table 5.1: Composition and dimensions of the blanket components.

Layer #	Material	Thickness (cm)
1	HT9	0.5
2	Breeder/Coolant	1
3	HT9	0.5
4	Breeder/Coolant	100
5	HT9	0.5
6	Breeder/Coolant	50
7	HT9	0.5
8	Graphite	100

in Fig. 5.4.

It was necessary to alter the SMORE's source code to account for the changes in the input. The subroutines that were altered are outlined below:

- `datin.f90`: This subroutine, called from the SMORES driver, was not altered for the purposes of the source specification, but is important to note it here and describe its function. The purpose of this subroutine is to read information from the SMORES input that is needed by XSDRNPM, such as the information in the geometry section. It then calls the subroutine `xsdRNA.f90` to use all the information gathered and create the XSDRNPM input file.
- `rdgeom.f90`: This subroutine, called by `datin.f90`, reads in the input geometry section and stores the entries of the input into variables. Lines of code were added to read in the source specifications and stored them in two variables: `iqpm` and `aqpm` for the forward and adjoint sources, respectively. Counters were also created to keep track of the total number of forward and adjoint sources. The variables and the counters are globally stored in `All_Parameters_M.f90`. Lastly, statements were included to output information about the source along with the other geometry specifications.
- `Recreate_Input.f90`: When `datin.f90` calls `rdgeom.f90`, it does not read the geometry data from the original input but rather from input written to a scratch file by the subroutine `Recreate_Input.f90`. Thus, `Recreate_Input.f90` was modified to include the source specification parameters to be read and copied to the scratch input file.
- `rdzon.f90`: This subroutine is called by `datin.f90` after `rdgeom.f90`. It transfers the geometry information and stores it in a scratch file. Additional lines allow the source specification data in the scratch file to be stored with other information.
- `zondat.f90`: This subroutine reads the geometry data stored in the scratch by `rdzon.f90` and puts it in arrays. New arrays (`iqpm` for forward and `aqpm` for adjoint) were created to store the source specification data. Furthermore, the subroutine scans the geometry input and checks for any user errors. Additional lines of code were included to output an error if the source specification is anything other than 0, 1, or 2.

```

=smares   parm=centrm
sample problem 3
v7-200n47g
read comp
XENON      1  1.0000  900 end
XENON      2  1.0000  900 end
CARBON     3  2.12e-3  900 end
SILICON    3  1.61e-3  900 end
CHROMIUM   3  0.1347  900 end
MANGANESE  3  0.0106  900 end
IRON       3  0.8751  900 end
NIOBIUM    3  9.37e-6  900 end
MOLYBDENUM 3  7.81e-6  900 end
TUNGSTEN  3  2.87e-3  900 end
LITHIUM    4  1.0000  900 end
LEAD       4  1.0e-15  900 end
BARIUM     4  1.0e-15  900 end
LITHIUM    5  1.0000  900 end
LEAD       5  1.0e-15  900 end
BARIUM     5  1.0e-15  900 end
LITHIUM    6  1.0000  900 end
LEAD       6  1.0e-15  900 end
BARIUM     6  1.0e-15  900 end
GRAPHITE   7  1.0000  900 end
end comp
read geometry
spherical      end
  1  0.1  1  vary=no  end
  2 1300.4 10 vary=no  end
  3 1300.5 1  vary=no  end
  4 1301.5 1  vary=yes end
  3 1302  1  vary=no  end
  5 1402  10 vary=yes end
  3 1402.5 1  vary=no  end
  6 1452.5 5  vary=yes end
  3 1453.0 1  vary=no  end
  7 1553.0 5  vary=no  end
end geometry
read parm
isn=32
end parm
read optim
evref  maxitrs=1 prtflag=2  converg=1.-8  end
wghtz= 11.46  1.85  2.3  1.1054  11.344  0.90  0.923  0.9982  end
matnam= puo2 beryllium concrete d2o lead paraffin poly-h2o h2o end
end optim
end

```

mixture, radius, #
 meshes,
 varied zone = yes/no

Figure 5.2: Standard SMORES input modeled with an IFE reactor.

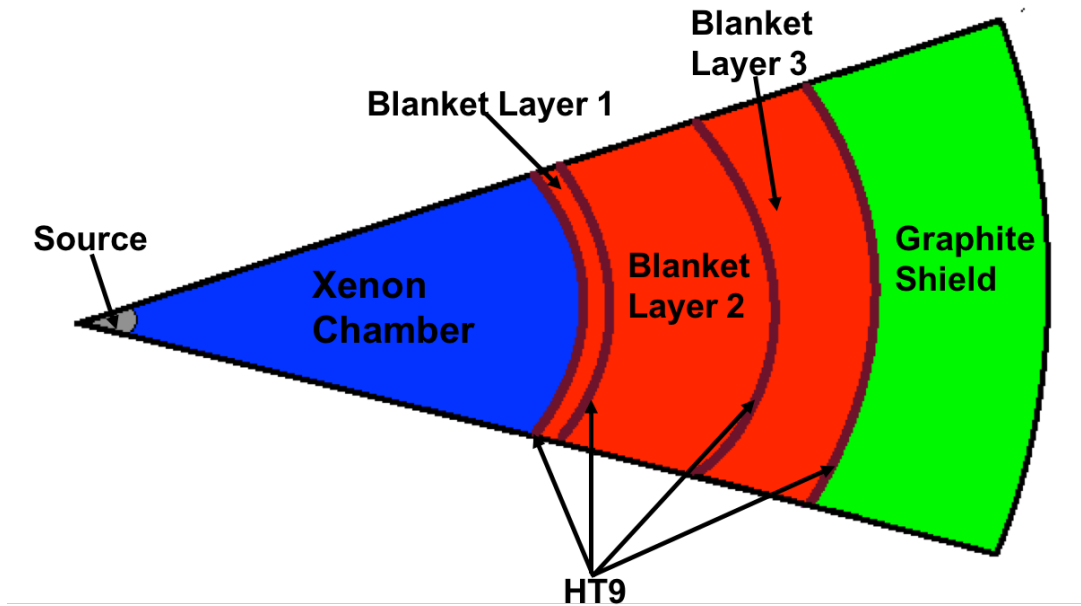


Figure 5.3: 1-dimensional chamber model of IFE reactor.

spherical			end			
1	0.1	1	1	0	vary=no	end
2	1300.4	10	0	0	vary=no	end
3	1300.5	1	0	0	vary=no	end
4	1301.5	1	0	1	vary=yes	end
3	1302	1	0	0	vary=no	end
5	1402	10	0	1	vary=yes	end
3	1402.5	1	0	0	vary=no	end
6	1452.5	5	0	1	vary=yes	end
3	1453.0	1	0	0	vary=no	end
7	1553.0	5	0	0	vary=no	end

end geometry

forward src , adjoint src
 0 = no source
 1 = volumetric
 2 = surface

Figure 5.4: Geometry section of SMORES input with added source specification. The zone with a volumetric forward source is highlighted in blue. The zones with a volumetric adjoint source are highlighted in yellow.

- `xsdRNA.f90`: This subroutine reads in all the data passed by `datin.f90` and utilizes it to create a formatted XSDRNPM forward or adjoint input file that is executed through the SCALE driver. Changes in the call of `xdrna.f90` from `datin.f90` now include the two arrays, `iqpm` and `aqpm`, that store zone dependent source information for the forward and adjoint sources, respectively. Once the information is passed, `xdrna.f90` translates the source specified by zone to corresponding sources designated by mesh interval. It then uses this information to create data block 3, line 30\$, of the XSDRNPM input.

Now that the source locations are specified, the next step involved the addition of source definitions in the input for every forward and adjoint source specified in the geometry section. To do this, new sections were created after the geometry section that allows the user to define each source individually. The forward section begins and ends with the keywords **read fwsrc**, and **end fwsrc**. This section is shown in Fig. 5.5 with the keywords highlighted in yellow. In between these two keywords the source is specified in neutrons/second for each energy group. The number of energy groups is based on the chosen cross-sectional library; in the case described here, it is the ENDF/B-VII library for shielding with 200 neutron energy groups and 47 gamma groups [76]. The format for this section is in free form rather than FIDO, which means that every energy group must be specified individually, even when the source is zero in consecutive energies. As a result, the total number of entries in Fig. 5.5 is 247.

Similarly to the forward source, the adjoint source section starts with the keyword **read adjsrc**, followed by all the sources related to the functional that is maximized/minimized, and ends with the keyword **end adjsrc**. In the case of the fusion blanket, sixteen adjoint sources must be defined, one for each mesh specified in Fig. 5.4. The number of entries in each adjoint source is based on the number of energy groups in selected library, and is the same as the forward source. In this case, each adjoint source will have 247 entries. Each entry will depend on the functional considered. For example, if the adjoint source is related to the EMF, it would be defined as the group-wise average heating numbers divided by flux in MeV-barns. Instead, if the functional to optimize was the TBR, the adjoint source would be the group-wise $\Sigma_{n,t}$ cross section in barns. An example of this section with two EMF adjoint sources defined for the first and last blanket meshes is shown in Fig. 5.6. The first source is highlighted in yellow, while the last source is highlighted in green. In between both sources in the figure, a line is used as a place holder for the fourteen additional sources that should be included in between but was chosen not to in the figure to take up less space.

Currently, only adjoint sources for the functional to be optimized can be defined. If the user includes a functional with a restraint, a third adjoint case of XSDRNPM must be ran internally through SMORES. Therefore, an additional section with adjoint source definitions for the restraint must be added to the user input. The section would start with the keyword **read adjres**. The number of adjoint sources for the restraint parameter is the same as for the optimal parameter. Everything that will be described in the next section regarding to the subroutines that read the adjoint source and store its values, equally applies to the restraint adjoint source. Thus, it can be assumed that the information described for the subroutines in the following bullets regarding the optimal parameter adjoint sources can apply exactly to adjoint sources for the restraint. These are outlined below:


```

read adjsrc
0.00000E+00 0.00000E+00 0.00000E+00 0.00000E+00 0.00000E+00 0.00000E+00 0.00000E+00 0.00000E+00
2.30136E-01 2.26627E-01 2.25546E-01 2.23725E-01 2.20230E-01 2.17926E-01 2.17095E-01
2.23865E-01 2.31611E-01 2.39808E-01 2.43258E-01 2.42365E-01 2.39485E-01 2.32976E-01
2.26610E-01 2.20228E-01 2.14638E-01 2.08679E-01 2.04002E-01 2.00649E-01 1.96013E-01
1.89882E-01 1.80697E-01 1.70284E-01 1.64399E-01 1.58223E-01 1.50498E-01 1.37140E-01
1.16073E-01 9.62731E-02 8.50970E-02 7.88099E-02 7.29533E-02 6.73711E-02 6.21886E-02
5.71978E-02 5.29710E-02 5.09594E-02 5.02278E-02 4.91260E-02 4.69909E-02 4.35990E-02
4.03322E-02 3.80120E-02 3.58839E-02 3.40414E-02 3.24104E-02 3.09604E-02 2.96089E-02
2.81491E-02 2.64968E-02 2.47235E-02 2.29750E-02 2.09884E-02 1.94751E-02 1.75676E-02
1.59880E-02 1.50706E-02 1.42129E-02 1.35455E-02 1.29721E-02 1.25177E-02 1.21576E-02
1.18809E-02 1.16841E-02 1.15431E-02 1.14332E-02 1.13814E-02 1.13762E-02 1.14002E-02
1.16521E-02 1.22764E-02 1.30474E-02 1.38706E-02 1.57994E-02 2.09406E-02 2.53227E-02
2.63201E-02 2.72429E-02 2.95768E-02 3.54396E-02 4.58273E-02 4.30474E-02 3.97166E-02
3.44138E-02 2.98095E-02 2.57033E-02 2.24158E-02 2.02901E-02 1.85459E-02 1.73711E-02
1.64797E-02 1.61126E-02 1.58557E-02 1.57830E-02 1.37339E-02 1.13844E-02 1.10410E-02
1.08394E-02 1.09461E-02 1.07362E-02 1.07526E-02 1.13044E-02 1.16434E-02 1.17955E-02
1.24403E-02 1.28897E-02 1.36339E-02 1.49893E-02 1.60585E-02 1.71332E-02 1.70608E-02
1.87342E-02 1.69096E-02 1.85899E-02 1.83764E-02 1.94530E-02 2.05973E-02 2.30863E-02
2.68373E-02 2.88298E-02 2.82751E-02 3.35677E-02 3.57289E-02 4.36588E-02 5.58878E-02
4.42929E-02 4.48454E-02 5.04698E-02 9.23454E-02 7.26081E-02 5.68888E-02 5.48528E-02
5.16919E-02 6.60911E-02 5.32424E-02 8.75906E-02 7.63595E-02 1.02058E-01 1.52473E-01
1.35952E-01 1.29487E-01 1.25739E-01 1.46455E-01 2.89661E-01 1.86910E-01 2.10641E-01
1.93587E-01 4.10246E-01 2.38442E-01 2.65627E-01 3.02234E-01 3.37940E-01 3.84367E-01
4.36013E-01 5.00008E-01 5.70048E-01 6.39804E-01 7.27751E-01 8.27200E-01 9.34941E-01
1.06012E+00 1.16328E+00 1.23990E+00 1.28875E+00 1.31501E+00 1.33994E+00 1.38510E+00
1.46623E+00 1.58310E+00 1.67098E+00 1.79049E+00 1.88463E+00 2.00148E+00 2.17247E+00
2.30482E+00 2.46829E+00 2.70658E+00 2.98835E+00 3.31789E+00 3.63952E+00 4.01754E+00
4.64308E+00 5.50603E+00 6.44409E+00 7.30392E+00 8.67014E+00 1.07004E+01 1.31524E+01
1.60156E+01 0.00000E+00 0.00000E+00 0.00000E+00
1.39655E+00 1.03102E+00 8.19935E-01 6.23798E-01 5.25481E-01 4.80917E-01
4.37549E-01 3.96427E-01 3.55507E-01 3.16952E-01 2.80218E-01 2.44824E-01
2.10437E-01 1.81260E-01 1.59063E-01 1.44362E-01 1.34761E-01 1.25726E-01
1.17196E-01 1.07249E-01 1.00926E-01 9.56036E-02 9.19979E-02 8.90257E-02
8.60671E-02 7.97265E-02 7.25394E-02 6.63045E-02 6.16276E-02 5.75167E-02
5.33372E-02 4.99446E-02 4.87414E-02 4.81160E-02 4.78436E-02 5.03928E-02
5.75079E-02 7.07115E-02 1.00009E-01 1.61370E-01 2.86891E-01 3.98079E-01
4.62621E-01 6.04304E-01 8.59739E-01 6.43688E-01 2.73682E+00
14 OTHER SOURCES INCLUDED HERE (not shown) ....
0.00000E+00 0.00000E+00 0.00000E+00 0.00000E+00 0.00000E+00 0.00000E+00 0.00000E+00
2.29773E-01 2.26590E-01 2.25541E-01 2.23196E-01 2.20155E-01 2.17950E-01 2.17255E-01
2.23771E-01 2.31481E-01 2.39723E-01 2.43249E-01 2.42369E-01 2.39692E-01 2.33079E-01
2.26522E-01 2.20208E-01 2.14693E-01 2.08488E-01 2.04011E-01 2.00827E-01 1.95898E-01
1.89945E-01 1.81167E-01 1.70130E-01 1.64512E-01 1.58090E-01 1.50651E-01 1.37490E-01
1.16014E-01 9.64973E-02 8.50606E-02 7.88778E-02 7.29915E-02 6.74454E-02 6.20396E-02
5.71356E-02 5.30579E-02 5.09634E-02 5.01713E-02 4.90975E-02 4.70419E-02 4.36589E-02
4.03455E-02 3.80099E-02 3.58931E-02 3.40418E-02 3.24145E-02 3.09805E-02 2.96209E-02
2.81448E-02 2.64874E-02 2.47423E-02 2.29801E-02 2.09761E-02 1.94651E-02 1.75469E-02
1.59782E-02 1.50560E-02 1.42014E-02 1.35389E-02 1.29631E-02 1.25139E-02 1.21578E-02
1.18784E-02 1.16844E-02 1.15424E-02 1.14319E-02 1.13815E-02 1.13761E-02 1.14005E-02
1.16505E-02 1.22851E-02 1.30527E-02 1.38512E-02 1.58241E-02 2.06820E-02 2.53304E-02
2.63158E-02 2.72543E-02 2.95690E-02 3.53269E-02 4.58862E-02 4.30617E-02 3.96845E-02
3.44789E-02 2.97416E-02 2.56306E-02 2.25923E-02 2.02500E-02 1.85685E-02 1.73669E-02
1.64757E-02 1.60984E-02 1.58733E-02 1.57902E-02 1.36214E-02 1.13828E-02 1.10399E-02
1.08188E-02 1.09365E-02 1.07358E-02 1.07106E-02 1.12180E-02 1.16180E-02 1.17422E-02
1.23431E-02 1.28104E-02 1.35186E-02 1.48540E-02 1.58905E-02 1.67770E-02 1.64867E-02
1.81016E-02 1.68630E-02 1.85443E-02 1.81162E-02 1.93360E-02 2.04892E-02 2.29117E-02
2.65363E-02 2.80378E-02 2.77711E-02 3.22442E-02 3.48146E-02 4.18758E-02 5.13682E-02
4.31302E-02 4.35599E-02 4.93488E-02 8.84132E-02 6.88474E-02 5.52807E-02 5.28081E-02
4.92633E-02 6.24845E-02 5.24117E-02 8.11868E-02 7.43703E-02 9.33363E-02 1.37672E-01
1.30323E-01 1.25057E-01 1.22069E-01 1.44855E-01 2.44061E-01 1.77750E-01 2.04989E-01
1.92740E-01 3.81344E-01 2.39200E-01 2.66224E-01 3.01479E-01 3.40886E-01 3.86367E-01
4.38289E-01 4.96590E-01 5.68382E-01 6.37189E-01 7.24019E-01 8.20520E-01 9.30194E-01
1.05294E+00 1.15997E+00 1.23231E+00 1.28599E+00 1.31067E+00 1.33677E+00 1.39573E+00
1.47678E+00 1.57013E+00 1.67023E+00 1.78014E+00 1.88057E+00 2.00362E+00 2.16416E+00
2.29752E+00 2.47007E+00 2.70768E+00 2.99071E+00 3.30946E+00 3.64236E+00 4.03000E+00
4.63523E+00 5.52744E+00 6.41575E+00 7.27863E+00 8.55704E+00 1.04221E+01 1.25220E+01
1.64222E+01 2.25793E+01 3.80564E+01 0.00000E+00
0.00000E+00 1.05643E+00 8.12317E-01 6.40756E-01 5.18505E-01 4.83103E-01
4.35551E-01 3.87402E-01 3.64666E-01 3.15415E-01 2.87868E-01 2.51621E-01
2.11003E-01 1.80826E-01 1.58350E-01 1.45759E-01 1.34597E-01 1.25655E-01
1.16853E-01 1.08592E-01 1.00731E-01 9.55401E-02 9.17152E-02 8.91476E-02
8.55042E-02 8.01805E-02 7.29584E-02 6.63555E-02 6.17836E-02 5.73200E-02
5.33162E-02 4.99525E-02 4.87413E-02 4.81164E-02 4.78399E-02 5.03323E-02
5.74979E-02 7.06076E-02 9.98074E-02 1.61643E-01 2.90620E-01 3.98187E-01
4.63207E-01 6.14497E-01 8.64682E-01 6.44986E-01 2.70242E+00
end adjsrc

```

Figure 5.6: Example of the adjoint source section of new SMORES input. First source is highlighted in yellow. Last source is highlighted in green. The line in between both sources signifies the fourteen additional sources that would be defined (omitted to take up less space).

- **Key_Find.f90** and **Recreate_Input.f90**: **Key_Find** rewrites the input file so that the "read" keywords start in new lines. This means that the source keywords must be included. Similarly, **Recreate_Input** writes the entire input into a scratch file, which now includes the new sections that define the source.
- **datin.f90**: As previously described, this subroutine reads input data and calls on subroutines to process the data so that it can be written to an XSDRNPM input. It reads the input file by scanning the keywords for each section, and calls a corresponding subroutine to interpret that section's data. Additional code was created to read the forward and adjoint source section keywords. When it does, it calls a brand new subroutine, defined below.
- **source.f90**: A new subroutine that reads and stores forward or adjoint source definitions into an array (the entire routine can be found in Appendix G. It is called by **datin.f90**, which passes two parameters to it: 1. a boolean that specifies whether the sources in the section are forward or adjoint, and 2. an empty array whose dimensions are (# of energy groups \times # forward/adjoint sources). Once the information is passed to **source.f90**, the subroutine first determines what type of source it is dealing with, forward or adjoint. Secondly, it calls the integer global variable that indicates the total number of forward/adjoint sources defined by the user. It also grabs the global variable that specifies the number of energy groups from the chosen library. Next, it iterates through the total number of sources and for each source an inner loop goes through the number of energy groups. For each energy group in the inner loop, the value of the source is recorded into the column and row of the array that was passed from **datin.f90**. By the end of the subroutine, the array, which now includes all the source information, and is passed back to **datin.f90**. Other features include finding and outputting errors when the number of sources defined in the source sections is not equal to the total number specified by the user in the geometry section. The code will also give an error when the number of values defined per source does not equal the number of energy groups specified by the chosen cross sectional library.
- **xsdRNA.f90**: This subroutine, previously mentioned, creates an XSDRNPM forward or adjoint input file. **datin.f90** passes all the information that this subroutine needs, including the source arrays recorded in **source.f90**. Once passed, the source array is formatted and written into block 3, line 31 of the XSDRNPM input. Additionally, it alters block, line 1\$, entry #10 to specify that the problem is for a fixed source rather than a k calculation.

In summary, the changes outlined above allow the user to specify and define forward and adjoint sources in the input. Additionally, it enables the source code to read and correctly interpret the source information so that it is included in the forward and adjoint XSDRNPM inputs. Nevertheless, additional work is necessary to fully adapt SMORES to fixed source problems. This work will be completed in the future, and is outlined in the next section.

5.2.2 Future Work

The last section listed the modifications already implemented into SMORES. Nevertheless, there is still a lot of work to complete before SMORES can be executed with fixed source problems. This involves additional changes to the input file, editing more subroutines in the SMORES functional module, and making changes to the optimization functional module, SWIF. The following sections provide a brief explanation, and recommends changes if this work is continued.

Input File Modifications

All of the changes previously made to the SMORES code and its input file allow the 1D deterministic code, XSDRNPM to run problems with fixed sources. Nothing has yet been done to the optimization module and its corresponding section in the input file. The optimization specification section beginning with the keyword **read optimize**, was shown in the input of Fig. 5.2. Recommended changes for this section and other additions are described next.

1. Add the restraint adjoint source definition section to the input, and include this information in corresponding subroutines, as described in the previous section.
2. The first parameter specified in the optimization section of the input is the type of optimization. Before this, the user should identify if the optimization is for a fixed source problem or a k eigenvalue problem. This can be written with an integer identifier such as 1 corresponding to k optimization and 2 corresponding to fixed source optimization.
3. With regards to the first parameter mentioned in the previous point, new optimization types should be added to the already existing ones. As an example in Fig. 5.2, an equal volume effectiveness calculation (EVREF) was requested [55]. New types of functions can include: optimize a functional without a restraint (OPF), optimize a functional with imposed restraint (OPR).
4. If either OPF or OPR options are chosen, it should be followed with a statement that indicates if the functionals should be maximized or minimized. If OPF is chosen, there should be one entry (functional to optimize), while OPR should have two entries (functional to optimize and functional to restrain). They can be indicated by integers, 0 for minimize and 1 for maximize.
5. If either OPF or OPR options are indicated, after the declaration above, the user should indicate the number of linear functionals. Maximum number should be 2. There is something similar to this in the SWAN input in Ref. greenspan1973swan
6. The second to last keyword in the first block of the current optimization section allows the user to input the k_{eff} for a minimum critical mass calculation. For fixed source problems, the user can enter the restraint in place of the k_{eff} . For example, if the restraint is a TBR of 1.02, then 1.02 would be entered.

7. A new section should be made for adjoint sources of fixed source calculations. This section can start with the keyword **read adjoint**. Here, the user can specify the materials of the adjoint sources. Additionally, the user should list the reaction rate (MT) number of both, the optimal and restraint adjoint sources, for each material indicated. See Table M4.B.1 in the SCALE manual for ENDF MT reaction types [76].

Modifications to Subroutines of SMORES

In addition to the changes made in the SMORES subroutines described in Section 5.2.1, the following subroutines might be of interest to review and alter:

- **readsw.f90**: This subroutine reads in the input parameters that are needed in the SWIF module. It only reads the first input section and calls on **rdwif.f90** to read the rest. Both of these subroutines must be checked so that the parameters in the current version of the code do not need any new information for fixed source problems. If new parameters are necessary, they must be added here.
- **updtbn.f90**: This subroutine reads in the new densities calculated in the optimization module. It calls on **cntlbn.f90** to update the input files of the modules that process the materials information and cross sections. There might not be a need to fix the code at all since both fixed source and criticality problems calculate new densities. Nevertheless, the code should be reviewed once all fixed source data is implemented to ensure that new densities are being passed successfully.
- **doswif.f90** and **nexswif.f90**: These subroutines are directly called by the driver, SMORES, to read and gather information from a direct access file. They call on other subroutines such as **cpyflx.f90** and **cpxsdn.f90** to copy information from the XSDRNPM output. The gathered information is copied into a file called XTROUT containing flux and geometry information, to be utilized by SWIF. **doswif.f90** is called in the first iteration, while **nexswif.f90** is called from the second plus iterations. These files needs to be checked in case there is any missing information that is needed from the XSDRNPM output.

Modifications to Subroutines of SWIF

There have not been any changes made to the functional module SWIF. The recommended changes are outlined below:

- **driv.f90**: This subroutine checks the type of optimization calculation. Extra code must be included to accommodate the new parameters described in Section 5.2.2. The convergence criteria, which is based on k_{eff} optimization is checked in this subroutine. A different convergence criteria is needed for fixed source problems and can be found in another subroutine, **newden.f90**. This criteria originated from the SWAN subroutine under the same name and was never deleted. For fusion and other fixed source systems, **driv.f90** can be altered so that it calls on **newden.f90** to check the convergence. Another option would be to directly include the convergence criteria of **newden.f90** in **driv.f90**.

- `setup.f90` and `unit3.f90`: These two subroutines read information from the XTROUT file. If `doswif.f90` and `nexswif.f90` (see previous section) are modified to include parameters for fixed sources, then these two subroutines will probably need to be modified as well. Furthermore, `setup.f90` calls on all the subroutines that calculate the effectiveness functions, new densities, etc. If new subroutines are created, their calls can be added here.
- `effect.f90`: This subroutine calculates the effectiveness functions. Presently, it only supports the calculation of functions for homogenous problems. A few lines of code are needed to incorporate Eq. 5.2 for inhomogenous systems. The new code must grab problem-specific cross sections to calculate the reaction rate in Eq. 5.5. The cross sections are specified by the MT numbers in the input file as described in Section 5.2.2 (point 6 on the list).
- `newden.f90`: As previously discussed, this subroutine checks the convergence criteria and calculates the new density compositions. The convergence criteria is implemented from the SWAN code, which can be utilized to check convergence in fixed source problems. The calculation of the densities has been modified from the original subroutine in SWAN to account for errors. This part will probably not need any additional changes but must be reviewed nonetheless.
- `awrite.f90` and `cwrite.f90`: These subroutines create different arrays that are used in the output and must include new information related to fixed source problem calculations.
- `asource.f90`: In fixed source problems, the adjoint source changes in every iteration of SMORES as the densities of the variable materials are recalculated. This means that the adjoint source array, to be utilized by the adjoint XSDRNPM calculation, must be updated in every iteration. A new subroutine should incorporate this by gathering the microscopic adjoint source cross sections from `effect.f90`, and multiply them by the new densities from `newden.f90`. The result can be stored in an array that is eventually transferred back to the SMORES functional module along with the rest of the updated optimization data.

5.3 Conclusion

This chapter outlined an alternative implementation of perturbation theory for the optimization of fixed source problems with deterministic codes. Currently, there is no code available that can do this. Nevertheless, it was discovered that the SCALE package includes a code, SMORES, that solves optimization problems for critical systems. The framework of SMORES originated from SWAN, a code developed specifically to solve problems for fusion blankets. Consequently, one can naturally alter the SMORES code to allow it to solve optimization problems utilizing the inhomogenous transport equation and operator. Modifications to the code and the input had been made. The code can now read in both forward and adjoint fixed source specifications and definition, and transfer this data to the 1D deterministic code, XSDRNPM. This work will not be continued in this dissertation due

to time constraints, and thus, suggestions for future implementation to the code were listed. The finished version of the code will have the ability to optimize the composition of the lithium-based ternary alloy blanket for IFE reactors with just one execution. Furthermore, the composition of each blanket region will be optimized individually to create the most efficient system. This type of calculation can run at a fraction of the time it takes to run a Monte Carlo simulation. However, it cannot fully model the system in three dimensions which leads to higher uncertainties in the results. The best solution would be to create a hybrid optimization method that combines this method with the methods described in Chapter 4. SMORES, the deterministic code, is first executed to obtain an estimate of the optimal composition. Using this result, a Serpent Monte Carlo simulation can be performed by simulating a region around the optimal composition to determine a more accurate result. Utilizing the deterministic code in the first iteration as opposed to Monte Carlo (described in Chapter 4) removes the hassle of simulating the entire ternary for each alloy and reduces the number of simulations from 29 to four (one for the deterministic iteration, and three Monte Carlo runs for each blanket result). A flowchart of this method is shown in Fig. 5.7.

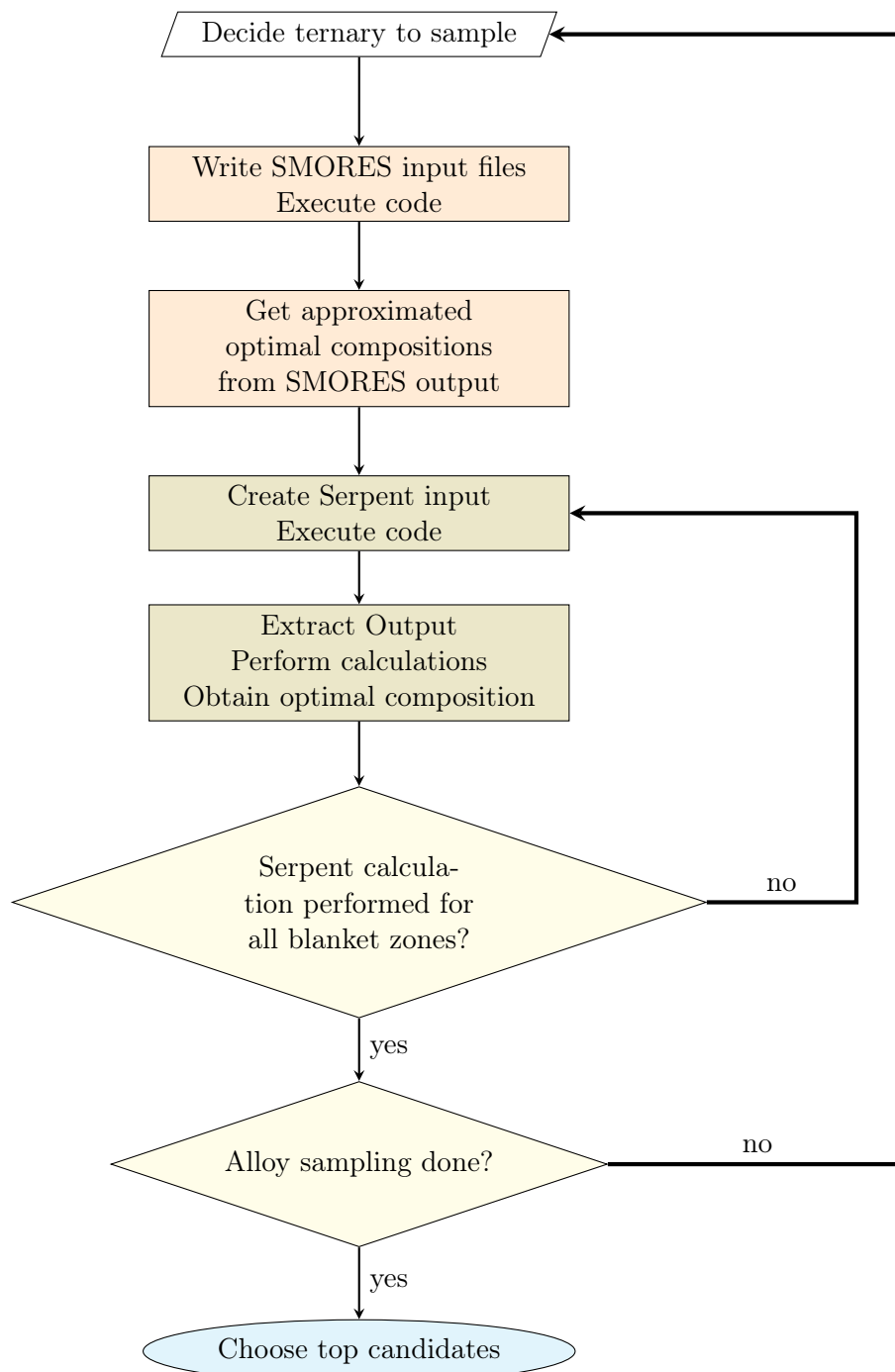


Figure 5.7: Flowchart of hybrid optimization method. Deterministic steps are defined in orange. Monte Carlo steps are defined in green.

Chapter 6

Review of Chemical Reactivity Experiments for Lithium Ternary Alloys

6.1 Introduction

Lithium is often the preferred choice as breeder and coolant in fusion blankets as it offers high tritium breeding, excellent heat transfer and corrosion properties, and most importantly, it has a very high tritium solubility and results in very low levels of tritium permeation throughout the facility infrastructure [86]. However, lithium metal vigorously reacts with air and water and exacerbates plant safety concerns [34]. Consequently, Lawrence Livermore National Laboratory (LLNL) is attempting to develop a lithium-based alloy—most likely a ternary alloy—which maintains the beneficial properties of lithium (e.g. high tritium breeding and solubility) while reducing overall flammability concerns for use in the blanket of an Inertial Fusion Energy (IFE) power plant [39, 111]. The IFE engine employs inertial confinement fusion (ICF) through the use of lasers aimed at an indirect-driven target composed of deuterium-tritium fuel. The fusion driver/target design implements the same physics currently operating at the National Ignition Facility (NIF). The IFE plant uses lithium in both the primary coolant and blanket; therefore, lithium-related hazards are of primary concern. Reducing chemical reactivity is the primary motivation for the development of new lithium alloys, and it is therefore important to come up with proper ways to conduct experiments that can physically study this phenomenon. This paper will begin to explore this area by outlining relevant past experiments conducted with lithium/air reactions and lithium/water reactions. Looking at what was done in the past will then give us a general idea of how we can setup our own experiments to test a variety of lithium alloys.

6.2 Lithium Reactions with Air

High energy reactions of lithium with air can occur during an accident. Such accidents involve a rupture or leak in plant components, which results in the release of

lithium into the containment atmosphere. The following sections outline past experiments conducted with lithium reacting with air and with LiPb reacting with air.

6.2.1 Handford Engineering Development Laboratory (HEDL) Experiments

HEDL conducted tests in the late seventies and early eighties to examine the effects of lithium reactions with a multitude of materials [74, 112]. Those of interest here are nitrogen, dry air and moist air. Tests were conducted in which 10 kg pounds of lithium at a chosen temperature were transported to a preheated reaction pan with an exposed surface area. The reaction pan was enclosed by a carbon steel containment vessel with a controlled atmosphere. Fig. 6.1 shows the geometry of the facility. Results from experiments in which lithium was exposed to a limited amount of normal humidity air showed that the original lithium pool temperature does not have an effect on the maximum pool and flame temperatures reached in the reaction. Two of the experiments showed that half of the lithium reacted with nitrogen while the other half reacted with oxygen. The maximum pool temperature in these cases was 1000°C. The largest aerosol product formed from these reactions was Li₂O. A much larger scale experiment with a total of 45.4 kg of lithium and unlimited amount of air produced different results, yielding 94% of lithium oxide and 29.4% of lithium carbonate aerosol. Aerosols were created when lithium would randomly ignite and burn in normal humidity air. Lithium carbonate aerosol was more stable than lithium oxide or hydroxide. Additionally, at high temperatures when there is enough oxygen available to react, lithium-oxygen reactions overrode lithium nitrogen reactions. Experiments were also performed with moist air, showing a more rapid oxidation of lithium, igniting and burning with a yellow-red flame. Lithium interactions with moist air added an additional component from the lithium-water vapor interaction producing lithium hydroxide.

In addition to experimenting with air, lithium was combined with isolated components of air to examine its reaction. Lithium-oxygen reactions showed the formation of an oxide film. When lithium was combined with nitrogen, a buildup of nitride was observed, which reduced the reaction rate. Additionally, the heat of reaction was lower than that in air and therefore the reaction was less vigorous than that of lithium with air. When lithium reacted with carbon dioxide at a low temperature, below 300°C, only a surface reaction was observed. However, at high lithium temperatures, above 500°C, lithium reached temperatures higher than its melting point and was ignited and produced a flame of about 1400°C.

HEDL conducted tests with LiPb and air. These tests were performed to model reactor accident scenarios. LiPb alloy pool reaction tests with air were performed to predict accidents where the lithium alloy leaks from the blanket to form a pool that will be exposed to an atmosphere of either air, nitrogen, or carbon dioxide. LiPb reacted the least with nitrogen; it did not form any aerosols or combustible gas and produced only a slight amount of heat. The alloy had similar results when reacting with air when the initial temperature of the pool was of 450°C. However, with a pool temperature of 750°C, lithium and lead aerosols were released. The reaction with limited quantities of carbon dioxide was exothermic at an initial alloy temperature of 450°C. It is assumed that aerosols would have formed if a larger amount of carbon dioxide was used.

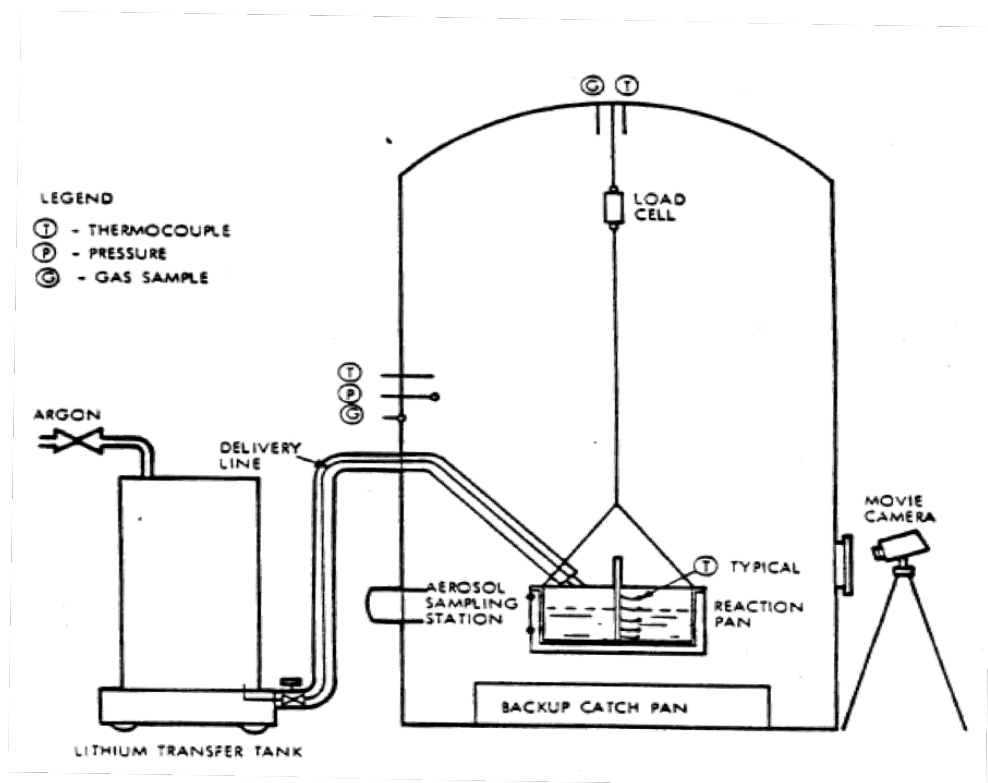


Figure 6.1: Geometry of HEDL lithium-atmosphere reaction experiments [74].

6.2.2 MIT Liquid Lithium Reactions with Oxygen-Nitrogen Mixtures

The first experiments conducted at MIT were performed in 1984 to study lithium-nitrogen reactions [113]. A diagram of the experimental set-up is shown in Fig. 6.2. Purified nitrogen flowed constantly from a tank (tank 1) on to a preheated reaction site and preheated. At the reaction site, the gas reacted with pure liquid lithium at specified temperature. The generated aerosols passed through the heat exchanger and the filter and were stored in a separate tank (tank 2). Pressure gauges on tanks 1 and 2 recorded the respective losses and gains of pressure. Thermocouples recorded gas temperatures; from this, the ideal gas law was used to calculate losses and gains (in moles). The difference between the amount of gas accumulated in tank 2 and the amount lost from tank 1 equals the amount of gas lost to the lithium-nitrogen reaction. This information, plus the time from the internal clock in the data acquisition system, allowed the reaction rate to be calculated. There were at least five types of uncertainties in this experiment, and they were accounted for in the results. The first was related to the accumulation of a nitride layer, which slowed the reaction rate. This, however, is a common part of the lithium-nitrogen reaction. Secondly, uncertainties were observed due to the increase of the lithium pool surface area caused by the spreading of molten lithium along the walls of the container due to the high surface tension of lithium, and by a non-flat surface of lithium during the reaction. As a result, the reaction rate increased. The third uncertainty was from the impurities found in both nitrogen and lithium. Additionally, there was human errors stemming from readings, recordings, and measurement. Other uncertainties accounted for was due to insufficient gas flow at high temperatures, causing reaction rates to depend on the amount of gas flow. In addition, the lithium pool temperature experienced drastic changes at high temperatures caused by vigorous reactions, and therefore caused uncertainties in measurements.

In 1986, experiments at MIT were conducted to examine the kinetics of lithium-nitrogen and oxygen reactions. The experiments were designed to understand how lithium reacts with air under a non-humid environment. The experiments were conducted under dry conditions first to understand the kinetics of lithium with mixed nitrogen and oxygen. Afterwards, water vapor could be added, and its role as a catalyst of the reaction rate could be obtained. Experiments using the nitrogen and oxygen mixtures were conducted at temperatures ranging from 350°C to 1100°C, while the pure nitrogen experiments were done at a range of 450°C to 700°C. The flow was kept constant with a rate of 2.0 to 3.5 liters per minute. Some of the experiments over 900°C needed higher flow rates of 5.5 liters per minute to gather measurements that were independent of gas flow. The area of the lithium pool surface was only 3.88 cm² in order to prevent a large release of energy in the case of an accidental fire. Pressures and temperatures were monitored every 3 seconds. This experiment was found to be one of the most thorough regarding lithium/air type reactions and thus will be discussed in detail in the following sub-sections.

Experimental Process

A diagram of the setup is illustrated in Fig. 6.3. Tanks 1 and 2 were filled with nitrogen and argon, respectively, and released to the atmosphere several times in order to purge out impure gases and have the purity of each gas reach 99.9% or higher. The

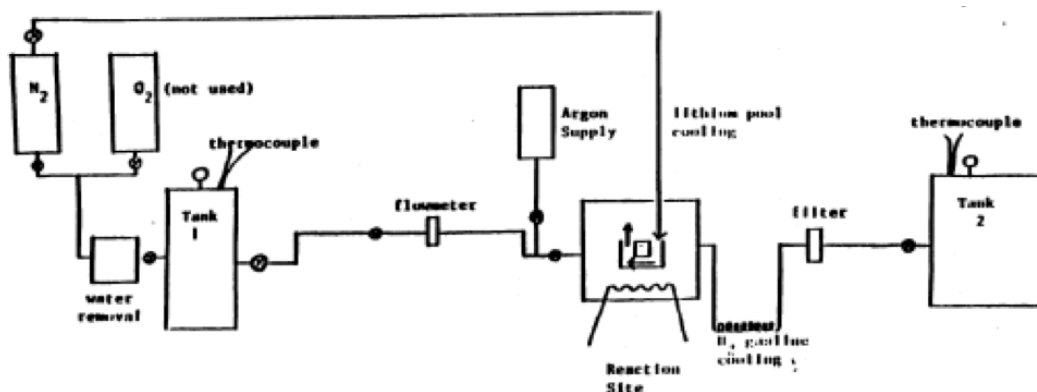


Figure 6.2: Experimental set-up for MIT 1984 lithium-nitrogen experiments [113].

oxygen fractions that were bled into tank 1 to combine with nitrogen varied from 5 to 20%. Oxygen was not bled into tank 1 right away to avoid a decrease in pressure from unavoidable leaks, rather it was done when lithium in the reaction chamber was heated to a desirable temperature. The lithium was held in a stainless steel container. Above the container there was a cap; a nickel o-ring was inserted in the gap between the container and cap. The container where pure lithium (after inspected) was inserted contained pure argon gas. Although as many impurities as possible were extracted from the lithium, some still remained. Impurities were problematic in experiments performed in the low temperature range ($\leq 500^\circ\text{C}$) because they increased the melting temperature of the lithium. To ensure all the lithium was melted, it was heated up to about 600°C first, and then brought down to the desired temperature. Nevertheless, it was predicted that these impurities could affect the consistency of the reaction rate. This was not a problem in the high temperature cases since the impurities would most likely have sunk to the bottom of the container.

To conduct the experiment, valves were opened so the gas could flow from tank 1, through the reaction chamber, to the second tank. The gas flow to the second tank was stopped at the time in which the gas composition after the reaction took place could be measured. By knowing the final gas composition, one could decipher the amount of oxygen and nitrogen that reacted with the lithium in the container.

During the experiment some inaccuracies were observed and accounted for. The first and largest occurred at lower temperatures due to impurities found in the lithium. These impurities increased the lithium melting temperature from 185°C to about 400°C . The second inaccuracy encountered was the spreading of the reaction products along the walls of the container, increasing the reaction rates. Surface irregularities observed in the temperature range from 400°C to 700°C also increased the reaction rates up to 20%. Additionally, a third error was observed regarding the accuracy of the oxygen composition; the maximum difference in the oxygen fraction of the mixed gas was about 20%. This occurred in the cases with the least amount of oxygen. To maintain the assumption that the same fraction of nitrogen and oxygen was consumed for a reaction after the data points were collected, a valve located in front of tank 2 was closed to store only the gas that had just passed through the container. This prevented any form of error that might have arisen if the valve was left open.

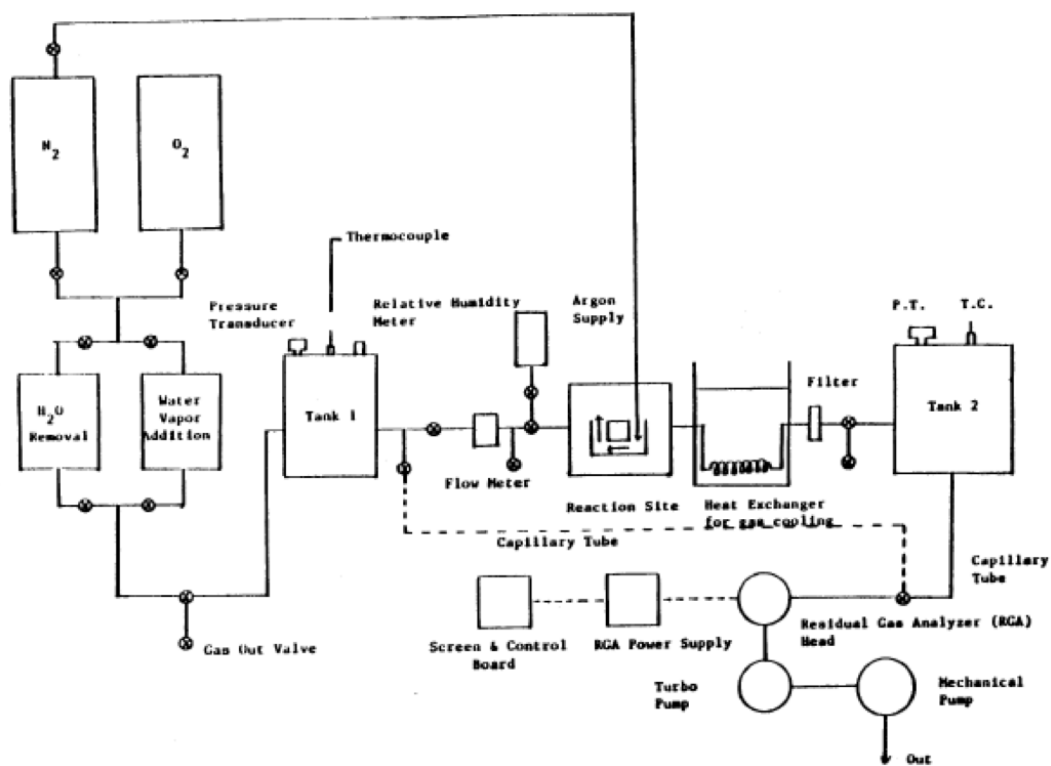


Figure 6.3: MIT 1986 lithium-nitrogen/oxygen experimental setup [113].

The fourth major source of error that occurred in low temperature cases was the formation of a lithium nitride layer which considerably lowered the reaction rates. A lithium oxide layer was also formed but unlike lithium nitride, it could easily be scraped off. Only a few data points could be obtained in such cases since the reaction product prevented additional reactions. The fifth source of error was related to the gas-flow dependency of the reaction rates with oxygen at temperatures above 900°C. One solution was to increase the flow rate of the gas mixture from 3.5 liters/min to 5.5 liters/min. Nevertheless, when temperatures were high, enough oxygen would react with lithium that the rates were gas-flow dependent. Error propagation was performed on some of these errors (oxygen composition, surface area enlargement, and surface irregularities) and calculated to be 28%.

Experimental Results and Analysis

The first measurement was conducted after the full flow rate was established to prevent measuring temperatures from the lithium flame or from radiative heat generation during the reaction process. Results for nitrogen reactions agreed with the previous 1984 experiment. All the lithium in the lithium-oxygen reaction was consumed. Part of the container melted due to the temperature of the lithium flame which was probably higher than the 316 stainless steel melting temperature (1300°C). The environment in this type of reaction was very corrosive.

For the lithium-mixed gas experiments three compositions were used: 1) 80% N₂, 20% O₂; 2) 90% N₂, 10% O₂; 3) 95% N₂, 5% O₂. The reasoning behind utilizing multiple concentrations was to observe how the reaction rate changes as the fraction of oxygen in the mixed gas decreases. To obtain the reaction rates, first, the decrease in nitrogen and oxygen pressures in tank 2 from the reactions was calculated. Once those pressures were known the ideal gas law could be employed to calculate the number of moles of N₂ and O₂ consumed, which were divided by the time of the reaction to obtain the reaction rate. Lithium nitride was formed in the surface of the pool with lithium oxide on top. Lithium oxide was a white, powder-like substance which could easily be scraped off. At high temperatures, lithium oxide is more likely to be formed as aerosols.

Results demonstrate that the lithium-nitrogen reaction rates decreased due to the presence of oxygen. One parameter studied in the analysis was the nitrogen inhibition factor, defined as the ratio of the lithium-nitrogen reaction rate with the presence of oxygen to the lithium-nitrogen reaction rate without oxygen presence. The inhibition factor was dependent on both oxygen concentration and lithium pool temperature. Within temperatures of 800°C and 1000°C the inhibition factor increased which means that lithium-nitrogen reactions were strong enough that nitrogen was competing with oxygen to react with lithium. Contrarily to lithium-nitrogen reactions, lithium oxygen reactions were gas-flow dependent; most of the oxygen was consumed by the reaction at high temperatures, and the reaction rate would reach a finite value that corresponded to the concentration of oxygen in the mixture. It was also discovered that lithium oxygen reactions are dependent on the temperature of the lithium pool. As previously discussed, lithium nitride and oxide were the two major reaction products. At temperatures lower than 800°C, lithium nitride formed at the pool surface, and lithium oxide formed on top of it. At higher temperatures, most of the layer was lithium nitride since lithium oxide formed aerosols. The behavior of the reaction is mostly

dominated by the parabolic law, found when the rate controlling the reaction is diffusion of one of the reactants through a surface film; in this case the surface film is identified as the reaction product layer. Additionally, the results showed cracks forming during the reaction. More cracks formed at higher oxygen concentrations and higher lithium pool temperatures. Cracks increased the reaction rate, and therefore offset the reduction of the reaction rate from the formation of the nitride layer. It was concluded that the reaction rate at lithium pool temperatures lower than 800°C were controlled by the thickness of the nitride layer, while at high temperatures three factors controlled the reaction rate: 1) thickness of nitride layer; 2) concentration of oxygen; and 3) cracks on the surface of the pool.

6.3 Lithium Reactions with Water

For reactions with water, the past experiments involving reactions of LiPb will be examined as opposed to the reactions of pure lithium. This is because lithium alone is less dense than water unlike the alloys that will be used in future experiments and LiPb. Therefore, the setup of LiPb experiments will more likely resemble the type of experiments we want to perform. Past studies investigated reactions of LiPb with both water and vapor. Five possible contact modes of lithium with water were determined:

1. Pressurized injection of water into the lithium.
2. Pouring the lithium alloy into water.
3. Pouring the water into the lithium alloy so it is layered on top.
4. A lithium alloy pool surrounded by a steam environment.
5. Lithium alloy spray into a steam environment [34].

6.3.1 Small Scale Experiments

Small scale experiments were run for LiPb and water interactions to determine the rate of hydrogen production. If the hydrogen production rate is known, proper dynamic mixing models can be used to estimate the amount of hydrogen produced during accident conditions. Experiments included dropping droplets of the alloy into water and vice versa, injecting the alloy into water, or even passing steam over the alloy. A few conclusions were derived from these experiments [69]:

1. The amount of hydrogen produced is loosely dependent on temperature but largely dependent on the contact area between the metal and water.
2. The contact area is dependent on the amount of force used to bring the water and alloy together.
3. If the species react chemically, it prevents an explosive pressure rise.
4. The hydrogen reaction rate of lithium/water reactions is higher than that of LiPb/water reactions.

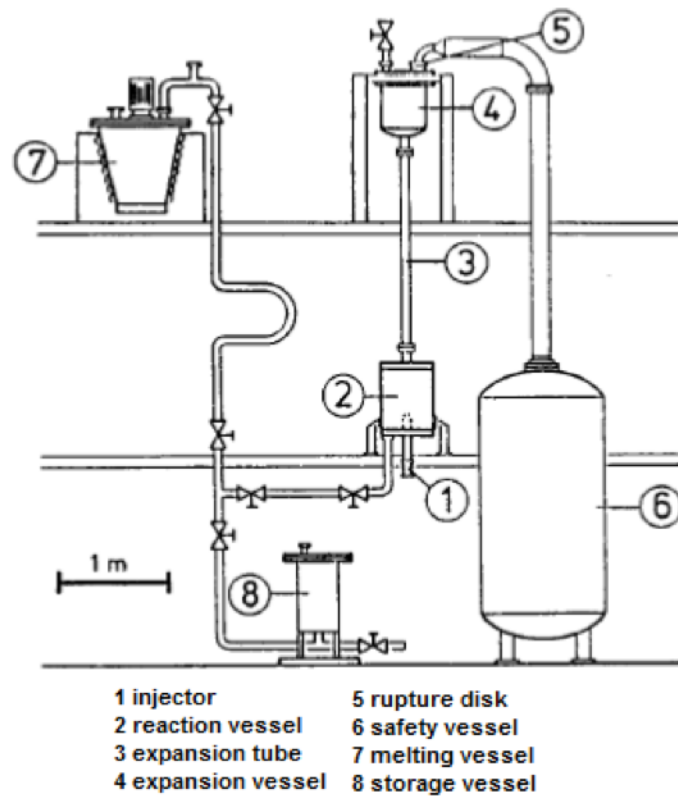


Figure 6.4: BLAST experimental facility [34].

6.3.2 Large Scale Experiments

BLAST Experiments

Large scale experiments are able to properly simulate the contact modes previously described. One accident case that was found to be investigated was a steam-generator-tube rupture. Contact of water and steam with LiPb can create both a chemical and thermal reaction. The BLANKet Safety Test (BLAST) simulated a large break by injecting sub cooled-to-saturated water, at a maximum pressure of 10 MPa, into a stagnant pool of 470 kg of LiPb [34]. The tests were conducted to examine how the pressure changes when a significant amount of LiPb reacts with water at different injection temperatures. The main parts of the experimental model are the reaction vessel with the injector, the expansion tube, and the expansion vessel. A diagram of the setup is given in Fig. 6.4. The maximum amount of water that can be injected is 5 kg with a maximum temperature of 300°C at 10 MPa. The pressure history in the reaction and expansion vessel were recorded along with the pressure and temperature in the injection, expansion and safety vessel.

The results from this experiments show an increase in pressure in the reaction vessel with a peak at the beginning. After depressurization, the pressure rises again. In the experiment where the rupture disk did not fail, BLAST 4, water injection automatically stopped once the reaction vessel reached the injection pressure. This is due to the lack

of pressure difference between the injector and reaction vessel. It is interesting to note that for the expansion vessel, the gradient is the same as the reaction vessel after 500 ms. The reason for this was divided into three phases: 1. At $t < 1$ ms, pressurization of the injected water is mainly due to system compressibility and reaction vessel geometry. 2. At $t < 250$ ms, a pressure increase in the reaction vessel forces the reaction products into the expansion tube. Water vaporization, hydrogen production, and geometries of the reaction and expansion vessels affect the pressure. 3. At $t > 250$ ms hydrogen production dominates the pressurization in the system which affects the reactor vessel, expansion tube, and expansion vessel. It was concluded that the injection pressure limits the pressure in the reaction area.

Later experiments of this nature were conducted including radioactive species to examine which and how much radioactive materials were released. About 0.5-0.55 moles of hydrogen were released per mole of water injected. Solid aerosols included potassium, bismuth, lithium thallium, tellurium, and lead. Mercury gas was also released.

Hanford Engineering Development Laboratory Experiments

HEDL large scale experiments consisted of injecting steam at 7 g/s into an insulated reaction container with a 200 kg pool of 500°C LiPb for 325 seconds [69]. The experimental facility is outlined in Fig. 6.5. A reaction vessel was placed within a vessel containing an argon atmosphere. A condenser, attached the reaction chamber, condensed steam to allow the release of hydrogen to the containment atmosphere where it was measured with a hydrogen monitor. Five thermocouples measured the temperature of the LiPb pool. After 240 seconds into the experiment, the LiPb pool reached its maximum temperature of 870°C. All of the steam reacted with lithium. Most of the hydrogen released occurred during those first 240 seconds. First, steam reacted with lithium to form LiO_2 along with hydrogen. After lithium started to be depleted, the steam reacted with LiO_2 to form LiOH . Consequently, LiOH reacted with lithium to form additional hydrogen. Reaction products were found on top of the pool. It was also concluded that both lithium and water were entirely mixed in the reaction chamber since both completely reacted with one another. Chemical analysis of the reaction products showed that only 0.37% of the total amount of lithium remained by the end of the experiment. Moreover, the amount of hydrogen released was measured as 0.56 mole per mole of lithium that reacted.

A similar experiment was conducted with pure lithium and steam. In this case, 320°C steam was injected at 2.6 g/s into a reaction vessel for 510 seconds. The reaction vessel contained 10 kg of lithium at 580°C. Similar to the previous experiments, both components were well mixed throughout the experiment. The main reaction products in this case were Li_2O and LiH . It was found in this case that the rate of heat production was three times greater than that of the LiPb/water reaction.

University of Wisconsin Experiments

The experiments performed by the University of Wisconsin (UW) consisted of pouring water into a LiPb pool. This case is most likely linked to an accident scenario where water comes into contact with lithium, forming of stratified layers with different densities

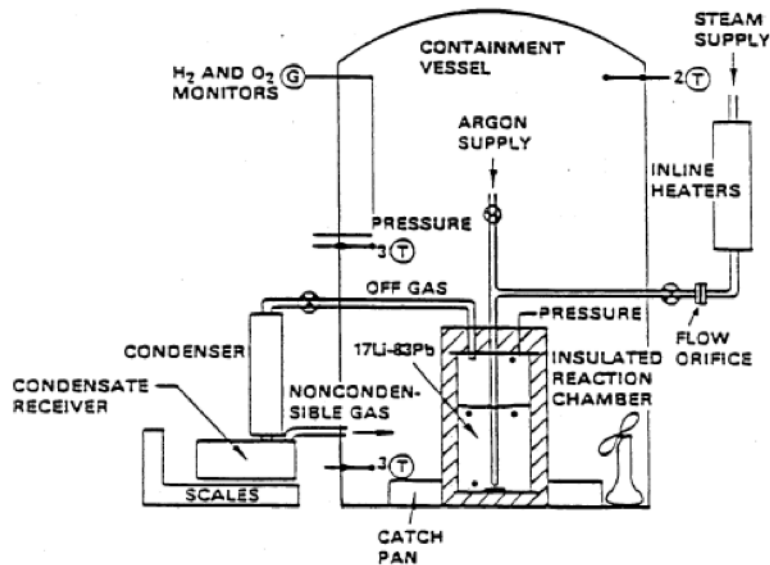


Figure 6.5: HEDL LiPb/steam experiments facility [69].

[69]. These large-scale experiments were run to determine the rate of hydrogen production. The setup consisted of a stainless-steel cylindrical vertical column containing the reactant and products, shown in Fig. 6.6. About 20-65 g of liquid metal in the lower portion was inserted through a drilled cavity. On top of the liquid metal pool was a butterfly valve which kept the liquid metal, below the valve, and water, above the valve, separated. The amount of water held above the valve was around 1 liter. After the metal and water were heated to the desired temperatures, the valve was opened to let the water pour into the liquid metal pool. A closed volume was purposely designed to collect and measure the amount of hydrogen. The size of the liquid cavity was designed such that the contact area between metal and water was kept relatively constant through the experiment. The liquid metal was heated by two semi-cylindrical electrical heating units that formed an annulus around the lower portion of experimental apparatus. The metal temperature ranged from 350°C to 650°C. The temperature of the water ranged from 60 to 90°C and was controlled by a water cooling circuit. The cooling circuit contained a temperature controller that exhibited both heating and refrigeration units. This arrangement allowed the water to be heated to the desired temperature before the experiment was actually performed. A temperature control loop was also in the upper region of the apparatus to remove heat formed during the reaction. To ensure that the contact area between the two components was made up of liquid metal and water vapor, the initial temperature of the water was chosen such that film boiling (i.e., a thin layer of steam and hydrogen covering the liquid-metal surface) occurred at the surface of the alloy. The experiment was performed under an argon atmosphere. Argon was also used with a pressure equalization line to remove the pressure difference between the water and liquid metal sections before they were combined while they were in the process of heating up. This pressure equalization line would allow argon to flow from the gas region on top of the liquid metal pool to the gas region above the water column, and out of the

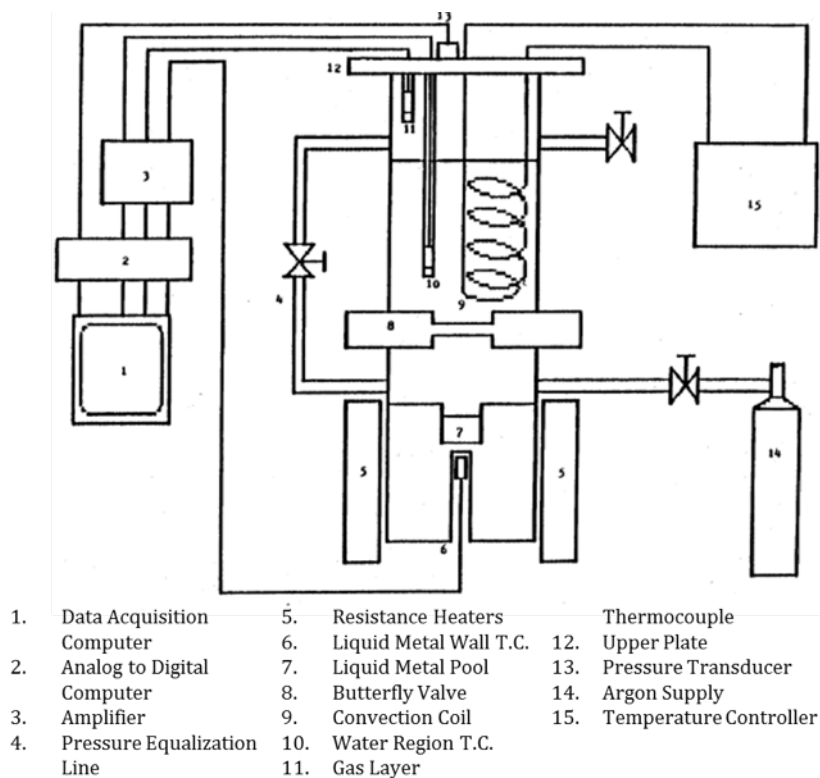


Figure 6.6: University of Wisconsin lithium-lead/water tests facility [69].

system. A pressure transducer and three thermocouples measured the two variables of the experiment. One thermocouple was located at the bottom of the apparatus to measure the temperature of the liquid metal. The other two were placed in wells connected to the top portion where the water was, in order to measure the bulk water temperature and the temperature of the gas above the water. Once the experiment was conducted and the bulk water temperature, the gas layer temperature, and the system pressure were recorded, a computer program analyzed these data and solved for the pressure and mass of hydrogen generated from the reaction. Since the gas from the reaction was composed of a mixture of argon and hydrogen, by knowing the argon mass, the program was able to derive the hydrogen mass. Details on how this was done are explained in the referenced paper [69].

At the beginning of the experiment, the combination of unequal boiling and condensation rates, and the delay of the gas thermocouple made it exceedingly difficult to accurately measure the partial pressure of hydrogen. Measurements were much more precise after thermodynamic liquid-vapor equilibrium was reached, which occurred after 100-150 seconds. Therefore, the results of this experiment were only accounted for after 200 seconds. Hydrogen pressure corrections were made on the results due to additional deficiencies in the gas thermocouple.

Results concluded that the extent of the reaction between the metal and water was not dependent on initial water temperature. What affected the rate of hydrogen production was the diffusion in the metal sample and the temperature of the liquid metal. Using the

data from the experiment, a kinetics model was developed to calculate the hydrogen mass produced and subsequently the reaction rate. The model assumed that the reaction was determined by the rate of diffusion of lithium atoms and products such as Li_2O and LiOH at the liquid metal surface. More detail on the model is outlined in the reference [69]. From the calculations, it is clear that the amount of hydrogen generated was a function of the initial temperature of the lithium alloy and that the reaction rate was linear. When water first interacted with the lithium, all the lithium atoms at the surface were quickly consumed in the reaction. After this point, the rate of the reaction was dependent on the diffusion of lithium atoms to the surface and of lithium hydroxide away from the surface. Additionally, it was determined that the amount of hydrogen generated in moles was equal to half of the moles of lithium consumed. One thing to note was that only the initial temperatures of the water and liquid metal were accounted for as variables in the experiment; other variables such as the volume of the water and pressure of the system could be changed and evaluated to see if they affect the reaction rate. If this type of experiment were to be replicated, changes should be made to make the results more accurate, such as changing the location of the thermocouples.

6.4 Experimental Recommendations

The first thing to consider when deciding how to conduct this type of experiment is whether it will be small-scale or large-scale. Past small-scale experiments were instructive, but a lot were performed before conducting large-scale experiments, or to use the data to create computational models. In the same way, we may benefit from conducting simple small-scale experiments already existing, such as a type of bomb-calorimetry experiment. Additionally, they could serve as initial verification of modeled estimates of thermodynamic and simple kinetic data, and the use of commercial, off-the-shelf equipment should allow these experiments to be conducted relatively quickly and inexpensively. Ultimately, though, large-scale experiments seem more appropriate for our purpose, as they would better depict how the alloys would behave in the actual reactor environment. Both air and water reactions should be considered when examining the potential chemical reactions of the lithium alloy. The MIT lithium/nitrogen and oxygen experiments can be used as a model when looking at the reaction of the lithium-alloy with air. One of the advantages of the experimental setup is the option to see how humidity from the gases affects the reaction rate. The way the reaction rates are calculated, i.e., utilizing two tanks to calculate how much is lost from one and gained from the other, is straightforward. Additionally, the use of an updated data acquisition system will allow the results to be obtained more easily. The study outlined all the uncertainties encountered in the experiment, such as impurities in the lithium and the accumulation of the nitride layer. Before conducting the experiment, an effort can be made to account for all the inaccuracies, but if this is not possible, awareness of them should be made when taking measurements. The MIT experiment can be used as a guide but essentially the setup can be redesigned with different materials, sizes of containers, and placement of thermocouples and pressure transducers to fit our needs and get the most accurate results. The same can be done with lithium alloy/water interactions and some of the past experiments. For experiments involving water reactions, the type of accident

scenario must be considered. In our case, the only place where water is found is in the steam generator. Therefore, we would most likely want to perform experiments involving a steam generator tube rupture similar to the BLAST experiments, or the HEDL steam injection experiments. The experimental setup of the BLAST studies is simple and straightforward. Similar to the lithium alloy/gas experiments, the BLAST setup can be used as a template for our own experiments while designing the experimental facility that meets our specific needs. If other types of lithium alloy/water interactions are to be considered, we can look into other past experiments, i.e., the UW pouring experiments, as a guide.

Chapter 7

Policy Issues Related Inertial Fusion Energy Reactors

The policy issues related to the dissertation work are broken up into two sub-categories: safety of fusion reactors and nuclear security of fusion reactors. The LiPb below discuss these topics and present solutions or recommendations for each.

7.1 Safety of Fusion Reactors

The primary issues associated with the safety of lithium-containing fusion reactors are: 1. lithium chemical reactivity. 2. tritium release. 3. waste and disposal of blanket materials. These issues will be discussed in detail in the subsequent sections.

7.1.1 Lithium Chemical Reactivity

Lithium is extremely chemically reactive because it is an alkali metal in nature [77]. Its high reactivity with air and water is a crucial problem in a reactor environment [34]. For example, high energy reactions of lithium with air can occur during an accident. Such accidents involve a rupture or leak in plant components, which results in the release of lithium into the containment atmosphere. Lithium also interacts with concrete due to its moisture content and leads to degradation of the concrete containment. In the worst case scenario a breach in the containment can occur which will result in the release of highly radioactive tritium gas into the environment. In addition to the moisture in the concrete, any other plant component containing water such as heat exchanger, or a small amount of moisture found anywhere within the plant can violently react with lithium. As a result, the structural integrity of such components is highly compromised. Extreme exothermic reactions of lithium with either air, water, or concrete can lead to lithium fires.

Although pure lithium exhibits many attractive properties making it a superior choice for fusion blanket's material, it is the reactivity concerns that led the research community to look for alternatives. This work investigates the use of lithium-based ternary alloy for fusion reactors in the hopes that candidate alloy can maintain the beneficial properties of lithium while reducing the chemical reactivity concern. Chapter 6 explores some of ways

past experiments on lithium reactivity were conducted and gives recommendations for future experiments with the new ternary alloys. Future work will involve conducting these experiments. Any alloy that shows poor performance based on the experiments will not be considered.

7.1.2 Tritium Release

The worst type of accident scenario that can occur in a fusion facility is some type of breach in the containment structure causing tritium gas to travel out of the containment and into the surrounding atmosphere. Additionally, tritium has the ability to permeate through plant components and structures and escape into the environment during regular operation. Since tritium is an isotope of hydrogen, it is nearly impossible to remove it from the environment [5], and therefore, it is highly probable that it will be absorbed in the surroundings and by the public. The health hazards that follow from the ingestion and absorption of tritium by an individual are nontrivial. As a result, tritium doses that can be absorbed by an individual through different pathways are accounted for in regulations enforced by the Nuclear Regulatory Commission (NRC) and Environmental Protection Agency (EPA). The National Emission Standards for Hazardous Air Pollutants under Title 40 Code of Federal Regulations (CFR) Part 61 requires that doses emerging from airborne radioactive isotopes from nuclear facilities during normal operation do not exceed 0.1 millisieverts (mSv) per year [4]. Additionally, contaminants found in drinking water are regulated through the EPA's Safe Water Drinking Act. The dose limit for drinking contaminated water is 40 microsieverts (μSv) per year, and was adopted into the National Primary Drinking Water Regulations under 40CFR141.16 [130]. The total annual dose limit to members of the public from all types of radiation exposure is 1 mSv per year. This limit is proposed by the NRC per recommendation by the International Commission on Radiological Protection (ICRP) and was included in 10CFR20.1301 [31].

The Department of Energy (DOE) came up with documentation (DOE-STD-6002-96) that presents requirements and recommendations for fusion reactors [4, 5]. The DOE Fusion Safety Standards has the same dose requirements for airborne, waterborne, and total dose as discussed in previously. Furthermore, a stricter total fusion radiological release requirement of 0.1 mSv per year was recommended. For accident scenarios, the NRC imposes under 10CFR100.21 (Reactor Site Criteria) that the total dose received by members of the public must not exceed 250 mSv within any 2-hour period of a release [5]. The DOE Fusion Safety Standards acknowledges that limit, but proposes an even lower limit for fusion of 10 mSv, for the same 2-hour period [5]. This is based on the requirement that design and operation of fusion facilities are carefully constructed to eliminate the need of any off-site evacuation during abnormal conditions.

The lithium-based ternary alloys examined in this work were analyzed to ensure that they do not exceed the accident dose limit proposed by DOE Fusion Safety Standard of 10 mSv. This not only includes tritium releases, but also any other highly-mobile isotope found in the alloy. All the information utilized for the analysis was based on the most conservative assumptions. More details on the calculations and its results can be found in Chapter 3. Any candidate alloy that did not meet the dose requirement or was deemed unsafe was eliminated from the selection. The flexibility of having the choice to select

materials that are the safest is an advantage of fusion reactor design compared to fission reactors. Moreover, the biological risks associated with the types of radioactive gases emitted from fission reactors, which are more hazardous than tritium, are not present in fusion reactors.

In addition to accident dose calculations, it is important to ensure that the amount of tritium released from the alloys to the environment during normal operation does not exceed the limits proposed by the NRC. The best way to do this is by evaluating the solubility of tritium in the alloy. If tritium is soluble in the liquid alloy, it will have more difficulty permeating nearby structures and escaping into the environment. The results from the work in Chapter 3 were part of a collaboration with Lawrence Livermore National Lab (LLNL) to come up with best ternary alloys based on multiple characteristics. One of the characteristics investigated under LLNL's project involved studying tritium permeation by conducting hydrogen solubility experiments. A colleague at LLNL is currently conducting these experiments at LLNL and will publish his findings.

7.1.3 Waste and Disposal of Blanket Materials

Any nuclear facility requires that its radioactive waste is properly disposed of. The waste created by any facility will have varying levels of radioactivity and decay heat. Therefore, the NRC has classified waste into different categories based on their levels of radioactivity, and requires the correct type of disposal for each type. This is found under 10CFR61 [32]. For example, high level waste (HLW) is made up of spent fuel from fission reactors containing isotopes that are highly radioactive and very hot. Any waste that isn't either HLW or transuranic waste, also from fission fuel, is classified as low level waste (LLW). LLW is composed of isotopes with much lower levels of radioactivity, and can be disposed by either shallow land burial or near surface burial. To determine the correct type of disposal requirements, LLW is divided into three different classes. Class A wastes are those with the lowest radioactivity out of all three types of LLW and requires near surface burial. Class B wastes, with higher radioactivity and heat content, are also buried near the surface but are covered to reduce surface radiation. Class C is the most radioactive of the three types of waste and requires burial at greater depths than Class A and B [143]. The waste in Class C has longer-lived radionuclides that do not decay to safe levels within 100 years and can still be potentially hazardous. After proper cooling, Class C waste can be buried five meters underground with proper natural or engineered barriers.

Fusion reactors do not produce any HLW or transuranic waste since it does not use any type of fissionable material. Therefore, all of the waste created in fusion systems can be stored as LLW [143]. Some of the products created in this type of system are long-lived radionuclides and will require deeper burial as identified by Class C, LLW. As a result, the fusion community came up with the waste disposal rating (WDR), a metric that determines whether waste can be disposed as Class C. The WDR is a ratio and if it is less than unity, the material of interest can be disposed of as Class C waste. The work in Chapter 3 calculates the WDR for candidate alloys to ensure that they can properly be disposed. If any of the candidates contained a WDR that was greater than one, it was eliminated from the selection.

Another approach considered to handle the discharged reactor materials is recycling. Unlike disposal, recycling involves taking the products discharged from the fusion

reactor and reprocessing them such that they can be reused in the reactor, or utilized for other purposes [28]. The recycling of radioactive material is done after the component is allowed to be cooled for a certain period of time so that the radiation emitted is reduced to adequate levels. The cooling time is aimed to be as short as possible so as to reduce the material inventory that is stored before recycling. A material's feasibility of recycling is determined by measuring its gamma contact dose rate. The proposed limits are below 10 $\mu\text{Sv/hr}$ for hand-on recycling, and below 10 mSv/hr for remote handling [49]. The results in Chapter 3 evaluate the ability to recycle the fusion blanket's alloy by means of remote handling. Because the alloy is in liquid form, hands-on recycling is not feasible.

Although the work presented in Chapter 3 analyzes an alloy's ability to meet waste disposal and recycling limits, no comparison was made between the two to see which one is more advantageous. Ideally, both methods would be beneficial. Recycling would allow the original alloy's components to be extracted so that it can be reused in the blanket. Other isotopes found in the discharged blanket material might be useful for other purposes. Nevertheless there will be specific blanket byproducts that will have no use whatsoever. After being separated from the useful component, this material can be properly disposed via shallow land burial.

7.2 Nuclear Security of Fusion Reactors

The main concern regarding the nuclear security of any type of nuclear facility is the proliferation risks associated with any material generated in the reactor. The following sections examine the risks involving the production of weapons-grade material in fusion facilities, and evaluates the need to monitor the production of tritium and the use of lithium, both of which are found in thermonuclear weapons.

7.2.1 Proliferation Risks in Fusion Reactors

Most nuclear fusion reactor designs do not include any type of fission process or material that could potentially create weapons-grade material. Nevertheless, there is the possibility of utilizing the neutrons from fusion reactions to irradiate fissionable material and thus create weapons-grade uranium and plutonium. Robert J. Goldston of the Princeton Plasma Physics Laboratory has evaluated the proliferation risks for fusion power plants [54]. His work was based on magnetic confinement fusion reactors, but can easily be translated to inertial confinement power plants. He concluded that the risk associated with proliferation in fusion reactors can be divided into three cases: 1. Use of an undeclared facility by a State or non-state actor to generate clandestine fissile material, 2. The same the first case but produced in a facility that is declared and safeguarded, and 3. Undisclosed production of fissile material in a declared facility. Case 3 is known as a breakout scenario, where the State or non-state actor openly generates material for weapon's purposes and violates international agreements, if agreements were made in the first place.

To covertly produce weapons-grade material in an undeclared facility, it would most likely be the goal for such facility to be as small as possible so it is not as easily detected. Kutev conducted a study to figure out what is the smallest possible size of a

fusion system to create fissile weapons material [85]. It was determined that the smallest reactor would create about 3.5 kg of ^{239}Pu or ^{233}U per year, which is less than half of what the International Atomic Energy Agency (IAEA) defines as a significant quantity (SQ). This does not mean that the State or organization with this facility would not be able to be successful and generate a substantial inventory of weapons-grade elements. In any case, even the smallest facility creating fusion with either magnets or lasers is quite complex and requires a multitude of components, including tritium reprocessing facilities, that its construction and operation would still be visible. Financially, producing fissile material in a fusion facility is much more expensive compared to other means, including building a small research fission reactor (many found in universities). Moreover, tritium can permeate through reactor components and easily escape into the environment, allowing it to be detected many kilometers away. For these reasons, it would be quite difficult to secretly build a fusion facility and go completely unnoticed.

Case 2 involves the covert production of fissile material in a declared and safeguarded fusion reactor. Unlike case 1, the reactor is not specifically built to create weapon's grade material so fissionable material must somehow be added to the reactor blanket. In the case of liquid coolant such as LiPb, it was found that the best way to introduce fissionable material would be in the form of TRISO particles (a tiny sphere with fuel in the center) [127] that could be inserted into the coolant and later be mechanically extracted. In one year, the use of 1 mm in diameter TRISO particles would create 8 kg of ^{239}Pu or ^{233}U per one cubed centimeter of coolant, which is considered a SQ by the IAEA. To prevent this from happening, detection techniques should be implemented to yearly inspections conducted by IAEA. ^{238}U , a precursor to plutonium production, can be detected within minutes. With regards to thorium fission, one of its products, ^{232}U , can be detected within seconds after the reactor has been operating for six months. With yearly inspections, the IAEA should be able to detect any fissionable material found within the fusion facility and take the necessary measures.

The last case that Goldston considers is the breakout scenario, in which a state declares that it will no longer abide by IAEA safeguards and begins to produce material for weapons as quickly as possible. This is a concern with fission reactors as exemplified by North Korea's resignation from the Non-Proliferation Treaty (NPT) in 2003 to carry out a weapon's program which subsequently led to its first weapon test in 2006. The production of substantial amounts of weapons material in a fission reactor could be undertaken in secret before the breakout scenario occurs. By the time the State announces breakout, it might be too late to take much action. In contrast, the case for a breakout occurring in a fusion reactor is much different. One scenario would involve creating an entirely new blanket to be replaced with the one existing at that time. The blanket, however, is specifically designed to create a self-sustaining fusion system which might not be possible if the make-up of the blanket material is completely altered. A more reasonable scenario would be to use TRISO particles in the blanket, as discussed previously, but to circulate them more rapidly. The amount of time that it would take to change blanket configurations and introduce these particles would be around a month. Goldston estimated that to effectively generate a significant amount of weapons material, about 500 tonnes of fissionable elements should be present in the TRISO particles inserted into the coolant. This could only be possible if the TRISO

particles are manufactured clandestinely much before the breakout occurs. The resulting amount of either ^{239}Pu or ^{233}U produced by 500 tonnes of fuel would be around 20 kg of per week, much higher than the SQ considered by IAEA. Nevertheless, it is very difficult and expensive to process TRISO particles in order to extract the fissile material. Extracting fissile material out of a TRISO particle involves multiple steps including both physical and chemical processes which are currently still being investigated. Furthermore, unlike a fission reactor, fusion facilities could be intercepted to stop the production of weapons grade material not long after the breakout. For example, the laser system of the inertial confinement fusion reactor discussed in this thesis could be disabled to prevent additional fusion reactors from occurring. In the case of magnetic fusion, the power input and power conditioning equipment that provides electricity to the magnets can be shut down [53]. Other components can also be deactivated, such as heat removal systems, all without creating a massive amount of nuclear contamination.

A breakout scenario would be much more difficult to intercept if the reaction was a fusion-fission hybrid. This means that the reactor includes an additional blanket containing fissionable material. Such a design is being proposed by China, who is currently developing a fusion reactor with a subcritical blanket consisting of transuranic spent fuel [148]. The inclusion of fissionable material in the reactor allows for clandestine production of a significant amount of weapons material before the breakout occurs. There is still, however, a chance to stop additional production of weapons material by disabling the fusion reactions as it was mentioned above. If the fission blanket remains subcritical after the breakout scenario and the fusion reactions are discontinued, the reactor should eventually shut down. This would halt any efforts to continue development of a State's weapons program.

7.2.2 Use of Lithium and Tritium from Fusion Reactors for Weapons

Every type of nuclear weapon designed to this date requires fissionable material. In any case, lithium and tritium are found in certain types of weapons. Tritium is utilized in boosted fission weapons, which increases the efficiency from a pure fission weapon [100]. It also helps miniaturize the weapon such that it can be mounted in a ballistic missile. Additionally, both tritium and lithium are found in thermonuclear weapons. Tritium is located in the primary stage of the weapon, whose function is the same as in the boosted fission design. On the other hand, lithium deuteride can be found in the secondary part of the bomb. Here, lithium creates tritium with neutrons from fission reactions. Tritium will then fuse with deuterium and create energy and additional neutrons [100]. Thermonuclear weapons are the most efficient type of nuclear bomb and produce the greatest yield of energy. Since the first design in the 1950s, various followed with the goal to miniaturize the weapons as much as possible [117].

Tritium is only found in small traces in the atmosphere and has a short half-life of 12.3 years. This, plus tritium's high mobility makes it unattainable naturally. Because tritium is necessary to create fusion reactions, all fusion reactor designs include a lithium containing blanket region that produces tritium. The lithium-based ternary alloy studied in this work creates thousands of grams of tritium, enough to power a multitude of either fission boosted or thermonuclear weapons. Clandestine production of tritium depends on how much tritium the blanket is producing. Fusion blankets only designed to produce enough tritium

to fuel the reactor will not have any additional quantities to use in a weapon unless it is not desired to keep the reactor running. A lot of blanket designs purposely breed enough tritium to supply fuel to future reactors [7]. In this case, the extra supply of tritium could instead intentionally be created for nuclear warheads. To hinder wrongful production of tritium in a declared facility, the IAEA should only allow a certain amount of tritium to be stored in an inventory; this will at least prevent storage of a large excess supply that could be used for numerous weapons. Additionally, detection methods can be implemented to check for any covert production of tritium hidden within the power plant. In the case that the facility is undeclared, the same argument discussed in the previous section applies, regarding the ability to easily locate a fusion facility due to its large size, and the financial disadvantage of utilizing a fusion reactor for the purpose of only breeding materials for weapons.

The case of lithium is a bit different since it is not created in a fusion reactor, but rather needed in the reactor from the beginning of operation. Nevertheless, a state with a fusion facility could be covertly storing a lithium inventory for use in nuclear weapons or to sell to others. This would prove to be more difficult with liquid breeders such as LiPb and the alloys discussed in this paper due to lack enrichment. Natural lithium is only enriched with 7.5% lithium-6, but most thermonuclear weapons require at least 40% of this isotope [138]. Thus, an additional enrichment facility is needed, which could potentially be discovered through IAEA inspections if it is nearby a declared fusion plant. Ceramic and molten salt blankets, on the other hand, require enrichment and would have the capabilities to secretly enrich lithium to the desired amount [24]. These types of inventories, if hidden properly, would be quite difficult to find and detect. Consequently, it is extremely important to maintain vigilance over lithium enrichment facilities and their operations.

The last case to consider is the theft of either or both lithium and tritium from fusion power plants. This would be quite difficult to achieve if the material is contained properly within the plant and if there is high security and surveillance available. The IAEA has addressed the issue of theft in various ways. For example, it has created the Incident Trafficking Database (ITDB) which aids participating States and organizations to prevent the trafficking of nuclear material [14]. The scope of the ITDB includes receiving and distributing information related to the possession of nuclear material acquired through theft, with or without crossing international borders. Additionally, many international legal frameworks are available to address this issue. In particular, the Convention on the Physical Protection of Nuclear Material (CPPNM) (INFCIRC/274) emphasizes the importance of detection and response to criminal and unauthorized acts. Article 5 of this document addresses what actions to take in the event of theft or robbery of nuclear material. Other documentation regarding theft can be found summarized in Ref.IAEA/ITDB. Lastly, the possibility of diversion of certain kinds of nuclear material during exportation is handled by the Nuclear Suppliers Group (NSG) [140]. The material it oversees includes the exchange of both enriched lithium and tritium between two groups.

7.2.3 General Recommendations Regarding Proliferation in Nuclear Reactors

As the development of fusion reactor designs continues, it is important to meet current protocols so that proliferation with these new technologies is prevented. First, existing

IAEA safeguard protocols can be implemented to fusion reactors with regards to detecting clandestine fusion facilities and covert operations of weapons-grade plutonium/enriched uranium in declared facilities. The comprehensive safeguard agreements (CSAs) of INFCIRC/153, specifically Paragraph 39, provide enough information that can be translated to include fusion reactors. Additional protocols (APs) should be implemented so that any operations in a nuclear fusion facility that is not similar to those currently taking place in fission reactors are added to each corresponding State. For a State to include APs, it should already have established CSAs under INFCIRC/153 [12] and accept all provisions of INFCIRC/540 [13].

The articles within the NPT are broad enough with regards to production of weapons grade material, that they can be applicable to fusion facilities without amendment. Specifically, Goldston mentions that the first sentence of Article III, Paragraph 1 of the NPT [114] is already worded in such a way that includes fusion reactors within the context even if they do not inherently contain fissionable material since they can still be utilized for production of fissionable materials. Specifically, the first and second paragraph of Article III [114] emphasizes safeguarding fissionable material produced in a nuclear facility or outside the facility. A fusion power plant can be regarded as a nuclear facility, allowing the NPT to remain intact.

Currently, fusion technology is still under development. The fusion community predicts that self-sustaining fusion can be achieved within the next fifty years. When construction of fusion plants begins in the future, it is necessary to incorporate materials within these plants that could be potentially used in nuclear weapons into IAEA safeguards and the NPT. The two materials that correspond to this are lithium and tritium. With regards to lithium, the IAEA must make amendments to INFCIRC/153 to include specific quantities of both natural and enriched lithium that must be met by facilities. Additionally, it must propose a limit on lithium enrichment. Most thermonuclear weapons require at least 40% enrichment of lithium-6. Thus, the limit proposed on INFCIRC/153 should be 39% at most. Additionally, the maximum quantity of lithium stored within a facility should be determined after thorough research and development, and added to INFCIRC/153. Next, CSAs for States with fusion reactors will be created so that the IAEA can conduct annual inspections and collect lithium samples for enrichment measurements. Lithium enrichment facilities should also be inspected. Moreover, lithium quantities must be accounted for in yearly inspections to guarantee that they meet the limit stated by INFCIRC/153. APs regarding fusion plants should include a State's provision of information about all aspects of the nuclear fuel cycle, including how lithium is obtained and if enrichment is required. Moreover the State must provide information about, while also providing IAEA short-notice access to, all buildings on site. Obtaining access to all buildings will allow the agency to determine if any excess lithium is being covertly stored within the facility.

The US fusion community has concluded that the typical amount of tritium stored in an inventory located within the facility is less than 200 grams [142]. This quantity, after validated with further research and development, can be added to INFCIRC/153. The addition of a tritium inventory limit will allow CSAs to be established for States operating fusion reactors so that their inventories fall below the limit. The CSAs should also require the State to provide evidence regarding the required tritium breeding ratio that must be achieved

in their reactor blanket. The information provided determines the total tritium inventory which includes the quantity of tritium needed to account for losses and radioactive decay between production and use, the supply tritium inventory for start-up of other reactors, and an additional stored inventory necessary for continued reactor operation under emergency conditions. The total tritium quantity stored must fall below the 20 gram limitation, and must be reported at beginning of operation along with all the evidence that supports its result. In its yearly inspection, the IAEA will guarantee that the quantity of tritium stored in the facility's inventory does not exceed the total reported. The APs discussed in the previous paragraph apply to tritium in the same manner. This includes information provided by that State about how tritium is handled and stored after plant operation, and information on, and IAEA short-notice access to, all buildings on site to ensure that no secret tritium inventories are found throughout the facility.

Once fusion power plants becomes a reality, amendments to the NPT regarding lithium and tritium should be considered. The end of Article III, Paragraph 1 states that safeguards must be applied to all source or special fissionable material within a State's territory [114]. Although its statement is not exclusive to only fissionable material, it might be wise to include special fusion material, i.e., lithium and tritium. This should also be added to the second paragraph of the same article. This small amendment can be requested by any State per Article VIII. If fusion technology is in the interest of many States by that point in time, there shouldn't be much difficulty for Parties of the NPT to include fusion material in the documentation.

The importance of detecting clandestine activities regarding the production of fissile isotopes such as uranium and plutonium should be emphasized over that of tritium and lithium. All nuclear bombs require a fission reaction to be present to successfully detonate it, no matter if tritium and lithium are present or not. A bountiful production of lithium and tritium without fissile material means that there are other motifs for this material, most likely selling it to other groups. For now, actions can be taken by utilizing the ITDB and CPPNM, and by the NSG.

The lithium-based ternary alloys analyzed in this dissertation contained only natural lithium, which means that in this case, lithium does not meet the required enrichment necessary in a thermonuclear weapon. Any type of enrichment facility discovered through satellite imaging and other means should raise a red flag. There shouldn't be any storage of pure lithium found anywhere on site due its high chemical reactivity with air (Chapter 6), increasing the difficulty of proper storage. IAEA inspections could easily locate pure lithium inventories, due to its special form of storage, usually inside a container filled with oil. Additionally, the minimum tritium breeding ratio constraint for a self-sustaining reactor is 1.02, much lower than magnetic confinement fusion systems. A lower tritium breeding ratio translates to a much lower inventory. Presently, there is no plan to include an additional reservoir of tritium to start-up other reactors, reducing the total inventory even more. As a result, any variational increase of tritium quantities in its inventory should be faster and probably easier detect. In conclusion, the inertial fusion energy reactor with lithium-based ternary blankets will continue to achieve and sustain proliferation-resistant nuclear systems.

7.2.4 Obtaining Lithium and Tritium Currently

In the present day, fusion technology is still in the developing stages and it will probably still take a few decades to build the first fusion commercial power plant. This means that there has to be other measures currently taken by States or non-state actors to obtain lithium and tritium for use in nuclear weapons. The latest was reported on March 9th, 2017 by the Wall Street Journal [138]. North Korea attempted to sell some form of lithium metal to "unidentified buyers." Lithium is found terrestrially through lithium brines, spodumene, and clay deposits [77]. North Korea is believed to have natural deposits of lithium in its soil. Similarly to centrifuges used for enriching uranium, methods for enriching lithium such as chemical exchange do not require extremely large facilities that could be as easily spotted. By producing lithium enriched with lithium-6, tritium can then be easily produced through neutron reactions. If a State like North Korea is creating weapons-grade uranium and plutonium, it would not be difficult to use the same facility to irradiate lithium and create tritium. The latest nuclear test conducted by North Korea in September of 2016 is believed to have created the largest yield to date, most likely by utilizing tritium in a boosted fission weapon. Additionally, obtaining both lithium and tritium could lead to the production of hydrogen bombs, which North Korea claims to have [41]. More importantly, they claim their weapon is miniaturized so that it can be hoisted on to a missile. The latest news on North Korea's attempts to sell lithium presents a security threat in two forms: 1. the proliferation of North Korea's illicit nuclear weapons program, and 2. the proliferation of weapons grade material to unidentified national buyers. With regards to the second point, the Nuclear Supplier's group should try to investigate if any of the buyers of lithium from North Korea are part of the group and if so, it should take necessary measures under their guidelines. It is most important to address the first point, whose solution would apply to the second. So far the solution to deal with North Korea's expanding weapon's program has been to impose economic sanctions, with the harshest given by the U.N. after the last weapons test in 2016 [137]. Imposing different types of sanctions to try to stop the State's capacity to develop weapons and missiles has not been very successful. The nation seems to find ways to adapt to the sanctions, find workarounds, and does not care if its population suffers due to the lack of economic development. Previous presidential administrations, including Clinton, Bush and Obama, tried to negotiate with North Korea if and only North Korea gives up its nuclear weapons. We have seen that North Korea is not willing to do that, specifically after it withdrew from the NPT [72] and Six Party Talks in 2008 [43]. North Korea has sent a clear message to the world that they are not willing to give up their weapon's program since its first test in 2006. Possessing nuclear weapons and missile capabilities allows North Korea to provide a deterrent against any aggression from the US and other top world nations; it is their key to survival. Giving up their weapon's program makes the country more susceptible to be attacked by powerful nations. In addition, the rest of the world would begin to lose interest in the country. Therefore the chances of North Korea giving up this powerful capability are slim to none. Per George Perkovich, Vice President for Studies at the Carnegie Endowment for International Peace, it is recommended for the US to take two actions [125]. The first, is for the US, along with its allies (South Korea, Japan, etc) to acknowledge that North Korea, at least in the short term, is not willing to give up its nuclear weapons. Once this is established, the second recommendation is for the US to negotiate

limitations on how far North Korea can advance its weapon's program, i.e. the size of the nuclear arsenal, range of missile systems. The limitations will provide North Korea with enough of a deterrent to protect themselves against powerful countries so that it doesn't feel threatened against attack. It also provides security for the rest of the world knowing that North Korea will not continue to advance their program to the point that it becomes a large offensive capability. The US should be prepared to give monetary compensation to North Korea for not extending their weapon's program beyond its necessary amount to provide a deterrent. Negotiations between the US and North Korea cannot be bilateral due to the United State's ties with its allies. Ultimately, these recommendations must be accepted by all other countries, specifically those that were part of the Six Party Talks. Critics may say that North Korea might still try to continue to advance its weapons program even with this type of deal due to its history of noncompliance. Nevertheless, if this type of action is not taken, the situation will be worse in the long term. Doing nothing or trying to stop their weapon's program altogether will lead to North's Korea nuclear weapon's proliferation at a much faster rate and with more urgency than by limiting its actions and rewarding it for it with money. Military engagements would lead to a full-scale war and/or North Korea's attempt to use a nuclear weapon.

Part III

Concluding Remarks

Chapter 8

Conclusions and Future Work

8.1 Summary and Conclusions

The work on this dissertation began as a joint effort with Lawrence Livermore National Laboratory to study and find attractive lithium-based ternary alloy candidates that will replace pure lithium in an inertial fusion energy reactor blanket. Lithium is an ideal choice as a breeder and coolant because it produces tritium, creating a self-sustaining system [86]. Additional reactions in the blanket can also transfer heat, and later convert it into electricity. The downfall of lithium and the reason alternatives are being investigated is due to its chemical reactivity [34]. Pure lithium is highly reactive with air and water which can degrade the surrounding components in the reactor. Reactions with the concrete containment can eventually create a breach, exposing the environment to highly radioactive and mobile tritium. Some alternatives have already been under analysis before this work, including binary alloys such as LiPb [10]. Regardless, this alternative abates some of the beneficial properties of lithium such as low corrosion, high thermal conductivity, and most importantly low tritium permeation. For this reason, lithium-based ternary alloys are considered in this work; these alloys should maintain the advantageous attributes of pure lithium as best as possible while minimizing the lithium concentrations to limit the chemical reactivity. This work is specifically focused on the neutronic properties of the alloy and the safety and environmental aspects.

The analysis of the neutronic properties, specifically tritium breeding ratio (TBR) [40] and energy multiplication factor (EMF) [103], of various alloys and selection of top candidates based on their performance was examined in Chapter 3. The TBR is defined as the ratio of tritium produced in the blanket to tritium consumed in the target. The EMF is defined as the ratio of the power deposited in the blanket and other regions of the fusion reactor chamber by neutrons, gammas, and alpha particles, to the power generated from fusion reactions. It was discovered that the performance of an alloy largely depends on nuclear properties of each of the elements in the alloy. The three main properties that can help infer the behavior of the ternaries are: 1. a low absorption cross section, 2. a large neutron multiplication cross section, and 3. a high (and positive) effective Q-value. A lot of the elements in the alloys exhibit two out of the three properties. For example, lead has a low probability of absorbing a neutron but when it does, it most likely will have an $(n,2n)$

reaction. Zinc, on the other hand, also has a low absorption cross section, but generates a high amount of energy in its reactions. As a result, combining lead and zinc will cover all three characteristics making it promising when alloyed with lithium. Two of the elements of interest, barium and tin, exhibit all three properties and not surprisingly displayed some of the best behavior when combined properly with a third component such as lead or zinc. This type of preliminary analysis was able to infer the performance and behavior of the ternaries, thus reducing the number of alloys to simulate by more than 70%, saving time and effort. To easily classify alloys in the Monte Carlo analysis, the TBR and EMF were divided into three categories: aggressive, conservative and semi-conservative. The aggressive pushes the TBR and EMF to its limits at 1.02 and 1.2, respectively. The conservative is the opposite of the aggressive, having the highest TBR limit at 1.1, and lowest EMF limit of at 1.1. The semi-conservative reduces the TBR of the conservative from 1.1 to 1.05. Results revealed that a large number of alloys who had the proper combination of properties previously mentioned were able to meet the conservative and semi-conservative constraints for a wide range of lithium concentrations. Most of the alloys had difficulty achieving the aggressive criteria due to the high demand on the EMF. The TBR and EMF competed against one another; when the lithium concentration was increased, the TBR subsequently increased where as the EMF decreased. The 1.2 EMF required the lithium concentrations to be lower than 50%, which was too low to achieve the desired TBR of 1.02. Nevertheless, a few alloys did meet the aggressive criteria. These included those with multipliers like lead and bismuth, or alloys with an element that exhibits all three desirable properties such as tin and barium. Additional neutronic analysis was performed on one of the alloys, LiSnZn, for enrichment studies. The alloy, containing 65% lithium was enriched with ^6Li from 10% to 90% by increments of 5%. It was observed that the TBR increased up to around 40% enrichment, where it reached its maximum. It then began to decrease due to the lack of additional neutrons and tritium from reactions with ^7Li . When the total lithium concentration is decreased, the effects of ^7Li are less pronounced and the peak TBR will be seen at higher enrichments. Moreover, the enrichment behavior will vary with each alloy due to the slight dependence on the other components of the alloy.

Chapter 3 selected eight candidate alloys (LiBaBi, LiPbBa, LiSnZn, LiCuPb, LiGaPb, LiSrPb, LiPbZn, and LiNaSn) from the neutronic analysis to perform activation analysis and observe some of the most important safety and environmental aspects to consider when designing a fusion reactor blanket. These included decay heat, contact dose rate, accident dose, and waste disposal rating. The safest alloy was found to be LiGaPb, which did not need any active cooling two weeks after shutdown, could begin its recycling process around the same time, and had an adequate accident dose. LiBaBi was concluded to be unsafe since it obtained the highest decay heats, contact dose rates, accident dose, and did not meet the waste disposal rating. In terms of the other alloys evaluated, most can be stored in dry containers around one year after shutdown, and can start the recycling process in small fractions around 9 years later. Overall, with the exception of LiBaBi, these alloys demonstrated that they can be considered as blanket candidates without posing any major environmental or safety concerns. Out of the eight alloys investigated the best four were determined to be LiPbBa, LiGaPb, LiSrPb, and LiPbZn.

The next two chapters focused on the optimization of the neutronic properties

of ternary alloys. Although the preliminary analysis of Chapter 3 reduced the combinations of potential candidates to investigate by more than 70%, each alloy required 231 MCNP calculations so that the entire phase space of the alloy was accounted for and could be evaluated. This methodology, no matter how automated, demanded a lot of computational time and manpower. This led to investigating more adept ways to select the desired alloy compositions for each ternary without having to run so many simulations. Optimization methods are based on perturbation theory and sensitivity analysis. Recently, new methods were developed with the Monte Carlo code Serpent to calculate sensitivity functions [15]. This methodology can actually be simplified to run one calculation with a reference alloy composition and a multitude of perturbed compositions that calculate their respective TBRs. The downfall to using Serpent is the lack of joint neutron-gamma transport which does not allow the EMF to be obtained. Nonetheless, it was decided to investigate the optimization of TBR for a minimum lithium concentration using this new implemented methodology, called Exact Perturbation Theory (EPT). A ternary was divided into 25 simulations of smaller triangles covering close to 5,000 compositions. Based on the results, the composition with the lowest lithium concentration that met a TBR constraint of 1.05 with an imposed EMF of 1.1 from the previous MCNP analysis was chosen for a second and third iteration. By the third iteration, the TBR composition was optimized. This new methodology demonstrated to be very promising. However, the further the perturbations were from the reference point, the greater the uncertainty was. High uncertainties found in the first iteration produced inaccurate results. Due to the location of the reference points being around the center of each smaller triangle, the highest uncertainties were found to be around the triangle's perimeter. This phenomenon was alleviated by either removing the most uncertain points altogether, or performing generalized least squares around each of the most uncertain points. The results demonstrated that the generalized least squares approach, specially when calculated for about half of the points in the first iteration, increased accuracy in the results. Consequently, the compositions for the second and third iteration were better determined. Moreover, when generalized least square results from the first iteration were plotted into the ternary, the entire phase space was depicted more accurately and deviations were almost gone. In summary, utilizing EPT can optimize the TBR composition of an alloy much more accurately and with better speed than by running individual MCNP simulations.

In addition to the EPT method, another optimization technique based on generalized perturbation theory was proposed. It involves either maximizing or minimizing a linear functional by observing the functional's response through perturbations of material densities. There is also an option to include a restraint most likely in the form of another functional. In this particular case the EMF can be maximized with a restraint on the TBR. A code that does exactly this was developed in the 1970s [63], but is now too outdated to run on a modern computer. Different iterations of this code were created throughout time, with the latest being the SMORES [55] code found in the SCALE [22] package. SMORES is based on this exact methodology but can only solve homogenous problems for fission systems. Therefore, instead of writing a new code of this kind to solve fixed source problems, it was decided instead to change the source code of SMORES. The work that has been done thus far is described in Chapter 5. Due to time constraints, the implementation was not completed. The rest of Chapter 5 gives a description of all of the subroutines that should

be altered to successfully finish the implementation of inhomogenous cases into SMORES.

The rest of the work included in this dissertation involved additional topics that when combined with the previous topics discussed create a synergistic approach to identify the best possible ternary alloys. The reason these alternate alloys are being investigated in the first place is due to chemical reactivity concerns of lithium. For this reason it is crucial to perform chemical reactivity experiments on candidate alloys identified from the neutronics and activation analysis. These types of experiments happen to be large scale, time consuming, and costly. Consequently, it was not possible to include them within the scope of the work. In any case, the types of experiments that must be conducted to study chemical reactions should be determined. Chapter 6 reviews past chemical reactivity experiments conducted on pure lithium and LiPb. These included experiments for reactivity with both air and water. The review concluded that air reactivity experiments can be based on the MIT lithium/nitrogen and oxygen experiments with the use of an updated data acquisition system [113]. The past study outlined all of the uncertainties associated with the results and these could be accounted for before conducting the experiments to allow for more accurate results. As for the lithium experiments with water, the type of alloy and water interaction should be considered. This was determined to involve a steam generator tube rupture. It is recommended to use the BLAnket Safety Test (BLAST) experiments [34] as the basis for water reactivity experiments. Both air and water interaction experiments can look to the older experiments as a guide but essentially redesign them with different materials, sizes of containers, and placement of thermocouples and pressure transducers to fit the needs of the current situation.

The last chapter of this thesis examines two categories of policy issues related to fusion reactors: safety and nuclear security. When it comes to safety, the main concern which has been emphasized throughout this work is the chemical reactivity related to lithium and alloys containing it. This issue has already been addressed in the previous chapter regarding the necessary experimentation that will be conducted in future work. A second safety aspect discussed in this chapter and the policies pertaining to it was tritium release. To make sure the limits based on DOE policy were met, accident scenario doses were calculated in Chapter 3. Additionally, tritium permeation concerns will be addressed by colleagues at Livermore National Lab through hydrogen solubility experiments. Lastly, waste disposal criteria was reviewed and applied to fusion technology. The adherence of this criteria was viewed in Chapter 3 with the calculation of the waste disposal rating for candidate alloys.

Nuclear security was the second issue discussed in Chapter 7, and involved studying different scenarios that will impact the security of fusion reactors. The first type of scenarios discussed were related to the production of fissile material in the reactor for use in nuclear weapons and was divided into three cases: 1. Use of an undeclared facility by a State or non-state actor to generate clandestine fissile material, 2. The same case2 but produced in a facility that is declared and safeguarded, and 3. A breakout scenario. Next, the use of lithium and production of tritium from fusion facilities for use in boosted fission and thermonuclear weapons was discussed. The discussion focused on covertly storing tritium and lithium inventories, and the theft of these two elements from the reactor. From this analysis, it is recommended that the IAEA begins to incorporate additional protocols to prevent any covert operations in fusion reactors or breakout scenarios. Additionally, it is

recommended to include fusion reactors in the non-proliferation treaty (NPT) [114]. The last section of this chapter examined the current ways in which state and non-state actors are getting hold of lithium and tritium. Particularly, it focused on the current case of North Korea selling a form of lithium to unidentified buyers. This presented a security threat in two forms: 1. the proliferation of North Korea's illicit nuclear weapons program, and 2. the proliferation of weapons grade material to unidentified national buyers. It is recommended for the US to take two actions. The first is for the US, along with its allies (South Korea, Japan, etc) to acknowledge that North Korea, at least in the short term, is not willing to give up its nuclear weapons. Once this is established, the second recommendation is for the US to negotiate limitations on how far North Korea can advance its weapon's program, i.e. the size of the nuclear arsenal, range of missile systems.

8.2 Future Work

In order to continue identifying candidate alloys and their specific composition successfully, optimization methods must be continued. The work described in Chapter 4 regarding the implementation of EPT into Serpent can be thoroughly expanded. Although the number of triangles within the ternary was specifically chosen, parametric studies can be performed to optimize this number so that efficiency is maximized and accuracy is maintained. The results testing the EPT method are only based on two alloys. Additional alloys should be investigated to strengthen the validity of this implementation. More specifically, a comparison of CPU time in each iteration for a various alloys should be made due to the big difference found between the two alloys investigated thus far. Another aspect of this work that requires improvement is automation of the entire process. Although most of the inputs and analysis of outputs are created utilizing Python scripts, each iteration requires various directories to be made and files to be copied so they can be analyzed. Ideally, a subroutine can be created to automate the cumbersome tasks that are done between iterations. This way, the user only really needs to run one or two scripts per iteration and the rest of the work is done automatically. Doing this would speed up the process increasing efficiency, and avoid any user-made mistakes. Similarly, scripts need to be written to automatically replace specific lines within the EPT subroutines called within the Serpent source code. Right now isotopes for the alloy have to be updated in these subroutines every time a new alloy is chosen. Creating a script to automate this process would remove this time-consuming step. Finally, a better implementation of the EMF into this methodology should be investigated. Even though Serpent does not solve joint neutron-gamma transport problems, it is able to do so separately and transfer information between one simulation to another. This should be considered so that the EMF can be included within the optimization studies, and the most adequate alloy composition can be chosen.

Chapter 5 has a lot of opportunities for future work and includes its own "future work" section describing all the specific alterations that should be made to the SMORES code. The modifications to still be made include alterations in the input file, subroutines within the SMORES module, and the optimization module, SWIF. One can refer to the section in the chapter for a detailed outline of all the tasks that need to be executed. The deterministic methodology of SMORES is advantageous over Monte Carlo optimization be-

cause each case can be ran at a fraction of the time. However, the accuracy of results is lower than Monte Carlo method due to modeling in one dimension as opposed to three. If the implementation of fixed source problems in SMORES is proven successful, a joint optimization between SMORES and Serpent could be created. To do this, first, the deterministic code (SMORES) is executed to obtain an estimate of the optimal composition. Secondly, Serpent performs one EPT simulation centered around the region of the optimal composition given by SMORES, and proceeds to calculate a better accurate alloy concentration. Using the deterministic code removes the hassle of simulating the entire ternary for each alloy and reduces the number of simulations from around 29 to 2-4, depending if one decides to optimize the blanket as a whole, or each blanket region separately. A diagram of this was shown in Fig. 5.7 in Chapter 5.

The importance of determining the effects of chemical reactivity of these new lithium-based ternary alloys has been stressed many times throughout this dissertation. Therefore, it is crucial to conduct experiments based on the advice given in the previous section and at the end of Chapter 6. Lastly, it should be noted that all of the policy issues regarding the safety of fusion reactors have been addressed for the most part in this work. However, issues pertaining to natural security should always be kept in mind when selecting candidate alloys.

Bibliography

- [1] <http://atom.kaeri.re.kr/>.
- [2] How ICF Works. <https://lasers.llnl.gov/science/icf/how-icf-works>.
- [3] <http://hyperphysics.phy-astr.gsu.edu/hbase/nucene/nucbin.html#c4>.
- [4] Safety of Magnetic Fusion Facilities Guidance. DOE-STD-6003-96, U.S. Department of Energy, 1996.
- [5] Safety of Magnetic Fusion Facilities' Requirements. DOE-STD-6002-96, U.S. Department of Energy, 1996.
- [6] A.A. Abagyan, A.A. Dubinin, Yu A. Kazanskii, V.V. Orlov, E.E. Petrov, and V. Ya Pupko. The optimization of nuclear shielding characteristics on the basis of variational methods. In *Proceedings Conference Physics Problem of Reactor Shielding*, volume 4, page 1098, 1967.
- [7] M A_ Abdou, EL Vold, CY Gung, MZ Youssef, and K Shin. Deuterium-tritium fuel self-sufficiency in fusion reactors. *Fusion Science and Technology*, 9(2):250–285, 1986.
- [8] M.A. Abdou, P.J. Gierszewski, M.S. Tillack, M. Nakagawa, J. Reimann, D.K. Sze, J. Bartlit, J. Grover, R. Puigh, and R.T. McGrath. Technical issues and requirements of experiments and facilities for fusion nuclear technology. *Nuclear Fusion*, 27(4):619, 1987.
- [9] M.A. Abdou and C.W. Maynard. Computational methods for nuclear heating-part I: theoretical and computational algorithms. *Nuclear Science and Engineering*, 56(4):360–380, 1975.
- [10] M.A. Abdou, N.B. Morley, A.Y. Ying, S. Smolentsev, and P. Calderoni. Overview of fusion blanket R&D in the us over the last decade. *Nuclear Engineering and Technology*, 37(5):401, 2005.
- [11] Mohamed Abdou, Neil B Morley, Sergey Smolentsev, Alice Ying, Siegfried Malang, Arthur Rowcliffe, and Mike Ulrickson. Blanket/first wall challenges and required R&D on the pathway to DEMO. *Fusion Engineering and Design*, 100:2–43, 2015.

- [12] International Atomic Energy Agency. INFCIRC/153.THE STRUCTURE AND CONTENT OF AGREEMENTS BETWEEN THE AGENCY AND STATES REQUIRED IN CONNECTION WITH THE TREATY ON THE NON-PROLIFERATION OF NUCLEAR WEAPONS, 1972. <https://www.iaea.org/sites/default/files/infcircs/1972/infcirc153.pdf>.
- [13] International Atomic Energy Agency. INFCIRC/540.MODEL PROTOCOL ADDITIONAL TO THE AGREEMENT(S) BETWEEN STATE(S) AND THE INTERNATIONAL ATOMIC ENERGY AGENCY FOR THE APPLICATION OF SAFEGUARDS, 1997. <https://www.iaea.org/sites/default/files/infcirc540.pdf>.
- [14] International Atomic Energy Association. *IAEA Nuclear Security Series No. 6: Combating Illicit Trafficking in Nuclear and other Radioactive Material*. IAEA, 2007.
- [15] Manuele Aufiero, Adrien Bidaud, Mathieu Hursin, Jaakko Leppänen, Giuseppe Palmiotti, Sandro Pelloni, and Pablo Rubiolo. A collision history-based approach to sensitivity/perturbation calculations in the continuous energy Monte Carlo code SERPENT. *Annals of Nuclear Energy*, 85:245–258, 2015.
- [16] D.E. Bartine, R.G. Alsmiller Jr., E.M. Oblo, and F.R. Mynatt. Cross-section sensitivity of breeding ratio in a fusion-reactor blanket. *Nuclear Science and Engineering*, 53(3):304–318, 1974.
- [17] D.E. Bartine, E.M. Oblo, and F.R. Mynatt. Radiation-transport cross-section sensitivity analysis—A general approach illustrated for a thermonuclear source in air. *Nuclear Science and Engineering*, 55(2):147–167, 1974.
- [18] Rainer Bass. Fusion of heavy nuclei in a classical model. *Nuclear Physics A*, 231(1):45–63, 1974.
- [19] Martin Becker, Jeffery Lewins, and Ernest Justus Henley. *Advances in Nuclear Science and Technology*. Plenum Press, 1977.
- [20] George I. Bell and Samuel Glasstone. *Nuclear Reactor Theory*, volume 252. Van Nostrand Reinhold New York, 1970.
- [21] L.V. Boccaccini et al. Present status of the conceptual design of the EU test blanket systems. *Fusion Engineering and Design*, 86(6):478–483, 2011.
- [22] Steven M. Bowman. Scale 6: comprehensive nuclear safety analysis code system. *Nuclear Technology*, 174(2):126–148, 2011.
- [23] J.F. Briesmeister. MCNP: a general Monte Carlo code for neutron and photon transport. Version 3A. Revision 2. Technical Report LA-7396-M-Rev.2, Los Alamos National Lab., NM (USA), 1986.
- [24] A. Cardella, E. Rigal, L. Bedel, P.h. Bucci, J. Fiek, L. Forest, L.V. Boccaccini, E. Diegele, L. Giancarli, S. Hermsmeyer, et al. The manufacturing technologies of the european breeding blankets. *Journal of Nuclear Materials*, 329:133–140, 2004.

- [25] J.P. Catalán, F. Ogando, and J. Sanz. Activation analysis for a He/LiPb dual coolant blanket for DEMO reactor. *Fusion Science and Technology*, 60(2):738–742, 2011.
- [26] M.B. Chadwick et al. ENDF/B-VII.0: next generation evaluated nuclear data library for nuclear science and technology. *Nuclear data sheets*, 107(12):2931–3060, 2006.
- [27] E.T. Cheng. Application of generalized variational principles to controlled thermonuclear reactor neutronics analysis. *Nuclear Science and Engineering*, 74(2):147–153, 1980.
- [28] E.T. Cheng, D.K. Sze, J.A. Sommers, and O.T. Farmer III. Materials recycling considerations for DT fusion reactors. *Fusion Science and Technology*, 21(3P2B):2001–2008, 1992.
- [29] Seungyon Cho et al. Overview of helium cooled ceramic reflector test blanket module development in Korea. *Fusion Engineering and Design*, 88(6):621–625, 2013.
- [30] Seungyon Cho et al. Design and R&D progress of Korean HCCR TBM. *Fusion Engineering and Design*, 89(7):1137–1143, 2014.
- [31] Nuclear Regulatory Commission. Standards of protection against radiation, 10CFR20. *US Office of the Federal Register, Washington, DC*, 1991.
- [32] US Nuclear Regulatory Commission. Licensing Requirements for Land Disposal of Radioactive Waste. title 10, Code of Federal Regulations, Part 61 (10CFR61). *Federal Register, FR47*, 57446, 1982.
- [33] Robert Conn and W.M. Stacey Jr. Variational methods for controlled thermonuclear reactor blanket studies. *Nuclear Fusion*, 13(2):185, 1973.
- [34] M.L. Corradini and D.W. Jeppson. Lithium alloy chemical reactivity with reactor materials: current state of knowledge. *Fusion engineering and design*, 14(3-4):273–288, 1991.
- [35] A.E. Costley. On the fusion triple product and fusion power gain of tokamak pilot plants and reactors. *Nuclear Fusion*, 56(6):066003, 2016.
- [36] Roger R. Coveyou, V.R. Cain, and K.J. Yost. Adjoint and importance in Monte Carlo application. *Nuclear Science and Engineering*, 27(2):219–234, 1967.
- [37] Kevin D. Crowley and John F. Ahearne. Managing the environmental legacy of u. s. nuclear-weapons production. *American Scientist*, 90(6):514–523, 2002.
- [38] James J. Duderstadt and Louis J. Hamilton. *Nuclear Reactor Analysis*, volume 84. Wiley New York, 1976.
- [39] M. Dunne et al. Timely delivery of laser inertial fusion energy (LIFE). *Fusion Science and Technology*, 60(1):19–27, 2011.

- [40] Laila A. El-Guebaly and Siegfried Malang. Toward the ultimate goal of tritium self-sufficiency: technical issues and requirements imposed on ARIES advanced power plants. *Fusion Engineering and Design*, 84(12):2072–2083, 2009.
- [41] Holly Ellyatt. Just what is a 'miniaturized' hydrogen bomb? *CNBC*, January 2016.
- [42] M.J. Embrechts. *Two-dimensional cross-section sensitivity and uncertainty analysis for fusion reactor blankets*. PhD thesis, Virginia Polytechnic Inst. and State Univ., Blacksburg, VA, 1981.
- [43] Robin Emmott. China sees chance of six-party talks with North Korea. *Reuters*, February 2017.
- [44] Mikiyo Enoda et al. Development of the water cooled ceramic breeder test blanket module in Japan. *Fusion Engineering and Design*, 87(7):1363–1369, 2012.
- [45] K.M. Feng et al. New progress on design and R&D for solid breeder test blanket module in China. *Fusion Engineering and Design*, 89(7):1119–1125, 2014.
- [46] H.O.M. Fisher. *A Nuclear Cross Section Data Handbook*. Los Alamos National Laboratory, 1989.
- [47] R.A. Forrest et al. *The European activation system: EASY-2007 overview*. Citeseer, 2007.
- [48] Robin A. Forrest and M.R. Gilbert. *FISPACT-2007: User manual*. EURATOM/UKAEA fusion association, 2007.
- [49] C.B.A. Forty and I. Cook. Low activation structural material candidates for fusion power plants. Technical report, UKAEA Government Division, 1997.
- [50] Jeffrey P. Freidberg. *Plasma physics and fusion energy*. Cambridge university press, 2008.
- [51] J.P. Freidberg. *Ideal magnetohydrodynamics*. Plenum Press, New York, NY, Jan 1987.
- [52] Augusto Gandini. Generalized perturbation theory (GPT) methods. A heuristic approach. In *Advances in Nuclear Science and Technology*, pages 205–380. Springer, 1987.
- [53] Alexander Glaser and Robert J Goldston. Proliferation risks of magnetic fusion energy: clandestine production, covert production and breakout. *Nuclear Fusion*, 52(4):043004, 2012.
- [54] Robert J. Goldston and Alexander Glaser. Safeguard Requirements for Fusion Power Plants. Technical report, Princeton Plasma Physics Laboratory (PPPL), Princeton, NJ (United States), 2012.

- [55] Sedat Goluoglu, L.M. Petrie, C.M. Hopper, Y. Karni, D. Regev, and E. Greenspan. SMORES—A New Scale Sequence for the Determination of Bounding Curves and Data. In *Proc. of ANS 2002 Annual Meeting: The Revival of the Nuclear Energy Option, Hollywood, Florida*, pages 114–116, 2002.
- [56] T. Goorley et al. Initial MCNP6 release overview. *Nuclear Technology*, 180(3):298–315, 2012.
- [57] N.M. Greene, L.M. Petrie, and M.L. Williams. XSDRNPM, a one-dimensional discrete-ordinates code for transport analysis. Technical Report ORNL/TM-2005/39, Vol. II, Book 1, Sec. F3, Oak Ridge National Laboratory, 2005.
- [58] E. Greenspan. Method for the optimization of fusion reactor neutronic characteristics. Technical Report CONF-730414–P2, Princeton Univ., NJ; American Nuclear Society. Michigan Section, 1973.
- [59] E. Greenspan. Variational versus generalized perturbation theories—are they different? *Nuclear Science and Engineering*, 57:250–251, 1975.
- [60] E. Greenspan. Developments in perturbation theory. *Advances in Nuclear Science and Technology*, 9:181–268, 1976.
- [61] E. Greenspan. SWANS: A prototypic SCALE criticality sequence for automated optimization using the SWAN methodology. Technical report, Oak Ridge National Lab., TN (US), 2001.
- [62] E. Greenspan, A. Kinrot, and P. Levin. Optimal blanket concepts for DT fusion reactors. *Fusion Technol.:(United States)*, 8(1):619–624, 1985.
- [63] E. Greenspan, W.G. Price Jr., and H. Fishman. SWAN: A code for the analysis and optimization of fusion reactor nucleonic characteristics. Technical Report MATT-1008, PPPL (Princeton Plasma Physics Laboratory (PPPL), Princeton, NJ (United States)), 1973.
- [64] MATLAB User’s Guide. The mathworks. *Inc., Natick, MA*, 5:333, 1998.
- [65] Alireza Haghghat and John C. Wagner. Monte Carlo variance reduction with deterministic importance functions. *Progress in Nuclear Energy*, 42(1):25–53, 2003.
- [66] John Harrison, Rich Leggett, David Lloyd, Alan Phipps, and Bobby Scott. Polonium-210 as a poison. *Journal of Radiological Protection*, 27(1):17, 2007.
- [67] C.K. Hayakawa, Jerome Spanier, Frédéric Bevilacqua, Andrew K. Dunn, Joon S. You, Bruce J. Tromberg, and Vasan Venugopalan. Perturbation monte carlo methods to solve inverse photon migration problems in heterogeneous tissues. *Optics letters*, 26(17):1335–1337, 2001.

- [68] O.W. Hermann and R.M. Westfall. ORIGEN-S: SCALE system module to calculate fuel depletion, actinide transmutation, fission product buildup and decay, and associated radiation source terms. *Vol. II, Sect. F7 of SCALE: A Modular Code System for Performing Standardized Computer Analyses for Licensing Evaluation, NUREG/CR-0200, Rev, 6*, 1995.
- [69] J.P. Herzog et al. Lithium-lead/water interactions: Experiments and analysis. In *Proceedings of ANS Meeting on Fusion Technology, Salt Lake City, UT (October 1988)*, 1989.
- [70] Andreas H. Hielscher, Raymond E. Alcouffe, and Randall L. Barbour. Comparison of finite-difference transport and diffusion calculations for photon migration in homogeneous and heterogeneous tissues. *Physics in Medicine and Biology*, 43(5):1285, 1998.
- [71] Thomas J. Hoffman, James C. Robinson, and Paul N. Stevens. The adjoint difference method and its application to deep-penetration radiation transport. *Nuclear Science and Engineering*, 48(2):179–188, 1972.
- [72] Wade L. Huntley. North Korea & the NPT. *Foreign Policy In Focus*, October 2005.
- [73] T. Ihli, T.K. Basu, L.M. Giancarli, S. Konishi, S. Malang, F. Najmabadi, S. Nishio, A.R. Raffray, C.V.S. Rao, A. Sagara, et al. Review of blanket designs for advanced fusion reactors. *Fusion Engineering and Design*, 83(7):912–919, 2008.
- [74] D.W. Jeppson. Interactions of liquid lithium with various atmospheres, concretes, and insulating materials; and filtration of lithium aerosols. Technical Report HEDL-TME-79-7, Hanford Engineering Development Lab., Richland, WA (USA), 1979.
- [75] A. Jolodosky et al. Neutronics and activation analysis of lithium-based ternary alloys in IFE blankets. *Fusion Engineering and Design*, 107:1–12, 2016.
- [76] W.C. Jordan, S.M. Bowman, and D.F. Hollenbach. Scale cross-section libraries. *Vol. III, Sect. M4 of SCALE: A Modular Code System for Performing Standardized Computer Analysis for Licensing Evaluation, NUREG/CR-0200, Rev, 7(3)*, 1997.
- [77] Conrad W. Kamienski, Daniel P. McDonald, Marshall W. Stark, and John R. Papcun. Lithium and lithium compounds. *Kirk-Othmer encyclopedia of chemical technology*, 2004.
- [78] Takeaki Kariya and Hiroshi Kurata. *Generalized least squares*. John Wiley & Sons, 2004.
- [79] Y. Karni and E. Greenspan. Minimum thickness blanket-shield for fusion reactors. *Fusion Engineering and Design*, 10:63–69, 1989.
- [80] G.L. Khorasanov, A.P. Ivanov, and A.I. Blokhin. Polonium issue in fast reactor lead coolants and one of the ways of its solution. In *10th International Conference on Nuclear Engineering*, pages 711–717. American Society of Mechanical Engineers, 2002.

- [81] Brian C. Kiedrowski and Forrest B. Brown. Adjoint-based k -eigenvalue sensitivity coefficients to nuclear data using continuous-energy Monte Carlo. *Nuclear science and Engineering*, 174(3):227–244, 2013.
- [82] Brian C. Kiedrowski, Forrest B. Brown, and Paul P.H. Wilson. Adjoint-weighted tallies for k -eigenvalue calculations with continuous-energy Monte Carlo. *Nuclear Science and Engineering*, 168(3):226–241, 2011.
- [83] D.C. Kocher and K.F. Eckerman. Dose conversion factors. Technical Report CONF-9203121-2, Oak Ridge National Lab., TN (United States), 1992.
- [84] E. Rajendra Kumar et al. Preliminary design of Indian test blanket module for ITER. *Fusion Engineering and Design*, 83(7):1169–1172, 2008.
- [85] B.V. Kuteev et al. Steady-state operation in compact tokamaks with copper coils. *Nuclear Fusion*, 51(7):073013, 2011.
- [86] Jeffery F. Latkowski et al. Chamber design for the laser inertial fusion energy (LIFE) engine. *Fusion Science and Technology*, 60(1):54–60, 2011.
- [87] J.F. Latkowski, J. Sanz, S Reyes, and J. Gomez del Rio. Selection of IFE target materials from a safety and environmental perspective. *Nuclear Instruments and Methods in Physics Research Section A: Accelerators, Spectrometers, Detectors and Associated Equipment*, 464(1):422–427, 2001.
- [88] John D. Lawson. Some criteria for a power producing thermonuclear reactor. *Proceedings of the Physical Society. Section B*, 70(1):6, 1957.
- [89] D. Laycak. Preliminary Study of Radiological Doses from Released Nuclides from LIFE Reactor LLNL Safety Division. Technical report, LLNL Safety Division, May 2012.
- [90] Der-Tsai Lee and Bruce J. Schachter. Two algorithms for constructing a delaunay triangulation. *International Journal of Computer & Information Sciences*, 9(3):219–242, 1980.
- [91] Jaakko Leppänen. *Development of a new Monte Carlo reactor physics code*. PhD thesis, Helsinki University of Technology, 2007.
- [92] Jaakko Leppänen. Performance of woodcock delta-tracking in lattice physics applications using the serpent monte carlo reactor physics burnup calculation code. *Annals of Nuclear Energy*, 37(5):715–722, 2010.
- [93] Jaakko Leppänen. Serpent—a continuous-energy monte carlo reactor physics burnup calculation code. *VTT Technical Research Centre of Finland*, 4, 2013.
- [94] Jaakko Leppänen, Manuele Aufiero, Emil Fridman, Reuven Rachamin, and Steven van der Marck. Calculation of effective point kinetics parameters in the Serpent 2 Monte Carlo code. *Annals of Nuclear Energy*, 65:272–279, 2014.

- [95] Peretz Levin and Nasr M. Ghoniem. Neutronic optimization of a LiAlO₂ solid breeder blanket. *Fusion Science and Technology*, 10(3P2B):1634–1639, 1986.
- [96] Jeffery Lewins. *Importance: The Adjoint Function*. Pergamon, New York, 1965.
- [97] John Lindl. Development of the indirect-drive approach to inertial confinement fusion and the target physics basis for ignition and gain. *Physics of Plasmas*, 2(11):3933–4024, 1995.
- [98] John D. Lindl. *Inertial confinement fusion: the quest for ignition and energy gain using indirect drive*. American Institute Of Physics, 1998.
- [99] John D. Lindl, Peter Amendt, Richard L. Berger, S. Gail Glendinning, Siegfried H. Glenzer, Steven W. Haan, Robert L. Kauffman, Otto L. Landen, and Laurence J. Suter. The physics basis for ignition using indirect-drive targets on the national ignition facility. *Physics of Plasmas*, 11(2):339–491, 2004.
- [100] Donald MacKenzie and Graham Spinardi. Tacit knowledge, weapons design, and the uninvention of nuclear weapons. *American Journal of Sociology*, 101(1):44–99, 1995.
- [101] Siegfried Malang and R. Mattas. Comparison of lithium and the eutectic lead-lithium alloy, two candidate liquid metal breeder materials for self-cooled blankets. *Fusion Engineering and Design*, 27:399–406, 1995.
- [102] W. Meier et al. Ternary Alloy Development for Enhanced Safety and Performance of Fusion Systems. Technical Report 14-EDR-035, Lawrence Livermore National Laboratory, 2015.
- [103] Wayne R. Meier and Edward C. Morse. Blanket optimization studies for the HYLIFE inertial confinement fusion reactor. *Fusion Science and Technology*, 8(3):2681–2695, 1985.
- [104] W.R. Meier. *Multivariable optimization of fusion reactor blankets*. PhD thesis, Univ. of California, Berkeley, CA, Jan 1984.
- [105] W.R. Meier. Fusion Power Multiplication for LIFE. Technical Report LLNL-MI-66681, Lawrence Livermore National Lab, Livermore, CA, February 2015.
- [106] W.R. Meier and P. Amendt. Communication, 2014.
- [107] George H Miller, Edward I Moses, and Craig R Wuest. The national ignition facility. *Optical Engineering*, 43(12):2841–2853, 2004.
- [108] R.G. Mills. Fusion power plant. Technical report, PPPL (Princeton Plasma Physics Laboratory (PPPL), Princeton, NJ (United States)), 1974.
- [109] Niel B. Morley et al. Recent research and development for the dual-coolant blanket concept in the US. *Fusion Engineering and Design*, 83(7):920–927, 2008.

- [110] Janice M. Morse. Approaches to qualitative-quantitative methodological triangulation. *Nursing Research*, 40(2):120–123, 1991.
- [111] E.I. Moses. The national ignition facility and the promise of inertial fusion energy. *Fusion Science and Technology*, 60(1):11–16, 2011.
- [112] L.D. Muhlestein and D.W. Jeppson. Liquid lithium containment and control. Technical Report HEDL-SA–1623, Hanford Engineering Development Lab., Richland, WA (USA), 1978.
- [113] L.D. Muhlestein and D.W. Jeppson. Kinetics of liquid lithium reaction with oxygen-nitrogen mixtures. Technical Report PFC/RR-86-1, Massachusetts Inst. of Tech., Cambridge (USA). Plasma Fusion Center, 1986.
- [114] United Nations. THE TREATY ON THE NON-PROLIFERATION OF NUCLEAR WEAPONS NPT, 2005. <http://www.un.org/en/conf/npt/2005/npttreaty.html>.
- [115] Yasushi Nauchi and Takanori Kameyama. Development of calculation technique for Iterated Fission Probability and reactor kinetic parameters using continuous-energy Monte Carlo method. *Journal of nuclear science and technology*, 47(11):977–990, 2010.
- [116] A.L. Nichols. Nuclear data requirements for decay heat calculations. *ICTP Lecture Notes*, 20:65–195, 2002.
- [117] Mary Beth Nikitin. North korea’s nuclear weapons: Technical issues. *Current Politics and Economics of Northern and Western Asia*, 22(3):377, 2013.
- [118] Masabumi Nishikawa. Tritium balance in a dt fusion reactor. *Fusion Science and Technology*, 59(2):350–362, 2011.
- [119] E.M. Oblow. General sensitivity theory for radiation transport. Technical Report ORNL-TM–4110, Oak Ridge National Lab., Tenn., 1973.
- [120] U.S. Department of Energy. MACCS2 computer code application guidance for documented safety analysis. Technical Report DOE-EH-4.2.1.4-MACCS2-Code Guidance, Sandia National Lab, June 2004.
- [121] J. Ongena, R. Koch, R. Wolf, and H. Zohm. Magnetic-confinement fusion. *Nature Physics*, 12(5):398–410, 2016.
- [122] R. Pampin and A. Davis. Novel tools for estimation of activation dose: Description, preliminary comparison and nuclear data requirements. *United Kingdom Atomic Energy Authority Report, UKAEA-FUS-549*, 2008.
- [123] L.R. Payne. The hazards of cobalt. *Occupational Medicine*, 27(1):20–25, 1977.
- [124] C.M. Perfetti and B.T. Rearden. Continuous-energy Monte Carlo methods for calculating generalized response sensitivities using tsunami-3d. In *PHYSOR*, Kyoto Japan, Sep. 28-Oct. 3 2014.

- [125] George Perkovich. North Korea's Nuclear Weapons Program. Interview with J.M. Lindsay and R. McMahon, 2017.
- [126] David A. Petti et al. Re-evaluation of the use of low activation materials in waste management strategies for fusion. *Fusion Engineering and Design*, 51:435–444, 2000.
- [127] David Andrew Petti, Jacopo Buongiorno, John Thomas Maki, Richard Redfield Hobbins, and Gregory Kent Miller. Key differences in the fabrication, irradiation and high temperature accident testing of US and German TRISO-coated particle fuel, and their implications on fuel performance. *Nuclear Engineering and Design*, 222(2):281–297, 2003.
- [128] Steven J. Piet, Edward T. Cheng, Steve Fetter, and J. Stephen Herring. Initial integration of accident safety, waste management, recycling, effluent, and maintenance considerations for low-activation materials. *Fusion Science and Technology*, 19(1):146–161, 1991.
- [129] Steven J. Piet, Edward T. Cheng, and Lisa J. Porter. Accident safety comparison of elements to define low-activation materials. *Fusion Science and Technology*, 17(4):636–657, 1990.
- [130] Frederick W. Pontius. *Appendix H: Outline of 40 CFR 141, 142, and 143, in Drinking Water Regulation and Health*. John Wiley & Sons, Inc., 2003.
- [131] Syed M. Qaim. *Nuclear Data for Science and Technology: Proceedings of an International Conference, Held at the Forschungszentrum Jülich, Fed. Rep. of Germany, 13–17 May 1991*. Springer Science & Business Media, 2012.
- [132] S. Reyes et al. LIFE tritium processing: a sustainable solution for closing the fusion fuel cycle. *Fusion Science and Technology*, 64(2):187–193, 2013.
- [133] Andrey Rzhetsky and Masatoshi Nei. Statistical properties of the ordinary least-squares, generalized least-squares, and minimum-evolution methods of phylogenetic inference. *Journal of molecular evolution*, 35(4):367–375, 1992.
- [134] Ryan Sacks et al. Parameter study of an inertial fusion energy chamber response using the 1-D BUCKY radiation hydrodynamics code. *Fusion Science and Technology*, 66(2):349–357, 2014.
- [135] Javier Sanz, Oscar Cabellos, Nuria García-Herranz, et al. ACAB inventory code for nuclear applications: User's manual V. 2008. *NEA-1839*, 6:475–480, 2008.
- [136] Jeffrey E. Seifried, Massimiliano Fratoni, Kevin J. Kramer, Jeffery F. Latkowski, Per F. Peterson, Jeffrey J. Powers, and Janine M. Taylor. Adjoint-based uncertainty analysis for essential reactions in a laser inertial fusion engine. *Fusion Science and Technology*, 60(2):692–697, 2011.
- [137] Laura Smith-Park and Richard Roth. Toughest UN sanctions yet to cost North Korea \$800 million. *CNN*, November 2016.

- [138] Jay Solomon. Pyongyang Hawked Nuclear-Weapon Metal. *The Wall Street Journal*, page A8, March 2017.
- [139] W.M. Stacey Jr. *Variational Methods in Nuclear Reactor Physics*, volume 10. Academic Press Inc, New York, 1974.
- [140] Tadeusz Strulak. The nuclear suppliers group. *The Nonproliferation Review*, 1(1):2–10, 1993.
- [141] J-Ch Sublet, James W. Eastwood, J. Guy Morgan, Michael Fleming, and Mark R. Gilbert. The fispack-ii user manual. *CCFE-R*, 11(11), 2012.
- [142] Dai Kai Sze. Tritium. On the exploration of innovative concepts for fusion chamber technology, APEX interim report (overview). Technical Report UCLA-ENG-99-206, UCLA-FNT-107, University of California, Los Angeles, California, 1999.
- [143] Neill P. Taylor, Edward T. Cheng, D. Petti, and Massimo Zucchetti. Overview of international waste management activities in fusion. *Fusion Science and Technology*, 39(2):350–358, 2001.
- [144] P.E.. Turchi. Thermodynamic assessment of the ternary alloy system Li-Sn-Zn. Technical Report LLNL report LLNL-TR-653675, Lawrence Livermore National Lab, Livermore, CA, April 2014.
- [145] W.F. Vogelsang. Breeding ratio, inventory, and doubling time in a DT fusion reactor. *Nuclear Technology*, 15(3):470–474, 1972.
- [146] C.R. Weisbin, E.M. Oblow, J.H. Marable, R.W. Peelle, and J.L. Lucius. Application of sensitivity and uncertainty methodology to fast reactor integral experiment analysis. *Nuclear Science and Engineering*, 66(3):307–333, 1978.
- [147] Mark L. Williams. Perturbation theory for nuclear reactor analysis. *CRC Handbook of Nuclear Reactors Calculations*, 3:63–188, 1986.
- [148] Yican Wu, Jieqiong Jiang, Minghuang Wang, M. Jin, FDS Team, et al. A fusion-driven subcritical system concept based on viable technologies. *Nuclear Fusion*, 51(10), 2011.
- [149] Yican Wu and F.D.S. Team. Design analysis of the China dual-functional lithium lead (DFLL) test blanket module in ITER. *Fusion Engineering and Design*, 82(15):1893–1903, 2007.
- [150] Yican Wu and F.D.S. Team. Design status and development strategy of China liquid lithium–lead blankets and related material technology. *Journal of Nuclear Materials*, 367:1410–1415, 2007.

Appendix A

Neutronic Blanket Functions

The primary functions of fusion reactor blankets are to utilize neutrons released by fusion reactions to breed tritium, and to convert the kinetic energy of these neutrons into heat, and are quantified through the tritium breeding ratio (TBR), and energy multiplication factor (EMF). The following two sections will describe these two metrics in detail.

A.0.1 Tritium Breeding Ratio

The tritium breeding ratio quantifies the blanket's ability to produce an adequate amount of tritium that can be recycled and utilized as fuel. It is defined as the ratio between the amount of tritium produced in fusion system (most commonly the blanket), to the amount of tritium burned in the fusion plasma. To be able to create additional source material this ratio must be greater than one. Abdou [7] specifically defined this as the required TBR. The required TBR is function of plasma physics and operating parameters. There are three parameters that must be met by the required TBR. First, tritium is highly radioactive and decays at a rate of about 5.5 percent per year. Thus, the required TBR must account for these losses. Second, because tritium does not occur naturally on earth, enough must be produced to start up additional reactors. Third, a determined amount tritium must be kept in reserve in case it is needed due to any disturbances or accidents during plant operation, including malfunctions in the tritium processing system. Additional parameters must also be accounted for that will affect the required TBR. For example, the burn-up of tritium in the plasma will determine how often the fuel has to be replaced, and therefore affect the amount of tritium in a start-up reserve. Another factor is the type of tritium processing utilized which accounts for the time it will take to process the tritium, and any type of inefficiencies found within the processing system. Other parameters include the combination of the permeability of tritium and how easily the reactor components can trap the tritium such that it can not be easily recovered. As an example, if the burn-up of the fuel is very low (less than 5%), it will also affect the amount of tritium in reserve both for start-up and for accidents. The low burn-up and high reserve will therefore have a pivotal effect on the required TBR [11]. It is important to note that the tritium inventory should be kept as low as necessary due to tritium's highly radioactive and mobile nature. Models have been created to quantify the required TBR and are found in Refs. [7, 118, 145].

The required TBR must be greater than unity. However, to achieve self-sufficiency

in the reactor the actual TBR that can be obtained from a operable blanket must be equal to or greater than the required TBR. Abdou calls this quantity the achievable TBR, and is mostly a function of the type of blanket and first wall design in the system [11]. Other factors that influence this quantity include other components that affect the plasma and its products, such as the hohlraum and xenon gas in the inertial fusion energy (IFE) system described in Chapter 1, and the confinement scheme. The achievable TBR can be calculated with either deterministic or Monte Carlo codes. Its calculation must account for uncertainties in the geometry and modeling of the code, and the uncertainties in the nuclear data utilized by the chosen code. Additional uncertainties in the calculated result will come from the system definition such as the defined thickness of the first wall, blanket, and structural components.

A.0.2 Energy Multiplication Factor

The energy multiplication factor determines how efficiently the energy released from fusion reactions is converted into heat. It is quantified as the ratio between the amount of energy created in the blanket to the amount of energy released from the fusion reactions. This ratio should be greater than unity. However, unlike the TBR, the EMF is not constrained by a specific number; rather, its goal is to be as high as possible. The more the blanket increases the kinetic energy of fusion neutrons through interactions, the more thermal energy that is available to be utilized for electricity. Therefore, the higher the energy multiplication factor, the higher the thermal output, and the lower the cost of electricity [103].

Appendix B

Source Reciprocity Relationship

If a neutron is introduced into a system at some time, t , the flux will be increased and therefore affect the contribution to some type of detector response, R . The change in the response caused by the introduction of the neutron in the system is the importance, $\psi^\dagger(\mathbf{r}, \hat{\Omega}, E, t)$. The importance is only accounted for in times $t_0 < t < t_f$, and thus is 0 when $t > t_f$. In this particular case, the initial condition is defined as:

$$\psi(\mathbf{r}, \hat{\Omega}, E, t) = S_o(\mathbf{r}, \hat{\Omega}, E) \quad (\text{B.1})$$

where S_o is defined by:

$$S(\mathbf{r}, \hat{\Omega}, E, t) = S_o(\mathbf{r}, \hat{\Omega}, E)\delta(t - t_o) \quad (\text{B.2})$$

where $\delta(t - t_o)$ is a dirac delta function. The adjoint source, $S_o^\dagger(\mathbf{r}, \hat{\Omega}, E, t)$ can similarly be characterized as:

$$S^\dagger(\mathbf{r}, \hat{\Omega}, E, t) = S_o^\dagger(\mathbf{r}, \hat{\Omega}, E)\delta(t - t_f) \quad (\text{B.3})$$

From the above equation, the response can then be expressed as the product of the adjoint source and forward flux at time t_f :

$$R = \left\langle S_o^\dagger(\mathbf{r}, \hat{\Omega}, E), \psi(\mathbf{r}, \hat{\Omega}, E, t_f) \right\rangle \quad (\text{B.4})$$

The response can also be interpreted as the contribution of neutrons originating from S_o weighted by their importances. Hence:

$$R = \left\langle S_o^\dagger(\mathbf{r}, \hat{\Omega}, E), \psi(\mathbf{r}, \hat{\Omega}, E, t_r) \right\rangle = \left\langle \psi^\dagger(\mathbf{r}, \hat{\Omega}, E, t_o), S_o(\mathbf{r}, \hat{\Omega}, E) \right\rangle \quad (\text{B.5})$$

At a time t between $t_0 < t < t_f$, the response will be defined by the contribution of neutrons with flux at t who originated from the original source, S_o (or fission sources in the case of a critical system), weighted by the importance of each neutron:

$$R = \left\langle \psi^\dagger(\mathbf{r}, \hat{\Omega}, E, t), \psi(\mathbf{r}, \hat{\Omega}, E, t) \right\rangle \quad (\text{B.6})$$

Comparing Eq. B.5 and B.6 indicates that the S_o^\dagger is equivalent to the importance function, ψ^\dagger at time t_f .

Lets now focus on a general case in the time interval (t_o, t_f) where both forward and adjoint sources are time-dependent rather corresponding to delta functions. By considering the relationships from the above equations, the overall response in this case comes from each neutron that originated within this time interval weighted by the expected contribution to adding a count to the detector measuring the response (importance). This is expressed as:

$$R = \int_{t_o}^{t_f} \langle \psi^\dagger(\mathbf{r}, \hat{\mathbf{\Omega}}, E, t), S(\mathbf{r}, \hat{\mathbf{\Omega}}, E, t) \rangle dt = \int_{t_o}^{t_f} \langle S^\dagger(\mathbf{r}, \hat{\mathbf{\Omega}}, E, t), \psi(\mathbf{r}, \hat{\mathbf{\Omega}}, E, t) \rangle dt \quad (\text{B.7})$$

Once integrated this becomes:

$$\langle \psi^\dagger, S \rangle = \langle S^\dagger, \psi \rangle \quad (\text{B.8})$$

which establishes the "source reciprocity relationship" found in Eq. 2.7.

Appendix C

Binary Plot Results

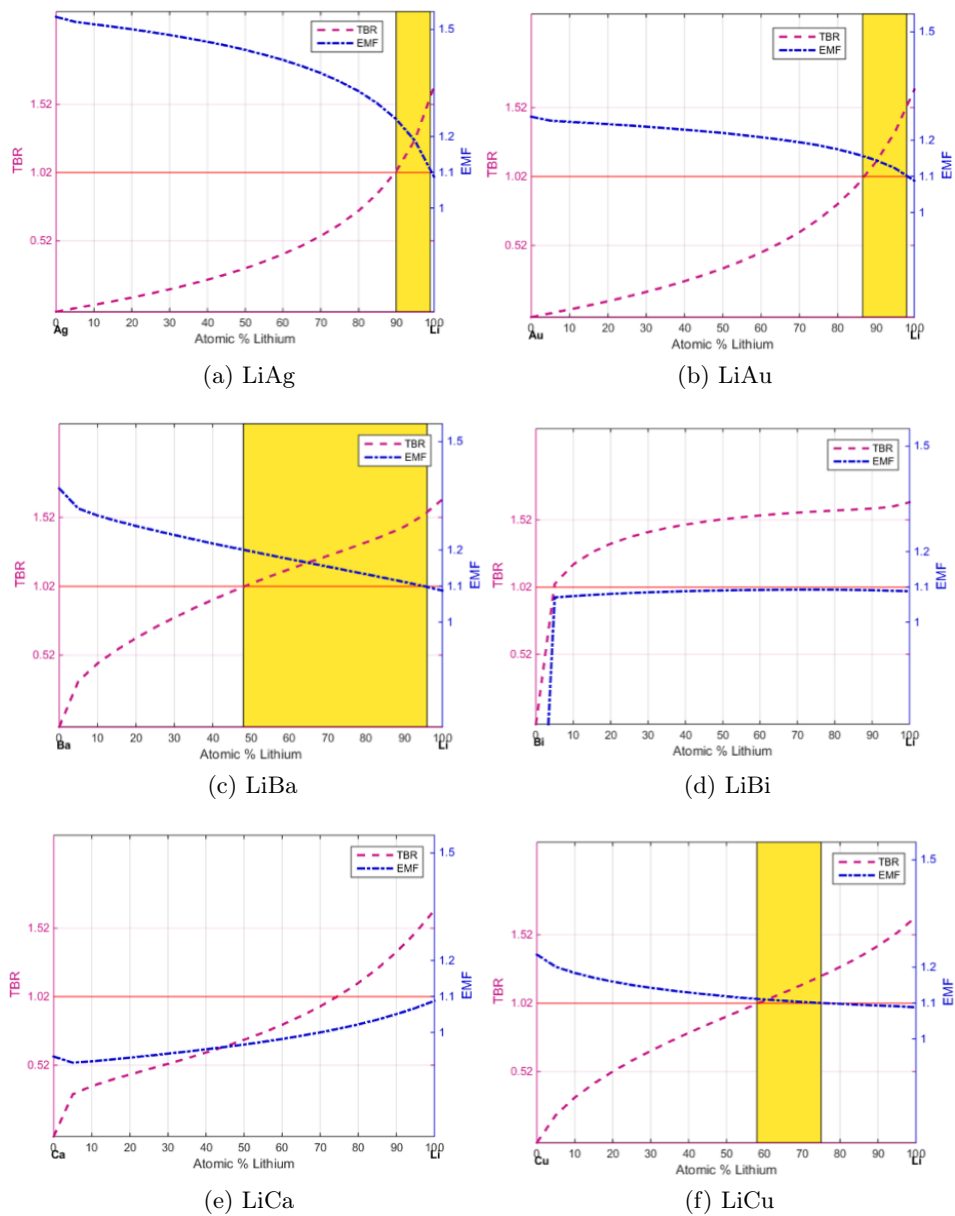


Figure C.1: TBR and EMF for various lithium-based binary alloys as a function of lithium concentration; the horizontal red line coincides with the minimum value for both TBR (1.02) and EMF (1.10), the shaded yellow area indicates the range of lithium concentration within which both constraints are met.

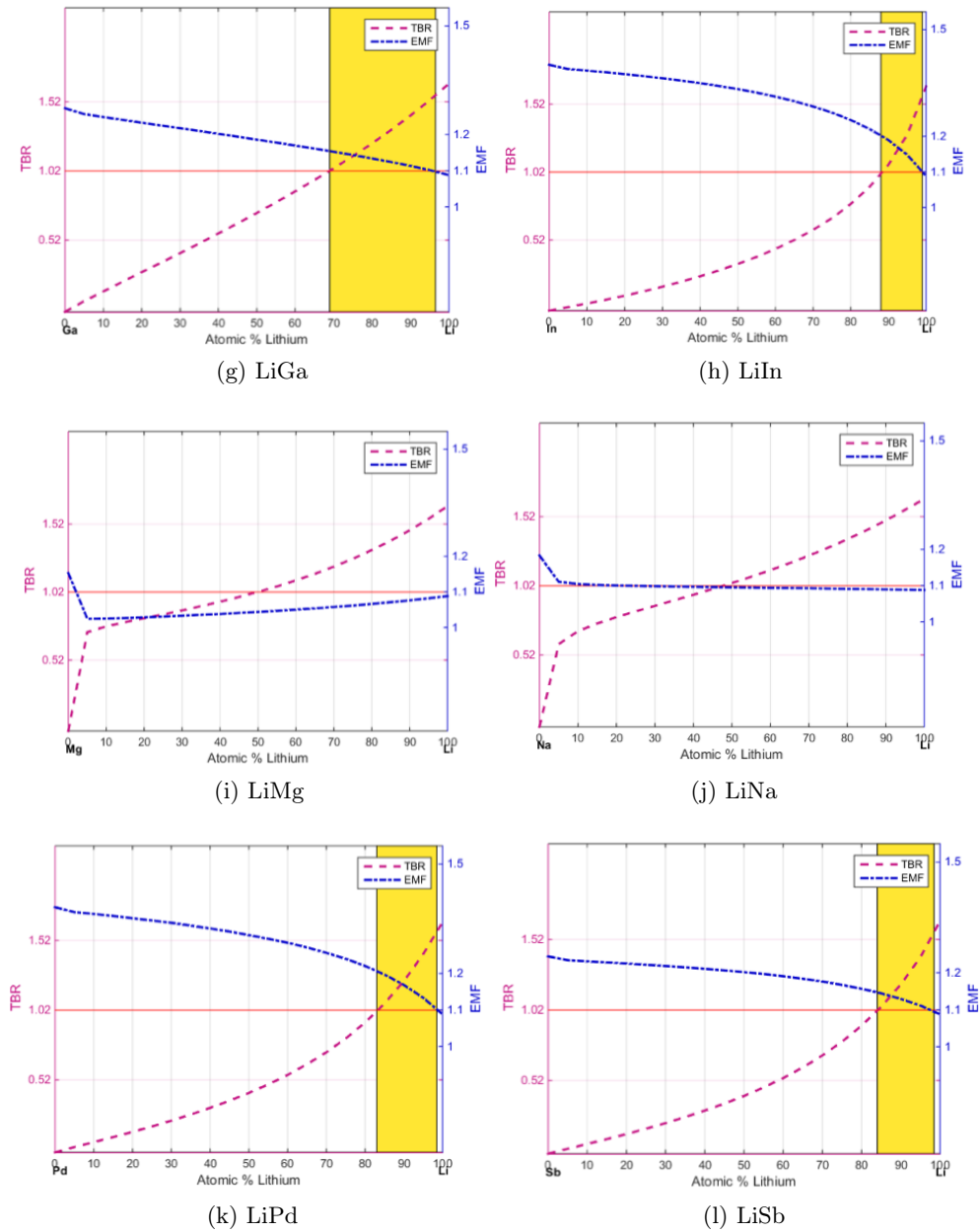


Figure C.1: TBR and EMF for various lithium-based binary alloys as a function of lithium concentration; the horizontal red line coincides with the minimum value for both TBR (1.02) and EMF (1.10), the shaded yellow area indicates the range of lithium concentration within which both constraints are met.

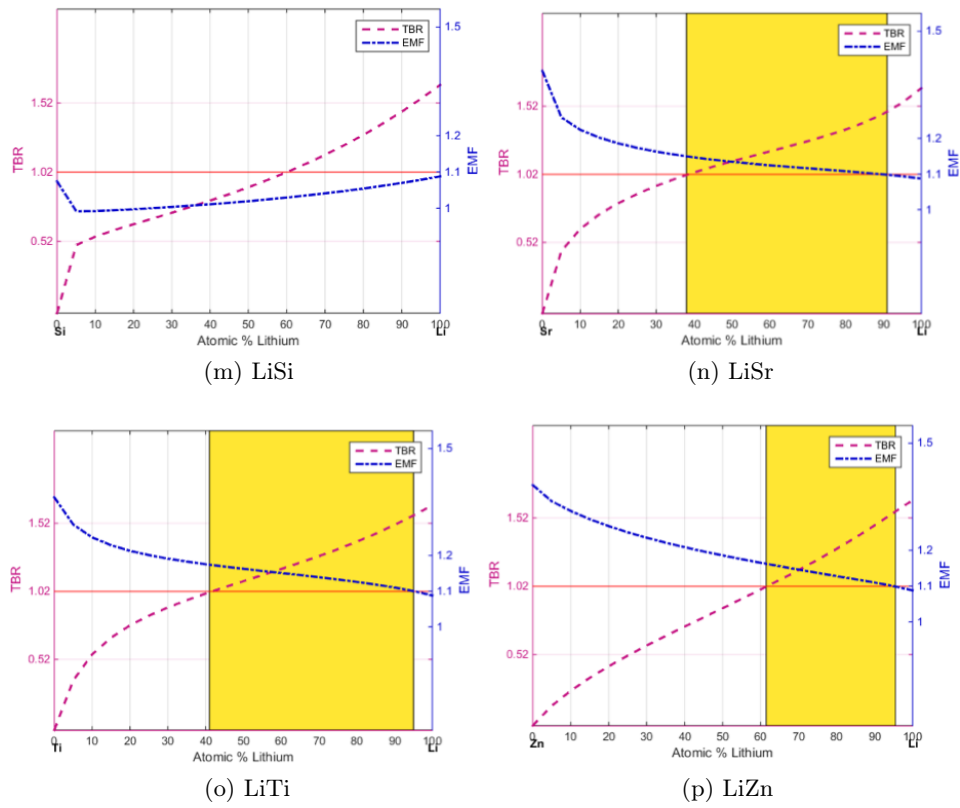


Figure C.1: TBR and EMF for various lithium-based binary alloys as a function of lithium concentration; the horizontal red line coincides with the minimum value for both TBR (1.02) and EMF (1.10), the shaded yellow area indicates the range of lithium concentration within which both constraints are met.

Appendix D

MCNP Lithium-based Ternary Alloy TBR and EMF Results

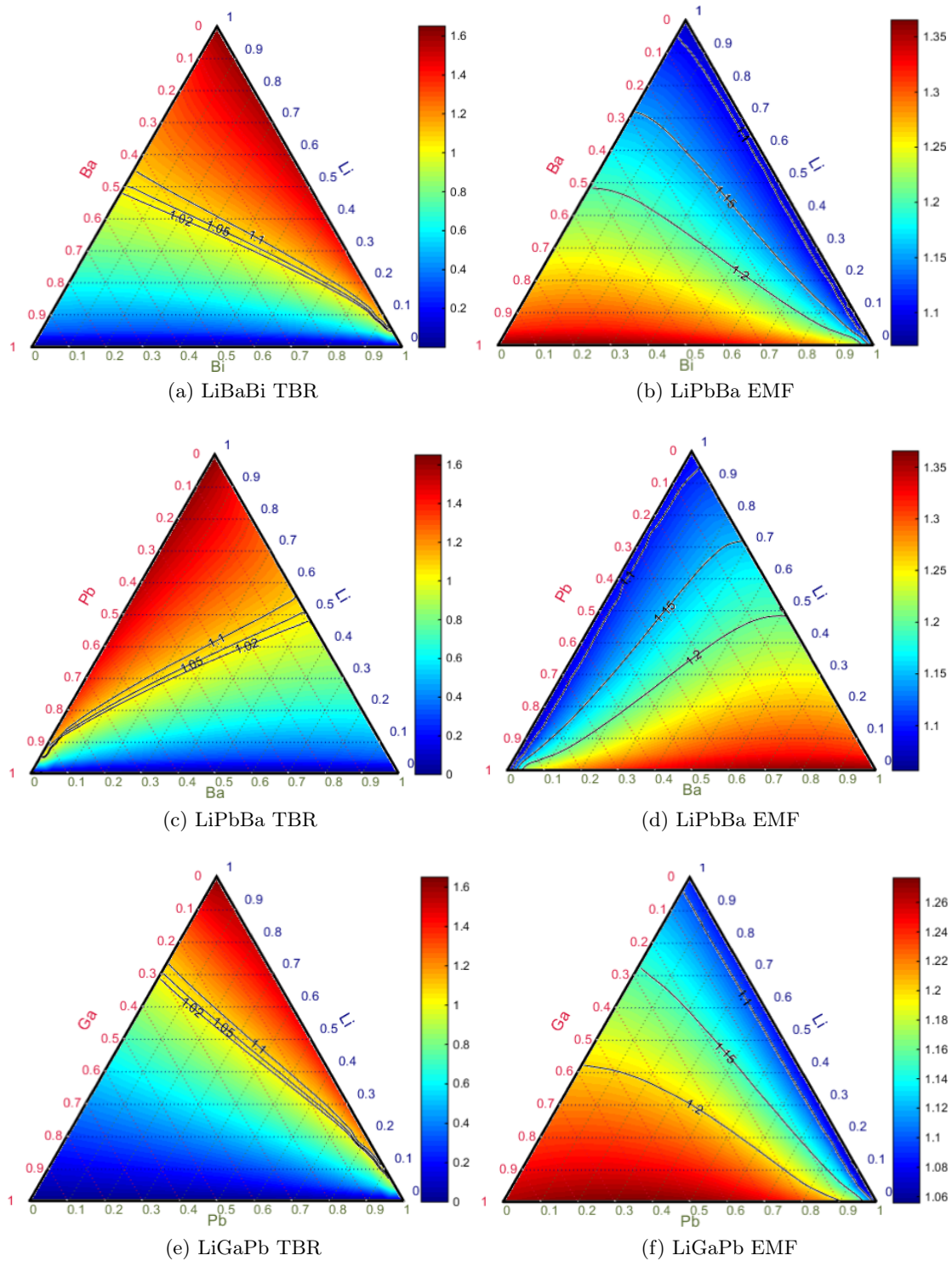


Figure D.1: Ternary Plots for various ternary alloys; TBR plots are on left, EMF plots are on right.

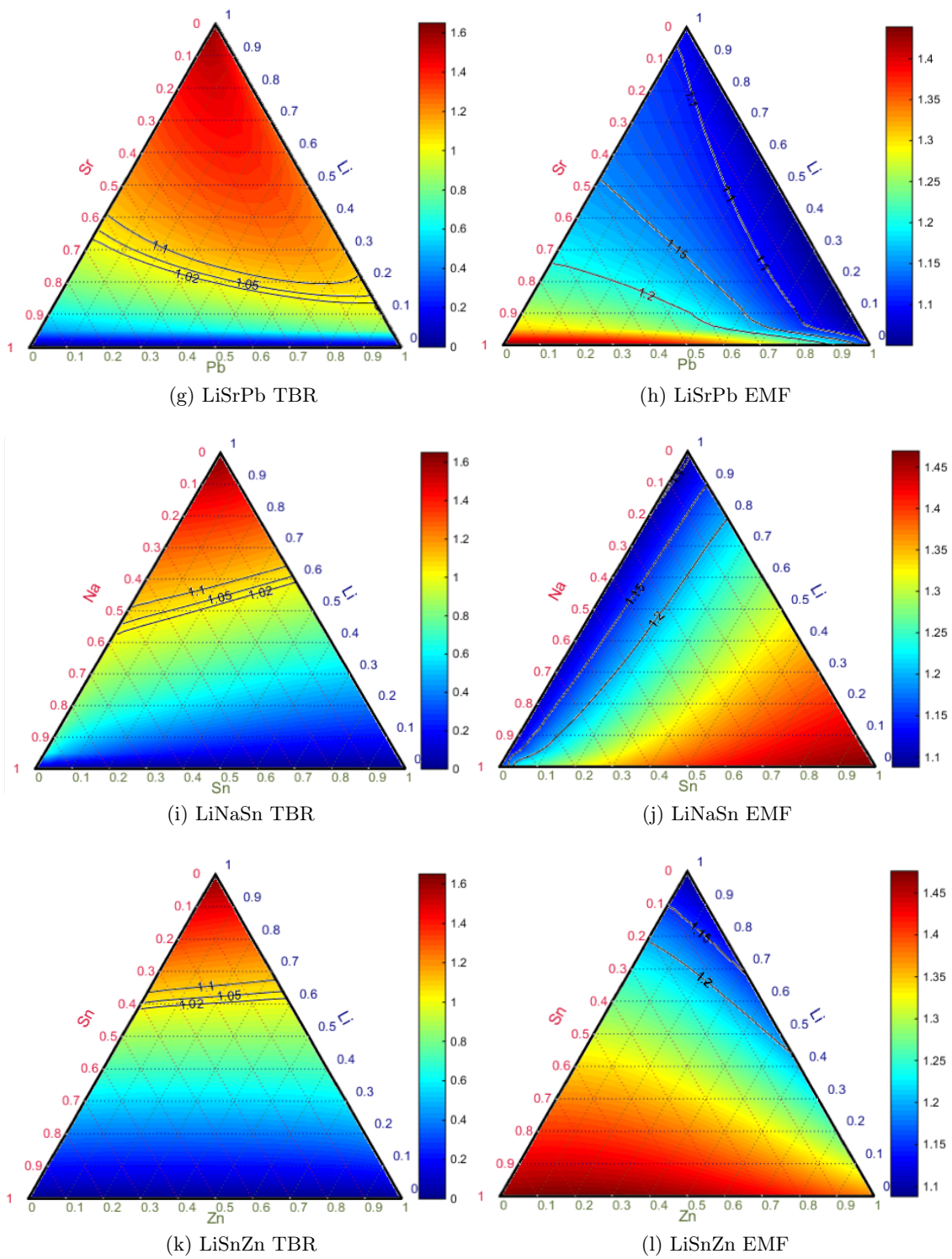


Figure D.1: Ternary Plots for various ternary alloys; TBR plots are on left, EMF plots are on right.

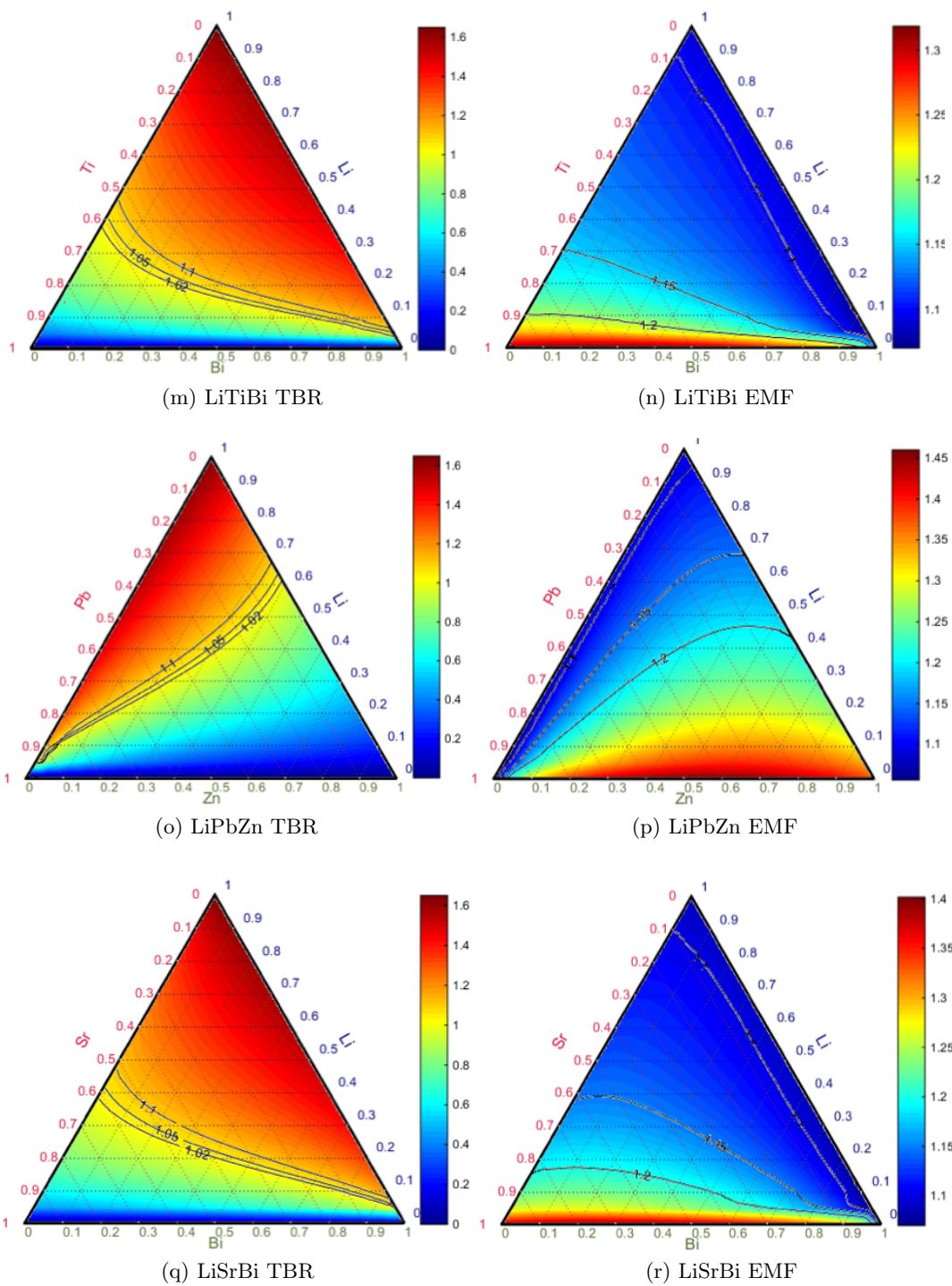


Figure D.1: Ternary Plots for various ternary alloys; TBR plots are on left, EMF plots are on right.

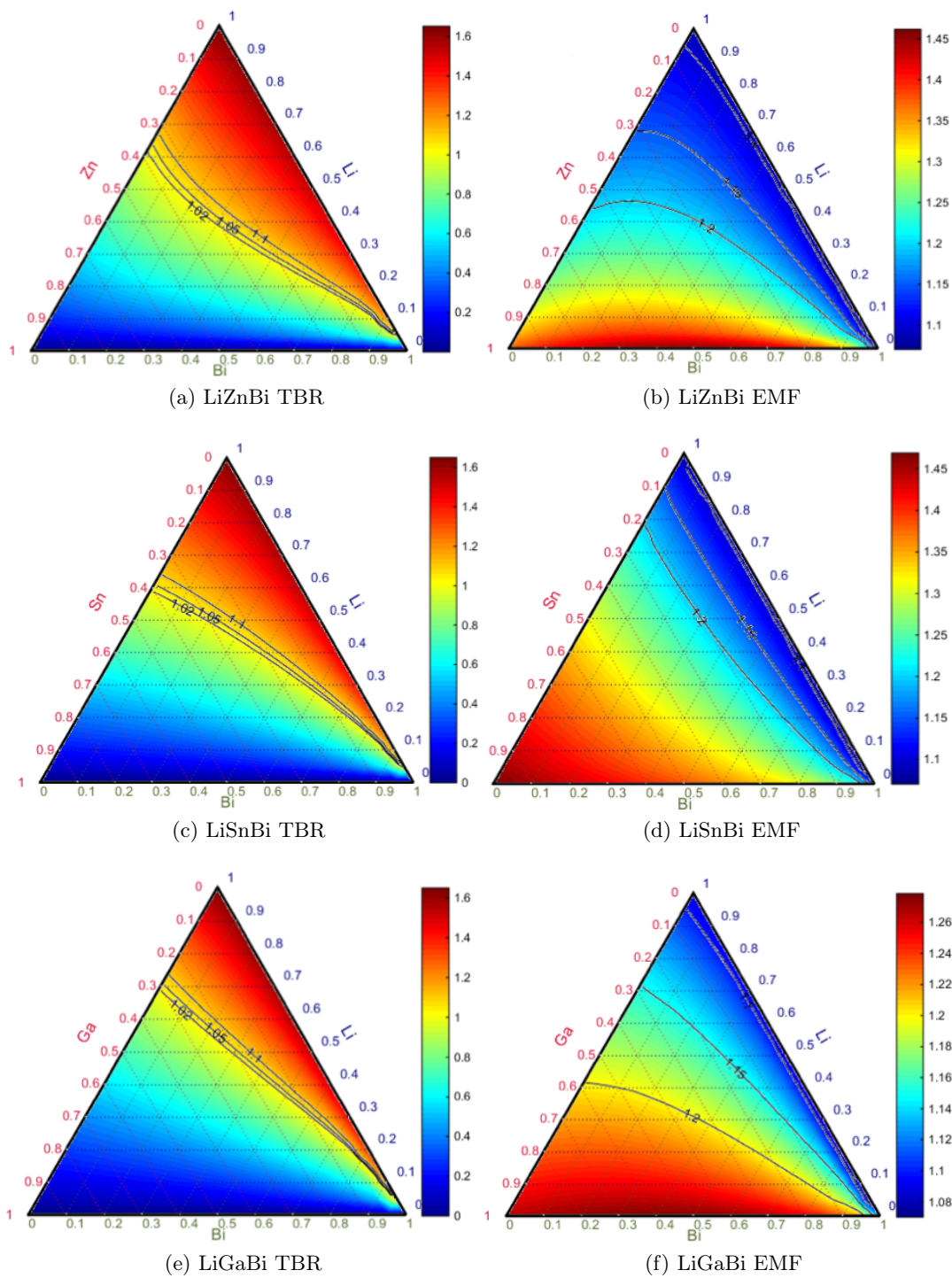


Figure D.2: Ternary Plots for various ternary alloys; TBR plots are on left, EMF plots are on right.

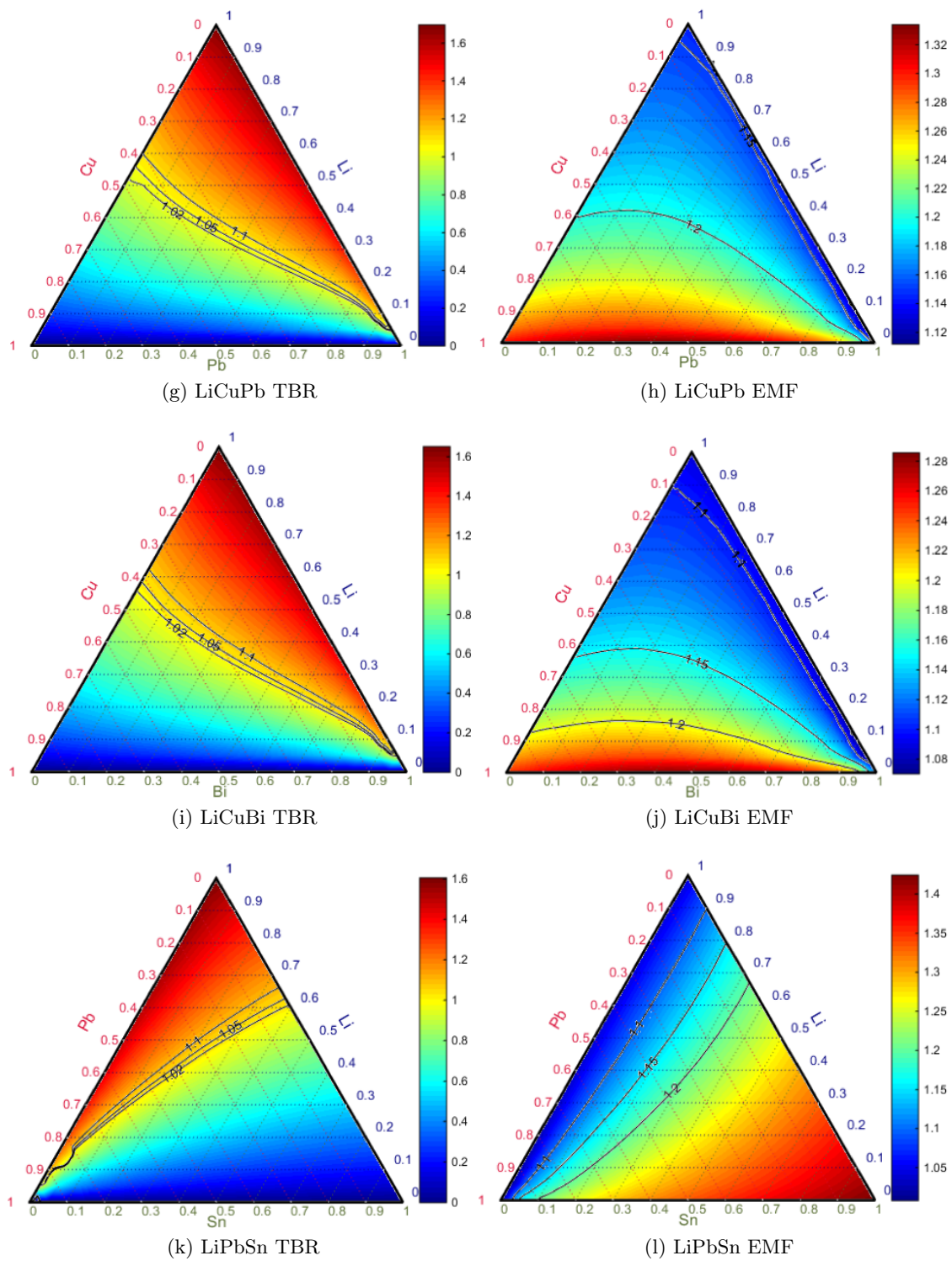


Figure D.2: Ternary Plots for various ternary alloys; TBR plots are on left, EMF plots are on right.

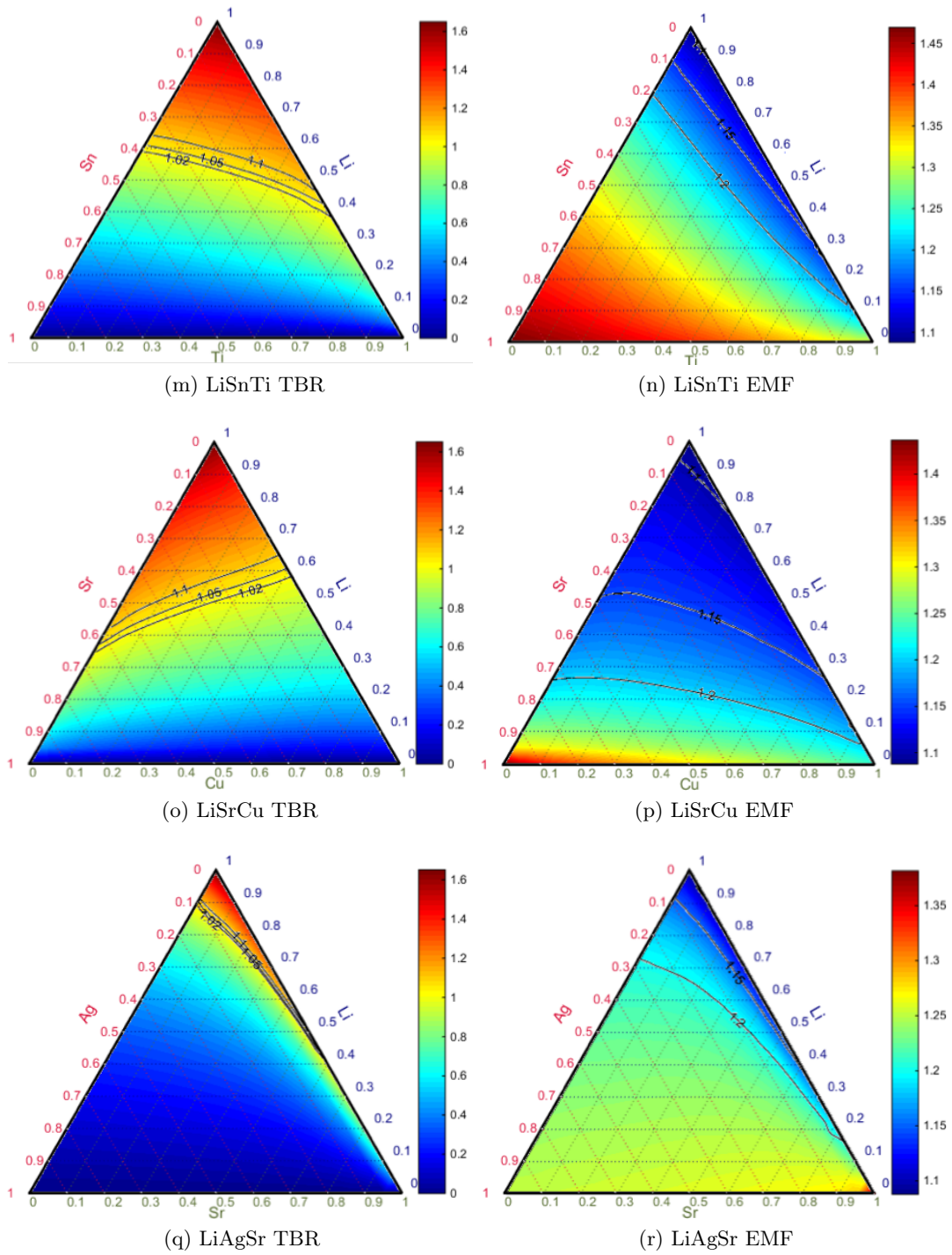


Figure D.2: Ternary Plots for various ternary alloys; TBR plots are on left, EMF plots are on right.

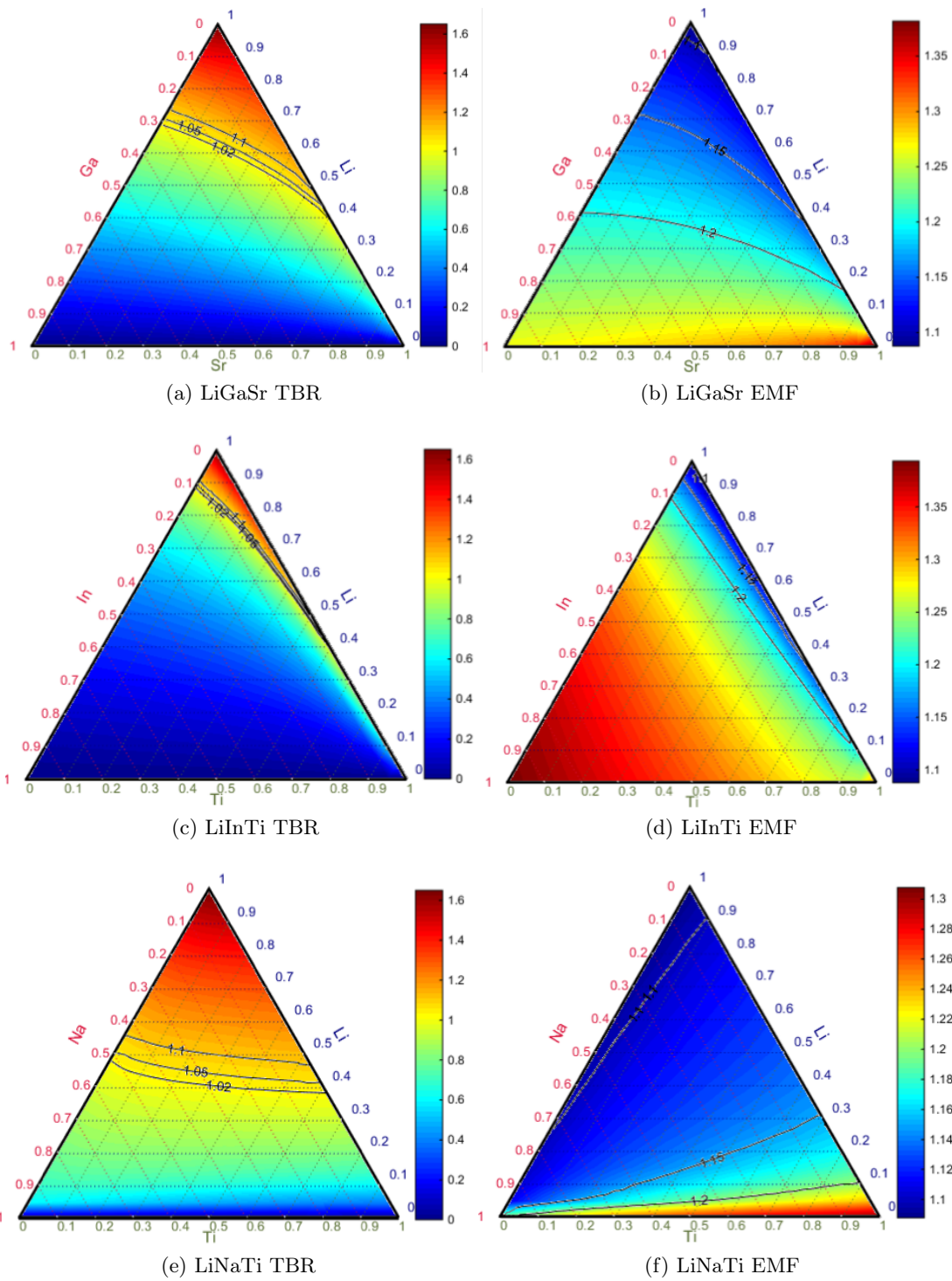


Figure D.3: Ternary Plots for various ternary alloys; TBR plots are on left, EMF plots are on right.

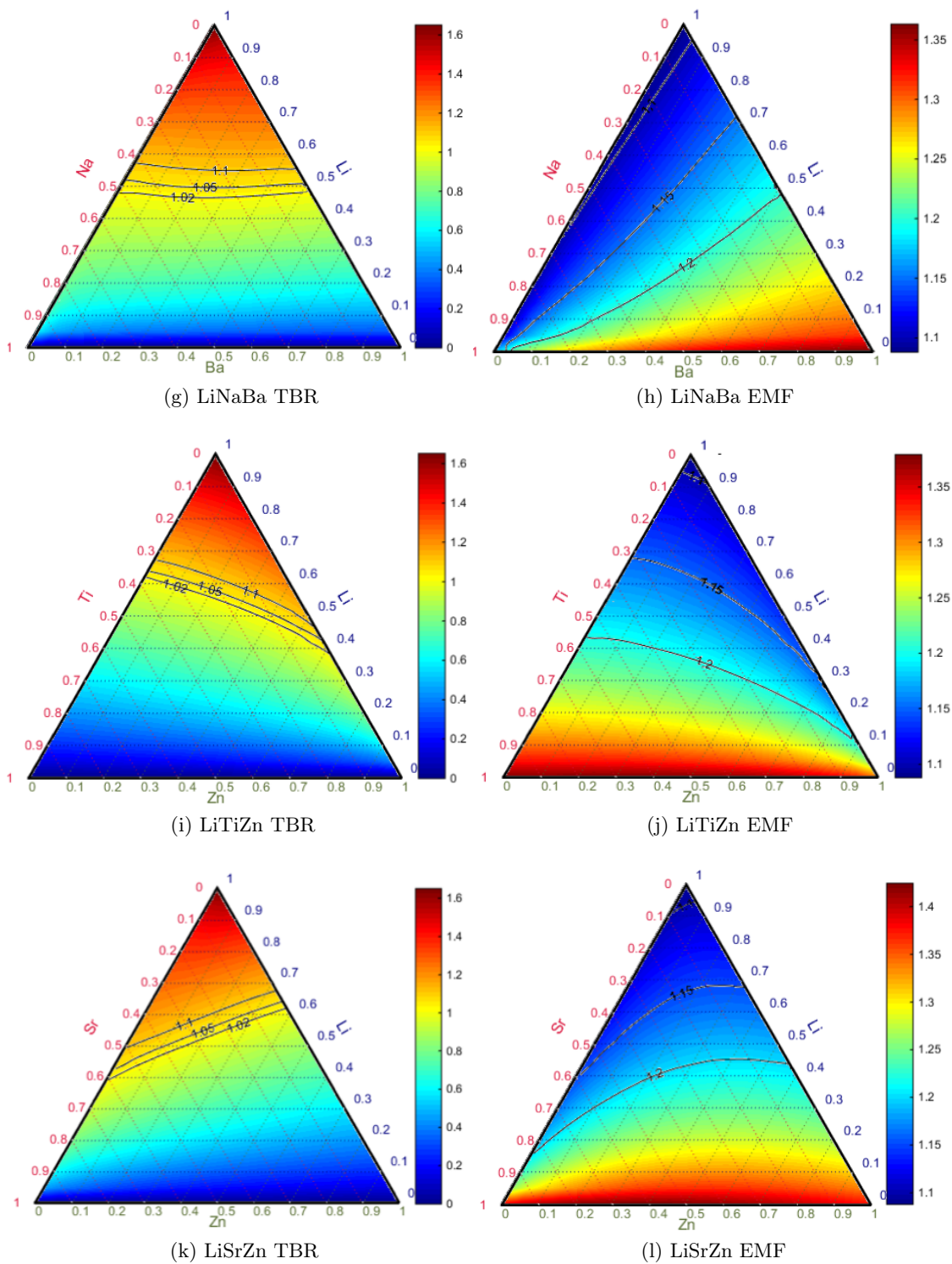


Figure D.3: Ternary Plots for various ternary alloys (Continued); TBR plots are on left, EMF plots are on right.

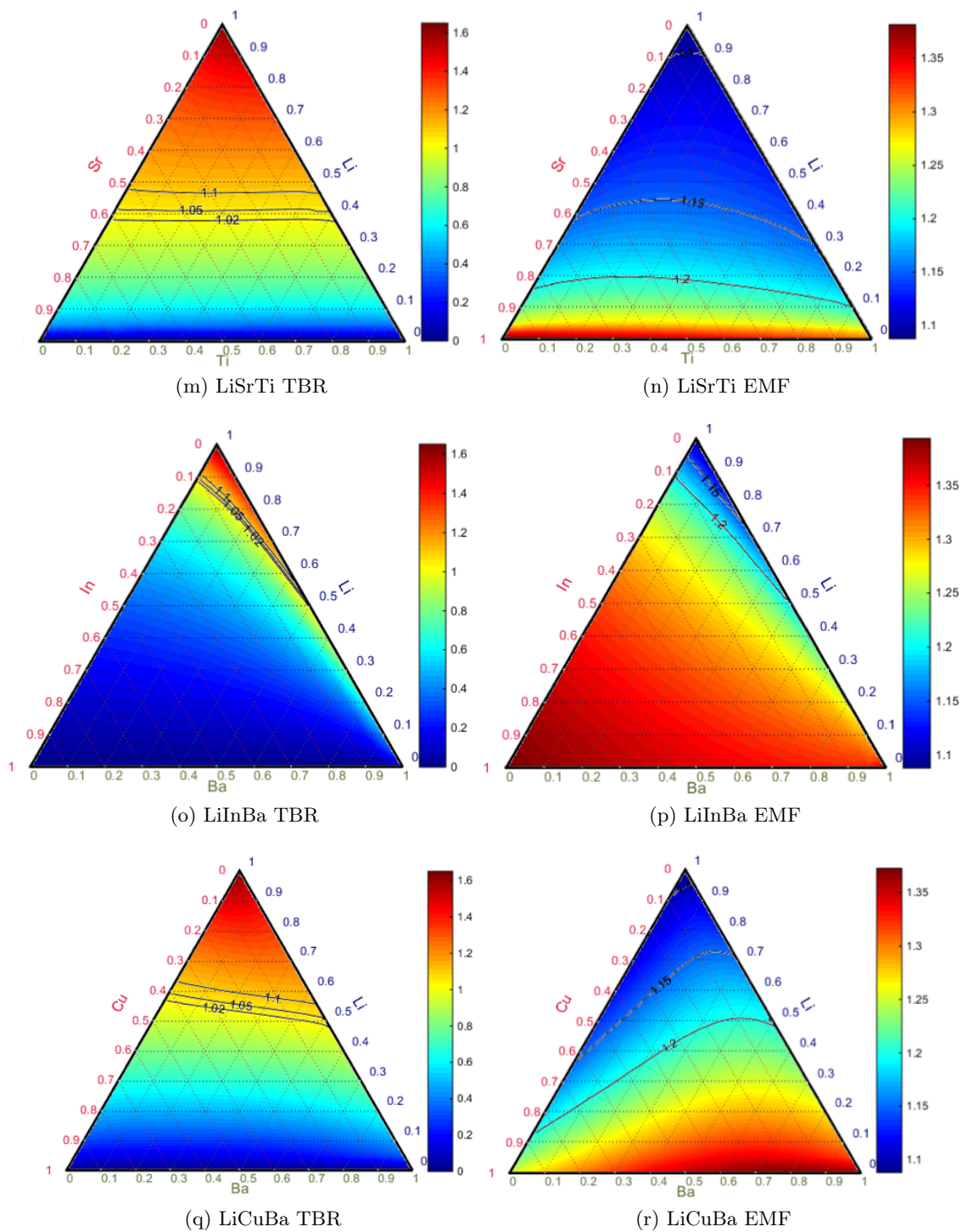


Figure D.3: Ternary Plots for various ternary alloys; TBR plots are on left, EMF plots are on right.

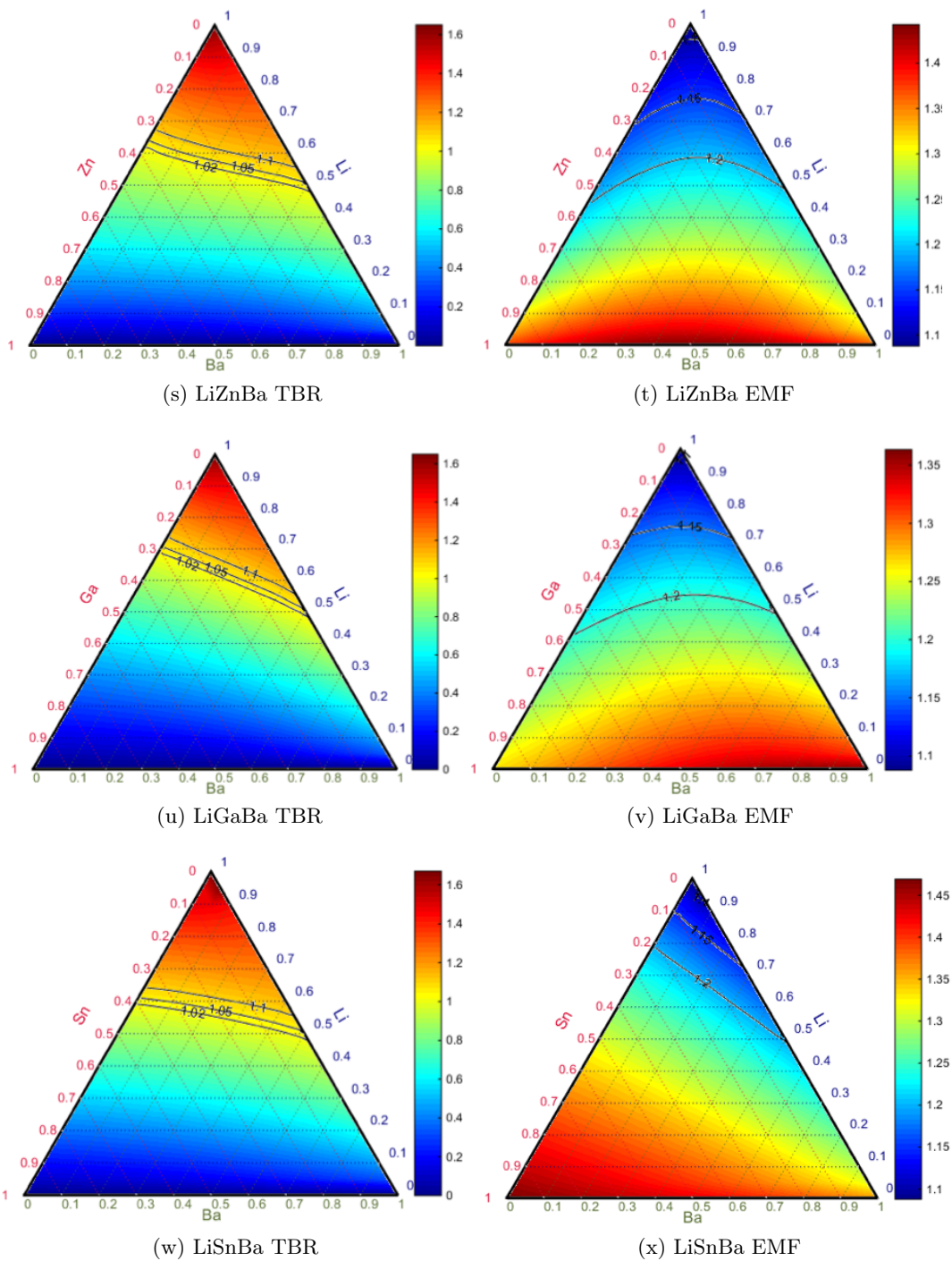


Figure D.3: Ternary Plots for various ternary alloys; TBR plots are on left, EMF plots are on right.

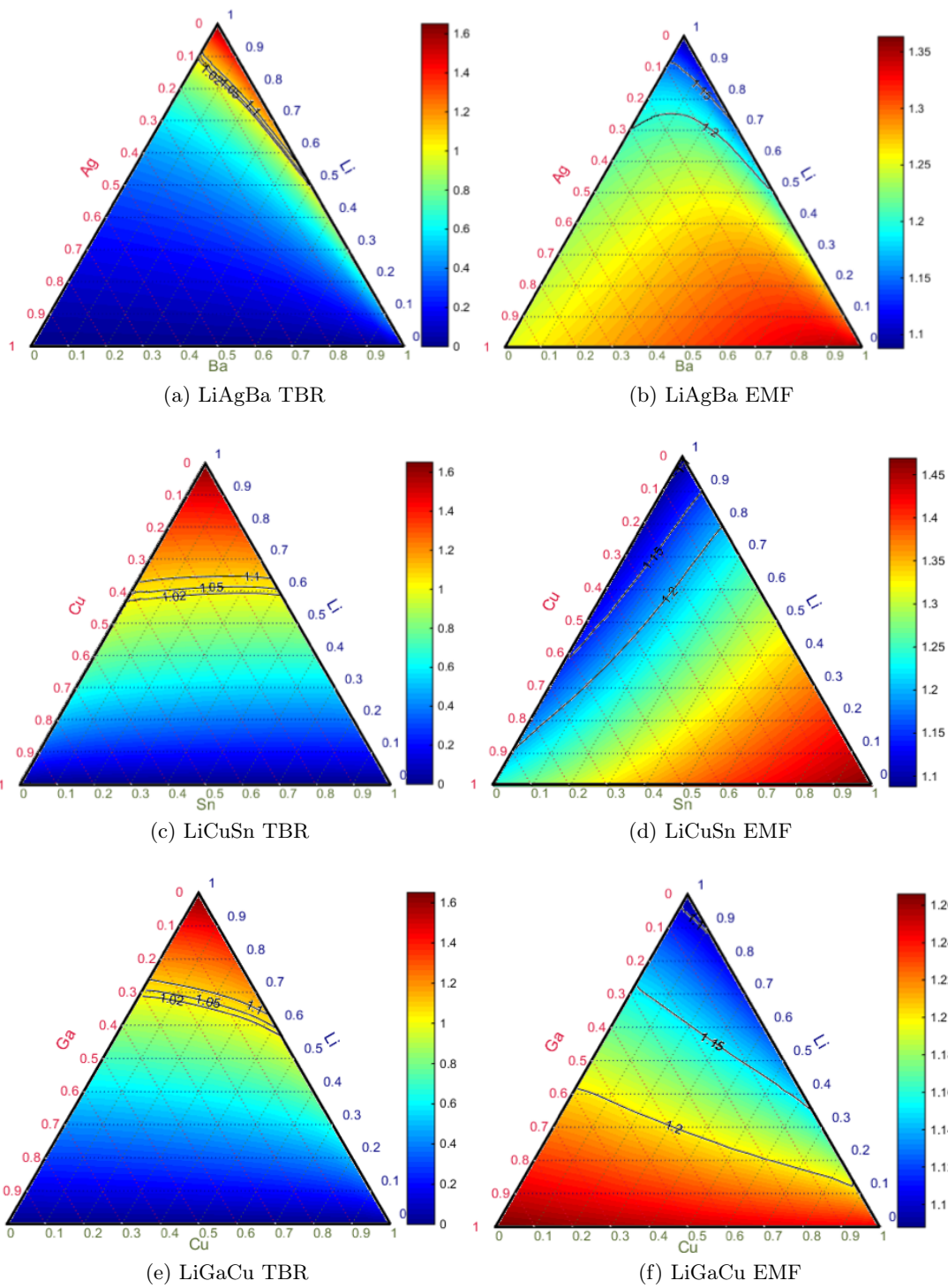


Figure D.4: Ternary Plots for various ternary alloys; TBR plots are on left, EMF plots are on right.

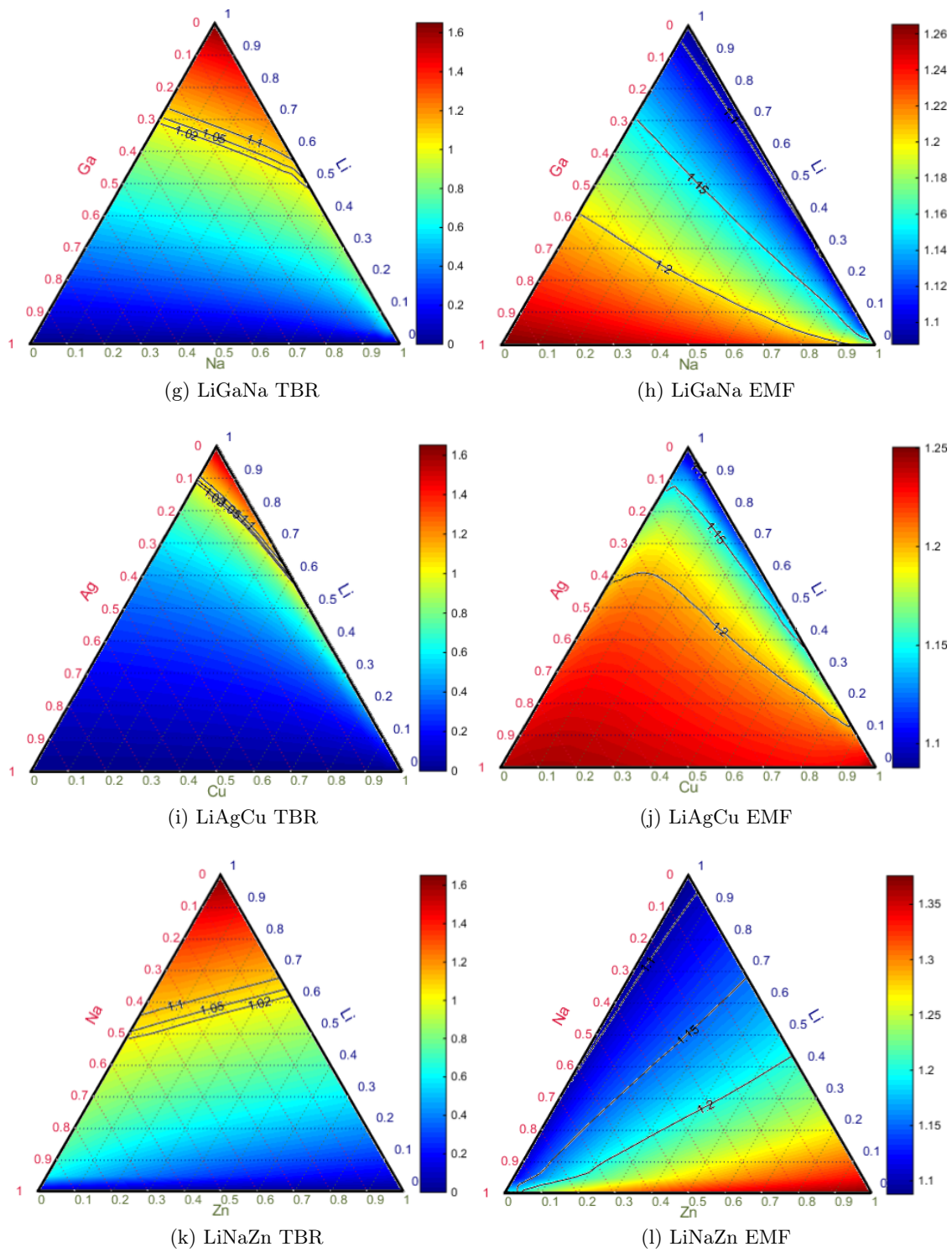


Figure D.4: Ternary Plots for various ternary alloys; TBR plots are on left, EMF plots are on right.

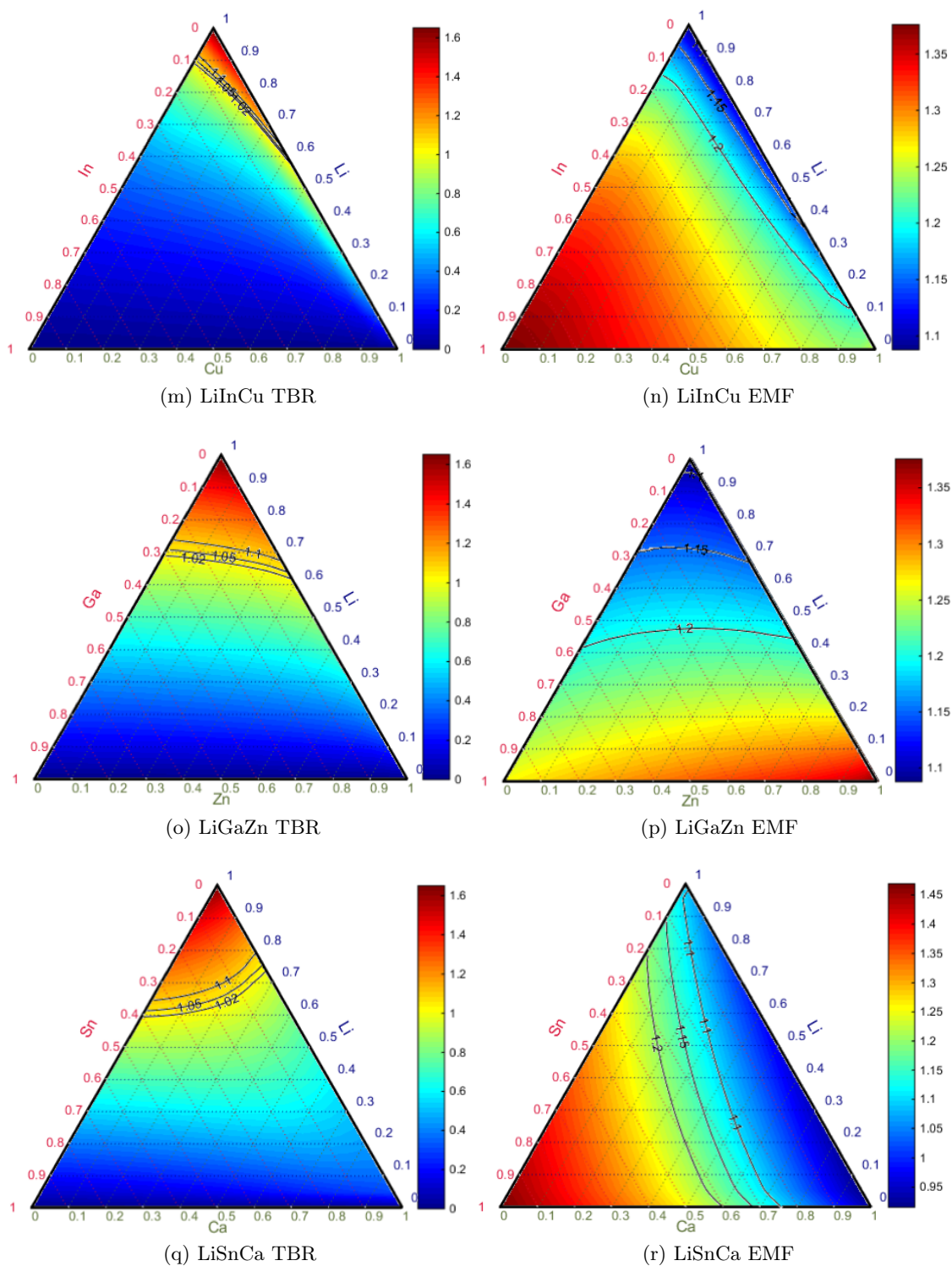


Figure D.4: Ternary Plots for various ternary alloys; TBR plots are on left, EMF plots are on right.

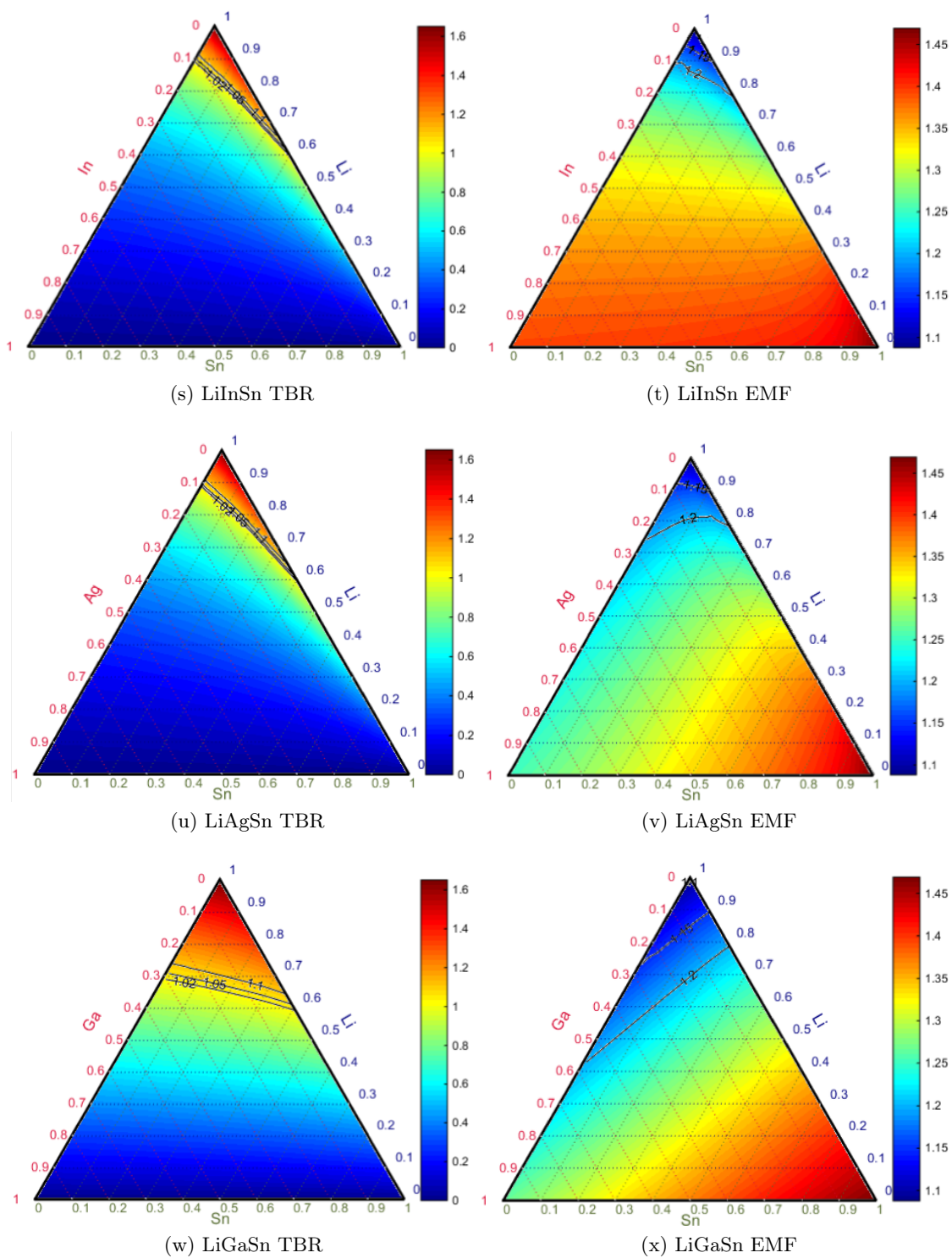


Figure D.4: Ternary Plots for various ternary alloys; TBR plots are on left, EMF plots are on right.

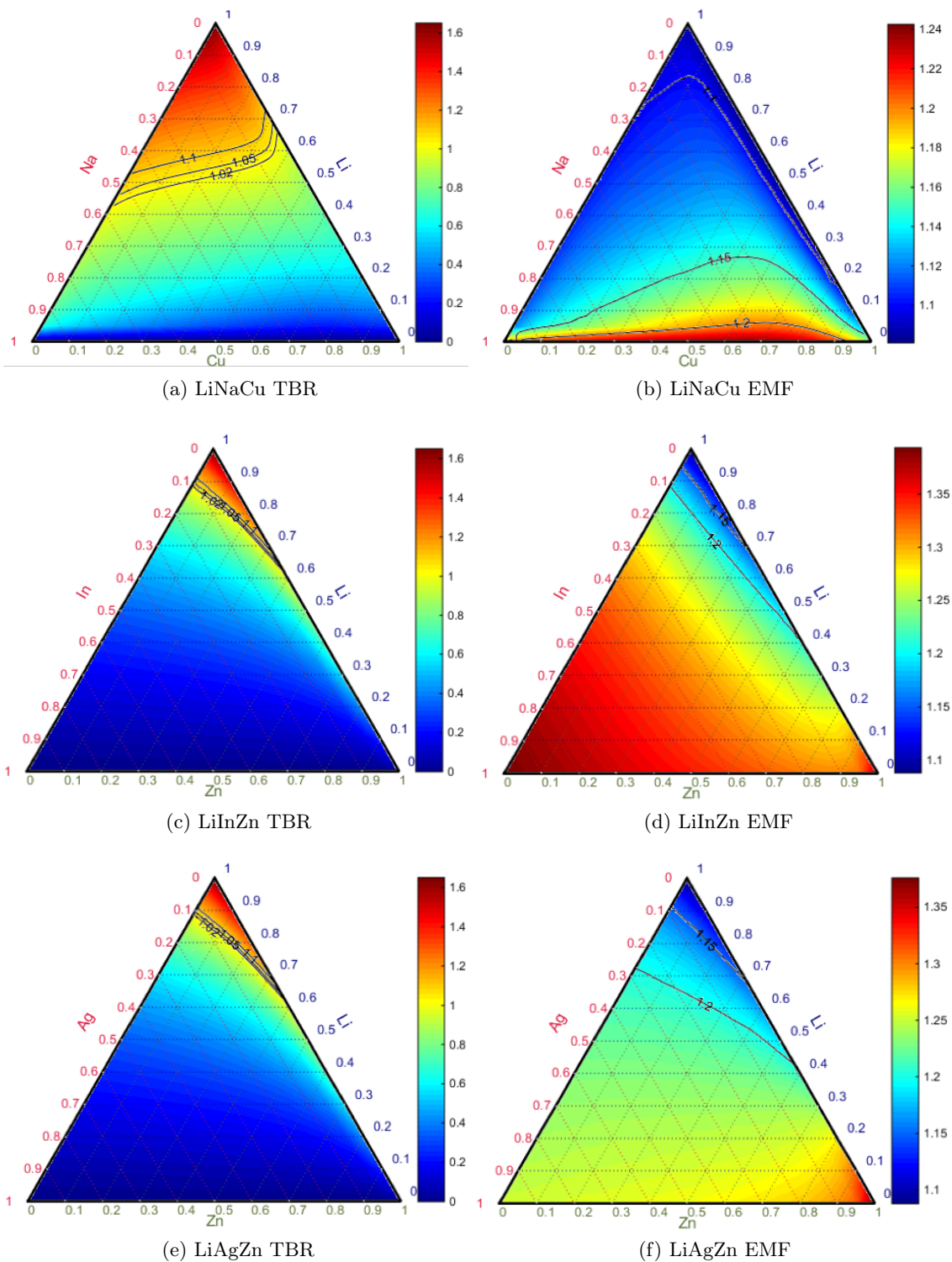


Figure D.5: Ternary Plots for various ternary alloys; TBR plots are on left, EMF plots are on right.

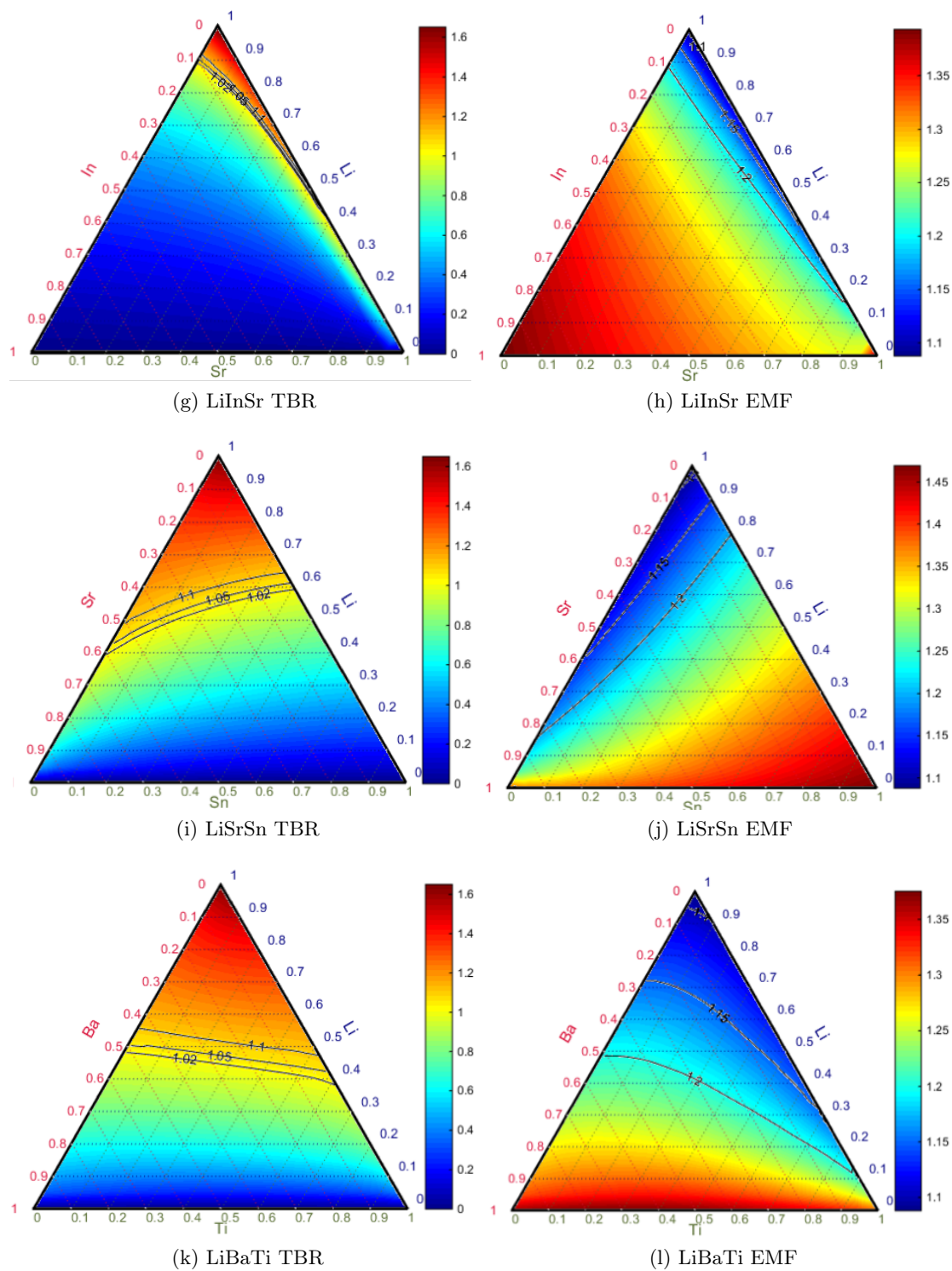


Figure D.5: Ternary Plots for various ternary alloys; TBR plots are on left, EMF plots are on right.

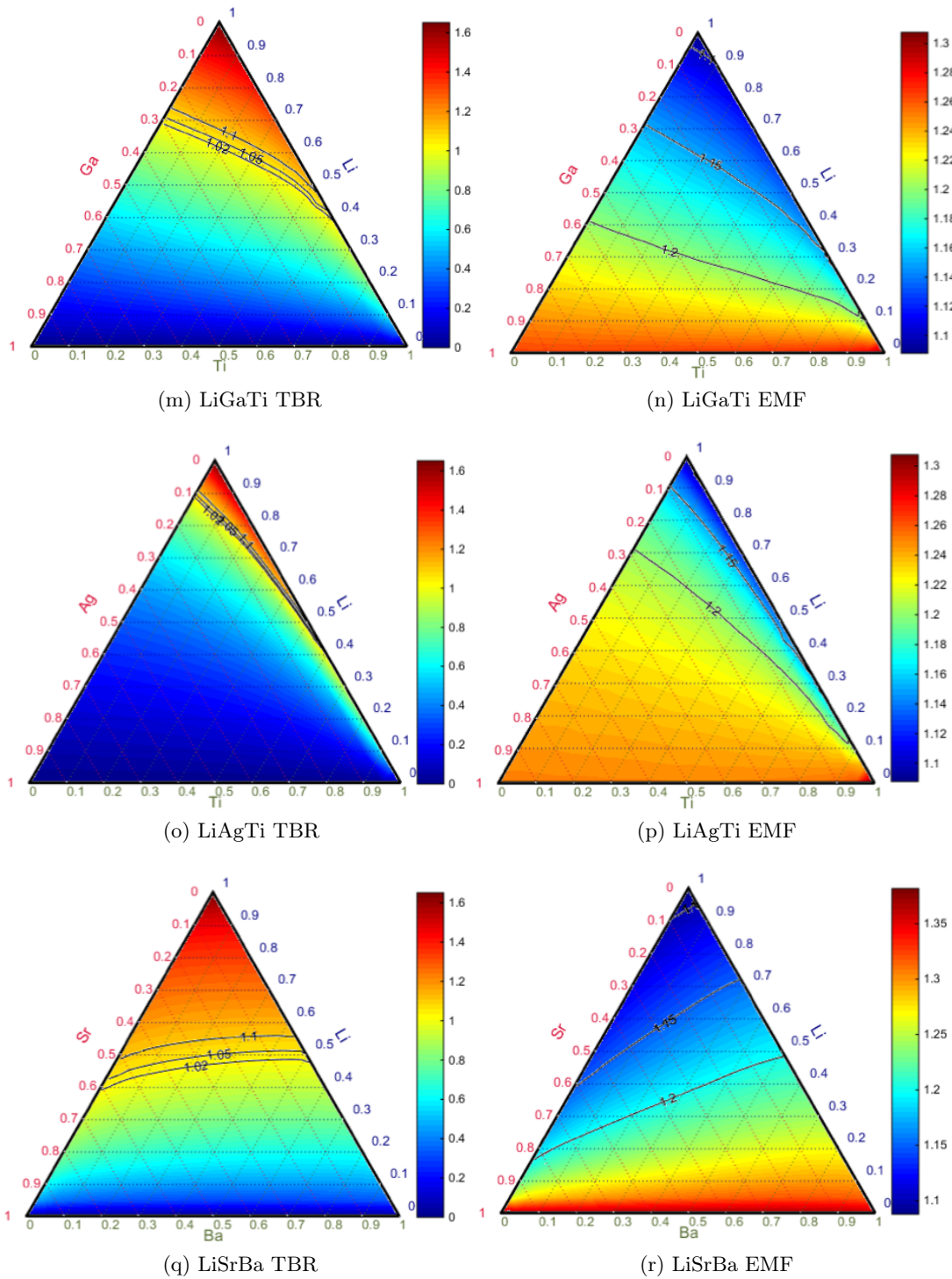


Figure D.5: Ternary Plots for various ternary alloys; TBR plots are on left, EMF plots are on right.

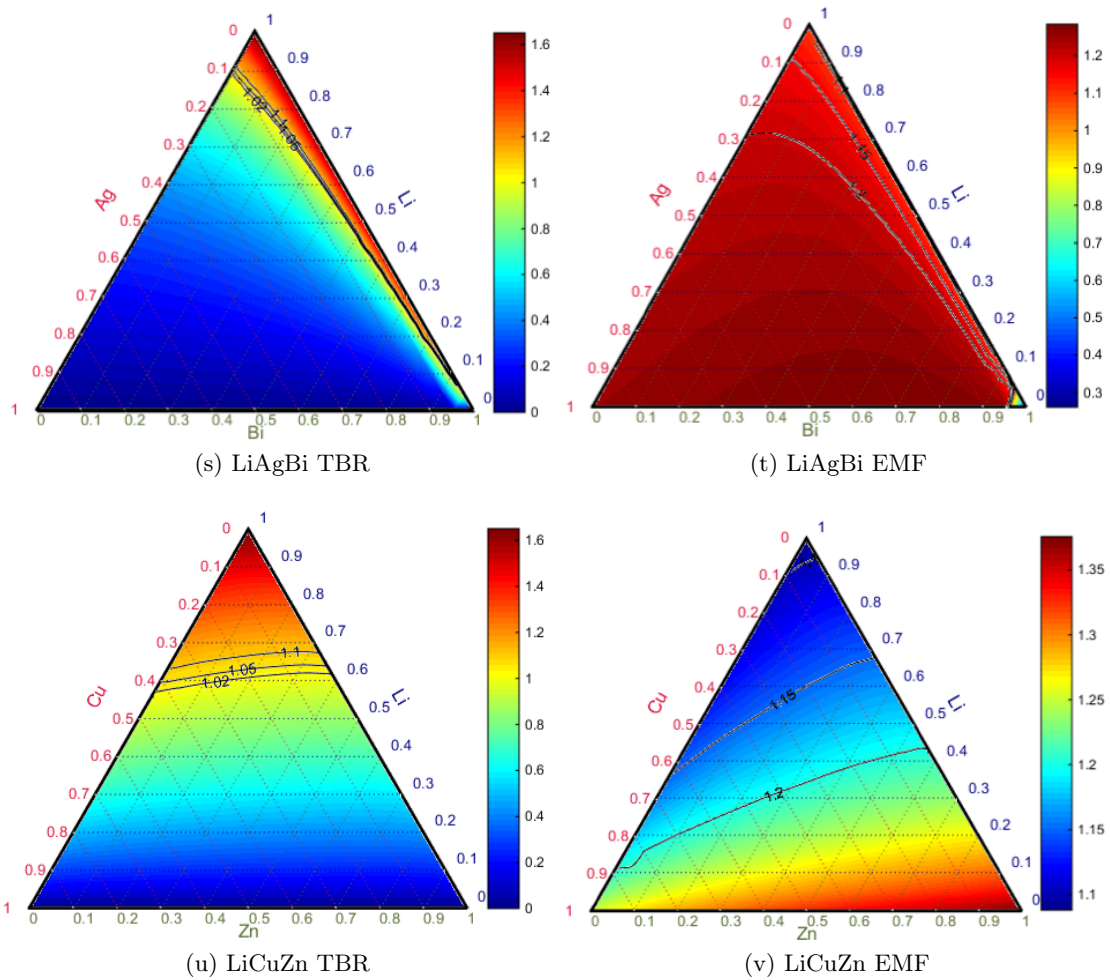


Figure D.5: Ternary Plots for various ternary alloys; TBR plots are on left, EMF plots are on right.

Appendix E

EPT Serpent Subroutines

E.1 AGPTFunctionsInit.c subroutine

The following subroutine was written by Dr. Manuele Aufiero. The author of this dissertation has edited the isotope arrays to simulate a LiPbBa ternary alloy. If a different alloy is desired, the isotope arrays must be replaced.

```
include "header.h"
#include "locations.h"

#define FUNCTION_NAME "AGPTFunctionsInit:"

double Li6vec[AGPT_FUNCTIONS];
double Li7vec[AGPT_FUNCTIONS];
double Ba130vec[AGPT_FUNCTIONS];
double Ba132vec[AGPT_FUNCTIONS];
double Ba134vec[AGPT_FUNCTIONS];
double Ba135vec[AGPT_FUNCTIONS];
double Ba136vec[AGPT_FUNCTIONS];
double Ba137vec[AGPT_FUNCTIONS];
double Ba138vec[AGPT_FUNCTIONS];
double Pb204vec[AGPT_FUNCTIONS];
double Pb206vec[AGPT_FUNCTIONS];
double Pb207vec[AGPT_FUNCTIONS];
double Pb208vec[AGPT_FUNCTIONS];

void AGPTFunctionsInit()
{
    long i;
    FILE *filePert;

    /*****/
```



```

        %lf\t%lf\t%lf\t%lf\t%lf\n",
        i, Li6vec[i], Li7vec[i], Ba130vec[i], Ba132vec[i],
        Ba134vec[i], Ba135vec[i], Ba136vec[i],
        Ba137vec[i], Ba138vec[i], Pb204vec[i], Pb206vec[i],
        Pb207vec[i], Pb208vec[i]);
    return;
}

```

E.2 AGPTScoreArbitraryFunctions.c subroutine

The following subroutine was written by Dr. Manuele Aufiero. The author of this dissertation has edited the isotope arrays to simulate a LiPbBa ternary alloy. If a different alloy is desired, the isotope arrays must be replaced.

```

#include "header.h"
#include "locations.h"

#define FUNCTION_NAME "AGPTScoreArbitraryFunctions:"

extern double Li6vec[AGPT_FUNCTIONS];
extern double Li7vec[AGPT_FUNCTIONS];
extern double Ba130vec[AGPT_FUNCTIONS];
extern double Ba132vec[AGPT_FUNCTIONS];
extern double Ba134vec[AGPT_FUNCTIONS];
extern double Ba135vec[AGPT_FUNCTIONS];
extern double Ba136vec[AGPT_FUNCTIONS];
extern double Ba137vec[AGPT_FUNCTIONS];
extern double Ba138vec[AGPT_FUNCTIONS];
extern double Pb204vec[AGPT_FUNCTIONS];
extern double Pb206vec[AGPT_FUNCTIONS];
extern double Pb207vec[AGPT_FUNCTIONS];
extern double Pb208vec[AGPT_FUNCTIONS];

void AGPTScoreArbitraryFunctions(long zai, long mt,
double E, double accrej, long part, long id)
{
    long j;
    double f;
    double relWgt;

    /*****/
    for(j = 0; j < AGPT_FUNCTIONS; j++)
    {
        f = 1.0;

```

```
if (zai == 30060)
    f = Li6vec[j];
if (zai == 30070)
    f = Li7vec[j];
if (zai == 561300)
    f = Ba130vec[j];
if (zai == 561320)
    f = Ba132vec[j];
if (zai == 561340)
    f = Ba134vec[j];
if (zai == 561350)
    f = Ba135vec[j];
if (zai == 561360)
    f = Ba136vec[j];
if (zai == 561370)
    f = Ba137vec[j];
if (zai == 561380)
    f = Ba138vec[j];
if (zai == 822040)
    f = Pb204vec[j];
if (zai == 822060)
    f = Pb206vec[j];
if (zai == 822070)
    f = Pb207vec[j];
if (zai == 822080)
    f = Pb208vec[j];

if (f == 1.0)
    continue;

if(accrej == -1.0)
    f = 2.0 - f;

relWgt = (1.0 + RDB[part + PARTICLE_FIRST_AP + j]);
relWgt = relWgt * f;
relWgt = relWgt - 1.0;
WDB[part + PARTICLE_FIRST_AP + j] = relWgt;
}

return;
}
```

Appendix F

Generalized Least Squares Subroutine for Ternary Alloys

The following subroutine utilizes generalized least squares to create a linear regression around a point of interest in a ternary alloy. The new TBR of this point is given by y-intercept of the regression. The uncertainty of the result is also obtained. This code utilizes two prefabricated arrays. The first array lists all of the points simulated in the ternary with their corresponding TBR and EMF obtained from Serpent simulated with exact perturbation theory (Chapter 4). Each row represents the compositions of each element in the ternary, followed by the TBR and EMF. The second array has the exact same format as the first, but only include points that have uncertainties above a prescribed threshold. The scripts to create the arrays were written in Python and are not included here.

```
% TBR_known = T0 + (Li-Li0)bb1+(Ba-B0)bb2+(Pb-Pb0)bb3
%Point Li0,Ba0,Pb0 is the MISSING point (regression point)
%Li,Bi,Pb are the other points around missing point (known_
%TBR_known = TBR from LiBaPb (other points around missing point)
%T0 ==> TBR that you want to find out
%bbs ==> slopes that you need for regression (do not need this info for
%anything else)
%y = TBR column matrix for each comp
%x = [li1,ba1,pb1
%      [li2,ba2,pb2] ....
%add a column of ones for first column of x
%X =[ones(size(x)),x]
%s ==>standard deviation column matrix for each comp
%V = diag(s.^2)
% [bb, stdx, mse] = lscov(X,y,V)
% first bb # in matrix ==> TBR that you WANT
% first stdx # in matrix ==> standard deviation of TBR (above)

%load array of all results
load lisenzn_new_3;
```

```

lines = size(tbr_un,1);

%load array of only results > uncertainty
load lisnzn_55e3_3;
uncerts = size(uncs);

newpts = zeros(size(uncs));

%loop through each point in uncertainty array
%and apply GLS to each point
for u=1:uncerts
    li_un = uncs(u,1);
    pb_un = uncs(u,2);
    ba_un = uncs(u,3);

%create ternary area around point of interest
    if li_un == 14
        li_min = li_un - 13;
        pb_min = pb_un - 13;
        ba_min = ba_un - 14;
        li_max = li_min + 20;
        pb_max = pb_min + 20;
        ba_max = ba_min + 20;
    elseif li_un == 13
        li_min = li_un - 12;
        pb_min = pb_un - 14;
        ba_min = ba_un - 14;
        li_max = li_min + 20;
        pb_max = pb_min + 20;
        ba_max = ba_min + 20;
    else
        li_min = li_un - 14;
        pb_min = pb_un - 12;
        ba_min = ba_un - 14;
        li_max = li_min + 25;
        pb_max = pb_min + 25;
        ba_max = ba_min + 25;
    end
    li0 = li_min;
    pb0 = pb_max;
    ba0 = ba_max;

%initialize arrays
newarr = zeros(230,5);

```

```

o_uns = zeros(1,5);

%loop through ternary area
%if the point of interest is in array, put in its own separate array
%all other points within this area are added to a new array
%the concentrations in array are X-X0
c = 1;
while li0 <= li_max
    pb0 = 100 - li0 - ba0;
    while pb0 <= pb_max

        for i=1:lines
            if tbr_un(i,1) == li0
                if tbr_un(i,2) == pb0
                    if tbr_un(i,3) == ba0
                        if li0==li_un && pb0==pb_un && ba0==ba_un
                            o_uns(1,1) = li0-li_un;
                            o_uns(1,2) = pb0-pb_un;
                            o_uns(1,3) = ba0-ba_un;
                            o_uns(1,4) = tbr_un(i,4);
                            o_uns(1,5) = tbr_un(i,5);

                        else
                            %array of all points in area
                            %without point of interest
                            newarr(c,1) = li0-li_un;
                            newarr(c,2) = pb0-pb_un;
                            newarr(c,3) = ba0-ba_un;
                            newarr(c,4) = tbr_un(i,4);
                            newarr(c,5) = tbr_un(i,5);

                            c = c + 1;
                        end
                    end
                end
            end
        end
        sar = size(newarr,1);

        ba0 = ba0 - 1;
        pb0 = 100 - li0 - ba0;

    end
    ba0 = ba_max;

```

```

        li0 = li0 + 1;
    end
    lim = c - 1;

    %create matrices to use when calling MATLAB GLS
    X = [ones(lim,1),newarr(1:lim,1:2)];
    y = newarr(1:lim,4);
    s = newarr(1:lim,5);
    V = diag(s.^2);
    [bb, stdx, mse] = lscov(X,y,V);
    std = stdx*sqrt(1/mse);

%add results of GLS to an array
    newpts(u,1) = li_un;
    newpts(u,2) = pb_un;
    newpts(u,3) = ba_un;
    newpts(u,4) = bb(1);
    newpts(u,5) = stdx(1);
end

final = zeros(size(uncs));
nc = 1;

%make sure GLS TBR results > 0
for x=1:uncerts
    if newpts(x,4) >= 0
        final(nc,1) = newpts(x,1);
        final(nc,2) = newpts(x,2);
        final(nc,3) = newpts(x,3);
        final(nc,4) = newpts(x,4);
        final(nc,5) = newpts(x,5);
        nc = nc + 1;
    end
end

end

tbrold = tbr_un;
tbr_un = zeros(size(tbr_un));

%create new array of all ternary results
%with new results obtained with GLS
for j=1:lines
    tbr_un(j,1) = tbrold(j,1);
    tbr_un(j,2) = tbrold(j,2);
    tbr_un(j,3) = tbrold(j,3);
end

```

```
for y=1:size(final,1)
    if final(y,1) == tbrold(j,1)
        if final(y,2) == tbrold(j,2)
            if final(y,3) == tbrold(j,3)
                tbr_un(j,4) = final(y,4);
                tbr_un(j,5) = final(y,5);
            end
        end
    end
end
if tbr_un(j,4) == 0
    tbr_un(j,4) = tbrold(j,4);
    tbr_un(j,5) = tbrold(j,5);
end
end

display(uncerts);
display(nc);
final = final(1:nc-1,:);
%save array
filename = 'szn_55e3_3';
save(filename, 'tbr_un');
clear all;
```

Appendix G

SMORES Source Subroutine

The new SMORES subroutine, `source.f90`, is presented below:

```

subroutine source (tots,sou,adjoint)
!Author: AJolodosky

use All_Parameters, only : fs,as
use free_form
use fixit_C
use common_unit, only: outpt, i0, i1, i2, i3, i4

!variables
integer, intent(in) :: tots
real, intent(inout) :: sou(igm,tots)
logical, intent(in) :: adjoint
character(4) :: eword
character(8) :: sword
integer :: iret, i, g, snum, curr
real :: poop

iret = 0
      call scanon
write(outpt,*) adjoint
write(outpt,*) tots
if ( adjoint ) then
      snum = as
      sword = 'adjoint'
      write(outpt,*) as
else
      snum = fs
      sword = 'forward'
      write(outpt,*) fs
end if

```

```

do i = 1,snum
  if ( iret > 0 ) then
    curr = i - 1
    write(outpt,*) '*****ERROR*****'
    write(outpt,300) "With number of ",sword,"sources"
    write(outpt,100,advance='no') "Only",curr,&
      " instead of",snum
    write(outpt,200,advance='yes') ' '
    write(outpt,*) '*****ERROR*****'
    ierro = ierro + 1
    exit
  end if
do g=1,igm
!add value of input to new source array
  sou(g,i) = fread (i0,iret)
  !write(outpt,*) sou(g,i)
  if ( iret > 0 ) then
    if ( g < igm ) then
      write(outpt,*) '*****ERROR*****'
      write(outpt,400) "With ",sword,"source:",i
      write(outpt, 100 ,advance='no') " Only",g, &
        " energy groups instead of",igm
      write(outpt,200,advance='yes') ' '
      write(outpt,*) '*****ERROR*****'
      ierro = ierro + 1
      exit
    end if
  end if
end do
  eword = aread(i4,iret)
  write(outpt,*) eword
end do

100 format (a,2x,i3,a,2x,i3)
200 format (a)
300 format (a15,a8,a)
400 format (a7,a8,a8,i2)
end subroutine source

```